DISS. ETH NO. 26674

SEARCHES FOR SUPERSYMMETRY IN THE FULLY HADRONIC AND HIGGS TO DIPHOTON FINAL STATES

A thesis submitted to attain the degree of

DOCTOR OF SCIENCES of ETH ZURICH
(Dr. sc. ETH Zurich)

presented by

MYRIAM SCHÖNENBERGER

M.Sc.Physics, ETH Zurich

born on 9 April 1990
citizen of Mosnang SG

accepted on the recommendation of

Prof. Dr. R. Wallny, examiner
Prof. Dr. G. Dissertori, co-examiner

2020

Searches for physics beyond the Standard Model (SM) are a main focus of the physics program at the Large Hadron Collider at CERN. I present in this thesis two searches for supersymmetry (SUSY), using data collected with the Compact Muon Solenoid detector.

The first search is a broad range search for SUSY in the tails of the stransverse mass distribution M_{T2}. Data collected in the year 2016 corresponding to an integrated luminosity of 35.9 fb^{-1} are used to obtain data driven estimates of the $Z \to \nu\nu$, lost leptons and QCD multijet backgrounds. No sign of SUSY has been found. Upper limits on the production cross section of simplified models of SUSY are set. Gluino masses up to 2 TeV are excluded for a massless lightest supersymmetric particle (LSP). Squark masses up to 1 TeV(1.6 TeV) for one (four) light squark type(s) for a massless LSP are excluded.

The second search explores strong and electroweak SUSY production through the final state of a Higgs boson decaying to a photon pair analyzing 77.5 fb^{-1} of integrated luminosity collected in 2016 and 2017. The nonresonant diphoton background is estimated from fits to the data, while the resonant background from the SM Higgs boson production is estimated from simulation. To increase sensitivity with respect to the backgrounds, categories with leptons, jets, b-tagged jets, M_{T2} and the transverse momentum of the Higgs boson are employed.

No significant excess over the SM prediction is found. Upper limits on the production cross section of simplified models of SUSY are set. Bottom squark masses up to 530 GeV are excluded for a massless LSP. For wino-like chargino-neutralino production masses below 220 GeV for a gravitino LSP mass of 1 GeV are excluded. For the higgsino-like chargino-neutralino production with 100% branching fraction $\tilde{\chi}_1^0 \to H\tilde{G}$ masses up to 275 GeV and with 50% branching fraction to $\tilde{\chi}_1^0 \to H\tilde{G}$ and $\tilde{\chi}_1^0 \to Z\tilde{G}$ masses up to 190 GeV are excluded for a gravitino mass of 1 GeV.

Eines der Hauptziele des Physikprogammes am Large Hadron Collider am CERN ist die Suche nach neuen physikalischen Phänomenen, die über das Standard Modell (SM) hinausreichen. Ich präsentiere in dieser Doktorarbeit zwei Suchen nach Supersymmetrie (SUSY) mit Daten des Compact Muon Solenoid (CMS) Experimentes am CERN.

Die erste Suche ist eine breit gefächerte Suche nach SUSY in den Ausläufern der M_{T2} Verteilung. Die Daten des Jahres 2016 mit einer integrierten Luminosität von 35.9 fb^{-1} werden benutzt für die Abschätzung der $Z \to \nu\nu$, abhandengekommenen Leptonen und QCD Multijet Hintergründe. Es wurde kein Indiz für SUSY gefunden und obere Grenzen für die Produktionswirkungsquerschnitte von vereinfachten SUSY Modellen werden gesetzt. Für ein masseloses leichtestes supersymmetrisches Teilchen (LSP) werden Gluinomassen von bis zu 2 TeV ausgeschlossen. Bei einer (vier) leichte(n) Squark Art(en) für ein masseloses LSP werden Squarkmassen von bis zu 1 TeV (1.6 TeV) ausgeschlossen.

Die zweite Suche, durchgeführt mit einem Datensatz von 77.5 fb^{-1} an integrierter Luminosität, erfasst in den Jahren 2016 und 2017, beschäftigt sich mit der SUSY Produktion mittels der starken und elektroschwachen Wechselwirkung im Endzustand mit einem Higgs-Boson, das zu einem Photonenpaar zerfällt. Der nichtresonante Hintergrund von zwei Photonen ist gefitted an den Daten. Der resonante Hintergrund von Higgs-Bosonen produziert im SM ist abgeschätzt mittels Simulation. Um die Sensitivität gegenüber diesen Hintergründen zu verbessern, werden die Ereignisse in Regionen mit Leptonen, Jets, b-tagged Jets, M_{T2} und dem transversalen Impuls des Higgs-Bosons kategorisiert. Kein signifikanter Überschuss an Ereignissen über der Erwartung vom SM wurde gefunden und obere Grenzen für die Produktionswirkungsquerschnitte von vereinfachten SUSY Modellen werden gesetzt. Bottom-Squarkmassen bis zu 530 GeV sind ausgeschlossen für ein masseloses LSP. Für wino-mässige Chargino-Neutralino Produktion sind Massen bis 220 GeV für eine Gravitinomasse von 1 GeV ausgeschlossen. Für die higgsino-mässige Chargino-Neutralino Produktion bei einer Gravitinomasse von 1 GeV mit 100% Zerfallswahrscheinlichkeit $\tilde{\chi}_1^0 \to H\tilde{G}$ sind Massen bis zu 275 GeV ausgeschlossen, während für das Modell mit jeweils 50% Zerfallswahrscheinlichkeit $\tilde{\chi}_1^0 \to H\tilde{G}$ und $\tilde{\chi}_1^0 \to Z\tilde{G}$ Massen bis zu 190 GeV ausgeschlossen sind.

Contents

1 Introduction 1

I Theoretical background 3

2 The Standard Model 4
2.1 The particles of the SM . . . 4
2.2 Symmetries and gauge fields . . . 6
2.3 The SM symmetry group . . . 7
2.3.1 Quantum chromodynamics . . . 7
2.3.2 The electroweak interaction . . . 7
2.4 The SM Higgs boson . . . 9
2.5 The experimental success of the SM . . . 11

3 Supersymmetry 13
3.1 Unsolved problems of the SM . . . 13
3.2 The concept of SUSY . . . 14
3.3 Minimal supersymmetric standard model . . . 15
3.4 Simplified models of SUSY . . . 17

II Experimental setup 21

4 CERN and the Large Hadron Collider 22

5 The Compact Muon Solenoid detector 25
5.1 Tracker system . . . 27
5.1.1 Inner Tracker system: Pixels . . . 27
5.1.2 Outer Tracker system: Strips . . . 28
5.2 Electromagnetic calorimeter . . . 28
5.3 Hadronic calorimeter . . . 30
5.4 Solenoid . . . 31
5.5 Muon systems . . . 32
5.6 Trigger system and data acquisition . . . 33

6 Reconstruction 35
6.1 Track construction . . . 35

6.2 Vertex reconstruction . . . 35
6.3 Calorimeter cluster reconstruction . . . 36
6.4 The particle flow algorithm . . . 36
6.5 Physics objects . . . 37
6.6 Higher level objects . . . 40

III Search for SUSY in the fully hadronic final state **45**

7 Final states with large M_{T2} **46**
7.1 Selection . . . 46
7.1.1 Trigger . . . 46
7.1.2 Simulation . . . 47
7.1.3 Baseline selection . . . 48
7.2 Classification . . . 50
7.3 Backgrounds . . . 54
7.3.1 QCD multijet . . . 54
7.3.2 Lost lepton . . . 64
7.3.3 Z to invisible . . . 70
7.4 Results . . . 77
7.4.1 Signal regions . . . 77
7.4.2 Super signal regions . . . 78
7.4.3 Interpretation in the context of simplified models of SUSY . . . 83
7.5 Conclusion . . . 88

IV Search for SUSY in the diphoton final state **89**

8 Final states with a Higgs boson decaying to two photons **90**
8.1 Selection . . . 91
8.1.1 Trigger . . . 91
8.1.2 Simulation . . . 91
8.1.3 Nonresonant photon suppression . . . 92
8.1.4 Baseline selection . . . 92
8.2 Classification . . . 94
8.3 Background estimation . . . 100
8.3.1 Nonresonant background . . . 100
8.3.2 Resonant background . . . 102
8.3.3 Systematic and statistical uncertainties . . . 103
8.4 Results . . . 104
8.4.1 Signal regions . . . 104
8.4.2 Interpretation in the context of simplified models of SUSY . . 106
8.5 Conclusion . . . 112

9 Conclusion 113

A Statistical method for signal extraction 115
A.1 Likelihood 115
A.2 Nuisance parameters 116
A.3 Test statistic and CL_s method 117

B Additional material on the search for SUSY in the fully hadronic final state 119
B.1 Alternative representation of results 119
B.2 Event display 129

C Additional material of the search for SUSY in the diphoton final state 131
C.1 Distribution of the kinematic variables 131
C.2 Nonresonant background fits 132
C.3 Event display 143

D Bibliography 145

E Acknowledgement 159

1 Introduction

Particle physics aims to describe and predict the constituents of the universe. The theory of the fundamental particles and forces by which they interact is called the Standard Model (SM) of particle physics which allows to describe a variety of processes. The Higgs boson discovery in 2012 completed the electroweak sector of the SM. But open questions remain about dark matter, how gravity could be integrated into the SM and many more.

One possible solution to some of the open problems comes via introducing an additional symmetry, the so called Supersymmetry (SUSY), which relates fermions and bosons to each other. In this way for each particle of the SM there is a SUSY partner particle with the spin shifted by 1/2. SUSY could manifest itself in two ways, either by the direct observation of heavy particles or through comparing precision measurements with theory predictions of rare processes, where SUSY particles contribute in the higher order corrections.

The searches for SUSY presented in this thesis are searches for strong and electroweak production of SUSY particles with data collected by the Compact Muon Solenoid (CMS) experiment in proton-proton collision at the Large Hadron Collider (LHC) at CERN. Two complementary searches are presented that test the theory at the energy frontier in the hard and the soft limit of the missing transverse energy.

This thesis is structured in four parts outlining the theoretical background in Part I, and the experimental background in Part II, followed by the two analyses in Part III and IV. I will start by summarizing the Standard Model of particle physics in Chapter 2. After showing its huge success in describing and predicting particle interactions, I will proceed to mention many of its shortcomings, segueing into the need for an extension of the model. One possible solution is SUSY, described in Chapter 3. The data used for the analyses come from high energy proton-proton collision provided by the LHC at CERN, described in Chapter 4, which are collected by the CMS experiment at the LHC described in Chapter 5. The event reconstruction is described in Chapter 6. Then it is finally time for the two searches for SUSY: Part III describes the fully hadronic search at the energy frontier; Part IV on the other hand describes the search with a Higgs boson decaying to two photons in the final state. The conclusions and outlook are summarized in Chapter 9. A brief discussion of the statistical methods necessary to extract results from the millions of events analyzed can be found in Appendix A.

Part I

Theoretical background

γνῶθι σεαυτόν

Ancient Greek aphorism

2 The Standard Model

Before diving into the unknown and possible signs of new physics, I will give a short description of the known particle physics and the way to describe it: the Standard Model (SM)[1]. I will not be able to cover all of the theory contributing in one way or another to the searches presented in this thesis, nor can I give a full account with the quality given elsewhere. The aim is rather to show the bits and pieces relevant for the later parts of this thesis describing the searches physics beyond the known, and to set the foundation for the next Chapter 3, where I will name multiple problems that the SM cannot answer and offer one possible solution.

First the particles of the SM are introduced in Section 2.1. In Section 2.2 the importance of gauge symmetries and in particular the gauge symmetries of the SM are outlined. The SM Higgs boson is of particular importance for the second analysis presented in this thesis and thus further important features are discussed in Section 2.4. Finally in Section 2.5 the experimental success of the SM is highlighted.

The description below follows the ones given in Ref. [1] and [2]. The notation in this thesis uses the Einstein summation convention and natural units. The electric charges are given in units of the absolute electron charge.

2.1 The particles of the SM

Quantum field theory (QFT) unites quantum mechanics and special relativity into one framework. The excitations of its constituents, the quantized fields, are the elementary particles that make up all matter and mediators of interactions. There are two types of particles:

- Fermions: spin $S = n + \frac{1}{2}, n \in \mathbb{N}$
- Bosons: spin $S = n, n \in \mathbb{N}$

The most important difference between them is that fermions have been shown follow the *Pauli exclusion principle*, according to which two (or more) identical fermions cannot occupy the same quantum state simultaneously. From this simple principle follow the electron "shells" of atoms, and thus the properties of the atoms. The general formalization of the exclusion principle means that the wave function of

[1]For some reason the name "Model" stuck, albeit that it is much more than a mere description of the observed data. This footnote is dedicated to the stranger going through the paper waste of my apartment building striking up a discussion about the difference between models and theories.

fermions transforms anti-symmetrically under their exchange[2].

Table 2.1 lists the known fermions of the SM with their mass and electric charge. There are three generations of two types of fermions, the leptons and the quarks, where only the later carry a color charge. All charged fermions have a corresponding antiparticle with the exact same properties as the particle except for the charge. In Table 2.2 the known bosonic particles of the SM are listed. The spin-1 bosons stem from the vector fields in the theory and are responsible for the interactions between particles. In Section 2.3.2 the way in which some of these bosons acquire mass is outlined. This mechanism gives rise to a spin-0 boson, the Higgs boson.

Table 2.1: List of the 3 generations of fermions of the SM with their mass and electric charge [4]. The neutrino flavor eigenstate masses are unknown and thus denoted with a "-".

Type	Generation	Particle	Mass	Charge
Leptons	1	e	511 keV	-1
		ν_e	-	0
	2	μ^-	105.7 MeV	-1
		ν_μ	-	0
	3	τ^-	1.777 GeV	-1
		ν_τ	-	0
Quarks	1	u	2.2 MeV	2/3
		d	4.7 MeV	-1/3
	2	c	1.275 GeV	2/3
		s	95 MeV	-1/3
	3	t	173 GeV	2/3
		b	4.18 GeV	-1/3

[2]In terms of everyday macroscopic physics, one would need to turn it by 720°, instead of only 360°, to reach its original orientation. An example in real life is to take a full glass and dance a Filipino dance called Binasuan, as demonstrated in Ref. [3].

Table 2.2: List of the bosons of the SM with their mass, electric charge and spin [4].

Particle	Mass	Charge	Spin
γ	0 eV	0	1
Z	91.2 GeV	0	1
$W^{\pm}$	80.4 GeV	± 1	1
g	0 eV	0	1
H	125.2 GeV	0	0

2.2 Symmetries and gauge fields

From Noether's theorem [5] follows that due to the invariance under symmetry transformations there are currents that are conserved, one current per generator of the symmetry[3].

There are two types of symmetries for elementary particles:

- Space-time symmetries act on the space-time coordinates:

$$x^{\mu} \mapsto x'^{\mu}(x^{\nu}), \mu, \nu \in 0, 1, 2, 3 \tag{2.1}$$

  For the SM, these are the Poincaré transformations in 4 dimensions.

- Internal symmetries act on the fields:

$$\phi^{\mu}(x) \mapsto \Lambda^{\mu}{}_{\nu}(x)\phi^{\nu}(x), \tag{2.2}$$

  where $\Lambda^{\mu}{}_{\nu}(x)$ is called a local or gauge symmetry if it depends on the position x, else it is called a global symmetry. In terms of the SM, it is described by the gauge symmetry $SU(3)_c \times SU(2)_L \times U(1)_Y$.

The importance of these symmetries becomes apparent in the example of a scalar field ϕ and the following Lagrangian:

$$\mathcal{L} = \partial_{\mu}\phi\partial^{\mu}\phi^{*} - V(\phi, \phi^{*}), \tag{2.3}$$

which is invariant under the rotation

$$\phi \mapsto \exp(i\alpha)\phi, \tag{2.4}$$

as long as α is a constant. If it depends on the position x, the covariant derivative has to be introduced

$$D_{\mu}\phi = \partial\phi_{\mu} + iA_{\mu}\phi. \tag{2.5}$$

[3] There are specific requirements on the type of symmetry for this theorem to hold, please refer to the Ref. [5] for further details.

If the potential A_μ transforms as $A_\mu - \partial_\mu \alpha$ the rewritten Lagrangian is gauge invariant:

$$\mathcal{L} = D_\mu \phi (D^\mu \phi)^* - V(\phi, \phi^*). \tag{2.6}$$

This gives then the interaction of the scalar field ϕ with the gauge field A_μ via the term $A_\mu \phi A^\mu \phi$. Similarly for the Dirac Lagrangian one ends up with the interaction $\bar{\psi} A_\mu \psi$, which in terms of the SM corresponds to the electromagnetic (EM) vertex.

No gauge invariant mass term (i.e. quadratic in A_μ) can be added to the Lagrangian, resulting in massless gauge fields, which at first glance contradicts the observation of the massive vector bosons W and Z. How their masses are introduced into the theory is desribed in the next section.

2.3 The SM symmetry group

The SM is described by the gauge symmetry group

$$SU(3)_c \otimes SU(2)_L \otimes U(1)_Y,$$

whose most important features I will discuss in the following.

2.3.1 Quantum chromodynamics

The *strong force* is described by Quantum Chromodynamics (QCD) which follows the $SU(3)_c$ gauge symmetry[4] with 8 generators corresponding to the 8 massless gluons. Since it is a non-abelian gauge theory the gluons carry color charge and self-interact, which leads to the short range of the strong interaction. As the coupling strength α_s increases with distance, no free colored particles are observed, and the color charge is confined in the hadrons, while as the distance decreases the color charged particles are asymptotically free [6]. For the experimental side this means that in the detector not single quarks and gluons are observed but they undergo a process called *hadronization*, where color neutral particles are created. The resulting collimated spray of particles is bunched together and called a jet.

2.3.2 The electroweak interaction

The electroweak (EW) sector is based on the $SU(2)_L \otimes U(1)_Y$ symmetry group. This group has 4 generators, 3 for $SU(2)_L$ called A^a_μ, $a = 1, 2, 3$, and 1 for $U(1)_Y$ called B_μ. The γ, Z and $W^\pm$ boson are mixed states of these generators as shown later. As a gauge theory the gauge bosons would be massless but only the photon fulfills this, while the Z and $W^\pm$ boson are massive as observed in experiment.

[4]The subscript c stands for color, as does the name *chromo*. The reasoning is that red, blue and green light summed up result in color neutral white light, similar to how the three quarks in a baryon result in a colorless state when summed up.

The electroweak Lagrangian consists of the following parts:

$$\mathcal{L}_{EW} = \mathcal{L}_{fermion} + \mathcal{L}_{gauge} + \mathcal{L}_H + \mathcal{L}_{Yukawa}$$

The interaction of the particles and the gauge fields are introduced again via the covariant derivative:

$$D_\mu = \partial_\mu - igA^a_\mu t^a - ig\prime YB_\mu,$$

where g and $g\prime$ are the coupling strengths of the $SU(2)_L$ weak isospin and $U(1)_Y$ hypercharge, respectively.

The weak force makes a distinction between right and left-handed fermions $\psi_{LR} = (1\pm\gamma_5)\psi$. The kinetic term can thus be split into the right and left-handed components:

$$\mathcal{L}_{fermion} = \bar{\psi_R}\not{D}\psi_R + \bar{\psi_L}\not{D}\psi_L,$$

where ψ_L transforms as a doublet and ψ_R as a singlet. Explicitly the covariant derivative acts on the spinors as:

$$D_\mu\psi_L = (\partial_\mu - igA^a_\mu t^a - ig\prime B_\mu Y)\psi_L, \quad D_\mu\psi_R = (\partial_\mu - ig\prime B_\mu Y)\psi_R$$

This difference of the weak interaction on left and right handed fermions gives rise to various asymmetries that have been experimentally measured.

The field strength tensors are given by $A^a_{\mu\nu} = \partial_\mu A^a_\nu - \partial_\nu A^a_\mu - g\epsilon^{abc}A^b_\mu A^b_\nu$ and $B_{\mu\nu} = \partial_\mu B_\nu - \partial_\nu B_\mu$ and thus the gauge interaction term in the Lagrangian reads as:

$$\mathcal{L}_{gauge} = -\frac{1}{4}A^a_{\mu\nu}A^{\mu\nu}_a - \frac{1}{4}B_{\mu\nu}B^{\mu\nu}.$$

To obtain the boson masses in a gauge symmetry conserving way, a complex scalar field ϕ is introduced via the Brout–Englert–Higgs mechanism [7–9]. The Higgs boson has a nonzero vacuum expectation value (vev), thus the $SU(2)_L \otimes U(1)_Y$ is *spontaneously broken.*

The Higgs boson part of the EW Lagrangian then reads

$$\mathcal{L}_{Higgs} = |D_\mu\phi|^2 + V(\phi)$$

with the Higgs potential

$$V(\phi) = \mu^2|\phi|^2 + \lambda|\phi|^4,$$

with $\mu^2 < 0$. The potential is visualized in Figure 2.1, from where it can be seen, that the minimum of the potential occurs at a nonzero vev of ϕ. Explicitly the vacuum expectation value can be expanded around one direction:

$$\langle\phi\rangle = \frac{1}{\sqrt{2}}\begin{pmatrix}0\\ v\end{pmatrix}.$$

The $U(1)_Y$ symmetry remains unbroken, leaving a massless photon, while the other EW bosons acquire a mass term.

Plugging the vev v into the kinetic term $|D_\mu\phi|^2$, the mass eigenstates and masses are obtained:

$$W^{\pm} = \frac{1}{\sqrt{2}}(A^1 \mp iA^2) \qquad m_W^2 = \frac{g^2v^2}{4}$$
$$Z = \frac{1}{\sqrt{g^2 + g\prime^2}}(gA^3 - g\prime B) \qquad m_Z^2 = \frac{(g^2 + g\prime^2)v^2}{4}$$
$$A = \frac{1}{\sqrt{g^2 + g\prime^2}}(g\prime A^3 + gB) \qquad m_A^2 = 0,$$

where the field A is identified as the photon γ.

Lastly the Yukawa coupling of the massive fermions with the Higgs boson introduces the mass terms in the Lagrangian of the form

$$\mathcal{L}_{Yukawa} = \frac{g_f v}{\sqrt{2}}\bar{\psi}_f\psi_f,$$

where the fermion mass $m_f = \frac{g_f v}{\sqrt{2}}$ depends on the coupling g_f of the fermion to the Higgs field. The fermion masses are thus free parameters of the theory that need to be measured.

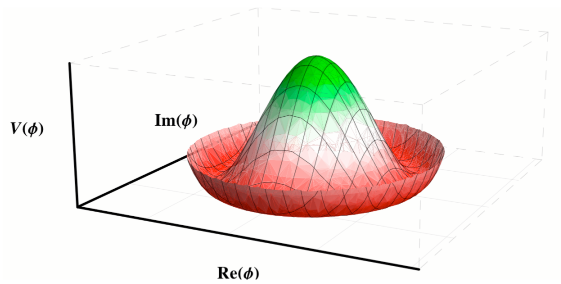

Figure 2.1: The so called Mexican hat potential of the Higgs field [10].

2.4 The SM Higgs boson

In Figure 2.2 the leading order production Feynman diagrams of a Higgs boson at the LHC for proton-proton collisions are shown. Although the Higgs boson does not directly couple to gluons, the dominant process in which it is produced is via gluon-gluon fusion (ggF). Other processes include vector boson fusion (VBF), the associated production with a vector boson (VH) or a pair of top or bottom quarks (ttH and bbH, respectively). Smaller contributions are negligible for the later introduced search and are thus omitted here. Figure 2.4 shows the production cross sections for the leading contributions as a function of the Higgs boson mass.

Similarly to the gluons the Higgs boson does not couple directly to photons. Thus all the leading order decay diagrams shown in Figure 2.3 contain loops, where the top quark gives the largest contribution in the fermion loop and the W boson gives

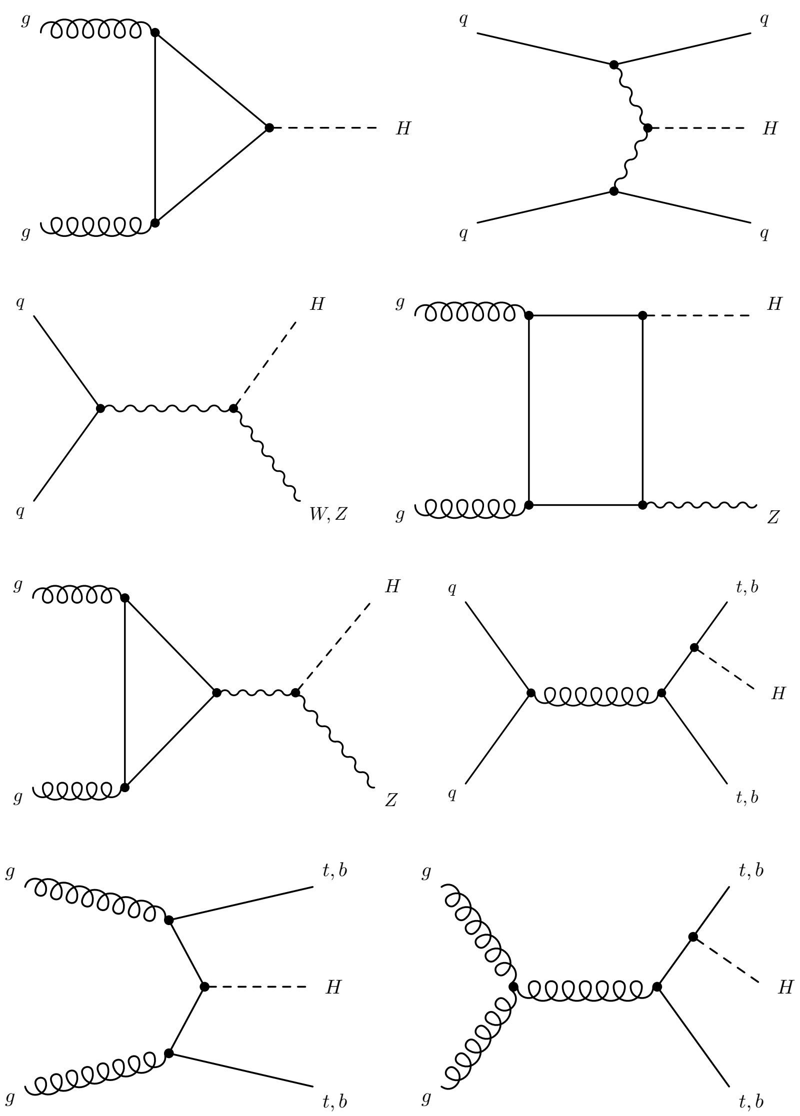

Figure 2.2: The leading order production processes for a Higgs boson as relevant for the analysis described in Chapter 8 [11].

the largest contribution in the scalar loop. Cancellations between the fermion and scalar loops lead to the small branching fraction of about 0.227% at 125 GeV, as is shown in Figure 2.4 (right), where the various branching fractions are shown as a function of the Higgs boson mass.

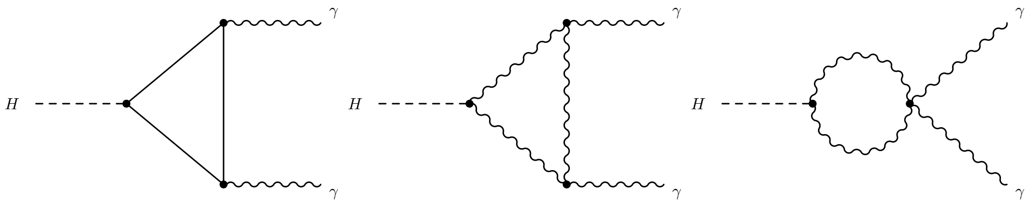

Figure 2.3: The leading order Feynman diagrams for the decay of a Higgs boson to two photons [11].

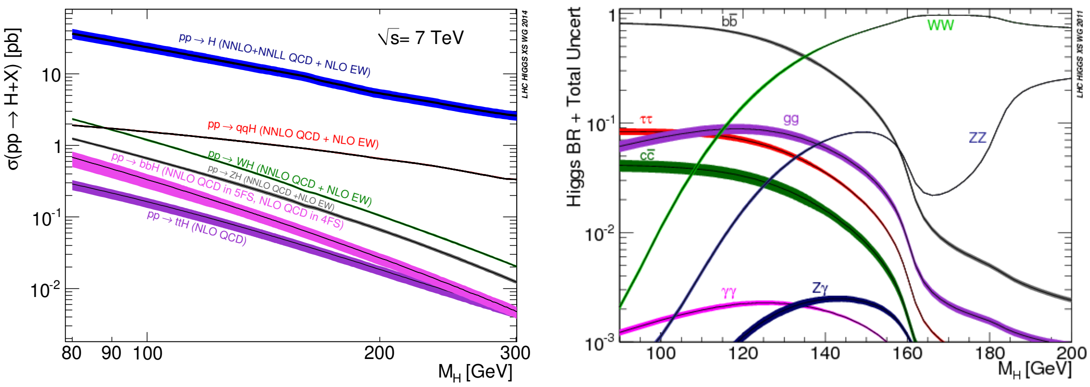

Figure 2.4: (Left) Higgs boson production cross sections at 7 TeV with the different channels indicated on the figure [12]. (Right) Higgs boson branching fractions as a function of the Higgs boson mass m_H [13].

2.5 The experimental success of the SM

The SM is able to describe vastly different processes. Figure 2.5 summarizes the measurements by the CMS collaboration (see Chapter 5), where cross sections spanning 9 orders of magnitude have been determined for the three center of mass energies of 7, 8 and 13 TeV.

It is also worth noting that the various Higgs boson branching fractions as shown in Figure 2.4 only depend on the mass of the Higgs boson m_H. Once this free parameter was measured the branching fractions were determined. Measuring the few free parameters of the SM thus allows to predict various processes.

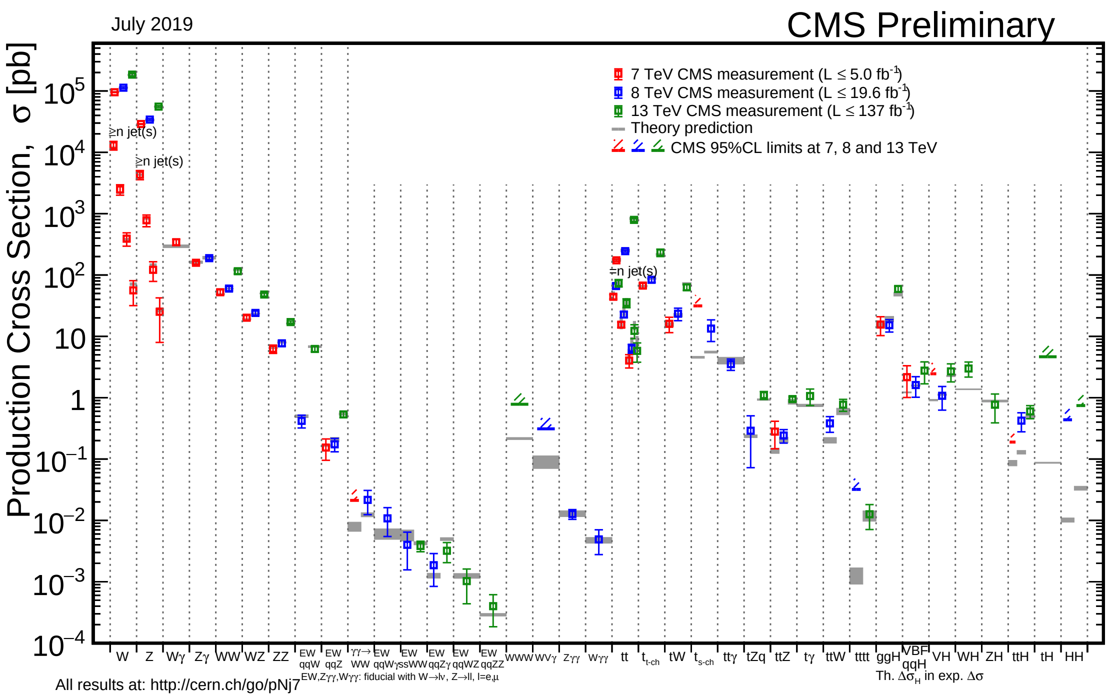

Figure 2.5: Summary of the cross section measurements of CMS at the different center of mass energies and integrated luminosities, along with the theory predictions and upper limits, where the data is not yet sufficient for a discovery [14].

3 Supersymmetry

The standard model describes and predicts a large number of phenomena. There are some pathological and aesthetic problems inherent to it, though. Many possible models that try to explain these discrepancies have been studied and tested. Supersymmetry (SUSY) is one of the few theories that has survived to this day as a viable option. At the same time it has also not been confirmed experimentally yet, thus motivating the writing of this thesis.

Similar to the matter-antimatter symmetry where each particle has an antiparticle partner with the charge flipped, SUSY introduces for every particle a SUSY particle, a sparticle, with the spin changed by $1/2$. Thus the fermions of the SM have bosonic superpartners and the bosons of the SM have a fermionic superpartner.

In Section 3.1 I will first introduce some of the problems of the SM to motivate searches for physics beyond the SM. Then the solution of some of these problems via SUSY is introduced in Section 3.2. The minimal supersymmetric extension of the SM is introduced in Section 3.3. The two searches presented later look for SUSY in two very different final states. Their simplified models of SUSY are introduced in Section 3.4.

3.1 Unsolved problems of the SM

While the previous chapter highlighted how well the SM describes the electroweak and strong interaction, one of the most important forces in everyday life has no renormalizable description in the SM yet: gravity. The discovery of gravitational waves by the LIGO and Virgo collaborations [15] affirmed the predictions of general relativity, but at small distances the description of gravity as a QFT breaks down. The spin-2 "quantum" of gravity, the graviton, thus neither has a description in the SM nor has there been an observation of such a spin-2 particle.

Astrophysical observations suggest the existence of dark matter (DM) which largely outweighs the observed matter at 27% versus 5%, with the remainder being dark energy [16]. This dark matter only interacts via the gravitational force but not the electromagnetic nor the strong force. This suggests the existence of a particle responsible for dark matter, but no such particle has been observed.

The vacuum energy (cosmological constant Λ) predicted by QFT is 120 orders of magnitudes larger than the observed values [17]. Furthermore the SM can not explain the baryon asymmetry of the universe.

The Higgs mechanism introduces the mass terms for all particles but the neutrinos, which have been observed to oscillate between their flavors and thus must be massive [18, 19]. How a mass term could be incorporated is currently the subject of many theories.

Since the Higgs boson couples to every massive particle, its mass becomes sensitive to the heaviest particle in the theory through quantum loop corrections. The ultraviolet cutoff scale Λ_{UV} is introduced to remove the divergences occurring in the integral over the momentum, that would in principle run to infinity. For a quantum field theory to be renormalizable the physical quantities have to be independent of Λ_{UV}. The contribution from a fermion of the form of $\Delta m_H = -\frac{|\lambda_f|^2}{8\pi}\Lambda_{UV} + ...$ to the Higgs boson mass either means a break down of the theory at the Planck scale without fine tuning or new phenomena have to be introduced above the electroweak scale such that the contribution cancels. The necessity of the fine tuning in the SM is called the hierarchy problem.

The reasons above and many more motivate searches for new physics beyond the SM. In the following I will outline how supersymmetry could solve some of these problems.

3.2 The concept of SUSY

The SUSY generator Q takes a fermionic state and turns it into a bosonic state, and vice versa:

$$Q\,|\text{Boson}\rangle = |\text{Fermion}\rangle\,, \qquad Q\,|\text{Fermion}\rangle = |\text{Boson}\rangle \tag{3.1}$$

In this way, SUSY introduces a supersymmetric partner to every SM particle, a scalar for a fermion, denoted by adding an "s" in front of the particle name, and a fermion for a scalar, denoted by the ending "-ino". The SUSY partner particle is called sparticle and they are denoted by a $\tilde{}$.

The particle and the sparticle are then part of the same supermultiplet. Since Q commutes with all of the SM gauge symmetries the entries of the supermultiplet have the same charges and mass [20]. As the sparticles have not been observed, the supersymmetry must be broken to allow masses to be heavier. This means that there is a scale Λ_{SUSY} above which the symmetry is fulfilled, while below this scale the symmetry is either broken spontaneously or softly.

By introducing a scalar sparticle for every SM fermion, the 1-loop correction to the Higgs mass, depicted in Figure 3.1, has a contribution not only from the top quark but also from its SUSY partner, the top squark or stop, that will cancel out in the sum. Explicitly the fermion loop gives

$$\Delta m_H^2 = -\frac{|\lambda_f|^2}{8\pi^2}\Lambda_{UV}^2 + ...$$

and the scalar loop gives

$$\Delta m_H^2 = \frac{\lambda_s}{16\pi^2}\Lambda_{UV}^2 + ...$$

The Higgs boson mass is thus sensitive to the heaviest particle in the theory unless there is a symmetry between fermions and scalars such that their contributions cancel. SUSY thus provides an elegant solution to the hierarchy problem.

Figure 3.1: The Higgs boson mass quantum correction at the 1-loop level from a fermion (left) and scalar (right) [20].

A side effect of SUSY is grand unification of the gauge couplings at a large energy scale ($\approx 10^{16}$ GeV). In this way the symmetry group of the SM $SU(3)_c \otimes SU(2)_L \otimes U(1)_Y$ is then the result of a broken $SU(5)$ or a higher rank symmetry group. Figure 3.2 shows the running coupling constants for the SM (left) and their grand unification in the case of a realization of SUSY, the MSSM, (right), which I will introduce next.

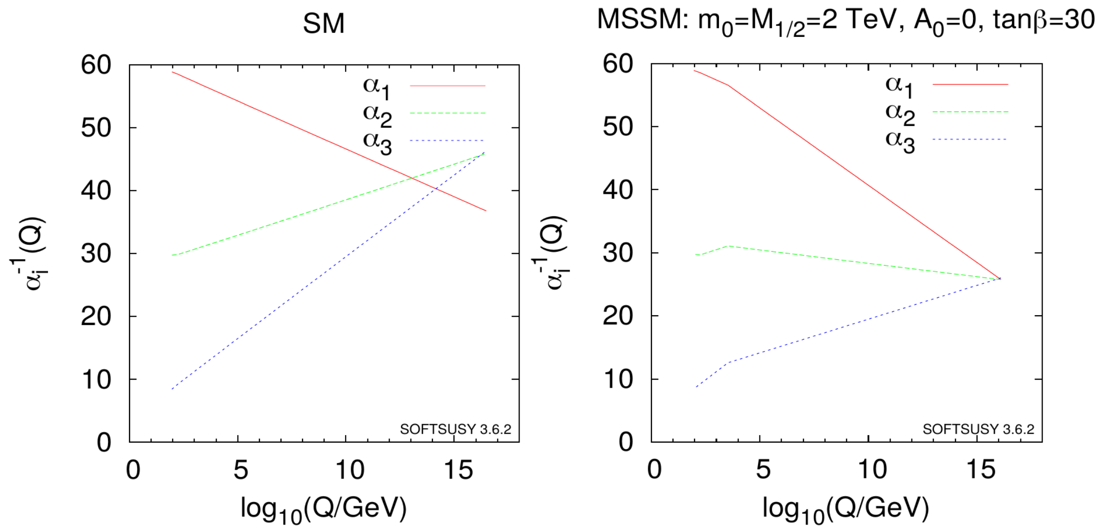

Figure 3.2: The running coupling constants for the SM (left) and the MSSM (right) [4].

3.3 Minimal supersymmetric standard model

The minimal supersymmetric extension of the standard model (MSSM) is a version of SUSY with the minimal particle content [20]. Table 3.1 lists the supermultiplets of the MSSM. The fermionic superpartner of the Higgs boson has a weak hypercharge of $Y = \pm 1/2$. Therefore two Higgs supermultiplets have to be introduced, one for each sign of the weak hypercharge, such that the electroweak gauge anomaly cancels [20].

The SUSY partners of the EW fields, the gauginos, and of the Higgs field, the higgsinos, mix into mass eigenstates that are electrically neutral, the neutralinos $\tilde{\chi}^0$, and charged, the charginos $\tilde{\chi}^{\pm}$.

Table 3.1: List of the chiral and gauge supermultiplets of the MSSM [20].

Name		spin 0	spin 1/2
squarks, quarks	Q	$\tilde{u}_L\,\tilde{d}_L$	$(u_L\,u_L)$
(3 families)	$\bar{u}$	$\tilde{u}^*_R$	$u^\dagger_R$
	$\bar{d}$	$\tilde{d}^*_R$	$d^\dagger_R$
sleptons, leptons	L	$\tilde{\nu}\,\tilde{e}_L$	$(\nu\,e_L)$
(3 families)	$\bar{e}$	$\tilde{e}^*_R$	$e^\dagger_R$
Higgs, higgsinos	H_u	$(H_u^+\,H_u^0)$	$(\tilde{H}_u^+\,\tilde{H}_u^0)$
	H_d	$(H_d^0\,H_d^-)$	$(\tilde{H}_d^0\,\tilde{H}_d^-)$
		spin 1/2	spin 1
gluino, gluon		$\tilde{g}$	g
winos, A bosons		$\tilde{A}^i$	A^i
bino, B boson		$\tilde{B}$	B

The predictions of any model of new physics have to comply with the observations of nature thus far. Since the supersymmetric partners of the known particles have not been observed at the same mass, SUSY has to be broken. In this way different masses for the particle and sparticle are introduced that allow to describe the SM as an effective field theory of SUSY. This symmetry breaking introduces further degrees of freedom though, notably the masses of the sparticles and the couplings, which are a priori unknown, have to be measured.

R-parity

The proton has a lifetime $> 10^{34}$ years [21]. Within the MSSM decays of the form shown in Figure 3.3 would result in a faster decay than observed. To avoid this unphysical effect a discrete symmetry is commonly introduced. This R-parity is defined as:

$$R_p = (-1)^{2s+3B+L} = \begin{cases} 1 & \text{for SM particles} \\ -1 & \text{for superpartners} \end{cases} \tag{3.2}$$

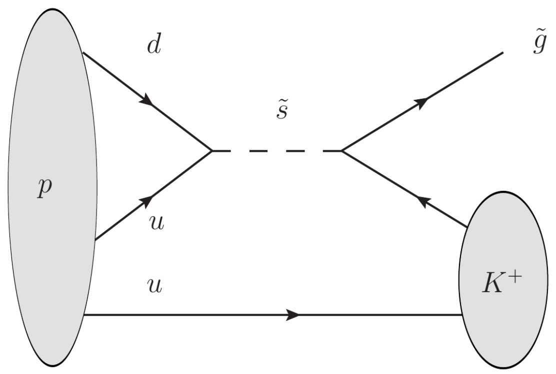

Figure 3.3: Possible proton decay diagram that would lead to a proton lifetime shorter than observed, in the case of an R-parity violating SUSY model [22].

where s is the spin, B is the baryon number and L is the lepton number.

The most important implications of R-parity conservation are that SUSY particles are created in pairs and that the Lightest Supersymmetric Particle (LSP) is stable and thus a DM candidate if it is neutral. Heavier SUSY particles will undergo decay chains where at least one LSP is produced.

3.4 Simplified models of SUSY

The MSSM has a lot of free parameters opening a phase space that we are not yet able to scan in its entirety. The ATLAS and CMS collaborations make use of simplified models of SUSY (SMS) [23–27], where the complexity is reduced by categorization according to their final states. Generally only the lightest and next-to-lightest supersymmetric particle are considered to be light enough to be detectable, while the rest of the SUSY spectrum is decoupled, meaning their masses are set to high values, such that they play no role in the decay chains of the other sparticles. Simplistic branching fractions are assumed, meaning that the decays have a 100% decay rate to a given final state or are simple mixes of two such processes.

The production cross section depends on the mass of the particles produced. This means the cross section decreases as the SUSY particle mass increases. The cross sections for strong and EW production as a function of the mass of the particle are shown in Figure 3.4.

The electroweak (neutralino and chargino) production cross sections are much smaller than the strong (gluino and squark) production. As the integrated luminosity at the LHC increases these rarer processes become accessible as well.

Simplified models of SUSY with fully hadronic final states

The models of SUSY considered for the first analysis are shown in Figure 3.5 where the LSP is the $\tilde{\chi}_1^0$. The first row are gluino mediated quark pair productions. In the

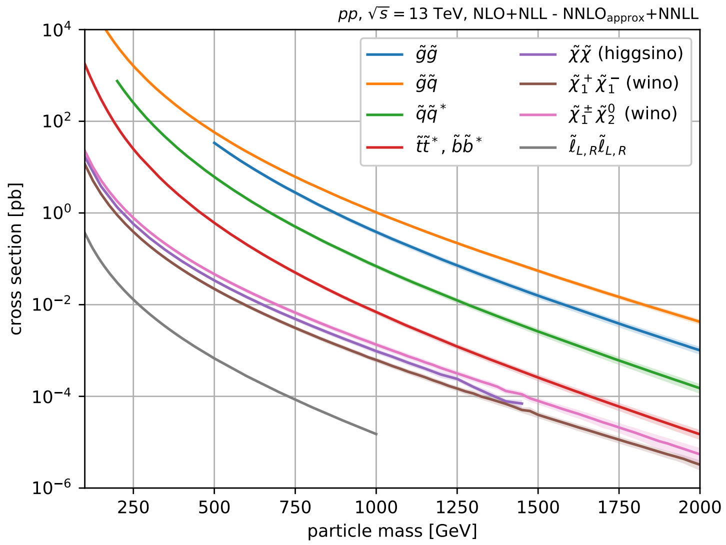

Figure 3.4: The cross sections of the SUSY production models as a function of the particle mass. The electroweak production cross sections of charginos and neutralinos (purple, brown and pink lines) are 1-2 orders of magnitude smaller than the strong production of gluinos and squarks (blue, orange, green and red lines) [28].

second row direct squark pairs are produced. Then finally in the third row alternative decay modes are considered for the top squark; these models allow to test the phase space where the mass difference $\Delta m = m_{\tilde{t}} - m_{\tilde{\chi}_1^0}$ is smaller than the top quark mass as shown in Figure 3.6. In Figure 3.5 (bottom left) the mass splitting reaches the minimum at the diagonal with the W boson mass, while in Figure 3.5 (bottom right) the splitting is smaller than the W boson mass and the top squark directly decays to the neutralino and a charm quark. Figure 3.5 (bottom center) considers a mixed model with a 50% branching fraction to either the top quark and neutralino or to a W boson, b quark and a neutralino via a chargino.

Simplified models of SUSY with a Higgs boson in the final state

In Figure 3.7 the SUSY models for the second analysis are shown. The bottom squark pair production model (Figure 3.7 top left) assumes again that all other SUSY particles are decoupled. Each of the bottom squarks decays to a bottom quark and a $\tilde{\chi}_2^0$. The $\tilde{\chi}_2^0$ subsequently decays to the $\tilde{\chi}_1^0$ and a Higgs boson. The neutralinos $\tilde{\chi}_2^0$ and $\tilde{\chi}_1^0$ have a mass splitting of 130 GeV to allow on-shell production of a Higgs boson.

The electroweak SUSY signals are generated under the assumption of nearly mass-degenerate $\tilde{\chi}_2^0$, $\tilde{\chi}_1^\pm$ and $\tilde{\chi}_1^0$, while the other sparticles are decoupled [30–32].

The next model, Figure 3.7(top right), considers the case of chargino-neutralino production. The wino-like $\tilde{\chi}_1^\pm$ and $\tilde{\chi}_2^0$ are mass-degenerate, while the $\tilde{\chi}_1^0$ is bino-like.

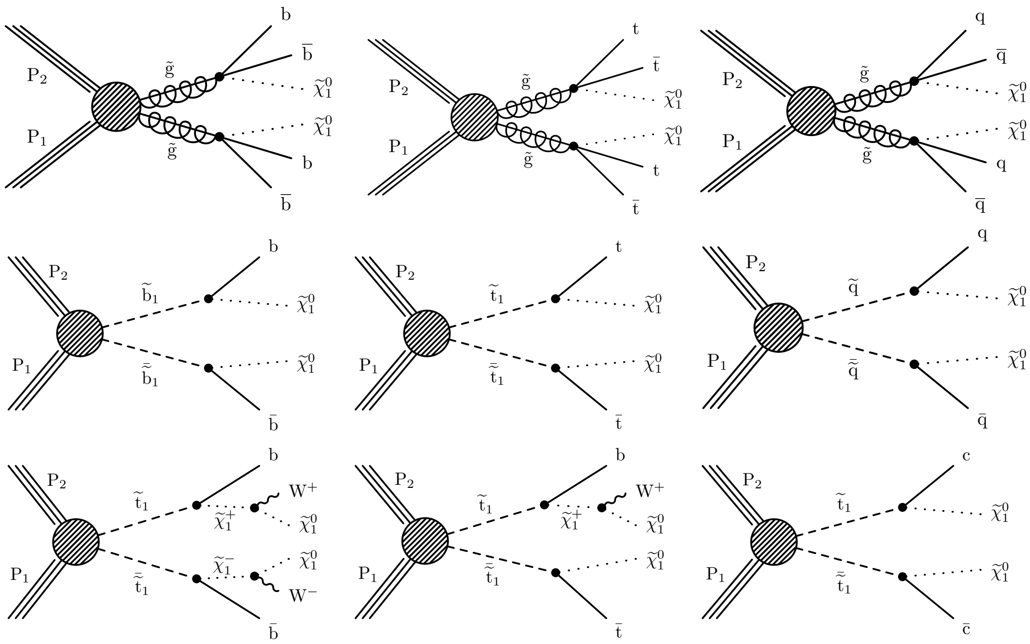

Figure 3.5: The simplified models of SUSY considered for the analysis targeting final states with large values of $E_{\mathrm{T}}^{\mathrm{miss}}$. In the first line from left to right: Gluino pair production decaying to a neutralino and a bottom quark pair, a top quark pair and light quark pair, respectively. The second line from left to right: bottom, top and light squark pair production, respectively. In the third line: Top squark pair production with alternative decay modes.

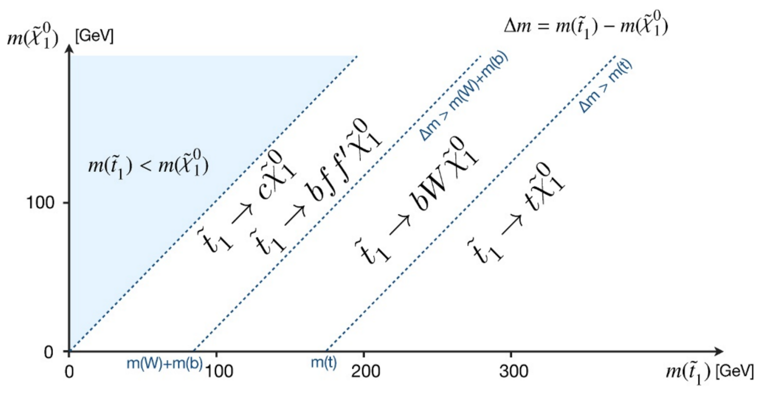

Figure 3.6: The allowed decay modes of a top squark as a function of the top squark mass ($m(\tilde{t}_1)$) and the LSP ($m(\tilde{\chi}_1^0)$) [29].

The chargino decays to a W boson and an $\tilde{\chi}_1^0$, while the $\tilde{\chi}_2^0$ decays to a Higgs boson and a $\tilde{\chi}_1^0$.

In gauge mediated symmetry breaking (GMSB) [33, 34] the gravitino $\tilde{G}$ is the LSP while the next to lightest supersymmetric particle (NSLP) is either a $\tilde{\chi}_1^0$ or a $\tilde{\chi}_1^\pm$. The two GMSB higgsino-like models considered are shown in Figure 3.7(bottom left and right). The neutralinos and charginos are practically mass-degenerate and thus produced in pairs of $\tilde{\chi}_1^0\tilde{\chi}_2^0$, $\tilde{\chi}_1^0\tilde{\chi}_1^\pm$, $\tilde{\chi}_2^0\tilde{\chi}_1^\pm$ or $\tilde{\chi}_1^\pm\tilde{\chi}_1^\mp$. Due to mass degeneracy the $\tilde{\chi}_2^0$ and the $\tilde{\chi}_1^\pm$ will both decay to a $\tilde{\chi}_1^0$ and soft particles, resulting in a signature alike to direct $\tilde{\chi}_1^0$ production. The $\tilde{\chi}_1^0$ then decays to either a Higgs or a Z boson plus the LSP, the $\tilde{G}$ in this scenario. The first of these models has a 100% branching fraction of $\tilde{\chi}_1^0 \to H\tilde{G}$, while the second model has a branching fraction of 50% for $\tilde{\chi}_1^0 \to H\tilde{G}$ and $\tilde{\chi}_1^0 \to Z\tilde{G}$ each.

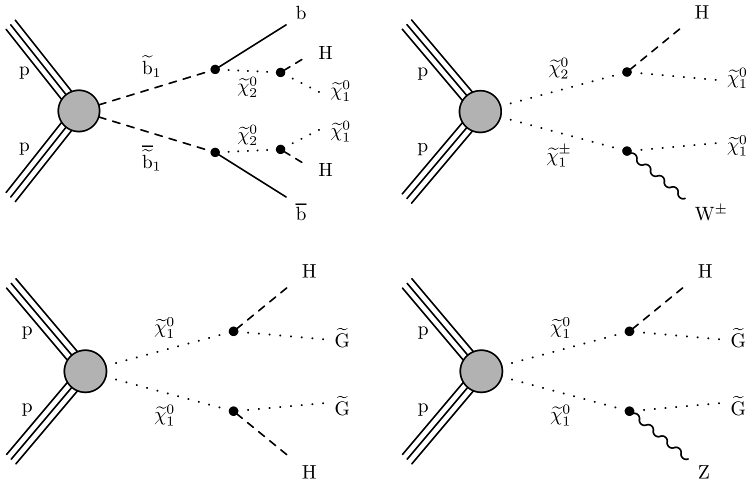

Figure 3.7: The simplified models of SUSY considered for the second analysis targeting final states with two photons from a Higgs boson decay. (Top left) bottom squark pair production; (Top right) Wino-like chargino-neutralino production; (Bottom left) higgsino-like chargino-neutralino production with 100% branching fraction of $\tilde{\chi}_1^0 \to H\tilde{G}$ and (bottom right) 50% branching fraction for $\tilde{\chi}_1^0 \to H\tilde{G}$ and $\tilde{\chi}_1^0 \to Z\tilde{G}$.

Part II

Experimental setup

The world is all that is the case.

Ludwig Wittgenstein,
Tractatus Logico-Philosophicus

4 CERN and the Large Hadron Collider

Since its foundation in 1954, the European Organization for Nuclear Research (CERN)[1] has been at the forefront of particle physics discoveries. The accelerator and collider complex, that has been developed in the years since, reached its current pinnacle in the Large Hadron Collider (LHC). In this chapter I will explain the basic properties of the LHC as relevant to the subsequent Chapter 5, where one of the detectors studying the products of the collisions is described. An in depth description of the LHC can be found in Ref. [35].

The 26.7 km tunnel of the previously installed Large Electron Positron collider (LEP) hosts the LHC. This limits the maximal energy of the accelerator by the following equation:

$$p[\text{TeV}] = 0.3 \cdot B[\text{T}] \cdot R[\text{km}], \tag{4.1}$$

where p is the momentum in TeV, B is the magnetic field strength in Tesla and R is the radius in kilometers[2]. At 1.4^{o} inclination, the tunnel lies between 45 m and 170 m below the Earth surface. As the name suggests, the LHC accelerates and collides hadrons, in particular protons, but also heavy ions.

Two counter-rotating beams are kept on a circular path with dipole magnets that use a twin-bore structure. The superconducting niobium-titanium magnets are cooled down to 2 K with superfluid Helium and are operated at nominal magnetic field strength of 8.33 T. To focus and steer the beams higher order magnets are used. The acceleration occurs in two radio frequency structures, each responsible for one of the beams.

At 4 points the two beams are crossed such that collisions occur at the 4 detectors: A Large Toroidal Apparatus (ATLAS) [36], Compact Muon Solenoid (CMS) [37], A Large Ion Collider Experiment (ALICE) [38] and the Large Hadron Collider beauty (LHCb) [39]. Figure 4.1 shows the accelerator complex and the location of these experiments at CERN. The particles are accelerated to 50 MeV, 1.4 GeV, 25 GeV, and finally to 450 GeV by a linear accelerator (LINAC2), the Proton Synchrotron Booster (PSB), the Proton Synchrotron (PS), and the Super Proton Synchrotron (SPS), respectively, before being injected into the LHC. The PS accelerator determines key properties of the bunches to contain $1.15 \cdot 10^{11}$ protons with a 25 ns spacing, which translates to a 40 MHz interaction frequency in the LHC.

The event yield per second, N_p, for a process p is determined by the instantaneous

[1] The original name *Conseil européen pour la recherche nucléaire* has given the abbreviation under which it is still known to this day.

[2] Even if one were able to build Fermi's Globatron around Earth with the LHC magnet technology one would still "only" reach about 10-20 PeV, which is still far from the GUT scale.

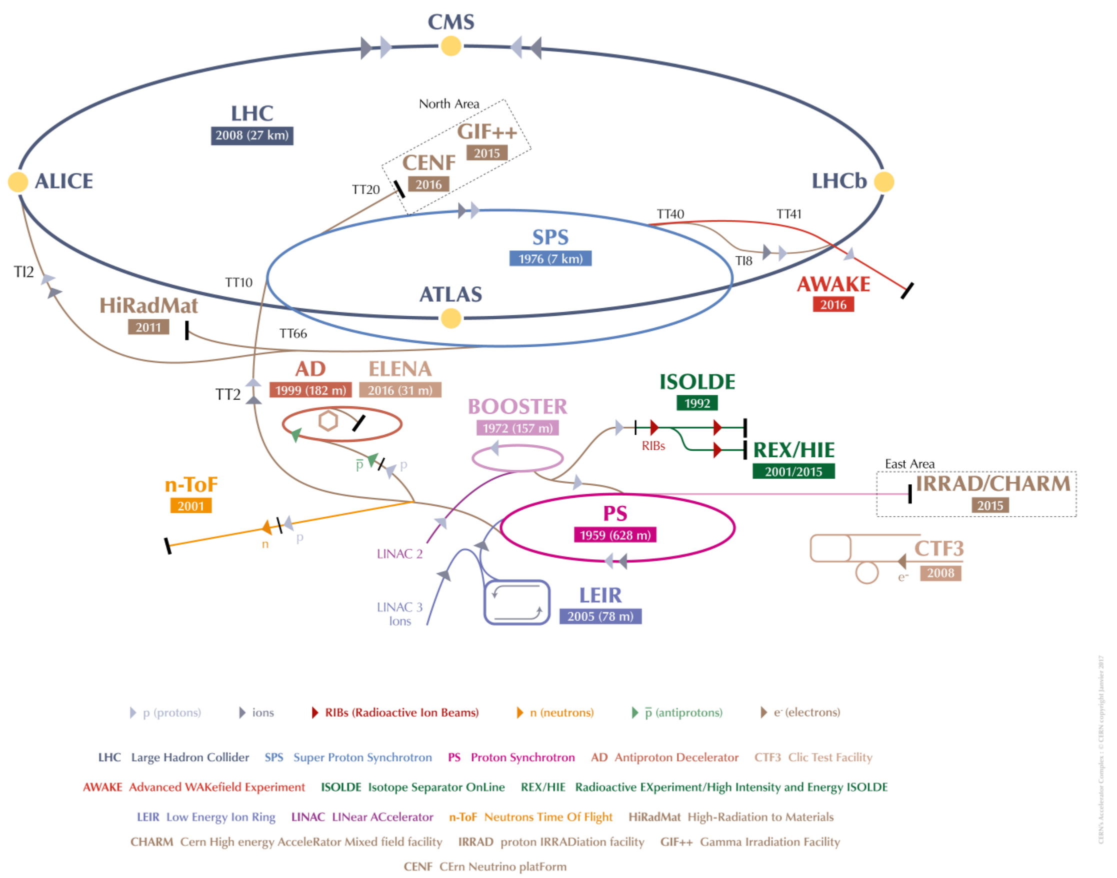

Figure 4.1: Schematic of the accelerators and experiments at CERN. The construction date indicated next to the names and the lines connecting the different parts nicely show how today's science literally builds on the achievements of the past [40].

luminosity $\mathcal{L}$ and the cross section σ_p

$$N_p = \mathcal{L}\sigma_p. \tag{4.2}$$

Assuming a Gaussian beam distribution, the instantaneous luminosity $\mathcal{L}$ at the LHC is given by

$$\mathcal{L} = F\frac{N_b^2 n_b f_{rev}\gamma_r}{4\pi\epsilon_n\beta^*}, \tag{4.3}$$

where $N_b, n_b, f_{rev}, \gamma_r, \epsilon_n$ and β^* are the number of particles per bunch, the number of bunches per beam, the revolution frequency, the relativistic gamma factor, the normalized emittance and the beta function, respectively. The form factor F accounts for the luminosity reduction due to the crossing angle, the bunch length and the beam size RMS.

The luminosity for proton-proton (pp) collisions at the ATLAS and CMS detectors was designed to reach $\mathcal{L} = 10^{34}\,\mathrm{cm}^{-2}\mathrm{s}^{-1}$. A peak instantaneous luminosity of $1.53\,\cdot$

$10^{34}\,\mathrm{cm}^{-2}\mathrm{s}^{-1}$ was reached in 2016 [41]. As the beams circulate during data taking the luminosity decreases with time mostly due to the collisions, but also scattering, beam-beam interactions and noise contribute.

On average more than 20 inelastic pp collisions occur durig each bunch crossing. Generally only one of these is of interest for the physics analyses, while the rest of the interactions are referred to as *pileup*.

For the analyses it is important to know how much luminosity was collected during a run time. It is thus useful to define the integrated luminosity, which is measured in cm^{-2}. For simplicity the unit barn is introduced, $1b = 10^{-24}\mathrm{cm}^2$. The integrated luminosity is then often expressed in terms of inverse femtobarns, fb^{-1}.

The data taking periods between long shutdowns are referred to as *Runs*. During Run1 $6.1\mathrm{fb}^{-1}$ and $23.3\mathrm{fb}^{-1}$ of data at a center of mass energy of 7 and 8 TeV, respectively, were taken. In 2015 Run2 started after the upgrade to $\sqrt{s} = 13\,\mathrm{TeV}$. The LHC delivered since then $4.2\mathrm{fb}^{-1}$ in 2015, $41.0\mathrm{fb}^{-1}$ in 2016, $49.8\mathrm{fb}^{-1}$ in 2017 and $67.9\mathrm{fb}^{-1}$ in 2018, concluding the Run2 data taking. In this thesis the data qualified as good of the years 2016 and 2017 corresponding to $35.9\ \mathrm{fb}^{-1}$ and $41.5\ \mathrm{fb}^{-1}$, respectively, are analyzed. The luminosity delivered by the LHC and recorded by the CMS experiment for those years are shown in Figure 4.2.

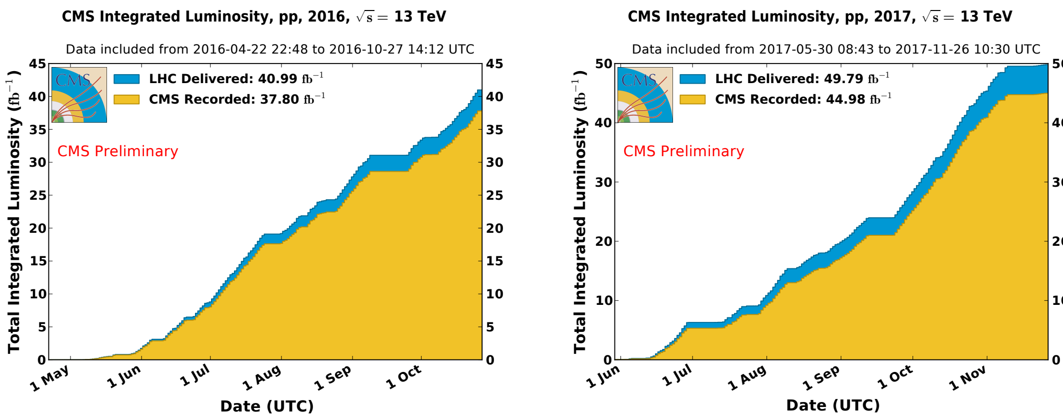

Figure 4.2: The delivered and recorded integrated luminosity as a function of the data taking time for the years 2016 (left) and 2017 (right) [42].

5 The Compact Muon Solenoid detector

The phenomena under study in this thesis are not observable by eye, with bubble chambers for example. Not only is the number of events produced at the LHC too high to investigate by hand, but also are the particles too energetic to be contained and measured in a simple photograph. What is needed are detectors that are faster in readout and denser so that they are able to stop the particles. What has to be measured in the events, though, has stayed similar through the years: energy, momentum and charge.

The Compact Muon Solenoid (CMS) detector is one of the four large scale experiments at the LHC, along with ATLAS, LHCb and ALICE. CMS and ATLAS are general purpose detectors aiming to measure a broad variety of signatures, while LHCb and ALICE are mainly dedicated to flavor and heavy-ion physics, respectively. As the name CMS suggests, a particular focus in its design was put on the compactness, thus influencing the calorimeter system design, the detection of muons and the magnetic field generated by the solenoid. Figure 5.1 shows a schematic of the detector system sliced open to expose the inner workings. At 21.6 m length, 15 m diameter and a weight of about 14 kilo-tonnes one can only call it "compact" in comparison to ATLAS, which measures 46 m and 25 m in length and diameter, respectively, while weighing about half of the CMS experiment.

The general layout is that of a cylindrical onion, where the layers are different subdetectors that are sensitive to different particles, thus enabling particle identification when taking into account the relative information of each subpart. The combination of the measurements in the subdetectors also gives an indirect measure of undetectable particles, neutrinos and possible new phenomena. It is thus imperative that the detector is as hermetic as possible to reduce holes in the acceptance that could artificially increase the rate of such events. To this end the detector is split in two regions: the cylindrical barrel region made of coaxial layers; and the two endcaps with layers perpendicular to the beam axis.

The x, y and z direction are defined as going from the center of the collisions towards the center of the LHC, towards the surface and along the beam line, respectively. They are shown in Figure 5.2 with respect to the LHC and the Jura mountains. The more commonly used system of coordinates is (r, ϕ, η), where r is the radial distance from the beam spot, ϕ denotes the angle with respect to the x-axis and the pseudorapidity η. It is defined as $\eta = -\ln\left(\tan\left(\frac{\theta}{2}\right)\right)$ with θ being the angle with respect to the z-axis. In the high energy limit, η is equivalent to the rapidity y: $\eta \to y = \frac{1}{2}\ln\left(\frac{E+p_z}{E-p_z}\right)$, with p_z being the z-component of the momentum. Since differences of y are invariant under Lorentz boost along the z-axis, so are differences in η in the high energy limit.

Angular distances are generally measured by $\Delta R = \sqrt{\Delta\phi^2 + \Delta\eta^2}$. Due to the unknown momenta of the colliding partons along the beam direction, generally the transverse energies and momenta are particularly important: $E_T = \sin(\theta)E$ and $p_T = \sqrt{p_x^2 + p_y^2}$.

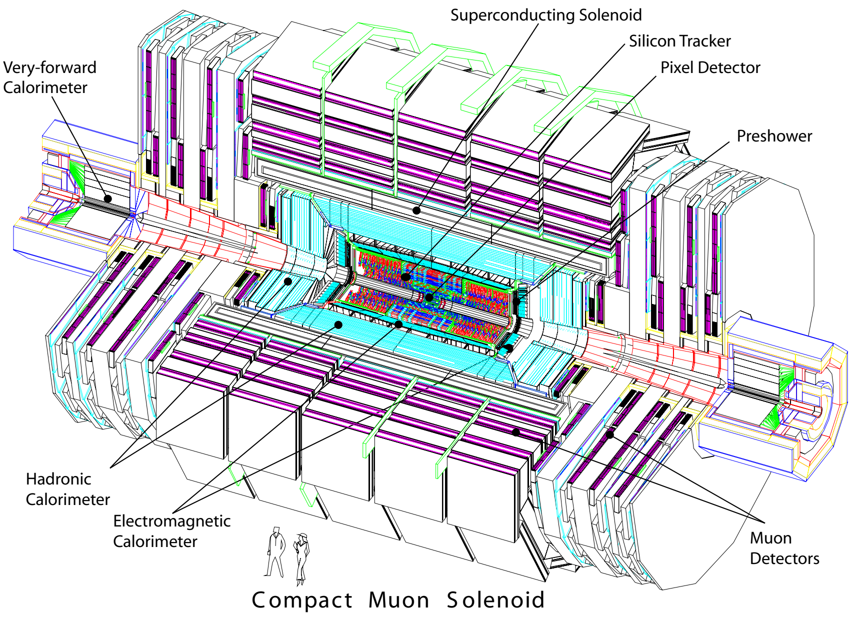

Figure 5.1: Schematic of the CMS detector indicating the different detector parts. Humans for scale [37].

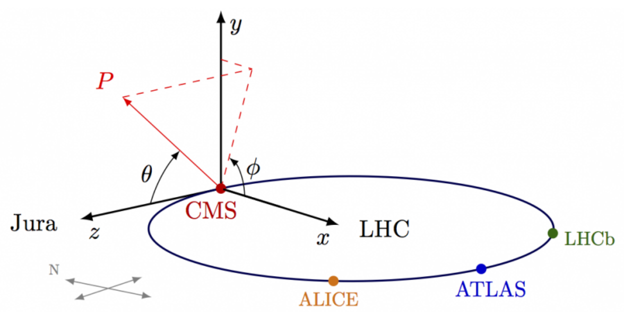

Figure 5.2: Schematic of the coordinate system of CMS with respect to the LHC and the Jura mountains [43].

In the following I will introduce the different layers of the detector system, from inside outwards: the silicon pixel and strip detectors (Section 5.1), the electromagnetic (Section 5.2) and hadronic (Section 5.3) calorimeter systems, the solenoid (Section 5.4) and finally the muon systems (Section 5.5). For a full description of the detectors see Ref. [44] on which this chapter is based.

5.1 Tracker system

The tracker system detects charged particles interacting with the approximately $200\,\mathrm{m}^2$ sensor material. As charged particles traverse the silicon sensor material, they leave electron-hole pairs in the semiconductor that are read out via a bias voltage. Fine segmentation and multiple layers allow for the reconstruction of trajectories and primary and secondary vertices from these *hits*. High granularity is thus imperative for a good spatial resolution. There are collisions every 25 ns, which means that a fast response of the detector is needed to attribute the hits to the correct bunch crossing. Since the calorimeters after the tracking system will determine the energy of the particles in a destructive way, the tracking system aims to be minimally invasive. In order to keep multiple scattering, bremsstrahlung, photon conversion and nuclear interactions limited, the material budget of the sensor and readout electronics is held to the minimum required for stable operation. Since the tracking detector is the closest to the beam pipe it receives a high particle flux, ionizing as well as non-ionizing. Radiation hardness is thus imperative for stable operation.

Close to the beam pipe finer segmentation is needed and pixels are used. Further away silicon microstrips are used. Figure 5.3 shows the tracker modules in the barrel and endcap regions in a longitudinal cross section. Along with an efficiency of nearly 100% a good momentum resolution of $\sigma(p_T)/p_T < 4\%$ is required for muons up to 100 GeV and $|\eta| < 2$. The two tracker systems that achieve this are introduced in the following.

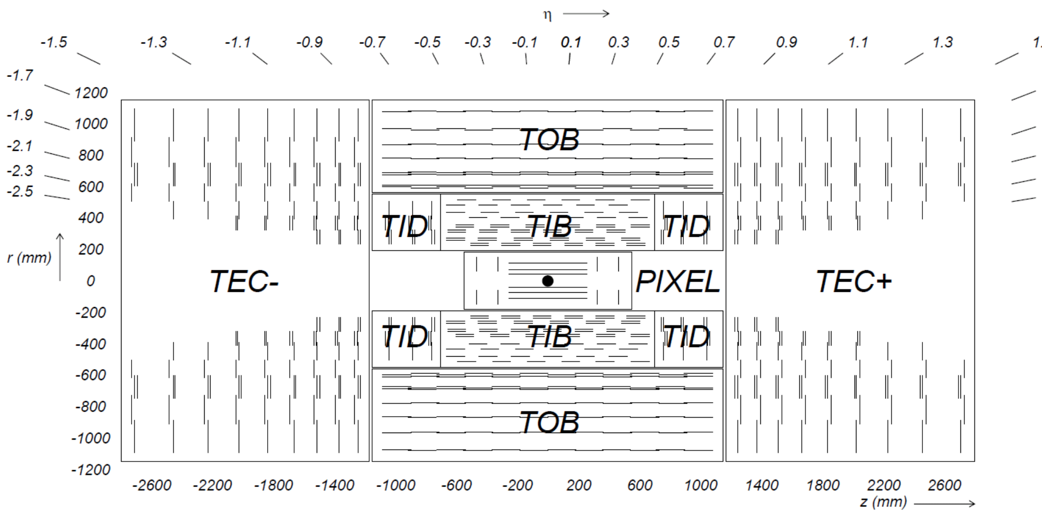

Figure 5.3: Longitudinal schematic of the tracker system, where each line corresponds to a strip or pixel module [44].

5.1.1 Inner Tracker system: Pixels

The pixel detector used until the end of 2016 consists of 3 layers at radii of 4.4-10.2 cm in the barrel and 2 discs for each of the endcaps. A total of 1440 pixel modules were installed that cover a pseudorapidity up to $|\eta| < 2.5$. The size of the pixels is $100\,\mu\text{m} \times 150\,\mu\text{m}$.

In 2017 a new pixel detector [45] was installed that would ensure stable operation at the expected $2 \cdot 10^{34}\,\text{cm}^{-2}\text{s}^{-1}$ of instantaneous luminosity. With an additional barrel layer and endcap disk on each side, an improved readout chip and moving the innermost layer to 2.9 cm the efficiency and resolution are improved, while keeping the material budget the same. Figure 5.4 shows the two pixel topologies used as seen from the r-z plane.

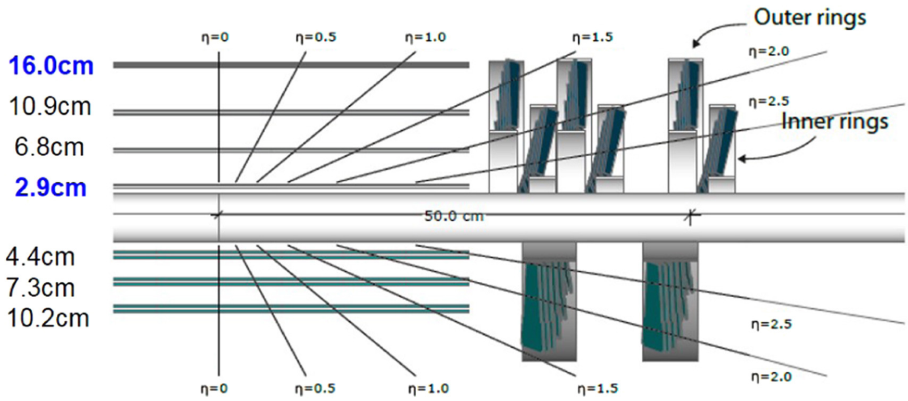

Figure 5.4: Schematic of the pixel detector in use up to the end of 2016 (bottom) and from 2017 onward (top) in the r-z plane [45].

5.1.2 Outer Tracker system: Strips

The inner ($20 < r < 55$ cm) and outer ($55 < r < 110$ cm) strip detectors use $320\,\mu$m and $500\,\mu$m thick silicon sensors, respectively. With 10 layers in the barrel region and 3+9 layers of the (inner+outer) endcap discs, the strip detector extends to $|\eta| < 2.5$, as visualized in Figure 5.3.

5.2 Electromagnetic calorimeter

Mainly electromagnetically interacting particles, photons, electrons and positrons, are detected and read out in the electromagnetic calorimeter system (ECAL). Calorimeters measure the energy of the incident particle in a destructive way, meaning that it is stopped in the subdetector. An avalanche of low energetic particles is produced in the material, for electrons and positrons mainly via ionization and Bremsstrahlung and for photons predominantly through the photoelectric effect and electron-positron pair production [4]. Completely stopping the particles inside the detector is important since the amount of scintillation photons produced is proportional to the energy of the incident particle.

The 75848 lead tungstate ($PbWO_4$) crystals extend up to a pseudorapidity $|\eta| < 3.0$. The choice of lead tungstate comes from its short radiation length ($X_0 = 0.89$ cm) and small Molière radius ($R_M = 2.2\,\text{cm}$), that allow to have a compact ECAL as the CMS experiment requires. About 80% of the scintillation light is emitted in 25 ns, the LHC bunch crossing time, thus providing sufficiently fast light collection. The organization of the ECAL in the barrel and endcap region is shown in Figure 5.5, with the barrel consisting of 36 supermodules spanning each half of the barrel region, and the endcap being organized in two half circles (Dee).

The barrel ECAL (EB) extends to $|\eta| < 1.479$ with a quasi-pointing geometry, meaning that there is a 3° angle in η and ϕ with respect to the vector connecting to the beam spot. The barrel crystals have a front face size of $22 \times 22\,\text{mm}^2$ and a rear face size of $26 \times 26\,\text{mm}^2$. Their length of 230 mm equates to $25.8X_0$. The crystals are read out by silicon avalanche photodiodes (APD) in the barrel region.

The endcap ECAL (EE) covers the pseudorapidity range $1.479 < |\eta| < 3$. The endcap crystals have a front face size of $28.62 \times 28.62\,\text{mm}^2$ and a rear face size of $30 \times 30\,\text{mm}^2$. Their length of 220 mm equates to $24.7X_0$. Instead of APDs, vacuum phototriodes are used due to their higher radiation resistance.

In front of most of the EE region the preshower (ES) [46] detector is installed. It covers $1.653 < |\eta| < 2.6$ with a sampling calorimeter made out of lead and silicon strips. With the additional spatial information the efficiency of identifying π^0 decays is improved.

The energy resolution σ_E is modelled by the stochastic (S), noise (N) and a constant (C) term as follows:

$$\left(\frac{\sigma_E}{E}\right)^2 = \left(\frac{S}{\sqrt{E}}\right)^2 + \left(\frac{N}{E}\right)^2 + C^2. \tag{5.1}$$

For the lead tungstate crystals used these terms have been measured to be $S = 2.8\%$, $N = 12\%$ and $C = 0.3\%$ [47]. The stochastic term mostly depends on the number of detected photons, the noise term is dominated by the electronic noise and pileup effect and the constant term stems from the error on the calibration of the response between crystals, their non-uniformity and longitudinal shower non-containment.

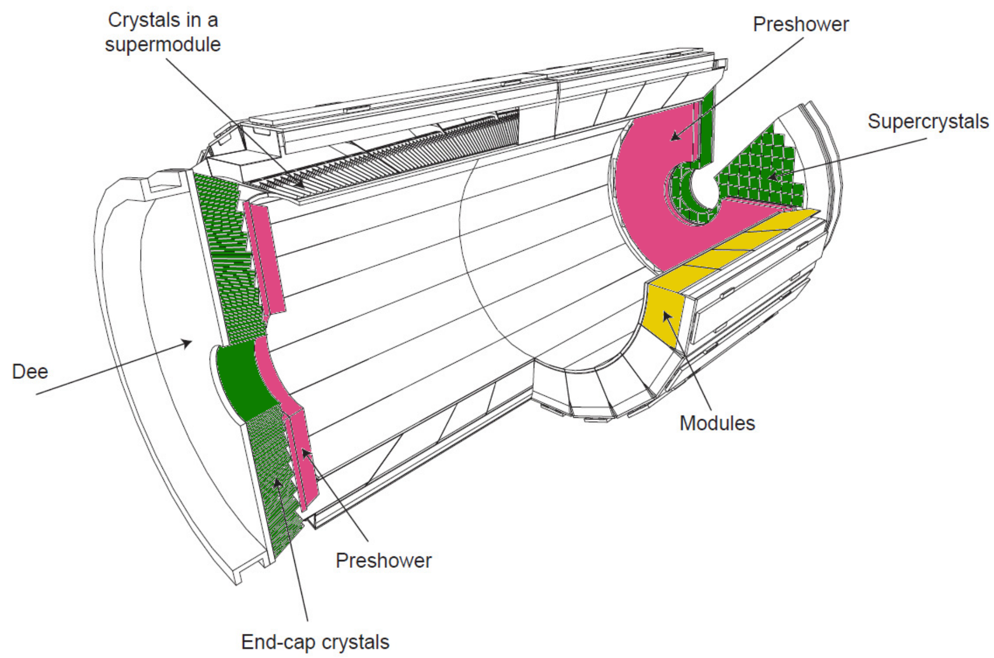

Figure 5.5: The ECAL system consisting of the EB (yellow), EE (green) and ES (magenta) [44].

5.3 Hadronic calorimeter

Charged and neutral hadrons are stopped in the hadronic calorimeter (HCAL). The HCAL at CMS consists of a barrel (HB) and endcap (HE) part contained inside the solenoid, as well as the Outer Hadronic Calorimeter (HO) positioned in the first muon detector layer outside the solenoid. In the forward direction the calorimeter system is extended by the Forward Calorimeters (HF) located at 11.2 m from the beam spot. Figure 5.6 shows a quarter of the r-z view of the HCAL components.

The Central Hadron Calorimeter consists of HB and HE, that cover a pseudorapidity range of $|\eta| < 1.4$ and $1.3 < |\eta| < 3.0$, respectively. They are sampling calorimeters with layers of plastic scintillator as active material. Brass, because of its short interaction length λ_I of 16.42 cm, is used as absorber material, except for the inner- and outermost layers which give structural support by using stainless steel. The layers are segmented in η and ϕ such that: $\Delta\eta \times \Delta\phi = 0.087 \times 0.087$. Each of the scintillator tiles is read out with a wavelength shifting fiber. Their signal is optically added and read out with a pixelated hybrid photodiode. The HO with one further layer of scintillator tiles, with the same η and ϕ geometry as HB, is placed outside of the solenoid and is read out separately.

The endcap part of the HCAL is set such that there is an overlap with the tower at highest η of HB. The brass absorbers are surrounded by 19 layers of scintillator tiles. The segmentation increases from $\Delta\eta \times \Delta\phi = 0.087 \times 0.087$ to $\Delta\eta \times \Delta\phi = 0.350 \times 0.175$

at high values of η.

The HF consists of steel absorbers embedded with quartz fibres. By reading out separately the long (1.65 m) and short (1.43 m) fibres, one gains basic information about the longitudinal shower shape, which later allows for a simple particle identification.

The resolution was measured in beam tests to be

$$\left(\frac{\sigma_E}{E}\right)^2 = \left(\frac{S}{\sqrt{E}}\right)^2 + (C)^2, \tag{5.2}$$

where $S = 0.847\,\mathrm{GeV}^{1/2}$ and $C = 0.074$ for the barrel and endcap region, while for HF $S = 1.98\,\mathrm{GeV}^{1/2}$ and $C = 0.09$ [48].

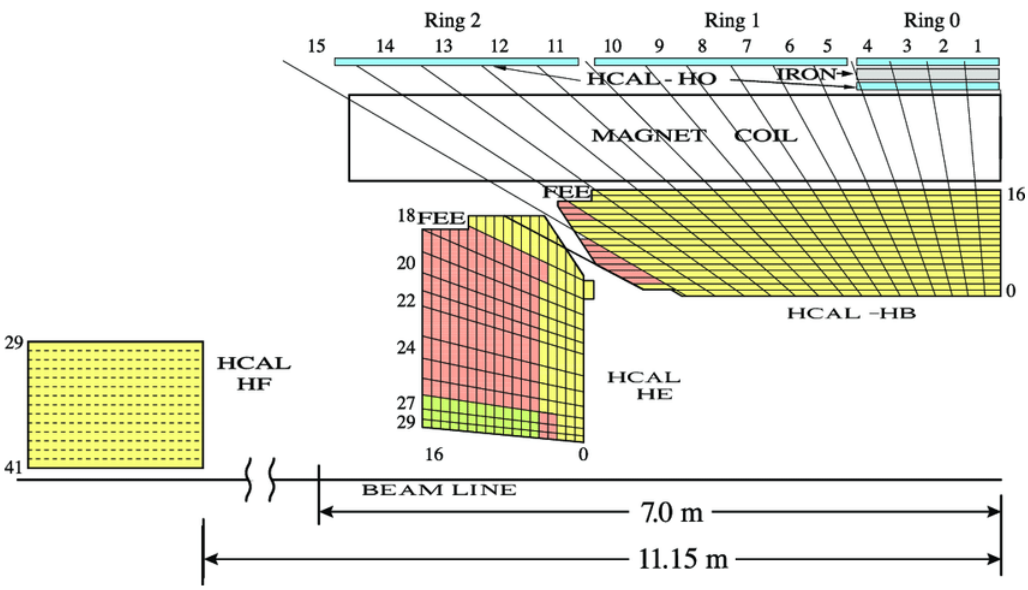

Figure 5.6: A quarter of the HCAL system in the r-z view indicating the location of the HB, HE, HO and HF [48].

5.4 Solenoid

A strong magnetic field is needed for a good momentum resolution of the tracks and muons. The solenoid of CMS was designed to produce a magnetic field of 4 T, currently it is operated at 3.8 T, which greatly improved the expected lifetime of the solenoid. The magnet has a diameter of 6 m and a length of 13 m, while keeping the coil relatively thin ($\Delta R/R \sim 0.1$) for optimal physics performance[1]. This is only feasible with a superconducting solenoid. Four layers of winding made of a NbTi superconducting alloy, encapsulated by pure Aluminium and reinforced by an Aluminium alloy, are used. The return yoke is composed out of 5 barrel wheels and

[1]Even then, the magnet corresponds to about $3.9\,X_0$, but since most of the particles will have been stopped before in the calorimeter system, this only affects the measurements of the muons.

6 endcap disks which weigh all together approximately 10 kt. They can be moved separately by a pneumatic system over the 1.23% inclined cavern floor. Figure 5.7 show the magnetic field strength $|B|$ and the magnetic field lines at 3.8 T. Between the layers of the return yoke the muon stations are located, as discussed next.

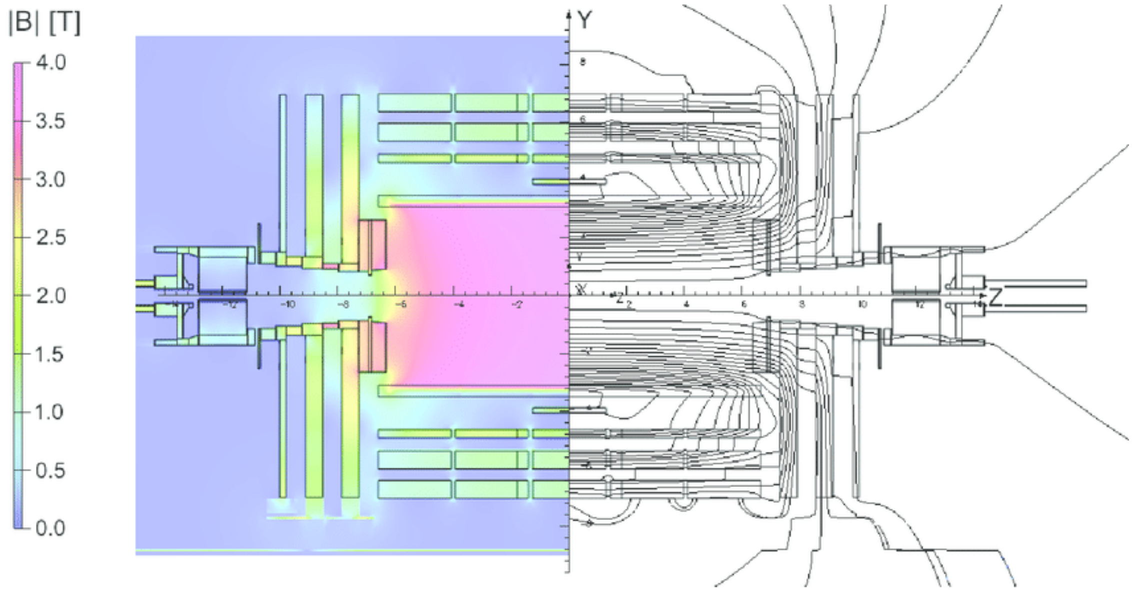

Figure 5.7: Longitudinal view of the magnetic field strength $|B|$ (left) and field lines (right) for a central flux density of 3.8 T [49].

5.5 Muon systems

Three types of muon detectors are used at the CMS detector, again with a barrel and two endcap parts as shown in Figure 5.8. With the calorimeter systems in front of the muon system only a negligible amount of punchthrough particles are registered such that most of the signals in the muons systems are in fact muons.

The barrel part has 4 stations of drift tube (DT) chambers up to a pseudorapidity $|\eta| < 1.2$. Each of the first 3 stations has 8 DT layers. These 8 layers consist of alternating chambers measuring in the r-ϕ plane and the z direction. In the fourth station there are only the r-ϕ plane chambers.

In the endcap region the muon and background rates are higher than in the barrel region, and the magnetic field is non-uniform. Thus radiation-hard and fast cathode strip chambers (CSC) are used in the region $0.9 < |\eta| < 2.4$. The four stations of 6 chambers per endcap are oriented perpendicular to the beam line. With the cathode strips going radially outward and the anode wires perpendicular to them, the CSC measures the r-ϕ, η and beam-crossing time of a crossing particle.

To ensure the measurement of the correct beam-crossing time at the demanding luminosity levels of the LHC a further system of muon detectors is installed. The resistive plate chambers (RPC) are an independent trigger system spanning up to the rapidity $|\eta| < 1.6$. They have a fast response as required for the trigger, and, being operated in avalanche mode, they ensure good operation also at high rates. However they have a coarser spatial resolution than the other two muon detector systems.

The momentum resolution for muons with $p_T < 100\,\text{GeV}$ is about 1% and 3% in the barrel and endcap, respectively. For transverse momenta $p_T < 200\,\text{GeV}$ the resolution is dominated by the tracker information, while above 200 GeV the muon system significantly improves the result, giving a resolution below 6% for muons with $p_T \approx 1\,\text{TeV}$ [50].

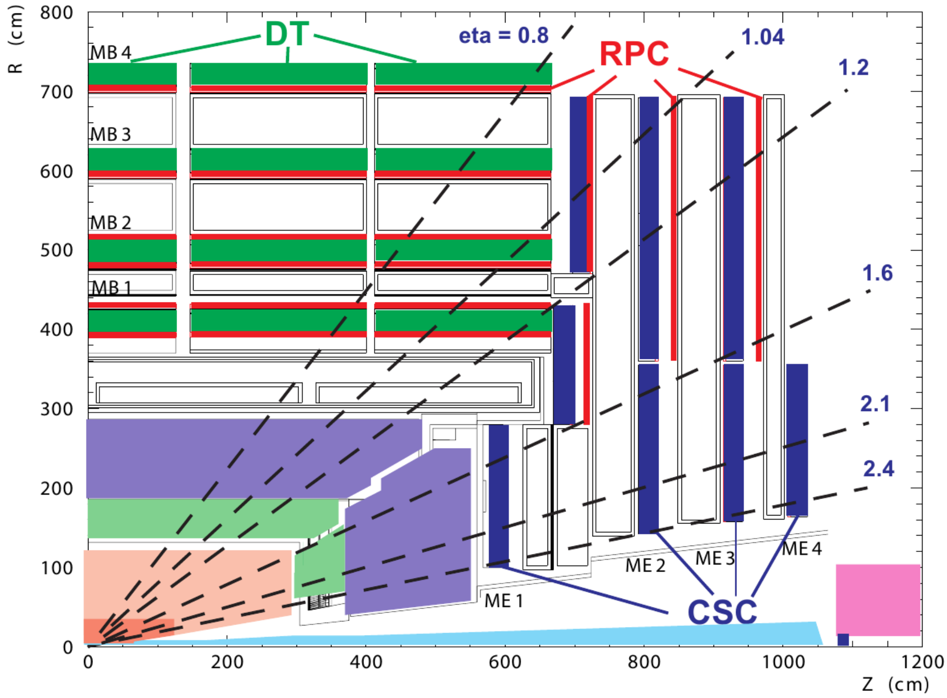

Figure 5.8: The DT (green), CSC (blue) and RPC (red) muon systems in the r-z plane [44].

5.6 Trigger system and data acquisition

At a crossing frequency of 40 MHz and size of 1-2 MB per event recorded, the data rate largely exceeds the current storage and bandwidth capability. Furthermore, a large fraction of the interactions is of little interest to the high energy physics community. Selecting the relevant events is an important task, since every physics analysis depends on the efficient selection of its specific events.

The rate is reduced in two levels: Level-1 (L1) Trigger [51] and the High-Level Trigger (HLT) [52]. The custom-made programmable electronics for the L1 Trigger in combination with the software based HLT system is able to reduce the rate by at least a factor of 10^6 to a rate of roughly 1 kHz.

In the first step the L1 Trigger preselects events based on coarse regions in the calorimeter system, segments of tracks or hits in the muon chambers. The L1 trigger decision can take up to $3.2\,\mu$s, the data is thus pipelined such that every bunch crossing can be analyzed.

The events that pass the L1 trigger are processed in the next step at computer farms that use a simplified and faster version of the offline reconstruction software. Based on these basic objects during approximately 300 ms a trigger decision has to be made, allowing for more complicated analyses than at the L1 trigger but still limiting the precision with which the decision can be made. Multiple HLT paths exist that tag an event independently for a physics process based on these basic objects. The logical OR of the HLT paths decides if an event is kept and written to disc. With the information of which HLT path has triggered the event a fast preselection at the analysis level can be made.

Once an event has been selected its raw data is written on tape at CERN (Tier0), where the first event reconstruction occurs. Copies are distributed to large data centers (Tier1), where the final reconstruction happens. The reduced data is then saved and distributed to the smaller centers. This worldwide multi-tier system allows analyzers easy and fast access to the data.

The data taking periods per year are further split into eras to distinguish the different operating settings. The eras relevant for this thesis with their corresponding integrated luminosities are listed in Table 5.1.

Table 5.1: List of run eras for the 2016 and 2017 data taking periods.

Eras 2016	$\mathcal{L}$ [fb^{-1}]	Eras 2017	$\mathcal{L}$ [fb^{-1}]
Run2016B	5.8	Run2017B	4.8
Run2016C	2.6	Run2017C	9.7
Run2016D	4.3	Run2017D	4.3
Run2016E	4.0	Run2017E	9.3
Run2016F	3.1	Run2017F	13.5
Run2016G	7.5	Run2017G	0.1
Run2016H	8.6	Run2017H	0.2

6 Reconstruction

The full reconstruction process mentioned in the previous chapter is outlined in this chapter. It serves two purposes: firstly to reduce the size of the data sample and secondly to translate the single hits into objects of interest for the analyses.

First I outline the reconstruction algorithms used for tracks in Section 6.1 and vertices in Section 6.2. The particle flow algorithm that takes the whole detector response into account is outlined in Section 6.4. Once the general objects are reconstructed in this way the particle are defined in Section 6.5 along with their most important identification variables. Higher level objects defined out of these are introduced in Section 6.6.

6.1 Track construction

The individual signals registered in the pixel and strip detectors are clustered into hits. The combinatorial track finder [53] reconstructs tracks out of these hits in six iterations with an adaptation of the Kalman filter [54]. The high purity and momentum tracks are constructed first and the assigned hits are removed successively, reducing the computation cost in each iteration. Once the tracks are constructed quality cuts are applied and the tracks' properties, e.g. their momenta, are determined.

6.2 Vertex reconstruction

For each bunch crossing there are on average about 25 pp collisions in 2016 and 32-37 pp collision in 2017. The reconstructed tracks are used to determine the primary vertex (PV) and the pileup vertices of these collisions.

A deterministic annealing [55] algorithm is used that assigns each track a probability between 0 and 1 to belong to a specific vertex. Starting from one vertex, additional ones are added if the probability is higher that the tracks originate from separate vertices.

For a vertex with a least two tracks the position is determined from its tracks with the adaptive vertex fitter [56]. A precision resolution in the three spatial dimensions of 10-12 μm is achieved [57].

In the analyses presented later events are required to have at least one primary vertex within 24 cm and 2 cm from the detector center in the direction along and perpendicular to the beam axis, respectively. The vertex with the highest $\sum p_T^2$ is selected as the PV in case there are multiple good vertices. Tracks of vertices other than the PV are ignored for the jet construction and the isolation variables.

6.3 Calorimeter cluster reconstruction

The energy deposits in the calorimeter cells are collected into clusters in each subdetector part (EE, EB, HB and HE) separately. With these clusters neutral particles are measured and with their position they can be separated from charged particles identified by their tracks. For charged particles with poor track quality or with very large p_T the energy measurement is improved with the cluster information.

Clusters are seeded by a cell that reaches the seed threshold and has a higher energy deposit than its neighbors. These neighbors are then added to the topological cluster if they exceed the noise level. To separate the clusters within a topological cluster the Gaussian-mixture model is used, where it is assumed that the deposits in the individual cells stem from as many Gaussian distributions as there are seeds. The position and energy of the Gaussians, and thus the clusters, are then iteratively determined with an expectation-maximization algorithm [58].

6.4 The particle flow algorithm

Figure 6.1 shows the main interaction processes in the CMS detector for the visible particles. To correctly attribute an energy deposit in one of the subdetectors to a particle the whole detector information is used, since also the absence of a deposit carries information. In particular for neutrinos, since they are not directly measurable with CMS, their determination depends entirely on the precise measurement of the visible signatures. The invisible information is summarized in the missing transverse energy, $E_{\mathrm{T}}^{\mathrm{miss}}$, introduced in Section 6.6. Also for the visible objects, especially the jets, the resolution is greatly improved by taking the whole detector information into account, as the calorimeter information is complemented by the momentum information of the tracks.

This process is achieved with the particle flow (PF) algorithm [58], which iteratively compares the compatibility of tracks, calorimeter clusters and muon tracks. Once a component has been associated to a PF candidate, it is removed from the list. Finally the objects are categorized as a PF candidate of a muon, electron, photon, a charged or a neutral hadron.

Muons are first identified by using the track extrapolated from the measurements in the tracking detectors and comparing it to the track determined by using both the tracker and muon detectors. If the two tracks are compatible it is identified as a muon. Then the ECAL clusters and tracks are combined to build electrons. The remaining tracks and HCAL deposits are in the following used to determine the charged hadrons. If the track p_T is smaller than the measurement of the HCAL cluster, a neutral hadron with the appropriate p_T is identified. Finally the photons are identified from the ECAL clusters without a track. Any remaining excess in the HCAL cluster compared to the ECAL one is attributed to a neutral hadron. The thus defined PF candidates are in the following used to build the particles and variables for the analyses as listed below.

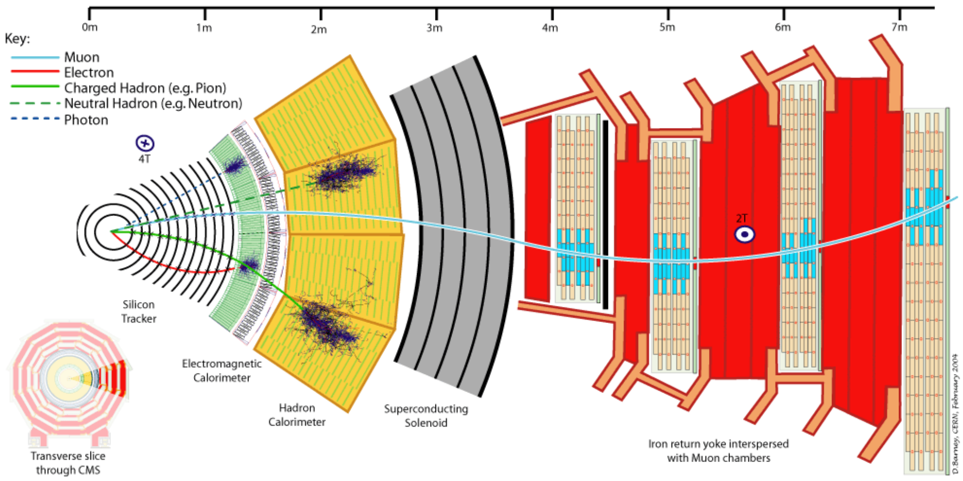

Figure 6.1: Schematic of the CMS detector indicating the different interaction patterns of the particles [59].

6.5 Physics objects

In the following the selection criteria on the objects used for the two analyses are introduced. Further specifications are given in the analyses chapters, where differences occur between the two analyses.

Muons

Muons are identified as detailed in Ref. [60]. The PF muons have to be either identified as such globally, i.e. by the track and muon chamber information, or just by the track information. Due to the tracker acceptance muons up to pseudorapidity 2.4 are considered. In addition a selection on the distance from the PV, the impact parameters, is applied:

- $|d_{xy}| < 0.2\,\mathrm{cm}$ in the plane transversal to the beam;
- $|d_z| < 0.5\,\mathrm{cm}$ in the beam direction.

Muons are required to be isolated according to the relative mini isolation (miniIso): $\mathrm{miniIso}/p_T < 0.2$, where miniIso means that the cone size decreases with p_T, according to Equation 6.1.

$$\Delta R = \begin{cases} 0.2 & \text{if } p_T < 50\,\mathrm{GeV} \\ 10\,\mathrm{GeV}/p_T & \text{if } 50 < p_T < 200\,\mathrm{GeV} \\ 0.05 & \text{if } p_T > 200\,\mathrm{GeV} \end{cases} \tag{6.1}$$

Electrons

Electrons often initiate an electromagnetic shower upstream of the ECAL. The Gaussian Sum Filter [61] takes the resulting larger changes in the momentum into account for the track reconstruction. The ECAL clustering algorithm accounts for the wider spread of the energy deposits in the ϕ direction due to the magnetic field [62]. The electron energy is calculated from the track and ECAL cluster, taking into account the tracker material.

Electrons up to $|\eta| < 2.4$ are considered, while the pseudorapidity region $1.44 < |\eta| < 1.56$ is excluded due to the acceptance gap between the ECAL barrel and endcap region. Selected electrons are required to be isolated, cutting on relative mini PF isolation: miniIso$/p_T < 0.1$, with the isolation variable defined above in Equation 6.1.

Photons

Photons are characterized by their deposit in the ECAL and the lack of a track and a (large) HCAL deposit. They can undergo conversion to an electron-positron pair in the upstream material resulting in the ECAL cluster being spread in the ϕ direction. Similarly to the electron, the clustering algorithm takes this effect into account when building the supercluster (SC) around the crystal with the highest registered deposit, the *seed* crystal.

The photon energy is measured from the SC, along with the preshower deposit where applicable, and corrected for the detector effects [63]. The radiation induced transparency loss is measured during data taking with a laser system. The different response of the crystals is corrected using the above spread in the ϕ direction and measurements using mesons and vector bosons. Corrections for the shower containment, upstream material and pileup are derived with a multivariate regression built with shower shape variables. In the last step $Z \to e^- e^+$ events are used to correct for the difference between data and simulation for the mass scale as well as the resolution.

The following variables, along with the isolation, are used for the photon identification:

- R_9 is the ratio of the energy in an3 $\times$ 3 crystal matrix over the energy of the SC: $R_9 = E_{3\times3}/E_{\mathrm{SC}}$.
- H/E describes the hadronic over electromagnetic energy fraction as measured in the HCAL and ECAL, respectively.
- $\sigma_{i\eta i\eta}$ is the shower covariance in the η direction measured in steps of the crystal size $i\eta$:

$$\sigma^2_{i\eta i\eta} = \frac{\sum_i w_i (i\eta_i - i\eta_s)^2}{\sum_i w_i}, \text{where } w_i = \max(0, 4.7 + \ln \frac{E_i}{E_{5\times5}}) \tag{6.2}$$

  where the sum runs over the 5x5 crystals surrounding the *seed* of the supercluster.

Only the second analysis makes use of photons, where photons in the barrel region are considered, $|\eta| < 1.44$.

Jets

The anti-k_T algorithm [64] with a distance parameter of $R = 0.4$ is used to cluster the PF candidates into a spray of particles resulting from the hadronization of the quarks and gluons, as described in Section 2.3.1.

The charged PF candidates from the primary vertex and all the neutral PF candidates are clustered in this way. The charged PF candidates from the pileup vertices are rejected in the so called charged hadron subtraction [58].

Jets which overlap with electrons or muons are removed as well as jets that likely stem from detector noise based on their neutral, charged, hadronic or electromagnetic energy fractions [65].

To obtain a better estimate of the original parton energy the jets are corrected in bins of p_T and η for the effects of pileup, noise, detector response non-uniformity and differences between the simulation and the data [66]. The jet energy corrections (JEC) restore the jet energy scale (JES) in the following way: an offset for the neutral energy of pileup interactions; relative corrections that yield a uniform response in the p_T and η bins; the resulting offset in the average jet response is mitigated; finally residual differences between data and simulation are corrected. The jet energy resolution (JER) is defined as the Gaussian spread of the jet energy response. For central jets $|\eta| < 0.5$ the JER is between 4-15%, while for forward jets, $3.2 < |\eta| < 4.7$, it is between 12-18% [66].

Jets are required to pass the requirement $p_T > 30\,\text{GeV}$ and to be within the tracker acceptance $|\eta| < 2.4$ for the two analyses.

B tagged jets

Bottom quarks hadronize to relatively long lived and usually boosted B mesons that travel for a few hundred μm until they decay away from the interaction point, at a *displaced vertex* with respect to the PV. This is made use of to identify jets originating from heavy quarks. The combined secondary vertex (CSV) [67] algorithm builds the discrimination from light-flavor and gluon jets on the secondary vertex and track information and the possible electron or muon inside the jet from a W boson decay. B-tagged jets pass a lower requirement on their transverse momentum, $p_T > 20\,\text{GeV}$, than not tagged jets, which adds extra sensitivity to signals where soft quarks are produced.

Isolated tracks

For the first analysis presented in this thesis efficiently rejecting leptons is fundamental in order to have a distinct final state with respect to searches with leptons as well as reducing backgrounds. To remove events with very soft leptons, isolated PF muons and electrons are selected with $p_T > 5\,\text{GeV}$ and a longitudinal impact parameter of $|dz| < 0.1\,\text{cm}$. PF hadron tracks with $p_T > 10\,\text{GeV}$ and $|dz| < 0.1\,\text{cm}$ are used to reject events where a lepton is present but fails the tighter lepton identification requirements.

6.6 Higher level objects

Missing transverse energy

Neutrinos, and other possible "weakly" interacting particles, e.g. the LSP, are not detected directly with CMS. Their existence is only inferred by an imbalance in the transverse energy. The missing transverse energy, $|\vec{E}_T^{miss}|$, is defined as the negative of the sum of the transverse momenta of the PF candidates:

$$\vec{E}_T^{miss} = -\sum_i \vec{p}_{T,i}. \tag{6.3}$$

The $E_{\mathrm{T}}^{\mathrm{miss}}$ performance is improved by applying the JEC as introduced in Section 6.5. Further instrumental effects can deteriorate the $E_{\mathrm{T}}^{\mathrm{miss}}$ determination:

- noisy sensors and electronics
- showers of noncollision events
- inefficiencies in the object reconstruction
- dead regions of the detector
- direct interaction of a particle with the readout electronics
- nonlinear response of hadrons in the calorimeter systems

These problematic events are removed with dedicated filters based on the timing information, pulse shape and masking of channels [68], thus reducing tails in the $E_{\mathrm{T}}^{\mathrm{miss}}$ distribution. Figure 6.2 shows the $E_{\mathrm{T}}^{\mathrm{miss}}$ distribution before and after the cleaning of these events (left) and the comparison of data to simulation in the dimuon channel of top quark, diboson and Z/γ^* decays (right).

H_{T} and $H_{\mathrm{T}}^{\mathrm{miss}}$

The scalar sum of the p_T of the jets, H_{T}, is a measure of the hadronic energy in an event. Similarly the vector sum of the p_T of the jets, $H_{\mathrm{T}}^{\mathrm{miss}}$, is a measure of the missing hadronic energy in an event. They are defined as:

$$H_{\mathrm{T}} = \sum_{jets} |\vec{p}_{T,j}| \quad \text{and} \quad H_{\mathrm{T}}^{\mathrm{miss}} = |-\sum_{jets} \vec{p}_{T,j}|,$$

where the sum runs over the jets passing the aforementioned definitions.

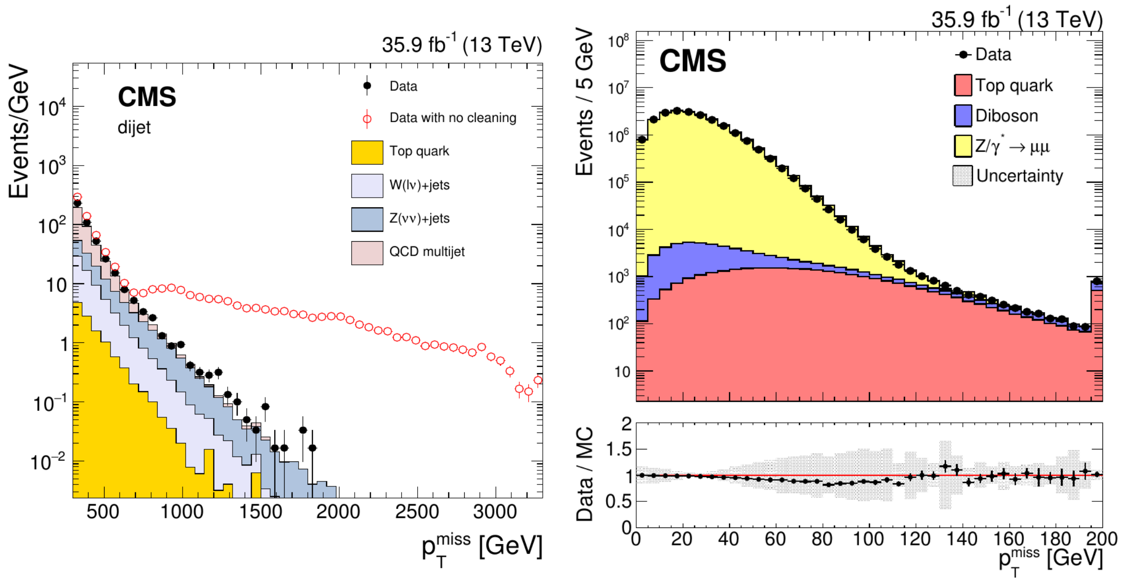

Figure 6.2: (Left) The $E_{\mathrm{T}}^{\mathrm{miss}}$ distribution in dijet data before (black markers) and after (red markers) the removal of problematic events. (Right) The $E_{\mathrm{T}}^{\mathrm{miss}}$ distribution of the dimuon data (black markers) compared to the simulation (histograms) and the corresponding uncertainty (grey hash) [68].

The M_{T2} variable

The M_{T2} [69] variable was introduced as a measure of the "mass" of a pair of particles, where the decay chain of each particle contains an undetected particle X with a mass m_X. Figure 6.3 shows an illustration of such a process in a pp collision. The sum of the detected particles in each chain defines the transverse momentum $\vec{p}_T^{\,\mathrm{vis}(i)}$, transverse energy $E_{\mathrm{T}}^{\mathrm{vis}(i)}$ and mass $m^{\mathrm{vis}(i)}$ of the two visible systems, $i = 1, 2$. The unknown transverse momentum of the undetectable particles is denoted as $\vec{p}_T^{\,X(i)}$ for the two chains i.

The transverse mass of each decay chain i can be written as: $E_{\mathrm{T}}^{\mathrm{vis}(i)}$ of the visible system i :

$$(M_{\mathrm{T}}^{(i)})^2 = (m^{\mathrm{vis}(i)})^2 + m_X^2 + 2\left(E_{\mathrm{T}}^{\mathrm{vis}(i)} \cdot E_{\mathrm{T}}^{X(i)} - \vec{p}_T^{\,\mathrm{vis}(i)} \cdot \vec{p}_T^{\,X(i)}\right). \tag{6.4}$$

As such, the $M_{\mathrm{T}}^{(i)}$ would not exceed the mass of the parent particle. However since the two momenta $\vec{p}_T^{\,X(i)}$ cannot be measured separately, the $M_{\mathrm{T}}^{(i)}$ are not accessible experimentally. On the other hand, the total $\vec{p}_{\mathrm{T}}^{\,\mathrm{miss}}$ can be measured, thus leading to a generalized definition of the transverse mass, M_{T2}, sometimes also called stransverse mass:

$$M_{\mathrm{T2}}(m_X) = \min_{\vec{p}_T^{\,X(1)} + \vec{p}_T^{\,X(2)} = \vec{p}_{\mathrm{T}}^{\,\mathrm{miss}}} \left[\max\left(M_{\mathrm{T}}^{(1)}(m_X), M_{\mathrm{T}}^{(2)}(m_X)\right)\right], \tag{6.5}$$

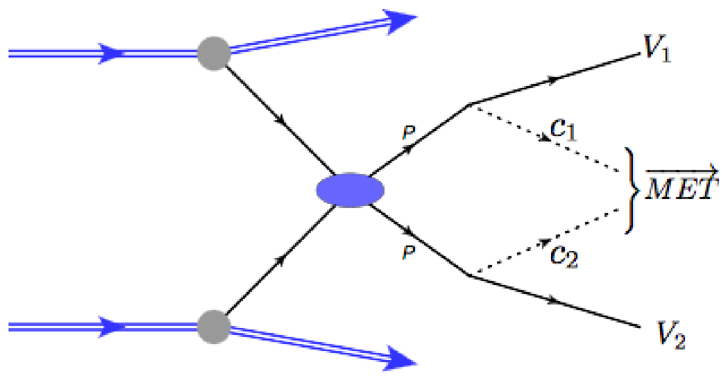

Figure 6.3: Sketch of a SUSY particle pair production in a pp collision where each particle P decays to an invisible $\tilde{\chi}$.

where the mass m_X of the undetected particle is a free parameter. For the minimization the momenta of the invisible particles are varied while fulfilling the constraint that their sum results in $\vec{p}_{\mathrm{T}}^{\mathrm{miss}}$. For the true mass of the undetected particle the M_{T2} distribution has an endpoint at the parent mass.

The SUSY signals in this thesis produce generally more than two visible objects in the final state. To generalize the definition above for more than two objects while not introducing an ambiguity by choosing two, all objects passing the analysis selection are clustered into two *pseudojets*, also referred to as hemispheres. The hemisphere algorithm as defined in Ref. [70], Section 13.4, is used for the clustering. First the two objects with the highest invariant mass $M(o_i, o_j)$, while neglecting their own mass $m_i = m_j = 0$, are chosen as the two axes. Then the remaining objects are assigned to one of these axes depending on their minimal Lund distance [71]. An object k is thus associated to the hemisphere i rather than the hemisphere j if

$$(E_i - p_i \cos\theta_{ik})\frac{E_i}{(E_i + E_k)^2} \leq (E_j - p_j \cos\theta_{jk})\frac{E_j}{(E_j + E_k)^2}. \tag{6.6}$$

When all objects have been assigned to an axis, the axes are recalculated from the sum of the p_T of the objects associated to it. To these new axes the objects are again assigned as above and new axes are calculated. This is repeated until no object changes from one axis to the other anymore.

In the limit of $m^{\mathrm{vis}(i)} << \vec{p}_T^{\,\mathrm{vis}(i)}$ the M_{T2} variable can be approximated as:

$$(M_{\mathrm{T2}})^2 \approx \vec{p}_T^{\,\mathrm{vis}(1)}\vec{p}_T^{\,\mathrm{vis}(2)}\left[2(1+\cos(\Delta\phi_{12})) + \left(\frac{m^{\mathrm{vis}(1)}}{\vec{p}_T^{\,\mathrm{vis}(1)}}\right)^2 + \left(\frac{m^{\mathrm{vis}(2)}}{\vec{p}_T^{\,\mathrm{vis}(2)}}\right)^2\right], \tag{6.7}$$

with the angle between the pseudojets being denoted as $\Delta\phi_{12}$. In the case of massive pseudojets the expression in Equation 6.7 can become large even if little $E_{\mathrm{T}}^{\mathrm{miss}}$ is present in the event. This leads to a sizeable contribution of QCD multijet events in the tails of the M_{T2} distribution due to its large cross section compared to the

SUSY signals. To reduce this background the mass of the pseudojets $m^{\mathrm{vis}(i)}$ is set to zero for the analyses presented in this thesis.

Under this constraint it follows further from Equation 6.7 that QCD dijet events, as they are generated in a back-to-back configuration, have $M_{\mathrm{T2}} \approx 0$ due to $\Delta\phi_{12} = \pi$. For QCD multijet events the pseudojets are not necessarily back-to-back and other methods to suppress the background are employed.

The SUSY signals and SM processes, such as $Z \to \nu\nu$ and $W^{\pm} \to \ell\nu$, have true $E_{\mathrm{T}}^{\mathrm{miss}}$ from the LSP and neutrino, respectively, and the pseudojets are thus not in a back-to-back configuration. Given that the two visible systems of the SUSY models are generally equal, $\vec{p}_T^{\,\mathrm{vis}(1)} \approx \vec{p}_T^{\,\mathrm{vis}(2)}$, M_{T2} will be large for these events.

The M_{T2} variable as defined above thus allows to suppress the QCD multijet background and improves the sensitivity to R-parity conserving SUSY models with pair-produced sparticles decaying semi-invisibly.

Part III

Search for SUSY in the fully hadronic final state

Be a nuisance when it counts.

Marjory Stoneman Douglas

7 Final states with large M_{T2}

Signs of SUSY could be detected in a plethora of ways with the CMS experiment. In Chapter 3.4 I have introduced the simplified models of SUSY and their production cross sections in Figure 3.4. The production of SUSY via the strong interaction, i.e. gluino- and squark-pair production, has the largest cross section, and thus the highest reach on the mass of the SUSY particles. Once the gluinos or squarks are produced, they will predominately decay hadronically. The fully hadronic final state thus probes SUSY at the energy frontier accessible at the LHC. The search conducted using the M_{T2} variable presented in this chapter targets exactly these phenomena.

Searches for SUSY in fully hadronic final states have been conducted previously by the CMS [72–74] and ATLAS collaborations [75–79]. This search is a continuation of previous searches conducted with $19.5\,\mathrm{fb}^{-1}$ of Run1 data at 8 TeV [80] and the first $2.3\,\mathrm{fb}^{-1}$ of Run2 data collected in 2015 [81] at 13 TeV. This search uses the data collected by the CMS detector in 2016, corresponding to an integrated luminosity of $35.9\ \mathrm{fb}^{-1}$, at $\sqrt{s} = 13\,\mathrm{TeV}$, which resulted in the paper [82].

The increase in center of mass energy, and thus increase in SUSY production cross section at a higher rate than the SM backgrounds, and the higher integrated luminosity allow for significant improvements over previous results. In Section 7.1 I describe the selection of data and simulation, which are then categorized into the search regions as described in Section 7.2. The backgrounds and their estimation is introduced in Section 7.3. The results and their interpretation in the simplified models of SUSY are shown in Section 7.4. A summary is given in Section 7.5.

7.1 Selection

This section describes the way events are selected and simulated. Events are selected by the triggers of the CMS detector as described in Section 7.1.1. How events are generated by the Monte Carlo (MC) simulation is described in Section 7.1.2. The baseline selection for the analysis is described in Section 7.1.3, starting from the trigger up to the analysis specific, beyond the basic object definition as described in Chapter 6.

7.1.1 Trigger

The final state for this analysis has at least one jet, but generally multiple jets or jets with hundreds of GeV of p_T are present along with missing transverse energy. To select these events at the trigger level a mix of pure H_{T} and mixed H_{T} and $E_{\mathrm{T}}^{\mathrm{miss}}$ triggers are used.

The pure H_T trigger has an online selection of 900 GeV, which was shown to be 99% efficient above 1000 GeV on H_T, once paired with a 450 GeV jet p_T trigger[1].

At lower values of H_T, a pure H_T trigger has to be prescaled and thus triggers with requirements on H_T and $E_\mathrm{T}^\mathrm{miss}$, so called cross triggers, are used instead. The 300 GeV H_T and 110 GeV $E_\mathrm{T}^\mathrm{miss}$ cross trigger reaches an efficiency of $98.7 \pm 0.1\%$ at $E_\mathrm{T}^\mathrm{miss} > 250$ GeV when combined with the $E_\mathrm{T}^\mathrm{miss} \times H_\mathrm{T}^\mathrm{miss}$ trigger with thresholds of 120 GeV in online $E_\mathrm{T}^\mathrm{miss}$ and $H_\mathrm{T}^\mathrm{miss}$. The latter trigger and its equivalent version with the additional requirement on the absence of muon chamber hits have also been shown to have a similar efficiency for offline $E_\mathrm{T}^\mathrm{miss} > 250$ GeV.

Overall, this trigger strategy allows to push the offline selection to the lowest possible values of H_T and $E_\mathrm{T}^\mathrm{miss}$ while maintaining (nearly) full efficiency. The baseline selection due to the trigger can be summarized as follows: $E_\mathrm{T}^\mathrm{miss} > 30$ GeV for $H_\mathrm{T} > 1000$ GeV else $E_\mathrm{T}^\mathrm{miss} > 250$ GeV. This information is visualized in Figure 7.1.

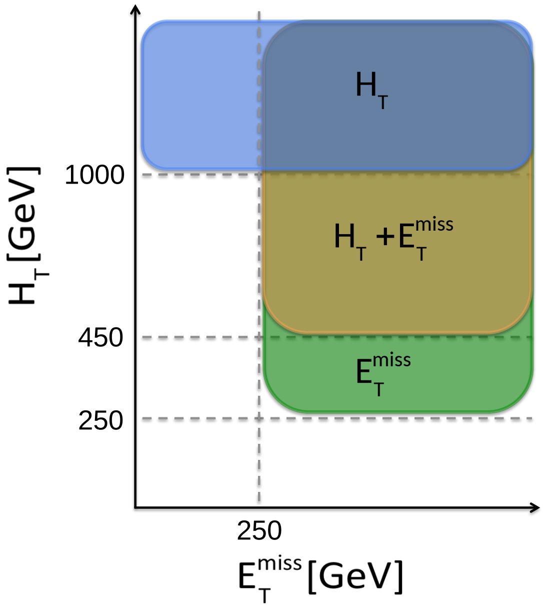

Figure 7.1: Schematic of the trigger coverage of the pure $E_\mathrm{T}^\mathrm{miss}$, pure H_T and the $E_\mathrm{T}^\mathrm{miss}$ and H_T cross triggers, along with their thresholds.

7.1.2 Simulation

Monte Carlo (MC) simulations are used to optimize the analysis, to test signal sensitivity, for the data driven estimates and for validation purposes. The number of extra partons considered in the matrix element calculations are up to four, three or two for V+jets (V=W,Z), $t\bar{t}$+jets and the signal samples, respectively. The

[1] This jet trigger recovers for the last run era of 2016 a known inefficiency at high H_T, which was caused by a saturation in the Level1 hardware tracking.

background samples (Z+jets, W+jets, $t\bar{t}$+jets) and the signal samples are generated with MADGRAPH 5 [83, 84] at leading order (LO) accuracy. The fragmentation and parton showering is generated by PYTHIA 8.2 [85]. The rare background samples $t\bar{t}$V (V=W,Z) are generated with up to two additional partons with the same generators. The single top samples are generated with MADGRAPH_aMC@NLO [83] or POWHEG [86, 87] at next-to-leading order (NLO) precision. Smaller contributions to the backgrounds, such as diboson production, were found to be negligible.

Once the events are generated they are passed to a detailed implementation of the CMS detector in GEANT4 [88] to simulate the detector response. In the digitisation step this response is converted into a digital signal taking into account the noise and trigger effects. The events are then reconstructed in the same way as the collision data. For the signal samples the so called fast simulation program [89, 90] is used, which accurately predicts the momentum resolution and the particle identification efficiencies. The most precise available cross sections are used for the normalization of the samples, generally at NLO and next-to-NLO precision [83, 86, 87, 91–94].

The MADGRAPH modeling of additional jets from initial state radiation (ISR) is improved in the following way: Events in a MADGRAPH $t\bar{t}$ sample are weighted according to the number of ISR jets (N_j^{ISR}) to match the shape in data. These weights are obtained from a $t\bar{t}$ enriched region in data by selecting events with two leptons and exactly two b-tagged jets. The weights vary from 0.92 for $N_j^{ISR} = 1$ to 0.51 for $N_j^{ISR} \geq 6$. The same reweighting procedure is applied to the signal MC.

7.1.3 Baseline selection

The particle flow candidates and higher level objects described in Chapter 6 are used to classify the events. Events with at least one jet and no isolated lepton (e, μ) nor charged PF candidate (track) are selected. The selection for jets and b-tagged jets, and the veto requirements on the leptons and tracks are listed in Table 7.1. The veto on the charged PF candidates further reduces the electron and muon background as well as hadronic tau decays.

From the trigger selection described in Section 7.1.1 follows the first requirement on $E_{\mathrm{T}}^{\mathrm{miss}}$ in Table 7.1. Jet are required to be well separated from $E_{\mathrm{T}}^{\mathrm{miss}}$ to reject events with a mismeasured jet, which would result in a $E_{\mathrm{T}}^{\mathrm{miss}}$ in its direction. A requirement on the maximal azimuthal separation between $E_{\mathrm{T}}^{\mathrm{miss}}$ and the four leading jets (j_{1234}) within $|\eta| < 4.7$ is applied as follows: $\Delta\phi_{min} = \Delta\phi(E_{\mathrm{T}}^{\mathrm{miss}}, j_{1234}) > 0.3$. Requiring $|\vec{E}_{\mathrm{T}}^{\mathrm{miss}} - \vec{H}_{\mathrm{T}}^{\mathrm{miss}}|/E_{\mathrm{T}}^{\mathrm{miss}} < 0.5$ reduces the backgrounds from events where the missing energy from the sum of jets and the sum of PF candidates differ by more than 50% of $E_{\mathrm{T}}^{\mathrm{miss}}$.

The M_{T2} variable as described in Chapter 6 rejects SM multijet production and to this end a lower bound is employed to keep those events a subdominant background. The selection on M_{T2} is applied only for events with at least two jets, since M_{T2} is undefined for events with only one visible object; $M_{\mathrm{T2}} > 200\,\mathrm{GeV}$ for $H_{\mathrm{T}} < 1500\,\mathrm{GeV}$, else $M_{\mathrm{T2}} > 400\,\mathrm{GeV}$. For events with exactly one jet the requirements are $p_T^{jet} > 250\,\mathrm{GeV}$ and $E_{\mathrm{T}}^{\mathrm{miss}} > 250\,\mathrm{GeV}$. Figure 7.2 shows the M_{T2}

distribution inclusively in the multijet region after the baseline selection is applied.

Table 7.1: Summary of the baseline selection.

Jet selection	$\Delta R < 0.4$, $p_T > 30\,\mathrm{GeV}$, $\lvert\eta\rvert < 2.4$
b-tagged jet selection	$p_T > 20\,\mathrm{GeV}$, $\lvert\eta\rvert < 2.4$
Veto muon	$p_T > 10\,\mathrm{GeV}$, $\lvert\eta\rvert < 2.4$, $p_T^{\mathrm{sum}} < 0.2 \times p_T^{\mathrm{lep}}$ or $p_T > 5\,\mathrm{GeV}$, $\lvert\eta\rvert < 2.4$, $M_{\mathrm{T}} < 100\,\mathrm{GeV}$, $p_T^{\mathrm{sum}} < 0.2 \times p_T^{\mathrm{lep}}$
Veto electron	$p_T > 10\,\mathrm{GeV}$, $\lvert\eta\rvert < 2.4$, $p_T^{\mathrm{sum}} < 0.1 \times p_T^{\mathrm{lep}}$ or $p_T > 5\,\mathrm{GeV}$, $\lvert\eta\rvert < 2.4$, $M_{\mathrm{T}} < 100\,\mathrm{GeV}$, $p_T^{\mathrm{sum}} < 0.2 \times p_T^{\mathrm{lep}}$
Veto track	$p_T > 10\,\mathrm{GeV}$, $\lvert\eta\rvert < 2.4$, $M_{\mathrm{T}} < 100\,\mathrm{GeV}$, $p_T^{\mathrm{sum}} < 0.1 \times p_T^{\mathrm{lep}}$
$E_{\mathrm{T}}^{\mathrm{miss}}$	$E_{\mathrm{T}}^{\mathrm{miss}} > 250\,\mathrm{GeV}$ for $H_{\mathrm{T}} < 1000\,\mathrm{GeV}$, else $E_{\mathrm{T}}^{\mathrm{miss}} > 30\,\mathrm{GeV}$ $\Delta\phi\left(E_{\mathrm{T}}^{\mathrm{miss}}, j_{1,2,3,4}\right) > 0.3$ $\lvert\vec{E}_{\mathrm{T}}^{\mathrm{miss}} - \vec{H}_{\mathrm{T}}^{\mathrm{miss}}\rvert / E_{\mathrm{T}}^{\mathrm{miss}} < 0.5$
M_{T2}	$M_{\mathrm{T2}} > 200\,\mathrm{GeV}$ for $H_{\mathrm{T}} < 1500\,\mathrm{GeV}$, else $M_{\mathrm{T2}} > 400\,\mathrm{GeV}$

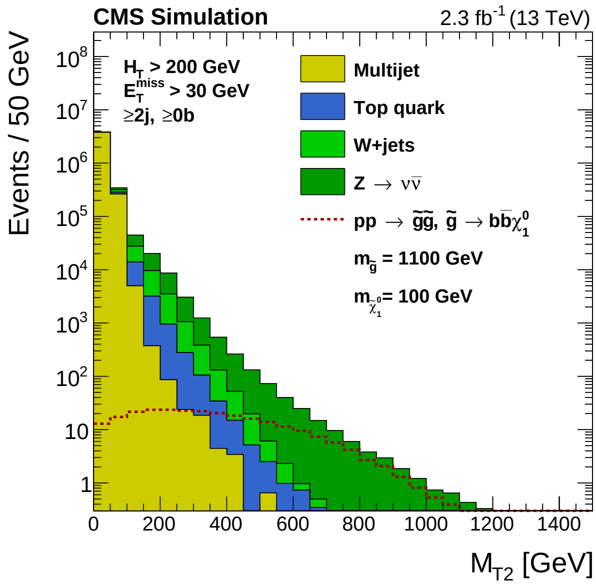

Figure 7.2: The M_{T2} distribution in simulation after the baseline selection and in the multijet region at $2.3\,\mathrm{fb}^{-1}$ [81]. The backgrounds are stacked, while the signal is overlayed as a red dashed line.

7.2 Classification

In the previous section I have described the circumstantial selections on the events, due to the trigger and for background rejection. In this section the aim is to optimally split the remaining phase space to test a multitude of simplified models of SUSY. These models have vastly different topologies, ranging from final states with few jets and no b-tagged jets in direct squark production, where the squarks decay to light flavor quarks; to topologies with high jet and b-tagged jet multiplicities in gluino mediated squark pair production, where the squarks decay to top quarks. Also within the models the final states can differ significantly, since the mass difference between the SUSY mother particle and the neutralino ranges from almost zero (compressed region) to hundreds of GeV (open spectrum region), resulting in no $E_{\mathrm{T}}^{\mathrm{miss}}$ to hundreds of GeV of $E_{\mathrm{T}}^{\mathrm{miss}}$, respectively. In order to cover this wide phase space, the signal regions are binned in H_{T}, jet (N_{jets}) and b-tagged jet ($N_{\mathrm{b-tags}}$) multiplicity and in the discovery variable M_{T2}.

Splitting in N_{jets} and $N_{\mathrm{b-tags}}$ allows to cover the different signal models, while also changing the background composition as shown in Figure 7.3. The splitting in H_{T} regions gives sensitivity to the energy scale of the SUSY particles in the event. There are five H_{T} regions in total, from *very low* to *extreme* H_{T}, as shown in Figure 7.4. Each category of (N_{jets}, $N_{\mathrm{b-tags}}$, H_{T}) is called *topological* region, and is part of the *multijet* region, where at least two jets are present.

Finally events are binned in M_{T2}, which is the discovery variable, introduced in Chapter 6. As shown in Figure 7.2 the backgrounds fall steeply as a function of M_{T2}, while the signal has an endpoint at the parent mass. Thus binning in M_{T2} allows to discriminate between signal and background and between different signal hypotheses. Tables 7.3 and 7.4 list the adopted M_{T2} binning for each of the 63 topological regions.

The *monojet* region, $N_{\mathrm{jets}} = 1$, targets the signals with compressed spectra. For events with exactly one jet $H_{\mathrm{T}} \approx p_T(jet_1)$, and thus the p_T of the jet has to satisfy $p_T \geq 250\,\mathrm{GeV}$. The events are split into the two categories with either zero or one b-tagged jet. Since there is only one jet in the events, M_{T2} is not defined and the events are classified in bins of $p_T(jet_1)$. Table 7.2 lists the categories of the monojet region.

There are 213 categories in total in this analysis. For easier reinterpretation *super signal regions* are defined which are simpler inclusive regions, that allow for an approximated interpretation. They will be discussed in more details in 7.4.

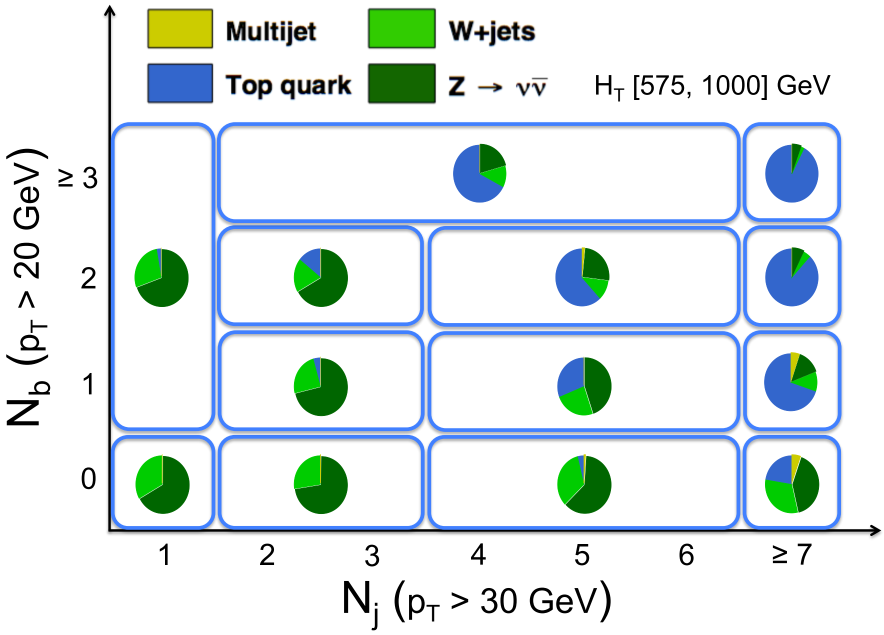

Figure 7.3: Background composition in the medium H_{T} region as a function of N_{jets} and $N_{\mathrm{b-tags}}$, integrated over M_{T2}.

Table 7.2: Summary of signal regions for the monojet selection.

$N_{\mathrm{b-tags}}$	jet p_T binning [GeV]
0	[250,350,450,575,700,1000,1200,∞]
≥ 1	[250,350,450,575,700,∞]

Table 7.3: Adopted M_{T2} binning in each topological region of the multijet search regions, for the very low, low and medium H_{T} regions.

H_{T} Range [GeV]	Jet Multiplicities	M_{T2} Binning [GeV]
[250, 450]	$2-3$j, 0b	[200, 300, 400, ∞]
	$2-3$j, 1b	[200, 300, 400, ∞]
	$2-3$j, 2b	[200, 300, 400, ∞]
	≥ 4j, 0b	[200, 300, 400, ∞]
	≥ 4j, 1b	[200, 300, 400, ∞]
	≥ 4j, 2b	[200, 300, 400, ∞]
	≥ 2j, ≥ 3b	[200, 300, 400, ∞]
[450, 575]	$2-3$j, 0b	[200, 300, 400, 500, ∞]
	$2-3$j, 1b	[200, 300, 400, 500, ∞]
	$2-3$j, 2b	[200, 300, 400, 500, ∞]
	$4-6$j, 0b	[200, 300, 400, 500, ∞]
	$4-6$j, 1b	[200, 300, 400, 500, ∞]
	$4-6$j, 2b	[200, 300, 400, 500, ∞]
	≥ 7j, 0b	[200, 300, 400, ∞]
	≥ 7j, 1b	[200, 300, 400, ∞]
	≥ 7j, 2b	[200, 300, 400, ∞]
	$2-6$j, ≥ 3b	[200, 300, 400, 500, ∞]
	≥ 7j, ≥ 3b	[200, 300, 400, ∞]
[575, 1000]	$2-3$j, 0b	[200, 300, 400, 600, 800, ∞]
	$2-3$j, 1b	[200, 300, 400, 600, 800, ∞]
	$2-3$j, 2b	[200, 300, 400, 600, 800, ∞]
	$4-6$j, 0b	[200, 300, 400, 600, 800, ∞]
	$4-6$j, 1b	[200, 300, 400, 600, 800, ∞]
	$4-6$j, 2b	[200, 300, 400, 600, 800, ∞]
	≥ 7j, 0b	[200, 300, 400, 600, 800, ∞]
	≥ 7j, 1b	[200, 300, 400, 600, ∞]
	≥ 7j, 2b	[200, 300, 400, 600, ∞]
	$2-6$j, ≥ 3b	[200, 300, 400, 600, ∞]
	≥ 7j, ≥ 3b	[200, 300, 400, 600, ∞]

Table 7.4: Adopted M_{T2} binning in each topological region of the multijet search regions, for the high and extreme H_T regions.

H_T Range [GeV]	Jet Multiplicities	M_{T2} Binning [GeV]
[1000, 1500]	$2-3$j, 0b	[200, 400, 600, 800, 1000, 1200, ∞]
	$2-3$j, 1b	[200, 400, 600, 800, 1000, 1200, ∞]
	$2-3$j, 2b	[200, 400, 600, 800, 1000, ∞]
	$4-6$j, 0b	[200, 400, 600, 800, 1000, 1200, ∞]
	$4-6$j, 1b	[200, 400, 600, 800, 1000, 1200, ∞]
	$4-6$j, 2b	[200, 400, 600, 800, 1000, ∞]
	≥ 7j, 0b	[200, 400, 600, 800, 1000, ∞]
	≥ 7j, 1b	[200, 400, 600, 800, ∞]
	≥ 7j, 2b	[200, 400, 600, 800, ∞]
	$2-6$j, ≥ 3b	[200, 400, 600, ∞]
	≥ 7j, ≥ 3b	[200, 400, 600, ∞]
[1500, ∞]	$2-3$j, 0b	[400, 600, 800, 1000, 1400, ∞]
	$2-3$j, 1b	[400, 600, 800, 1000, ∞]
	$2-3$j, 2b	[400, ∞]
	$4-6$j, 0b	[400, 600, 800, 1000, 1400, ∞]
	$4-6$j, 1b	[400, 600, 800, 1000, 1400, ∞]
	$4-6$j, 2b	[400, 600, 800, ∞]
	≥ 7j, 0b	[400, 600, 800, 1000, ∞]
	≥ 7j, 1b	[400, 600, 800, ∞]
	≥ 7j, 2b	[400, 600, 800, ∞]
	$2-6$j, ≥ 3b	[400, 600, ∞]
	≥ 7j, ≥ 3b	[400, ∞]

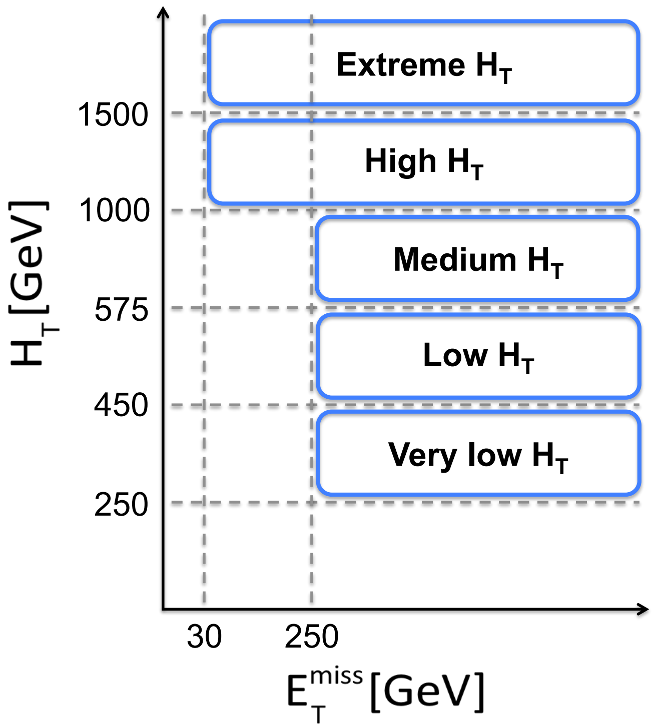

Figure 7.4: The H_T regions with their respective $E_\mathrm{T}^\mathrm{miss}$ bounds.

7.3 Backgrounds

There are three main backgrounds that share a similar topology to the signal events for this analysis. Similarly to the signal they produce events with large values of $E_\mathrm{T}^\mathrm{miss}$: instrumental $E_\mathrm{T}^\mathrm{miss}$ due to mis-measurement of jets in QCD multijet events, discussed in section 7.3.1; $E_\mathrm{T}^\mathrm{miss}$ due to the leptonic decay of a W boson, where the charged lepton is not recognized by the lepton veto, discussed in section 7.3.2; and finally $E_\mathrm{T}^\mathrm{miss}$ from the decay of a Z boson to two neutrinos, discussed in section 7.3.3. The following sections will discuss the origin of the backgrounds, their estimate from a control region in data and the systematic uncertainties associated with them. This chapter is largely based on the description of [82].

7.3.1 QCD multijet

Where protons collide, there be jets. In a perfect world, with a perfect detector, this section would not exist. But back to reality: when jets are mismeasured or fall out of the acceptance of the detector this gives rise to so-called *instrumental* missing transverse energy, since no genuine $E_\mathrm{T}^\mathrm{miss}$ is present in the event before its decay products reach the measurement instruments. This background is often referred to as QCD production of multijet events but it also comprises vector boson and top-quark pair production, as long as they decay hadronically.

The M_{T2} variable[2] is designed exactly to suppress this kind of background of instrumental $E_{\mathrm{T}}^{\mathrm{miss}}$. Everything that goes missing from the event is aligned with a jet that was either under- or over-measured. This angular information between $E_{\mathrm{T}}^{\mathrm{miss}}$ and the jets is exactly what M_{T2} relies on when the hemispheres are constructed. The minimal angle between the four leading jets (j_{1234}) within $|\eta| < 4.7$ and the missing transverse energy, $\Delta\phi(\mathrm{j}_{1234}, E_{\mathrm{T}}^{\mathrm{miss}})$ as described in section 7.1, is a further way to make use of the directional information present in the event. In the baseline selection for this analysis, the leading jets and $E_{\mathrm{T}}^{\mathrm{miss}}$ have to satisfy $\Delta\phi(\mathrm{j}_{1234}, E_{\mathrm{T}}^{\mathrm{miss}}) > 0.3$. The events at $\Delta\phi(\mathrm{j}_{1234}, E_{\mathrm{T}}^{\mathrm{miss}}) < 0.3$ have at least one jet close to $E_{\mathrm{T}}^{\mathrm{miss}}$. These events are used as the control region to estimate the yield of QCD multijet events in the signal region. Since the $\Delta\phi$ method depends on the extrapolation from events at low values of M_{T2}, and thus low values of $E_{\mathrm{T}}^{\mathrm{miss}}$, pure H_{T} triggers are required to record those events as described below.

For the monojet signal region, a separate way of estimating the background from jet mismeasurement has to be employed, since for this final state $E_{\mathrm{T}}^{\mathrm{miss}}$ points in the opposite direction of the jet.

The final part of this section discusses the statistical and systematic uncertainties associated with the estimate from the $\Delta\phi$ method and the monojet estimate.

Pure H_{T} control region triggers

The method to estimate the QCD multijet background relies on an extrapolation from low to high values of M_{T2}. For the low M_{T2} regime, the method relies on special triggers. The available triggers have no dependence on $E_{\mathrm{T}}^{\mathrm{miss}}$ and yet there is a necessity to cover signal regions from the lowest to highest H_{T} values. Pure H_{T} triggers without a $E_{\mathrm{T}}^{\mathrm{miss}}$ requirement would yield unreasonably high rates at low values of H_{T}. Thus they have a dynamic prescale that depends on the instantaneous luminosity. To obtain their effective prescale over the whole run period they have to be compared to an unprescaled trigger. Figure 7.5 shows the ratio between different H_{T}-only triggers as a function of H_{T}. The values indicated on the figure correspond to the (relative) prescale between the tested trigger and the unprescaled (another prescaled) trigger.

The integrated luminosity indicated on Figure 7.5 is only $27.7\mathrm{fb}^{-1}$ instead of $35.9\ \mathrm{fb}^{-1}$, which is due to the L1 trigger inefficiency affecting RunH of the data taking period. The trigger to recover these events is only efficient for $H_{\mathrm{T}} > 1000\,\mathrm{GeV}$, so while the signal region is not affected by this effect, the prescaled triggers are, and thus the regions where we obtain the factors r_ϕ, f_j and r_b described in the next section. In order to have a reliable estimate RunH is excluded for the control region.

The $\Delta\phi_{min}$ method

The multijet background in the high $\Delta\phi_{min}$ signal region is estimated from data in the low $\Delta\phi_{min}$ region. After subtraction of the non-QCD background using the

[2] A plethora of other variables have been designed for the same purpose.

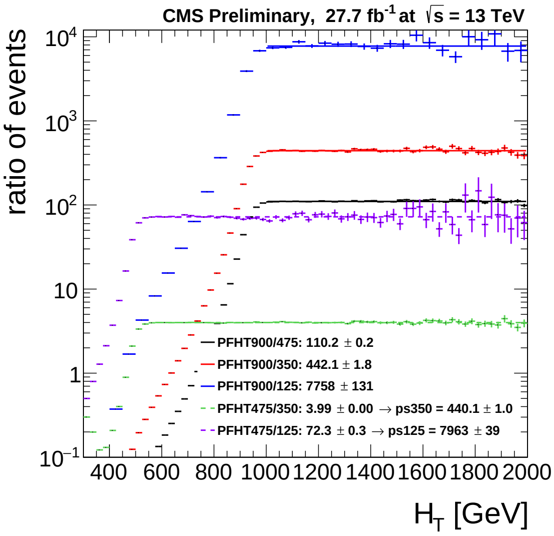

Figure 7.5: Ratio of the different H_{T} only trigger paths as a function of H_{T}. A constant is fit to the ratio once it reaches the plateau corresponding to the effective prescale, if the trigger in the denominator is unprescaled (HLT_PFHT900), and the relative prescale, if both triggers are prescaled.

simulation, the control region yield is multiplied by a ratio r_ϕ, defined as:

$$r_\phi(M_{\mathrm{T2}}) = \frac{\mathrm{N}(\Delta\phi_{min} > 0.3)}{\mathrm{N}(\Delta\phi_{min} < 0.3)}, \tag{7.1}$$

where $\mathrm{N}(\Delta\phi_{min} > 0.3)$ and $\mathrm{N}(\Delta\phi_{min} < 0.3)$ represent the yields of the QCD background in the respective $\Delta\phi$ region as a function of M_{T2}. The ratio is found to be well described by a power law function in the simulation

$$r_\phi(M_{\mathrm{T2}}) = a \cdot M_{T2}^b, \tag{7.2}$$

where the parameters a and b can be determined from a fit in each H_{T} region. The ratio is fitted in data at low values of M_{T2} and then extrapolated to high values of M_{T2} using these parameters.

The fit is performed in a range of M_{T2} where the QCD production is dominant: below 60 GeV of M_{T2} the main contribution to $E_{\mathrm{T}}^{\mathrm{miss}}$ is not from jet mismeasurement but from $t\bar{t}$ and V+jets production. At higher values of H_{T} non-instrumental $E_{\mathrm{T}}^{\mathrm{miss}}$ extends to higher values, thus jet mismeasurements become dominant only above 70 GeV of M_{T2} in the extreme H_{T} region. Above 100 GeV of M_{T2} the contributions from electroweak and top-quark production become large compared to the QCD multijet, as shown in Figure 7.2. The fit to the ratio is thus performed in the region $60(70) < M_{\mathrm{T2}} < 100$ GeV.

These bounds are varied up and down to asses the systematic uncertainty associated with the choice of the fit window. The lower bound is varied by 5 GeV up and down.

In case of the variation up of the lower bound, also the upper bound of the fit window is increased by 25 GeV to make up for the loss of statistics at the lower end. The resulting systematic uncertainty ranges from 14-42% above $M_{\mathrm{T2}} > 200\,\mathrm{GeV}$ and covers the variations. The fits in simulation and data are shown in Figures 7.6 and 7.7, respectively.

Since the QCD multijet background is the subdominant background in the signal region (at high values of M_{T2}), there are not enough events in the signal region to build the ratio for each of the analysis categories. Instead the ratio r_ϕ is built in each H_{T} region, meaning inclusively in N_{jets} and $N_{\mathrm{b-tags}}$. The estimates are scaled by f_j and r_b factors, corresponding to the fractions of events falling within an N_{jets} and $N_{\mathrm{b-tags}}$ bin, respectively.

The f_j and r_b fractions are obtained in the low $\Delta\phi_{min}$ region and for $100 < M_{\mathrm{T2}} < 200\,\mathrm{GeV}$. They are found to have no dependence on M_{T2}. While f_j does not depend on $N_{\mathrm{b-tags}}$, it is found to depend on H_{T}. For r_b, on the other hand, there is no dependence on H_{T} but a dependence on N_{jets}. Thus f_j is determined in each H_{T} bin integrated over $N_{\mathrm{b-tags}}$, and r_j is determined for each N_{jets} bin integrated over H_{T}. In Figure 7.8 f_j is shown in data for each of the five H_{T} regions and compared to the simulation. Figure 7.9 shows r_b for the three $N_{\mathrm{b-tags}}$ categories in data and in simulation.

Combining all of these inputs the yield in the signal region at high $\Delta\phi_{min}$ ($N_{SR}^{\Delta\phi_{min}>0.3}$) is calculated as follows:

$$N_{SR}^{(\Delta\phi_{min}>0.3)}(M_{\mathrm{T2}}, H_{\mathrm{T}}, N_{\mathrm{jets}}, N_{\mathrm{b-tags}}) = r_\phi(M_{\mathrm{T2}}, H_{\mathrm{T}}) \cdot f_j(N_{\mathrm{jets}}) \cdot r_b(N_{\mathrm{b-tags}}) \cdot N_{CR}^{(\Delta\phi_{min}<0.3)}(M_{\mathrm{T2}}, H_{\mathrm{T}}), \tag{7.3}$$

where $N_{CR}^{(\Delta\phi_{min}<0.3)}(M_{\mathrm{T2}}, H_{\mathrm{T}})$ is the number of events in data after subtracting the non-QCD background contribution.

Background estimation for the monojet regions

In the case of the monojet signal region the missing energy points opposite to the jet in the event. Thus the $\Delta\phi_{min}$ method cannot be applied. This background comes from events which have initially two jets, but one of them falls out of acceptance in p_T due to mismeasurement. These events are estimated from a control region that follows the same selection as the monojet region, except that two jets are required, making it orthogonal to the monojet signal region, and $\Delta\phi(\mathrm{j}_{1234}, E_{\mathrm{T}}^{\mathrm{miss}}) < 0.3$, making it orthogonal to the multijet signal region. The subleading jet p_T for this control region is shown in figure 7.10, where the events at $30 < p_T^{jet2} < 60\,\mathrm{GeV}$ are used as the higher bound on the events at $0 < p_T^{jet2} < 30\,\mathrm{GeV}$. Figure 7.10 shows a large contribution from electroweak processes that has to be subtracted. The fraction from these processes is obtained from simulation applying the same selection as to data. A 50% uncertainty is applied for this subtraction. Thus the final estimated number of events in a given monojet signal region with p_T^{jet1} is:

$$N_{QCD}(p_T^{jet1}) = N_{data}^{30-60}(p_T^{jet1}) \cdot f_{QCD}^{30-60}(p_T^{jet1}), \tag{7.4}$$

where N_{data}^{30-60} is the yield in data in the control region and f_{QCD}^{30-60} the fraction of QCD events from simulation, both in the range $30 < p_T^{jet2} < 60\,\mathrm{GeV}$.

Statistical and systematic uncertainties

The statistical and systematic uncertainties for the estimation of the multijet background are:

- Poisson uncertainty for the observed control region count in the low $\Delta\phi_{min}$ region;
- the statistical uncertainty on r_ϕ due to the number of events in the fit window;
- the systematic uncertainty on r_ϕ due to the choice of fit window obtained from varying the fit range up and down, and estimated to be $14 - 42\%$.
- the statistical uncertainty on f_j and r_b from the size of the low $\Delta\phi_{min}$ control region at $100 < M_{\mathrm{T2}} < 200\,\mathrm{GeV}$;
- the systematic uncertainties for the transfer factors f_j and r_b. The factors are obtained in varying $\Delta\phi_{min}$, M_{T2} and H_{T} regions and the maximal root mean square error of the variations for each f_j and r_b is taken as the systematic uncertainty:

Observable	f_{23}	f_{46}	f_{7+}	r_0	r_1	r_2	r_{3+}
Syst. error	25%	7%	20%	8%	20%	35%	70%

The statistical and systematic uncertainties for the estimation of the monojet background are:

- Poisson uncertainty for the observed dijet control region count;
- systematic uncertainty on the subtraction of the non-multijet background, estimated to be 50%.

The r_ϕ method is validated in the intermediate M_{T2} region ($100 < M_{\mathrm{T2}} < 200\,\mathrm{GeV}$) as shown in Figure 7.11 for the topological regions as indicated on the figure. The electroweak background from simulation is added to the prediction and their sum is compared to the data, good agreement is found within the uncertainties.

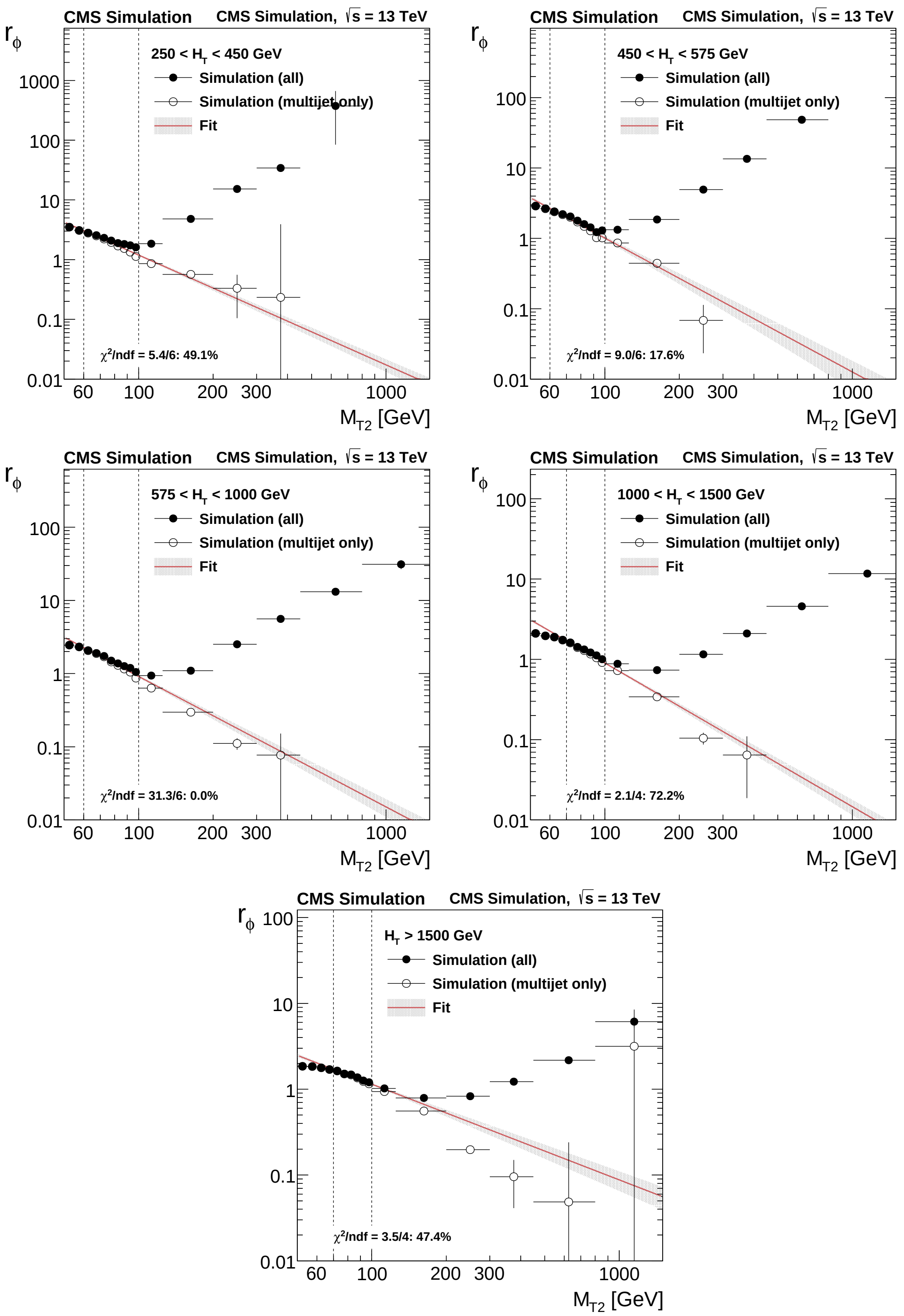

Figure 7.6: The ratio $r_\phi(M_{\mathrm{T2}}) = N(\Delta\phi_{\min} > 0.3)/N(\Delta\phi_{\min} < 0.3)$ in simulation as a function of M_{T2} in the very low (top left), low (top right), medium (middle left), high (middle right), extreme (bottom) H_{T} regions. The full and hollow points show the ratio as expected from simulation using all background components and only the QCD multijet part, respectively. The errors are statistical only. The power law fit to the ratio is represented in the red line and the band around it is the associated fit uncertainty.

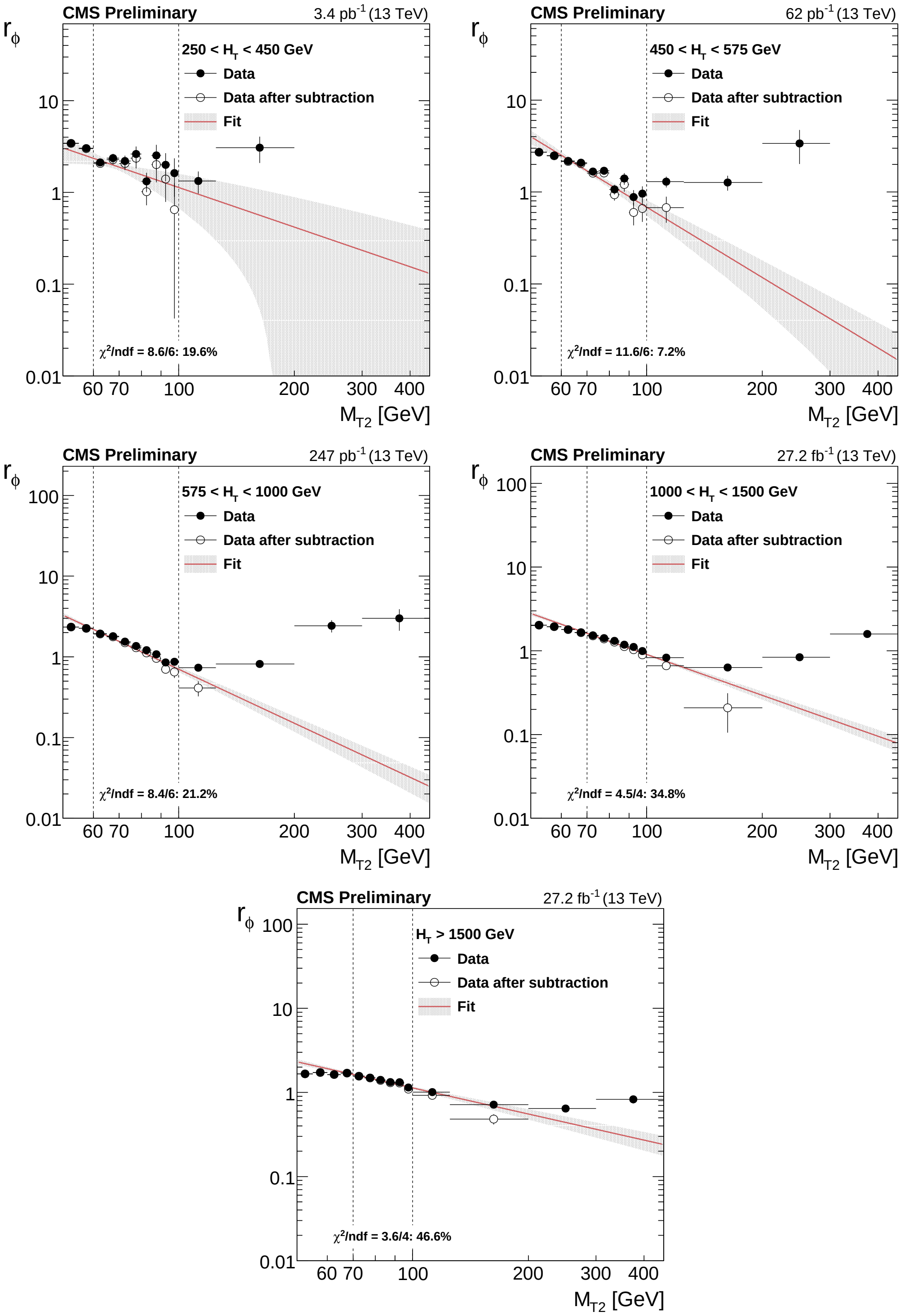

Figure 7.7: The ratio $r_\phi(M_{\mathrm{T2}}) = N(\Delta\phi_{\min} > 0.3)/N(\Delta\phi_{\min} < 0.3)$ in data as a function of M_{T2} in the very low (top left), low (top right), medium (middle left), high (middle right), extreme (bottom) H_{T} regions. The full points show the ratio in data, while the hollow points show the data after subtraction of the electroweak contribution. The errors are statistical only. The power law fit to the ratio is represented in the red line and the band around it is the associated fit uncertainty.

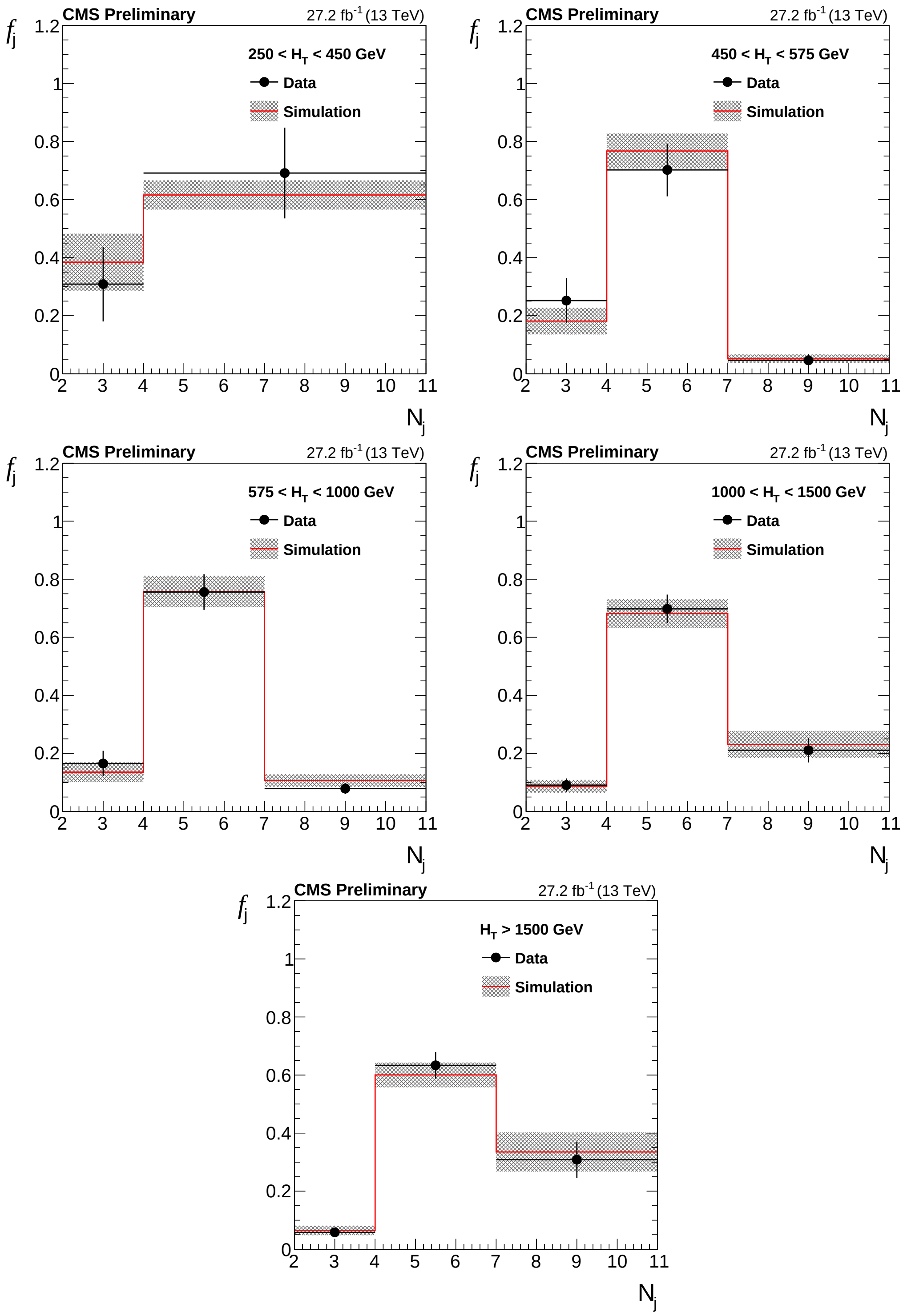

Figure 7.8: Comparison of f_j in data (black circles) and simulation (red line) measured in the region $\Delta\phi_{min} < 0.3$ and $100 < M_{\mathrm{T2}} < 200\,\mathrm{GeV}$, in the very low (top left), low (top right), medium (middle left), high (middle right) and high (bottom) H_{T} region. The uncertainties are the statistical plus systematic uncertainties.

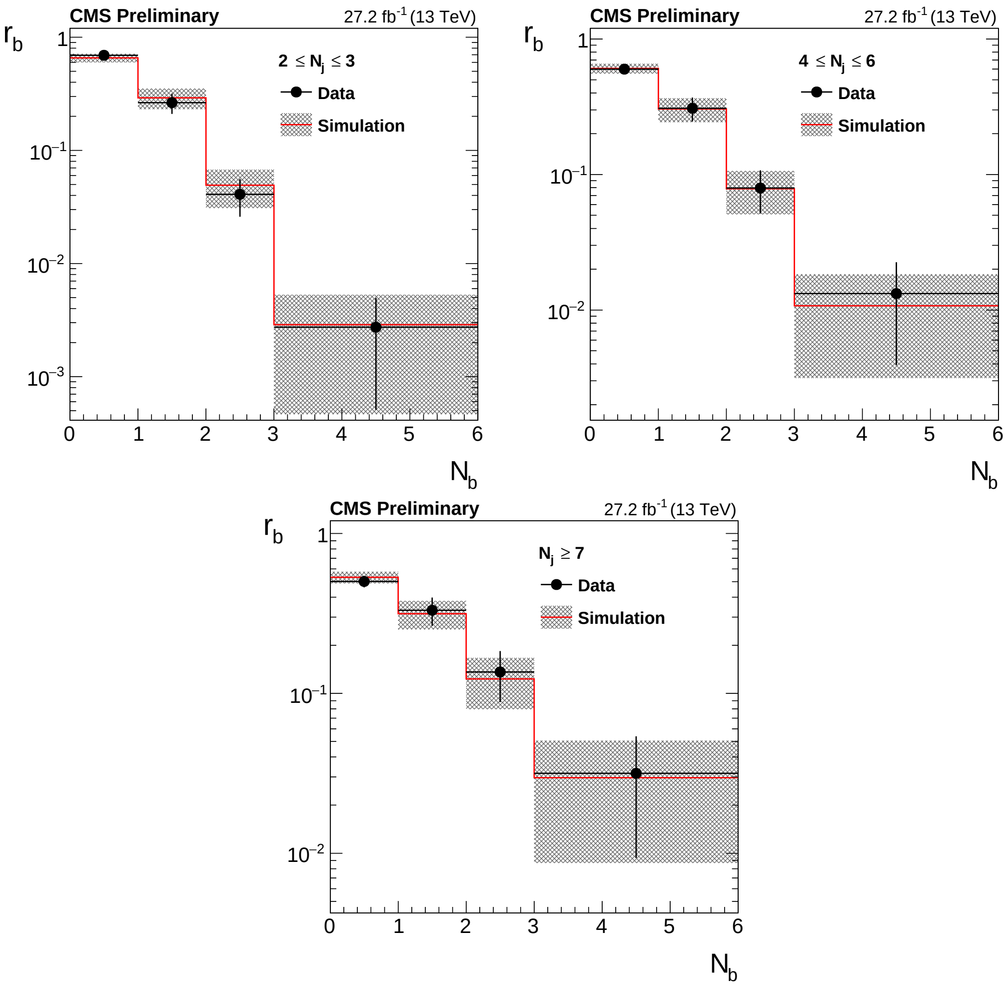

Figure 7.9: Comparison of r_j in data (black circles) and simulation (red line) measured in the region $\Delta\phi_{min} < 0.3$ and $100 < M_{\mathrm{T2}} < 200\,\mathrm{GeV}$, in the $2 \leq N_j \leq 3$ (top left), $4 \leq N_j \leq 6$ (top right) and $N_j \geq 7$ (bottom) region. The uncertainties are the statistical plus systematic uncertainties.

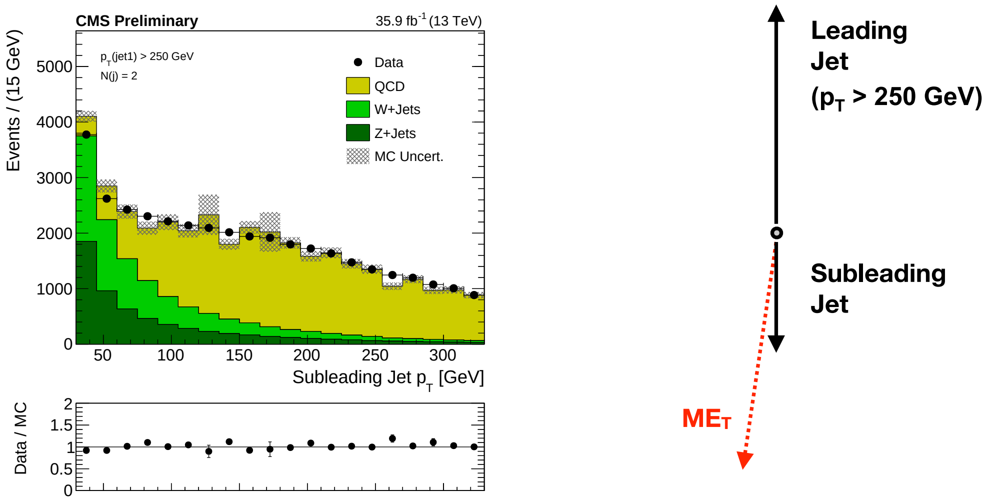

Figure 7.10: Distribution of the subleading jet in the monojet control region (left). The data (black marker) is compared to the sum of the simulation of QCD multijet (yellow), W+jets (light green) and Z+jets (dark green). The grey hash shows the systematic uncertainty on the simulation, which is propagated to the ratio of data over simulation in the bottom pad. Sketch illustrating the principle of the control region (right).

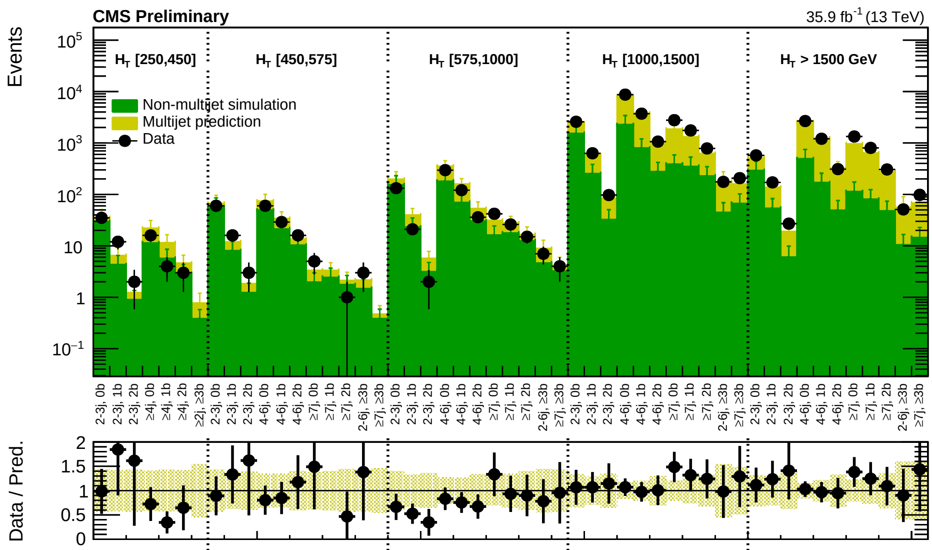

Figure 7.11: Data (black circles) versus the data driven QCD multijet estimate (yellow) plus the electroweak contributions from simulation (green) in the validation region $100 < M_{T2} < 200$ GeV. The H_T regions from very low to medium H_T use the prescaled triggers and the event yield is scaled according to the values obtained in figure 7.5.

7.3.2 Lost lepton

This search is looking for SUSY in the fully hadronic final state and thus relies on a lepton veto. There are multiple ways a lepton veto can fail, either due the analysis acceptance, isolation or reconstruction of the lepton. If such a lepton is missed it is called *lost*. The main production modes of leptons contributing to this background are leptonic W boson decays, either from W+jets or $t\bar{t}$ production, and small contributions from single top, $t\bar{t}W$, $t\bar{t}Z$ and $t\bar{t}H$. This background is estimated from a single lepton control region in data introduced below. The signal region yield is estimated from this control region by using the ratio of the one to zero lepton region in simulation, the so-called transfer factor. The subject of signal contamination is introduced and addressed. And finally the hybrid method as a way to make maximal use of the data for the M_{T2} shape is introduced.

Single lepton control region

The most straightforward way to construct a control region for the case of a lost lepton is by looking at a single lepton region. For this the lepton veto that is applied to the events selected by the signal triggers is removed from the baseline selection, and at least one electron or muon with $M_T(lep, E_{\mathrm{T}}^{\mathrm{miss}}) < 100\,\mathrm{GeV}$ is required. The cut on M_T is applied to reduce signal contamination. While leptonic W boson decays have an endpoint in M_T at the W boson mass, this is generally not the case for the SUSY models considered. The single lepton control region is shown in Figure 7.12 inclusively along the four binning axes. Since the MC simulation used is at LO, there is a small disagreement in the H_{T} and N_{jets} dimensions. This will not affect the final result since the analysis is conducted in bins of H_{T}, N_{jets} and $N_{\mathrm{b-tags}}$.

There are generally twice as many single lepton events than zero lepton events, except at high jet multiplicities $\geq 7j, \geq 2b$. There the control region's statistical power is low and signal contamination from T1tttt in $\geq 7j, \geq 3b$ has to be avoided. To this end the events with $\geq 7j, \geq 1b$ are estimated from the summed up region $\geq 7j$,$1{-}2b$. Otherwise the control regions have the same bounds as the signal regions in H_{T}, N_{jets} and $N_{\mathrm{b-tags}}$. The special case of the M_{T2} dimension is described later in the hybrid method.

The simulation is the sum of W+jets and $t\bar{t}$ (and the rarer processes mentioned above) and this sum is used as a total for the estimate. To validate that the two contributions from W+jets and $t\bar{t}$ also separately agree with the data, Figure 7.13 shows the W+jets enriched region with $N_{\mathrm{b-tags}} = 0$ and Figure 7.14 shows the $t\bar{t}$ enriched region with $N_{\mathrm{b-tags}} \geq 2$. The better agreement of data and simulation in the $N_{\mathrm{b-tags}} \geq 2$ region compared to the $N_{\mathrm{b-tags}} = 0$ one stems, as for the figures above, from using LO MADGRAPH simulation. The $t\bar{t}$ samples have a correction applied that improves the agreement of data and simulation as described in Section 7.1.2.

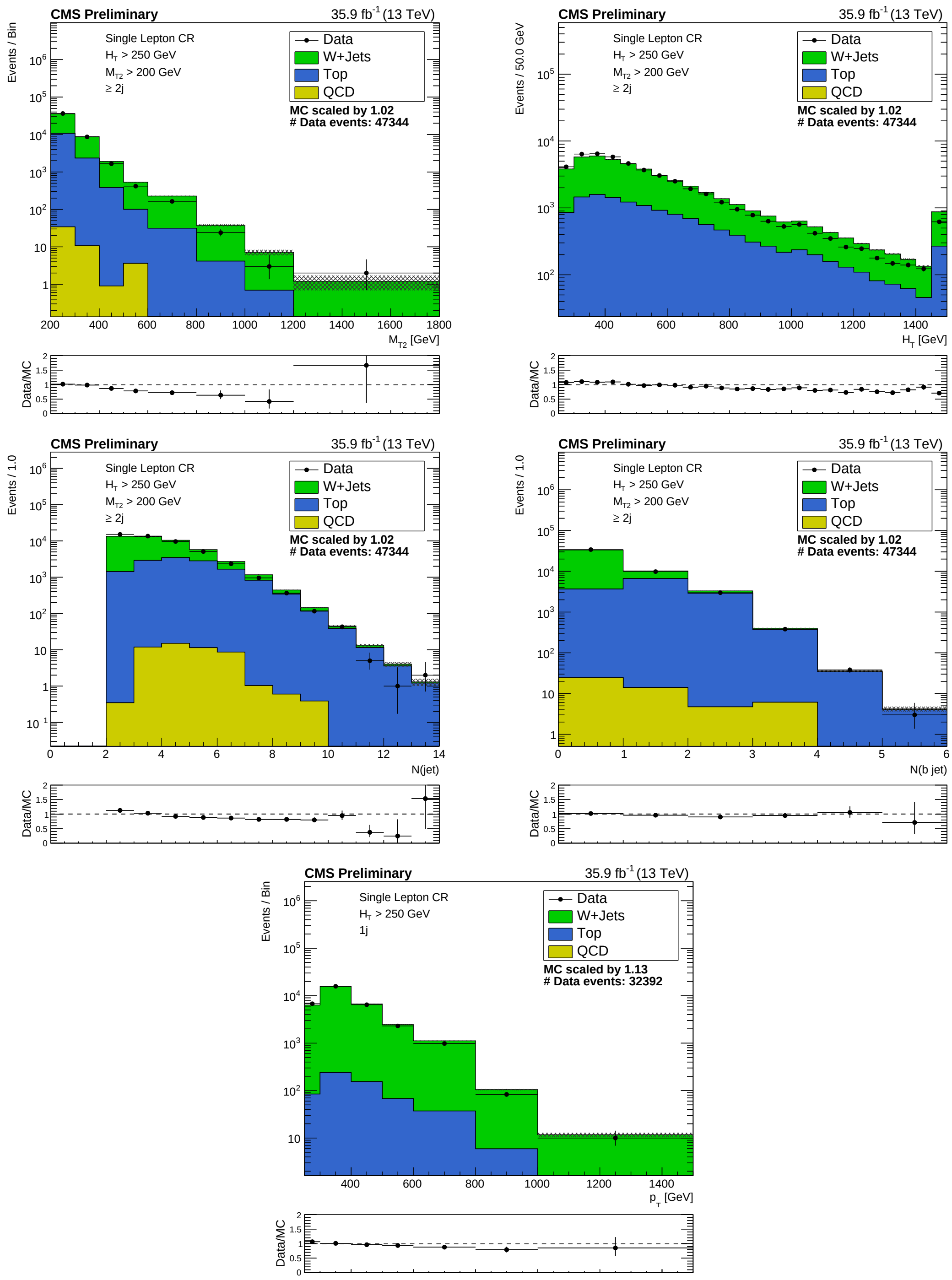

Figure 7.12: Comparison of data (black markers) to the sum of simulation in the inclusive multijet region for M_{T2} (top left), H_{T} (top right), N_{jets} (middle left) and $N_{\mathrm{b-tags}}$ (middle right), and for the monojet region for p_T (bottom). The simulation is scaled to the data yield by the number indicated on the figures.

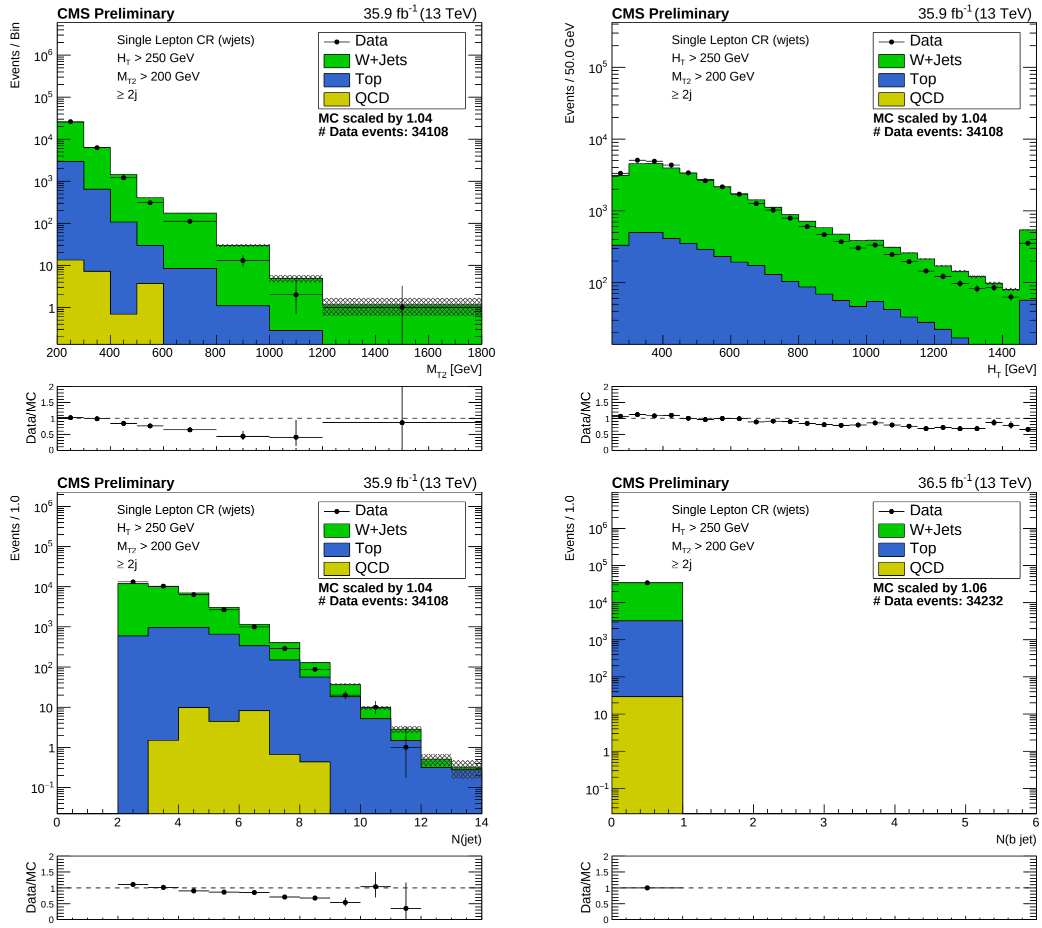

Figure 7.13: Comparison of data (black markers) to the sum of simulation in the W+jets enriched $N_{\mathrm{b-tags}} = 0$ multijet region for M_{T2} (top left), H_{T} (top right), N_{jets} (bottom left) and $N_{\mathrm{b-tags}}$ (bottom right). The simulation is scaled to the data yield by the number indicated on the figures.

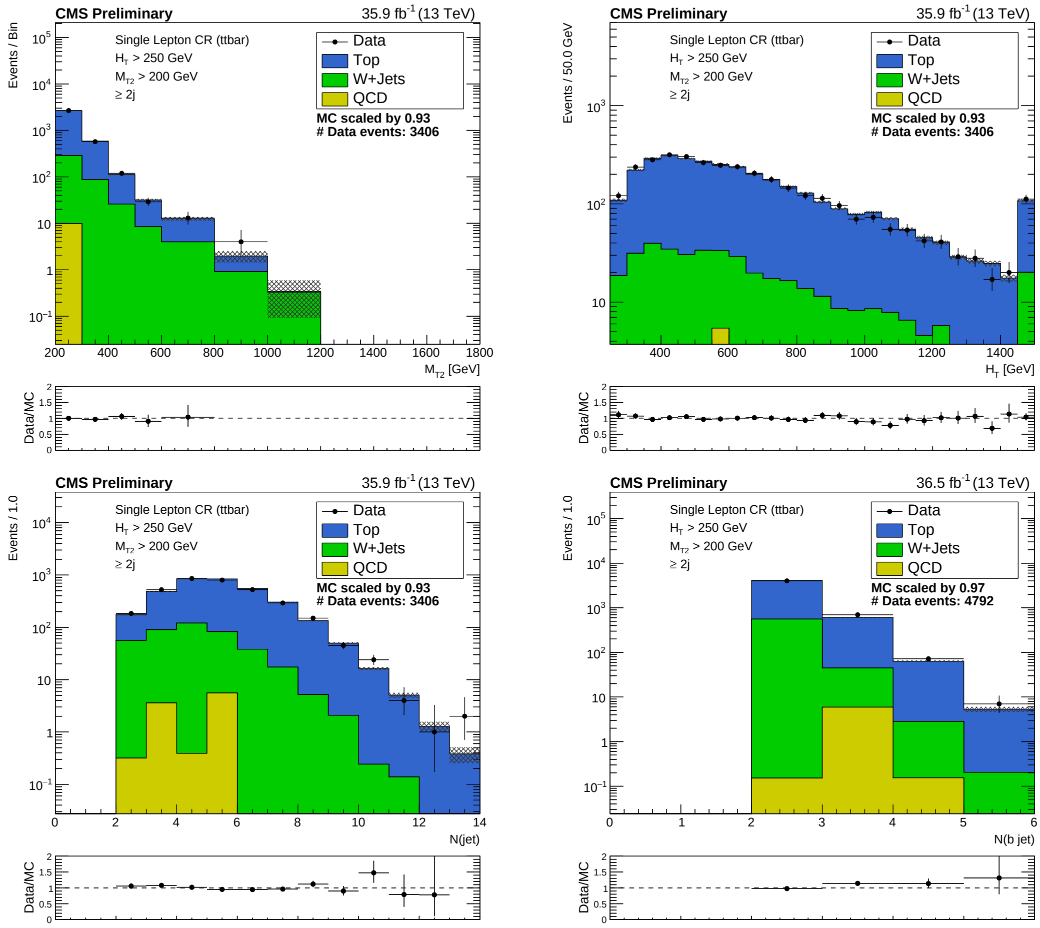

Figure 7.14: Comparison of data (black markers) to the sum of simulation in the $t\bar{t}$ enriched $N_{\text{b-tags}} \geq 2$ multijet region for M_{T2} (top left), H_{T} (top right), N_{jets} (bottom left) and $N_{\text{b-tags}}$ (bottom right). The simulation is scaled to the data yield by the number indicated on the figures.

Hybrid method for the M_{T2} extrapolation

The binning in M_{T2}, described in Section 7.2, is done in such a way that in the last bin there is about 1 event expected from the *sum* of the backgrounds. Estimating a background contribution to this last bin from a data control region that has roughly the same order of magnitude of events expected in it would result in a very large statistical uncertainty. One way around this is to sum up the data control region yields in each topological region and distribute this sum into the M_{T2} bins according to the simulation. But using the M_{T2} shape from simulation comes with the systematic uncertainty associated with higher order corrections. Thus using the simulation for bins with high yields would add an unnecessarily large systematic uncertainty. The *hybrid method* makes the best use of both worlds by using the data for as many bins as possible until the point is reached where the statistical uncertainty outweighs the systematic uncertainty from which point onward the MC shape is used.

Explicitly, the hybrid method sums up the yields in the bins starting from the highest M_{T2} bin to the lower bins until at least 50 expected events are reached. For these integrated bins the shape from simulation is used. All the bins further up the M_{T2} dimension are not summed up. The estimate for them is built in that specific (M_{T2}, H_{T}, N_{jets}, $N_{\mathrm{b-tags}}$) independently of the neighboring bins.

Figure 7.15 compares the M_{T2} distribution in data and compares it to the hybrid shape in the 1-lepton region for the inclusive multijet selection, on the left for $N_{\mathrm{b-tags}} = 0$ and on the right for $N_{\mathrm{b-tags}} \geq 1$.

The final estimate of the lost lepton background in the signal region, $N_{0\ell}^{SR}$, is calculated in the following way:

$$\begin{aligned} N_{0\ell}^{SR}(M_{\mathrm{T2}}, H_{\mathrm{T}}, N_{\mathrm{jets}}, N_{\mathrm{b-tags}}) =& [N_{1\ell}^{CR} \cdot R_{MC}^{0\ell/1\ell}](H_{\mathrm{T}}, N_{\mathrm{jets}}, N_{\mathrm{b-tags}}) \\ & \cdot k_{Hybrid}(M_{\mathrm{T2}}), \end{aligned} \tag{7.5}$$

where $N_{1\ell}^{CR}$ is the yield in the single lepton control region, $R_{MC}^{0\ell/1\ell}$ is the ratio in simulation of the signal to control region and k_{Hybrid} is the factor accounting for the hybrid method.

Signal contamination

The signal models considered for this analysis also decay to final states with one lepton. As mentioned above a cut on M_T reduces the signal contribution to the single lepton control region. But at $\geq 7j, \geq 2b$ there is still a sizable contribution from T1tttt and T2tt. These signals could thus contribute to the yield in the single lepton control region, artificially increasing the lost lepton background contribution in the signal region. This effect is generally treated by reducing the signal efficiency in the following way:

$$N_{signal}^{SR}{}' = N_{signal}^{SR} - \alpha \cdot N_{signal}^{CR}, \tag{7.6}$$

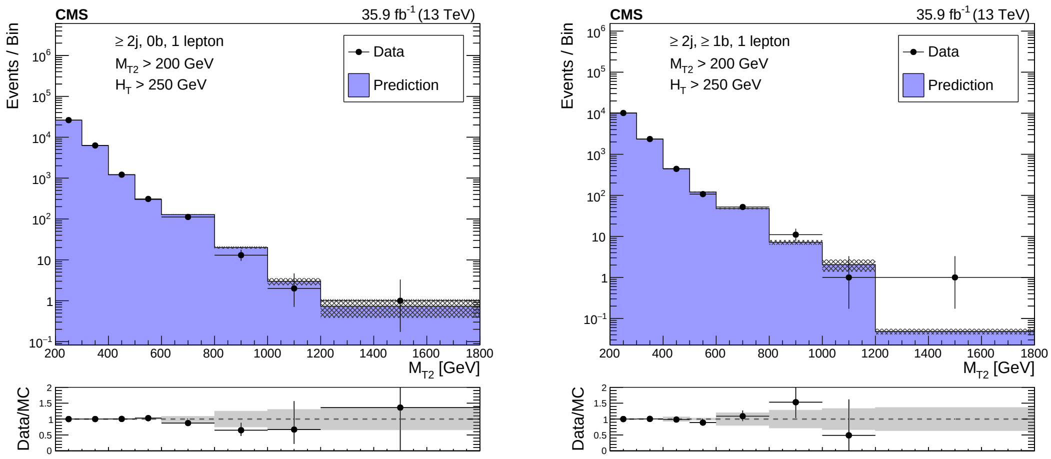

Figure 7.15: The M_{T2} distribution in the inclusive 1-lepton multijet region for data (black markers) and the hybrid shape (purple histogram) in the $N_{\mathrm{b-tags}} = 0$ (left) and $N_{\mathrm{b-tags}} \geq 1$ (right), corresponding to the W+jet and $t\bar{t}$ production, respectively.

where N^{SR}_{signal} and N^{CR}_{signal} are the signal yields predicted in the signal and control region bin, respectively, and α is the transfer factor computed as the ratio between the control region and the signal region yields. This reduced signal yield, $N^{SR}_{signal}{}' \leq N^{SR}_{signal}$, is then used in the rest of the analysis.

Statistical and systematic uncertainties

The statistical and systematic uncertainties for the estimation of the lost lepton background from the single lepton control region are:

- Poisson uncertainty for the observed 1ℓ control region count, uncorrelated among the control region bins;
- statistical uncertainty associated with the simulation, which is used for the transfer factor; it is uncorrelated among the signal bins;
- electron and muon selection efficiency, up to 7% in some bins, correlated in the signal regions;
- the simulation also includes τ leptons decaying leptonically and hadronically, and they are thus automatically included in the estimate. The efficiency for hadronic τ lepton decays is estimated from simulation, since there is no pure data control region. Varying this efficiency by its uncertainty has an effect of less than 3% on the lost lepton estimate. This uncertainty is taken correlated among the bins;
- the M_T cut efficiency estimated from simulation and verified in a $N_{\mathrm{b-tags}} = 0$, $Z \to l^+l^-$ control region, where one of the leptons has been removed and

added to $E_{\mathrm{T}}^{\mathrm{miss}}$ to mimic a leptonic W boson decay. A correlated among bins uncertainty of 3% has been shown to cover the largest observed difference in this efficiency;

- the b-tagging efficiency affects the estimate up to 4%. This uncertainty is correlated among the regions;
- variations of the jet energy scale are covered by a 5% uncertainty, correlated among the regions;
- the variations of the renormalization and factorization scale are generally of the size of a few percent up to 10% in the extreme regions. This uncertainty is correlated among the signal bins;
- a systematic uncertainty accounts for the effect from the extrapolation from simulation (renormalization and factorization scale, PDFs) and experiment (JEC, $E_{\mathrm{T}}^{\mathrm{miss}}$). A linear morphing is applied for the bins using the MC shape that increases with M_{T2} until the last bin where the maximum of 40% is reached. This is done in each (H_{T}, N_{jets}, $N_{\mathrm{b-tags}}$) bin independently and only for the bins that use the shape from simulation. The uncertainty is correlated among the M_{T2} bins of a topological region, but uncorrelated between different topological regions.

7.3.3 Z to invisible

This search heavily depends on the measurement of the missing transverse energy. Every process that produces neutrinos, and thus $E_{\mathrm{T}}^{\mathrm{miss}}$ will contribute to the background. For a Z boson decaying to two neutrinos the M_{T2} variable does not yield as strong a distinction as is the case for the multijet background, since there are in fact two undetected particles (the neutrinos) in the event. This makes the $Z \to \nu\nu$ events an irreducible background with respect to the baseline selection including M_{T2}.

The leading order production diagrams of a vector boson (W, Z or γ) plus a jet are shown in Figure 7.16. The diagrams are the same for the three bosons, but different couplings apply at the vertices and the masses of the W and Z bosons affect the final state at low boson p_T. At LO the Z+jets background has characteristically only one additional jet and no b-tagged jet, in comparison to the two aforementioned backgrounds, lost lepton and QCD multijet production. In the following I will explain the choice of the dilepton control region, the control region selection, the background subtraction method and finally the hybrid method for the M_{T2} extrapolation.

Choice of the control region

The two fermions that the Z boson decays to are either a pair of quark+anti-quark, charged lepton+anti-lepton or neutrino+anti-neutrino. The charged lepton pair is an ideal candidate to estimate the Z boson decay to neutrinos since it is basically the same process except for a multiplicative factor accounting for the coupling and the charged lepton masses. The signature of two opposite sign same flavor leptons, either electrons or muons, is very pure with only a small background contribution from leptonic top quark decays. The top decay modes either yield ee, $\mu\mu$ for the same flavor contribution, or $e\mu$ and μe for the opposite flavor contribution. The same flavor top quark background can thus be estimated with the opposite flavor events.

The downside of using $Z \to l^+l^-$ is that it is statistically limited since the branching ratio to muons and electrons only amounts to about 6.7% of the total decay width, compared to the 20.0% to neutrinos[4]. For this reason, in previous versions of these type of SUSY searches with lower integrated luminosity, other V+jets processes were used. While the statistical power of $\gamma + \text{jets}$ and $W^\pm \to \ell\nu$ is much larger than $Z \to l^+l^-$, the theoretical uncertainty associated with the difference of the LO to NLO calculations between the γ and Z boson is much larger and the mass peak of the dilepton system renders a cleaner selection of events than is possible for $W^\pm \to \ell\nu$. For the previous setup of this search using the $\gamma + \text{jets}$ control region, a systematic uncertainty for the double ratio $\frac{Z\to\nu\nu_{data}/Z\to l^+l^-_{data}}{Z\to\nu\nu_{MC}/Z\to l^+l^-_{MC}}$ was added that is generally $\leq 20\%$, but much larger in extreme regions.

Thus the choice of switching to the $Z \to l^+l^-$ control region from the $\gamma + \text{jets}$ one is a trade-off between systematic and statistical uncertainty. With the use of the $Z \to l^+l^-$ control region the systematic uncertainty is drastically reduced. On the other hand, the limited sample size of the dilepton final state requires extrapolation at high jet and b-tagged jet multiplicities. Since those regions are first, not abundant in the Z+jets background, and second, already at the outskirts of the categorization and thus statistically limited, the effect of the reduced statistical power of the $Z \to l^+l^-$ region is outweighed by the improvement with respect to the theoretical uncertainty.

Figure 7.17 shows the comparison to the $Z \to \nu\nu$ shape in M_{T2} from simulation (black squares) to the estimates from $\gamma + \text{jets}$ (red triangles), $W^\pm \to \ell\nu$ (green triangles) and $Z \to l^+l^-$ (blue hollow circles) for the five H_{T} regions, $N_{\text{jets}} \geq 2$ and integrated over $N_{\text{b-tags}}$. The grey band shows the systematic uncertainty on the M_{T2} shape.

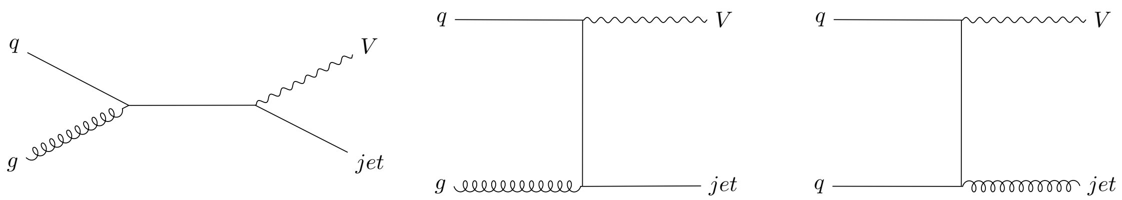

Figure 7.16: Leading order production diagrams at a pp collider of V+jets, where V = W, Z or γ.

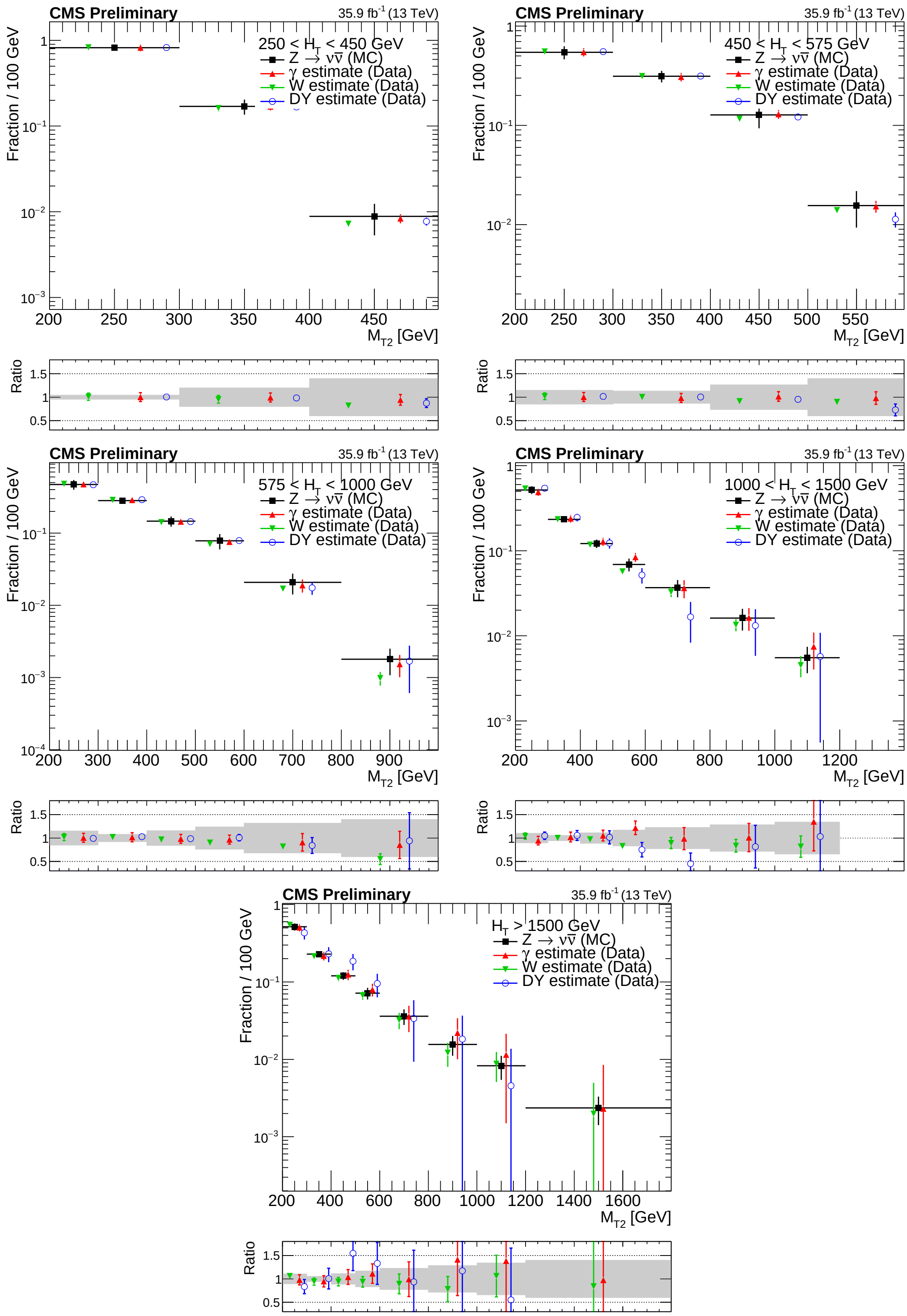

Figure 7.17: Comparison of the M_{T2} shape in the $Z \to \nu\nu$ simulation (black squares) to the estimates from $\gamma +$jets (red triangles), $W^{\pm} \to \ell\nu$ (green triangles) and $Z \to l^{+}l^{-}$ (blue hollow circles) for the five H_{T} regions, $N_{\mathrm{jets}} \geq 2$ and integrated over $N_{\mathrm{b-tags}}$.

The $Z \to l^+l^-$ control region

The $Z \to l^+l^-$ control region signature consists of two same flavor (SF) oppositely charged leptons, electrons or muons, that stem from a Z boson decay. These events are triggered by specific dilepton triggers since the signal triggers do not cover this phase space. The leptons for the $Z \to l^+l^-$ control region have to pass the following requirements:

- two same flavor leptons;
- $p_T(l_1) > 100\,\mathrm{GeV}$, $p_T(l_2) > 30\,\mathrm{GeV}$, where the high threshold for the leading lepton improves the trigger efficiency, while the later applied $p_T(ll) > 200\,\mathrm{GeV}$ cut has the same effect on the control region;
- opposite charge;
- $|m_{\ell\ell} - m_Z| < 20\,\mathrm{GeV}$, where m_Z is the mass of the Z boson.

To model the decay of the Z boson to two undetected neutrinos, the leptons are removed from the event and all the variables recomputed. Then the same analysis cuts are applied to these lepton removed variables. A comparison of data and simulation along the binning variables is shown in figure 7.18. The background to the $Z \to l^+l^-$ production (turquoise) are leptonic decays of top quarks (blue) and to a lesser part W+jets (light green) and WW production (dark green). Since the simulation only includes the LO terms, there are some discrepancies between these shapes in data and simulation. However only the ratio of the simulation enters the estimate and this effect cancels out. The agreement in the $N_{\mathrm{b-tags}}$ dimension is very good, thus permitting to use the simulation to extrapolate in the low yield region of $\geq 7j, \geq 1b$.

Top contamination

The Z boson can only decay to two same flavor leptons, while the non-Z background can also decay to two opposite flavored leptons. This asymmetry in the decay modes is made use of to subtract the non-Z contribution in the same flavor (SF) region by measuring it in the opposite flavor (OF) region. While the SF and OF contributions are equal at generator level, different efficiencies at trigger, reconstruction and identification level can result in their ratio

$$R_{SFOF} = \frac{ee + \mu\mu}{\mu e + e\mu} \tag{7.7}$$

to differ from unity. This ratio is estimated in data in a $t\bar{t}$ enriched region.

In Figure 7.19 the p_T of the Z boson is shown in the inclusive region with no M_{T2} cut. The events at low $p_T(Z)$ are dominated by leptonic top quark decays. Events below $p_T(Z) < 200\,\mathrm{GeV}$ and with an inverted cut on the invariant mass ($|m_{\ell\ell} - m_Z| > 20\,\mathrm{GeV}$) are enriched with the top background and orthogonal to the $Z \to l^+l^-$ control and signal regions. These events are used to estimate the ratio R_{SFOF}.

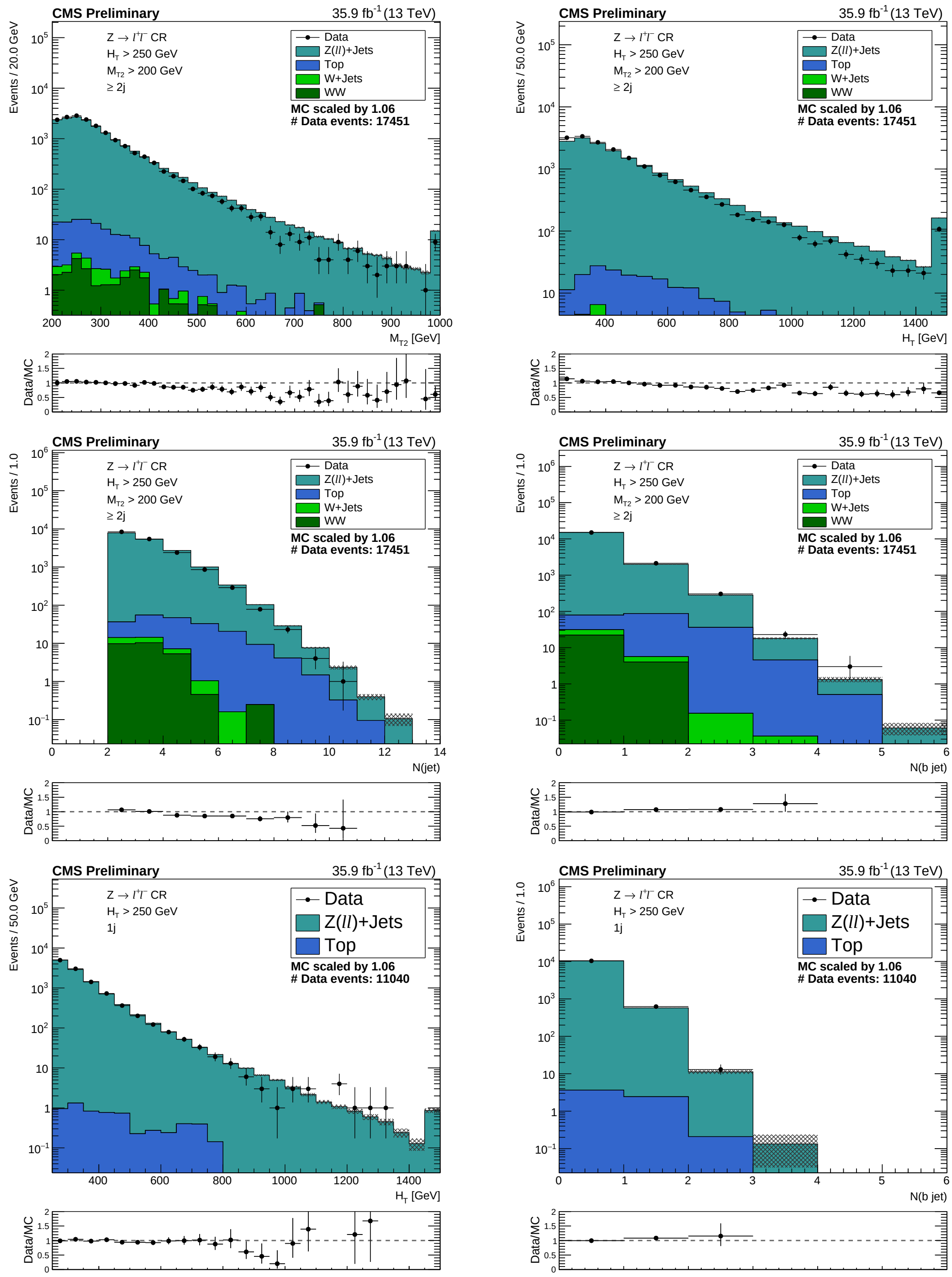

Figure 7.18: Comparison of data (black markers) to the sum of simulation in the inclusive multijet region as a function of M_{T2} (top left), H_T (top right), N_{jets} (middle left) and $N_{\text{b-tags}}$ (middle right), and for the monojet region for H_T (bottom left) and N_{jets} (bottom right). The simulation consists of the $Z \to l^+l^-$ production (turquoise) and leptonic decays of top quarks (blue), W+jets (light green) and WW production (dark green). The simulation is scaled by the number indicated on the figures such that the ratio in the bottom pad is centered at 1.

Figure 7.20 shows R_{SFOF} along the binning variables. No strong dependence was found and a flat value of $R_{SFOF} = 1.13 \pm 0.15$ is determined to account for the difference and cover the variance. The yield in the OF control region is then scaled by this ratio to obtain the contribution from leptonic top decays. This gives finally the purity $p_{\ell\ell}$ of the same flavor dilepton events:

$$p_{\ell\ell} = \left[N_{SF}^{CR} - N_{OF}^{CR} \cdot R_{SFOF}\right] / N_{SF}^{CR}, \tag{7.8}$$

where N_{SF}^{CR} and N_{OF}^{CR} are the yields in the same and opposite flavor region, respectively.

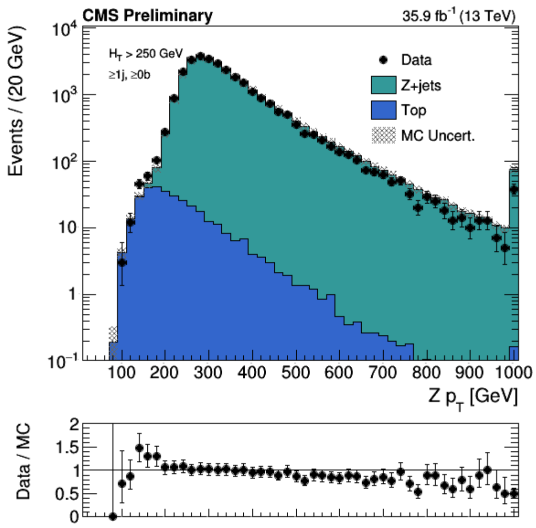

Figure 7.19: The p_T of the Z boson with the baseline selection applied except the cut on M_{T2} and the p_T of the Z boson.

Hybrid method for M_{T2} extrapolation

The hybrid method of using the shape in M_{T2} from data for as long as the statistical uncertainty stays small compared to the systematic uncertainty, as described in section 7.3.2 for the lost lepton background, is also applied for this background.

The estimate of the $Z \to \nu\nu$ events in each of the search regions is obtained as:

$$\begin{aligned} N_{Z\to\nu\nu}^{SR}(M_{\mathrm{T2}}, H_{\mathrm{T}}, N_{\mathrm{jets}}, N_{\mathrm{b-tags}}) =& [N_{\ell\ell}^{CR} \cdot p_{\ell\ell} \cdot R_{MC}^{Z_{\nu\nu}/Z_{\ell\ell}}](H_{\mathrm{T}}, N_{\mathrm{jets}}, N_{\mathrm{b-tags}}) \\ & \cdot k_{Hybrid}(M_{\mathrm{T2}}), \end{aligned} \tag{7.9}$$

where $N_{\ell\ell}^{CR}$ is the $Z \to l^+l^-$ control region yield, $p_{\ell\ell}$ the dilepton purity and $R_{MC}^{Z_{\nu\nu}/Z_{\ell\ell}}$ the ratio in simulation of $Z \to \nu\nu$ to $Z \to l^+l^-$ in each H_{T}, N_{jets} and $N_{\mathrm{b-tags}}$ bin. The final ingredient is $k_{Hybrid}(M_{\mathrm{T2}})$ which is the normalized M_{T2} hybrid shape.

It was observed in $Z \to l^+l^-$ simulation that the shape in M_{T2} does not depend on $N_{\mathrm{b-tags}}$ and that for the region $H_{\mathrm{T}} > 1500\,\mathrm{GeV}$ in particular it is also independent of N_{jets} for $M_{\mathrm{T2}} < 1\,\mathrm{TeV}$. Thus the M_{T2} shape is built in the same way as for the lost lepton estimate for each region, but integrating over $N_{\mathrm{b-tags}}$, and N_{jets} in case

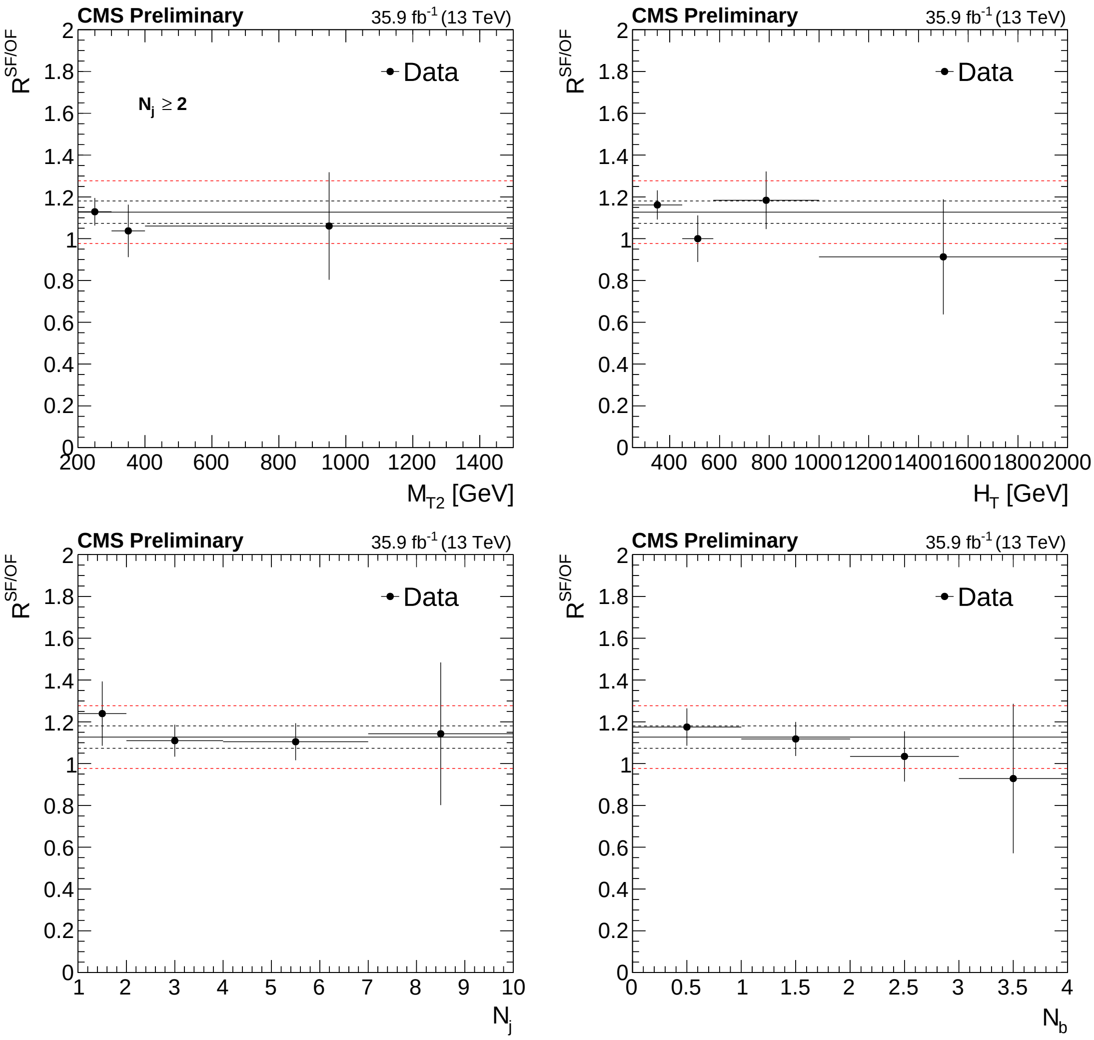

Figure 7.20: The ratio of same flavor over opposite flavor events inclusively along M_{T2} (top left), H_{T} (top right), N_{jets} (bottom left) and N_{jets} (bottom right). The solid black line shows R_{SFOF} with the red dashed lines accounting for the total uncertainty, while the black dashed lines account for the statistical uncertainty only.

of $H_{\mathrm{T}} > 1500\,\mathrm{GeV}$. The point from where to start with the extrapolation using simulation is determined again by requiring 50 expected events at 35.9 fb^{-1} to be contained in the sum of M_{T2} bins starting from the highest bin. The bins above and including this bin use the shape from simulation while the lower bins use the shape from $Z \to l^+l^-$ data, scaled by the ratio of the simulation $Z \to \nu\nu/Z \to l^+l^-$. In the regions where the MC is used for the extrapolation, the yield in data is summed and used to scale the shape in simulation of $Z \to \nu\nu$, further scaled by the integrated ratio of $Z \to \nu\nu/Z \to l^+l^-$ in MC.

Statistical and systematic uncertainties

The statistical and systematic uncertainties for the estimation of the $Z \to \nu\nu$ background from the $Z \to l^+l^-$ control region are as follows:

- Poisson uncertainty for the observed $Z \to l^+l^-$ control region count, uncorrelated among the control region bins;
- statistical uncertainty associated with the simulation statistics, which is used for $R(Z \to \nu\nu/Z \to l^+l^-)$; it is uncorrelated among the signal bins;
- a correlated 5.5% (syst.) on $R(Z \to \nu\nu/Z \to l^+l^-)$, mainly from the lepton efficiency;
- Poisson uncertainty for the observed opposite and same flavor region at $p_T(Z) < 200\,\mathrm{GeV}$ and $|m_{\ell\ell} - m_Z| > 20\,\mathrm{GeV}$ in the purity determination, uncorrelated among the control region bins;
- 15% on R_{SFOF} covering the statistical uncertainty and the variance along the binning axes, correlated among the control region bins;
- to account for the uncertainty in the extrapolation from generation (renormalization and factorization scale, PDFs) and experimental effects (JEC, $E_{\mathrm{T}}^{\mathrm{miss}}$), an uncertainty is applied that increases as function of M_{T2}, until the last bin where it is set to 40%. This covers the differences seen in figure 7.17 of up to 20% in the last bin, which is doubled due to the uncertainty regarding the NLO electroweak corrections. This uncertainty is correlated among the M_{T2} bins of a topological region, but uncorrelated between different topological regions.

7.4 Results

7.4.1 Signal regions

The background estimates are compared to the data in the signal regions in this section. For a general overview of the results, Figure 7.21 shows the comparison in the topological regions, i.e. in each bin of (H_{T}, N_{jets}, $N_{\mathrm{b-tags}}$) integrated over the

M_{T2} dimension. Then all of the bins are shown for the monojet and each of the H_{T} regions separately in Figures 7.22 to 7.27. The data (black marker) is compared to the sum of the background estimates: QCD multijet (yellow), lost lepton (blue) and $Z \to \nu\nu$ (green). The uncertainty band (grey hash) includes the statistical and systematic uncertainties. They are propagated to the bottom panel where the ratio of the data over the sum of the estimates is shown. The observed data is well in agreement with the predictions of the SM and no significant deviation has been observed.

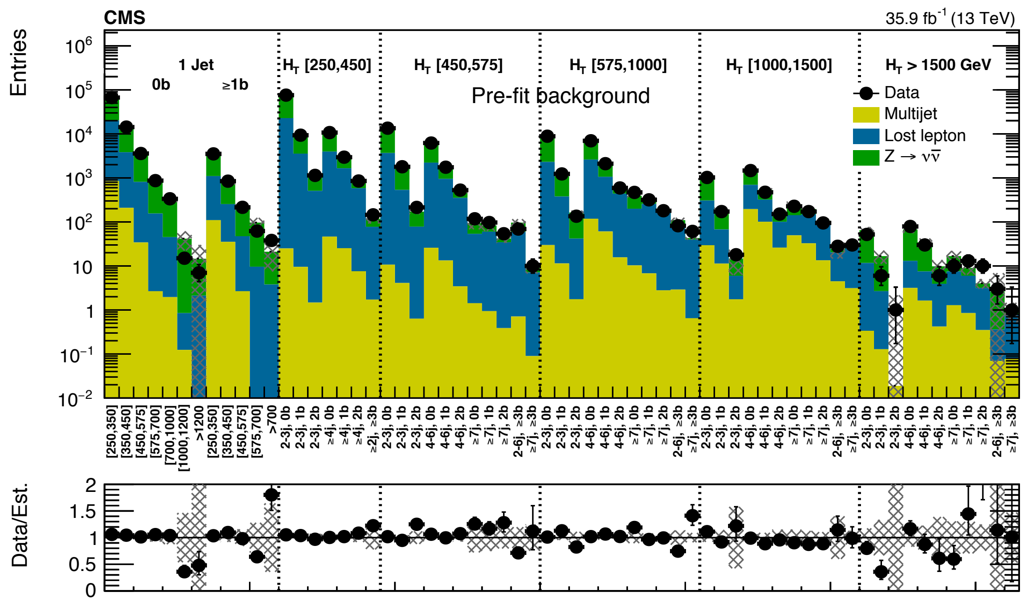

Figure 7.21: The data are compared to the background estimates for all of the kinematic bins, for $N_{\text{jets}} = 0$ each of the jet p_T bins are shown, while for the multijet regions, the bins are integrated along the M_{T2} dimension. The N_{jets} and $N_{\text{b-tags}}$ bins are indicated by the labels j and b, respectively. The hatched band corresponds to the full uncertainty.

7.4.2 Super signal regions

There are 213 signal regions in total. To simplify the reinterpretation of the analysis, the results are also shown in the super signal regions, that select the most sensitive regions, as shown in Table 7.5. For each region the selections in terms of N_{jets}, $N_{\text{b-tags}}$, H_{T} and M_{T2} are listed followed by the predicted and observed number of events and the range of the 95% CL upper limit on the number of signal events (N_{obs}) given a signal acceptance uncertainty range of $0 - 15\%$. The limit computation follows the description given in Appendix A.

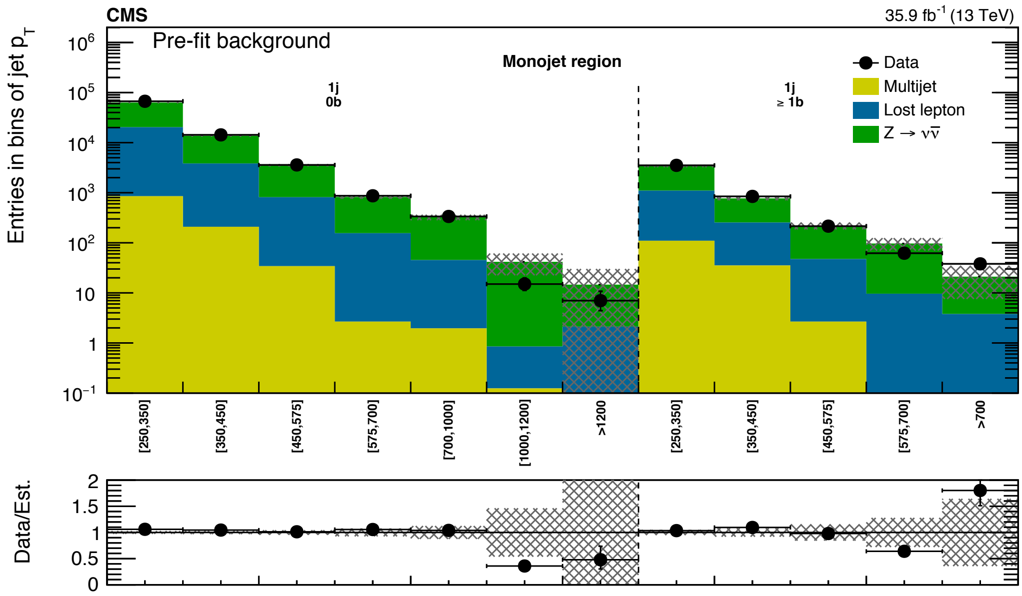

Figure 7.22: The data are compared to the background estimates for the monojet region. The N_{jets} and $N_{\text{b-tags}}$ bins are indicated by the labels j and b, respectively. The hatched band corresponds to the full uncertainty.

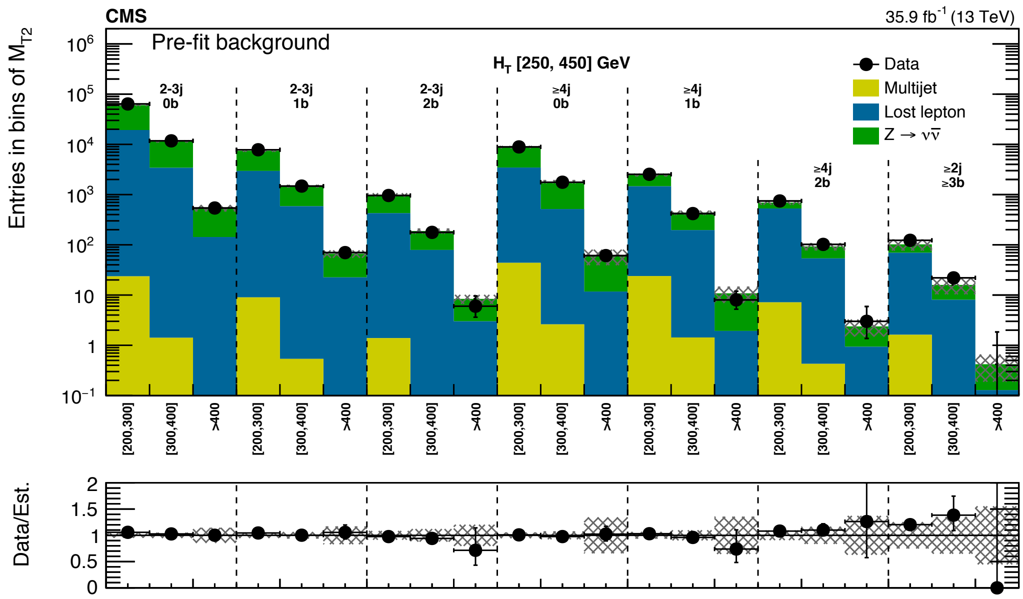

Figure 7.23: The data are compared to the background estimates for the $250 < H_{\mathrm{T}} < 450\,\text{GeV}$ region. The N_{jets} and $N_{\text{b-tags}}$ bins are indicated by the labels j and b, respectively. The hatched band corresponds to the full uncertainty.

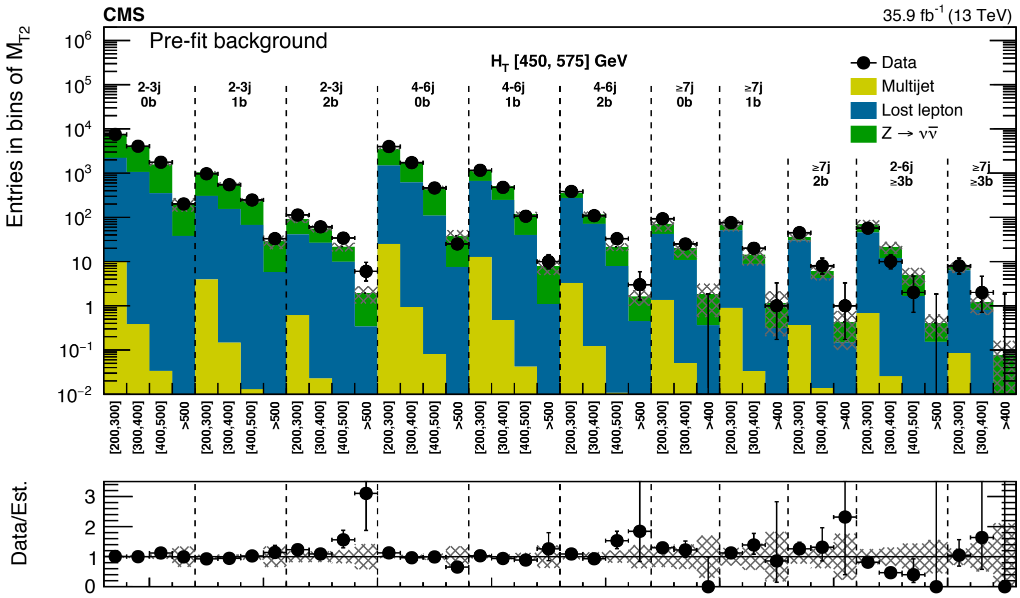

Figure 7.24: The data are compared to the background estimates for the $450 < H_{\mathrm{T}} < 575\,\mathrm{GeV}$ region. The N_{jets} and $N_{\mathrm{b-tags}}$ bins are indicated by the labels j and b, respectively. The hatched band corresponds to the full uncertainty.

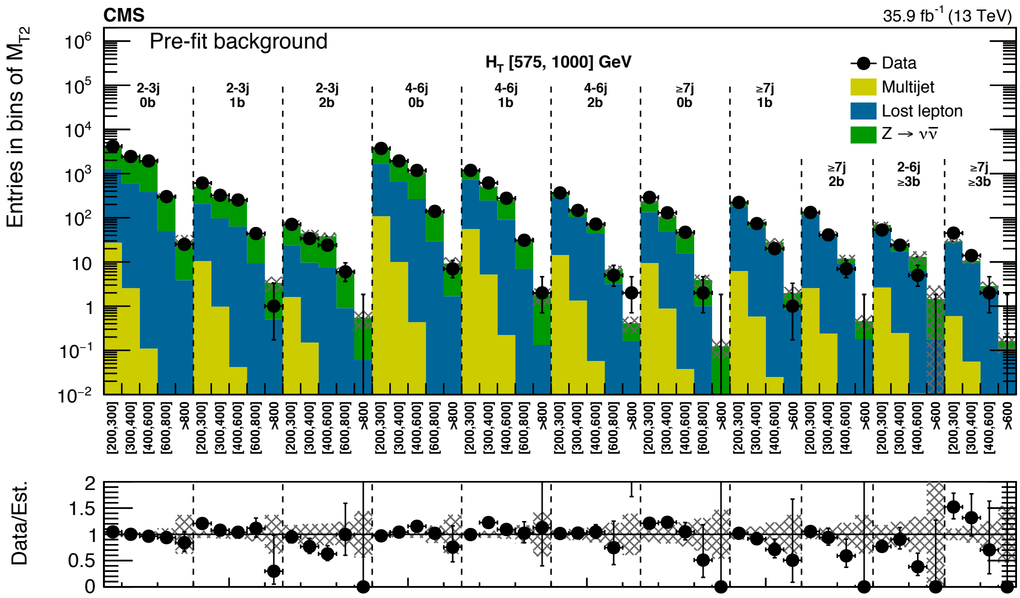

Figure 7.25: The data are compared to the background estimates for the $575 < H_{\mathrm{T}} < 1000\,\mathrm{GeV}$ region. The N_{jets} and $N_{\mathrm{b-tags}}$ bins are indicated by the labels j and b, respectively. The hatched band corresponds to the full uncertainty.

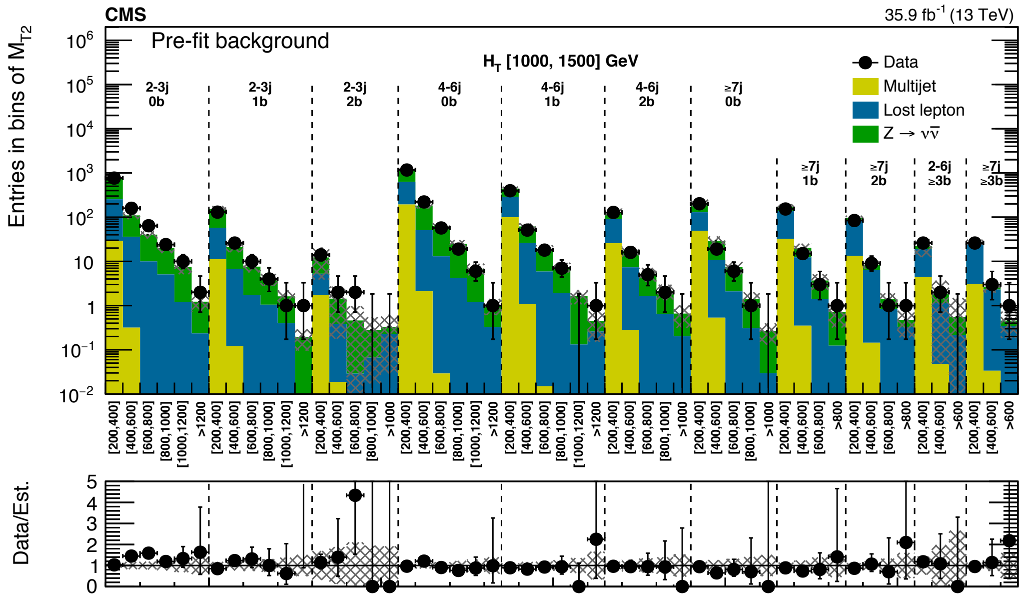

Figure 7.26: The data are compared to the background estimates for the $1000 < H_{\mathrm{T}} < 1500\,\mathrm{GeV}$ region. The N_{jets} and $N_{\mathrm{b-tags}}$ bins are indicated by the labels j and b, respectively. The hatched band corresponds to the full uncertainty.

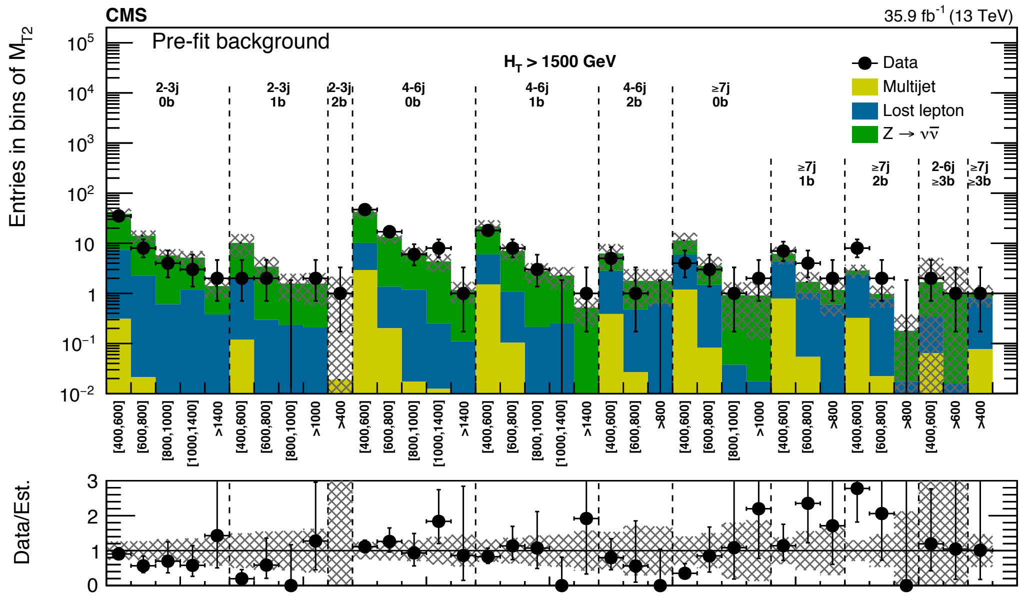

Figure 7.27: The data is compared to the background estimates for the $H_{\mathrm{T}} > 1500\,\mathrm{GeV}$ region. The N_{jets} and $N_{\mathrm{b-tags}}$ bins are indicated by the labels j and b, respectively. The hatched band corresponds to the full uncertainty.

Table 7.5: The names and definitions of the super signal regions (a dash means no requirement), the prediction, the observed data and the 95% CL upper limit on the number of signal events (N_{obs}) with a signal acceptance uncertainty of $0 - 15\%$.

Region	N_{jets}	$N_{\mathrm{b-tags}}$	H_{T} [GeV]	M_{T2} [GeV]	Prediction	Data	N_{95}^{obs}
2j loose	≥ 2	–	> 1000	> 1200	38.9 ± 11.2	42	26.6–27.8
2j tight	≥ 2	–	> 1500	> 1400	2.9 ± 1.3	4	6.5–6.7
4j loose	≥ 4	–	> 1000	> 1000	19.4 ± 5.8	21	15.8–16.4
4j tight	≥ 4	–	> 1500	> 1400	2.1 ± 0.9	2	4.4–4.6
7j loose	≥ 7	–	> 1000	> 600	$23.5^{+5.9}_{-5.6}$	27	18.0–18.7
7j tight	≥ 7	–	> 1500	> 800	$3.1^{+1.7}_{-1.4}$	5	7.6–7.9
2b loose	≥ 2	≥ 2	> 1000	> 600	$12.9^{+2.9}_{-2.6}$	16	12.5–13.0
2b tight	≥ 2	≥ 2	> 1500	> 600	$5.1^{+2.7}_{-2.1}$	4	5.8–6.0
3b loose	≥ 2	≥ 3	> 1000	> 400	8.4 ± 1.8	10	9.3–9.7
3b tight	≥ 2	≥ 3	> 1500	> 400	2.0 ± 0.6	4	6.6–6.9
7j3b loose	≥ 7	≥ 3	> 1000	> 400	5.1 ± 1.5	5	6.4–6.6
7j3b tight	≥ 7	≥ 3	> 1500	> 400	0.9 ± 0.5	1	3.6–3.7

7.4.3 Interpretation in the context of simplified models of SUSY

No significant deviation from the expected SM backgrounds was observed in the above shown results. Thus upper limits on the production cross section of simplified models of SUSY are set. The method described in Appendix A is used for the computation of the exclusion limits.

Systematic uncertainties

The following uncertainties on the signals are taken into account in the calculation of the limits:

- Integrated luminosity: 2.5% [41];
- Statistical uncertainty associated with the limited statistics in simulation: 0-100%;
- Initial state radiation: 0-30%;
- Renormalization and factorization scales variations: 5%;
- Jet energy scale: 5%;
- b-tagging efficiency: 0-40% for heavy flavour and $0-20\%$ for light flavour jet;
- Lepton efficiency: 0-20%;
- Full to fast simulation: 0-5%;
- Fast simulation pileup modeling: 4.6%;
- For the $t\bar{t}$ reweighting procedure half of the deviation from unity is assigned as the systematic uncertainty, since the weights are derived for a $t\bar{t}$ sample but are applied to the signal samples.

Interpretation

In Section 3.4 the discovery approach using simplified models of SUSY was discussed. The heavy supersymmetric parent particles decay via an effective vertex to quarks and the LSP. The cases of gluino mediated and direct squark production are considered, including alternative decay modes for the top squark. The nine models considered in this analysis were introduced in Figure 3.5.

The exclusion limits for these signals are shown in Figure 7.28 for the gluino pair production, in Figure 7.29 for squark pair production, and in Figure 7.30 for the alternative models for top squark decays. The black line encloses the observed excluded region; the dashed black lines show the effect on the exclusion limit due to the theoretical uncertainty on the signal cross section. The red line is the expected limit and the dashed red lines are the corresponding $\pm 1(2)\sigma$ bands. Gluino masses of up to 2 TeV are excluded for a massless LSP. Squark masses of about 1 TeV(1.6 TeV) are excluded for a massless LSP for one (4 light) squark type(s). The limits are summarized in Table 7.6.

Table 7.6: Summary of the 95% exclusion limits for different scenarios. The limits of the produced sparticles are shown for a massless $\tilde{\chi}_1^0$ in the second column, while for the $\tilde{\chi}_1^0$ the highest limit is shown in the third column.

Simplified model	Limit on sparticle mass [GeV]for $m_{\tilde{\chi}_1^0} = 0\,\text{GeV}$	Highest limit on $m_{\tilde{\chi}_1^0}$ [GeV]
Direct squark production:		
Bottom squark	1175	590
Top squarks	1070	550
Single light squarks	1050	475
Eight light squarks	1550	775
Gluino-mediated production:		
$\tilde{g} \to b\bar{b}\tilde{\chi}_1^0$	2025	1400
$\tilde{g} \to t\bar{t}\tilde{\chi}_1^0$	1900	1010
$\tilde{g} \to q\bar{q}\tilde{\chi}_1^0$	1860	1100

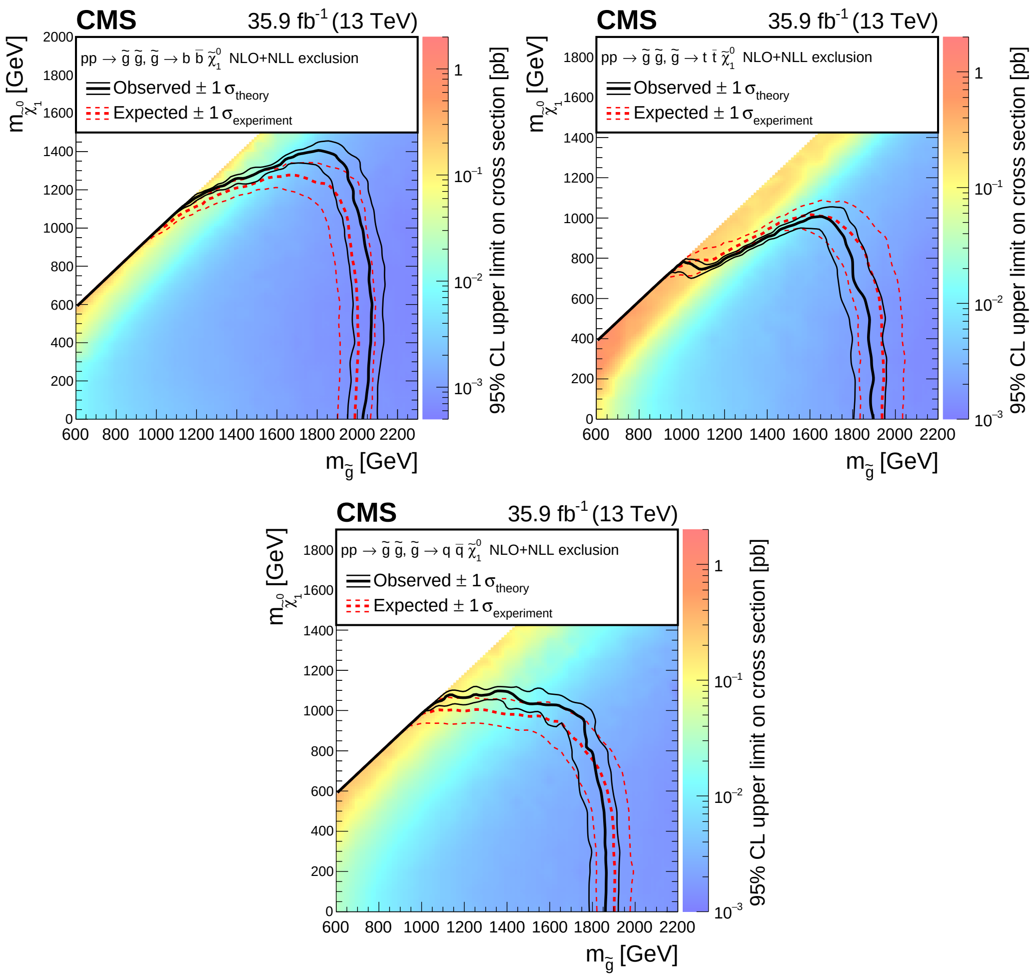

Figure 7.28: The 95% CL upper limits for gluino-mediated squark production, where the squark is either a bottom squark (top left), top squark (top right) or a light-flavor (u,d,s,c) squark (bottom). The black line encloses the observed exclusion region, and the dashed black lines correspond to the theory uncertainty on the signal cross section. The red line is the expected limit and the dashed red lines are the corresponding $\pm 1\sigma$ theory uncertainty band.

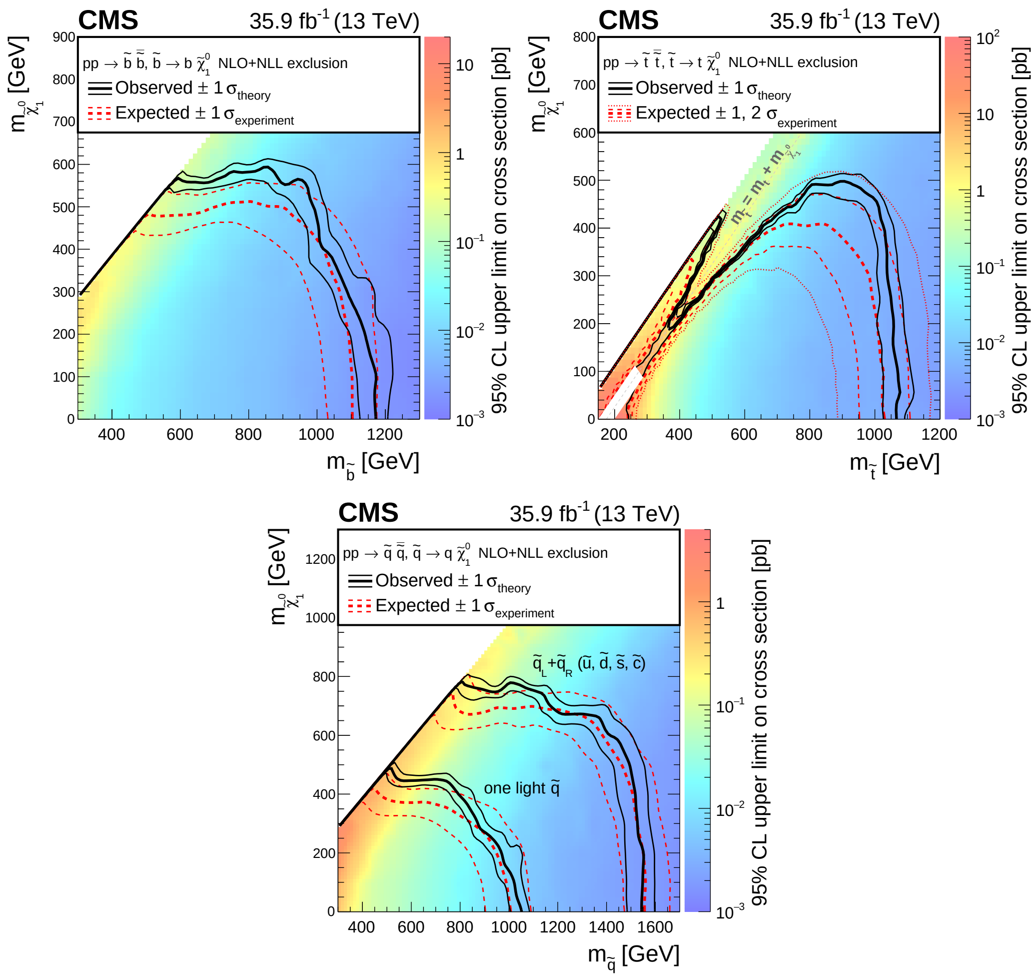

Figure 7.29: The 95% CL upper limits for direct squark production, where the squark is either a bottom squark (top left), top squark (top right) or a light-flavor (u,d,s,c) squark (bottom). The black line encloses the observed excluded region, and the dashed black lines correspond to the theory uncertainty on the signal cross section. The red line is the expected limit and the dashed red lines are the corresponding $\pm1\sigma$ theory uncertainty band. For the top squark production also the $\pm2\sigma$ band is shown. On the same figure the white diagonal band covers the region $|m_{\tilde{t}} - m_t - m_{\tilde{\chi}^0_1}| < 25\,\text{GeV}$ and low $m_{\tilde{\chi}^0_1}$, i.e. at top squark masses similar to the top quark mass and with little $E_{\text{T}}^{\text{miss}}$ in the events. Here the signal selection efficiency depends strongly on $m_{\tilde{t}} - m_{\tilde{\chi}^0_1}$, which due to the finite granularity of the simulation in the $(m_{\tilde{t}}, m_{\tilde{\chi}^0_1})$ plane results in an uncertain upper limit. This region is thus exempt from the limit calculation.

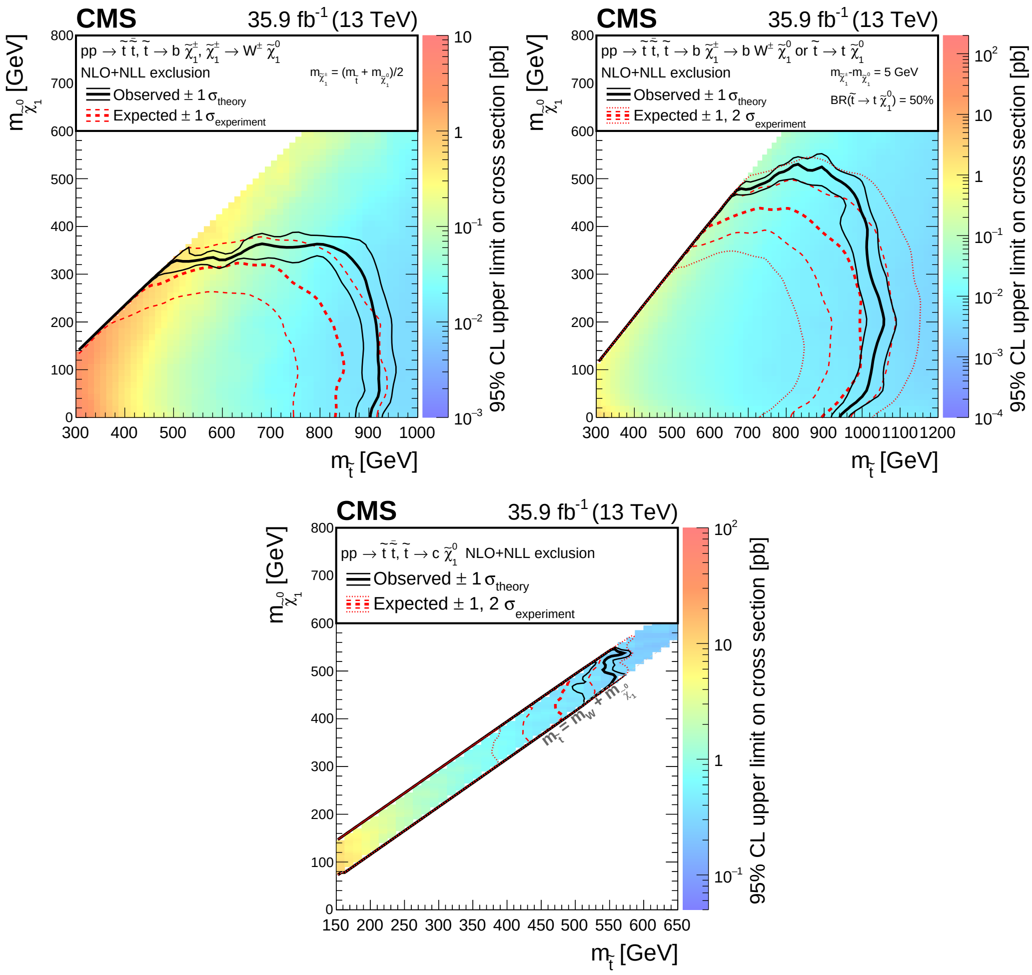

Figure 7.30: The 95% CL upper limits for direct top squark production, for the decay modes: $pp \to \tilde{t}\bar{\tilde{t}} \to b\bar{b}\tilde{\chi}_1^{\pm}\tilde{\chi}_1^{\mp}$, $\tilde{\chi}_1^{\pm} \to W^{\pm}\tilde{\chi}_1^0$ (top left); $pp \to \tilde{t}\bar{\tilde{t}}$, with 50% BR $t \to t\tilde{\chi}_1^0$ and 50% BR $t \to b\tilde{\chi}_1^{\pm}, \tilde{\chi}_1^{\pm} \to W^{*\pm}\tilde{\chi}_1^0$ and $\Delta m(\tilde{\chi}_1^0, \tilde{\chi}_1^{\pm}) =$ 5 GeV (top right); and finally $pp \to \tilde{t}\bar{\tilde{t}} \to c\bar{c}\tilde{\chi}_1^0\tilde{\chi}_1^0$ (bottom). The black line encloses the observed excluded region, and the dashed black lines correspond to the theory uncertainty on the signal cross section. The red line is the expected limit and the dashed red lines are the corresponding $\pm 1\sigma$ theory uncertainty band.

7.5 Conclusion

I have presented a search for supersymmetry in the fully hadronic final state with the M_{T2} variable using 35.9 fb^{-1} of data from the CMS experiment at the LHC at CERN. After the description of the event selection and their categorization, the three background sources and their data driven estimates have been presented. Significant improvements have been achieved with respect to the previous version of the analysis: the signal regions have been adapted to reflect the increase in data; this increase in data also results in sufficient yields in the very low H_{T} range to construct and fit the ratio r_ϕ; the $Z \to \nu\nu$ background is now estimated from a $Z \to l^+l^-$ control region, compared to the previously used $\gamma+$jets; and the range of the extrapolation in the M_{T2} dimension had been improved with the so called *hybrid method* to depend less on the simulation and use the data instead, where the event yield permits to do so.

No significant excess over the standard model predictions has been found. Exclusion limits are set on simplified models of supersymmetry for gluino and squark pair production. Gluino masses of up to 2 TeV are excluded for a massless LSP. Squark masses of about 1 TeV(1.6 TeV) are excluded for a massless LSP for one (4 light) squark type(s).

In the mean time the analysis has been repeated on the whole Run2 dataset corresponding to an integrated luminosity of 137 fb^{-1}[95]. Next to extending the exclusion limits on the models presented in this chapter another approach was added to target models with disappearing tracks.

Part IV

Search for SUSY in the diphoton final state

Curious, how often you humans manage to obtain that which you do not want.

Mr. Spock in Errand of Mercy

8 Final states with a Higgs boson decaying to two photons

This chapter describes the search for SUSY in the final state with a Higgs boson decaying to two photons with the data collected by the CMS detector in the years 2016 and 2017, corresponding to 35.9 fb^{-1} and 41.5 fb^{-1} of integrated luminosity respectively.

The SUSY signals with a Higgs boson in the final state considered for this analysis allow to probe a phase space of models vastly different from the ones considered for the previous chapter. By selecting the diphoton decay channel the SM backgrounds are suppressed. With this clear signature events at low values of $E_{\mathrm{T}}^{\mathrm{miss}}$ become accessible. Thus rather than optimizing the selection for events at the far end of the M_{T2} spectrum, the variable is used for the categorization, with no lower bound.

Previous searches for SUSY with the $H \to \gamma\gamma$ final state were conducted with the ATLAS and CMS detectors at 8 TeV [96, 97] and 13 TeV [98, 99]. The search presented here is one of the two analyses described in Ref. [100], which make use of the Razor[1] and M_{T2} variables to suppress the SM backgrounds further. The sensitivity is improved with respect to Ref. [98] with the inclusion of the 2017 data and by introducing categories with leptons and b-tagged jets. The two analyses were optimized for the discovery of strong (SP) and electroweak (EWP) production of SUSY respectively. In the following I will describe the SP analysis, which uses background estimates based on the methods of the measurement of the Higgs boson decaying to two photons [103] in conjunction with the M_{T2} variable.

In Chapter 3 the simplified models of SUSY producing a SM Higgs boson in the final state have been discussed. Due to R-parity conservation there are two SUSY decay chains in the models considered. By symmetry, if one decay chain produces a Higgs boson, the other also produces a boson, either a Higgs, Z or W boson. The final states investigated by this analysis require the production of two bosons, one necessarily being a Higgs boson decaying to two photons, while for the other boson all decay channels are allowed. The categorization is thus optimized for this second boson as well as the kinematic differences of SUSY with respect to the SM production of $H \to \gamma\gamma$.

The SM production of diphoton events relevant for this analysis either occur through a Higgs boson decay, thus having a resonance peak and referred to as the *resonant background*, otherwise the photons will stem from a quark or a meson and thus will not peak at the Higgs boson mass and are referred to as the *nonresonant background*.

[1]For a description of the Razor variables see Refs. [101, 102].

The event selection is introduced in Section 8.1. The events are categorized according to the criteria described in Section 8.2. The nonresonant background and the resonant SM Higgs boson background estimation is described in Section 8.3. In Section 8.4 the results are discussed, along with their interpretation in simplified models of SUSY. The conclusions are given in Section 8.5.

8.1 Selection

In the following I will describe the analysis specific selection applied for the final state with two photons. First the trigger selection requirements are described in Section 8.1.1. Then the Monte Carlo (MC) simulation samples are introduced in Section 8.1.2. Ways to suppress the nonresonant diphoton background are shown in Section 8.1.3. Finally in Section 8.1.4 the full baseline selection is summarized.

8.1.1 Trigger

The same trigger path as for the standard model measurement of the Higgs boson decaying to two photons is used. It selects events with at least two photons, where the leading photon (γ_0) has $E_\mathrm{T} > 30\,\mathrm{GeV}$ and the subleading photon (γ_1) has $E_\mathrm{T} > 18(22)\,\mathrm{GeV}$ for the 2016(2017) data taking. The photons have $R_9 > 0.5$ and the hadronic over the electromagnetic energy fraction (H/E) has to be smaller than 0.1. There is no requirement on H_T nor $E_\mathrm{T}^\mathrm{miss}$ in this trigger path, thus allowing to test a phase space inaccessible to most SUSY searches.

In order to reach the trigger plateau the following selections are applied at reconstruction level:

- $M_{\gamma\gamma} > 100\,\mathrm{GeV}$, where $M_{\gamma\gamma}$ is the invariant mass of the diphoton system, formed by the two photons γ_0 and γ_1 leading in p_T;
- $p_T(\gamma_0)/M_{\gamma\gamma} > 1/4$, $p_T(\gamma_1)/M_{\gamma\gamma} > 1/3$.

The selection on $p_T(\gamma_i)/M_{\gamma\gamma}$ rather than on $p_T(\gamma_i)$ has the advantage that it does not sculpt the $M_{\gamma\gamma}$ distribution with a turn on at the cut value.

8.1.2 Simulation

The Monte Carlo (MC) simulations are used for the analysis optimization and to model the SM Higgs boson background and the SUSY signals. The SM Higgs boson events are simulated at next-to-leading order (NLO) precision with the MADGRAPH_aMC@NLO generator [83]. They include the production via gluon fusion (ggH), vector boson fusion (VBF), in association with a W or Z boson (VH), as well as $\mathrm{b\bar{b}H}$ and $\mathrm{t\bar{t}H}$. The Higgs boson mass is set to 125 GeV, with the corresponding branching ratio to two photons of 0.227%. The cross sections are taken from Ref. [104], which are at next-to-leading order plus next-to-next-to-leading logarithm

(NLO+NLL) in the QCD coupling, at NLO in the electroweak coupling and N3LO in the gluon fusion process. For the ggH sample up to two extra partons from ISR are considered and the FxFx matching scheme of Ref. [105] is used. The MADGRAPH_aMC@NLO generator at leading order (LO) precision is used for the signal samples, considering up to two partons and employing the MLM matching scheme of Ref. [84]. The fragmentation and parton showering is modelled with PYTHIA v8.212 [106] with the CUETP8M1 [107] tune and PYTHIA v8.226 with the CP5 [108] tune for the 2016 and 2017 samples, respectively. For the parton distribution function the NNPDF3.0 [109] set is used for the 2016 and the NNPDF3.1 [110] is used for the 2017 samples. The generated events are then processed through a detailed simulation of the CMS detector's response in GEANT4 [88]. The signal samples are processed with the fast simulation program [89, 90].

The MADGRAPH modeling of ISR jets is improved in the same way as described in Section 7.1.2 for the bottom squark pair production model. For the EW production of SUSY the correction is based on Z+jets events to correct the transverse momentum of the chargino-neutralino pair (p_T^{ISR}). The weights vary between 1.18 and 0.78 for p_T^{ISR} in the range of 125 and 600 GeV. One half of the correction factors is taken as systematic uncertainty.

8.1.3 Nonresonant photon suppression

In this analysis the nonresonant background encapsulates all the production modes for diphoton events except the ones via a Higgs boson. Figure 8.1 shows the leading order diagrams for the Box and Born production of two photons, as well as the jet+γ and dijet production. For the latter two diagrams a neutral meson, predominantly π^0 and η, receives most of the p_T of the jet and thus appears like a photon. These production mechanisms generally result in photons accompanied by jets since they are radiated from a quark. This also means that they tend to be less centrally created in the detector and that they are nonisolated.

To suppress these nonisolated photons, only photons in the barrel region, $|\eta| < 1.44$, are considered, and it is required that the distance between photons and jets is $\Delta R(\gamma, \mathrm{jet}) \geq 0.4$. Since there is no massive particle from which the photons originate, the resulting distribution of the invariant mass of the photon pair is steeply falling.

8.1.4 Baseline selection

A loose working point with a 90% efficiency for photons approximately uniform in p_T and η, was chosen to allow for a high event yield. If a photon matches with an electron that is not compatible with a conversion, identified by missing hits in the inner tracker, the photon is discarded. Photons that are converted in the material to an electron are thus kept.

Also with a higher event yield in mind a loose working point is chosen for the electrons and muons, that are used to identify $W \rightarrow l\nu$ and $Z \rightarrow l^+l^-$. Jets are clustered with the anti$-k_{\mathrm{T}}$ algorithm [64] in a cone of size $\Delta R = 0.4$. The ones

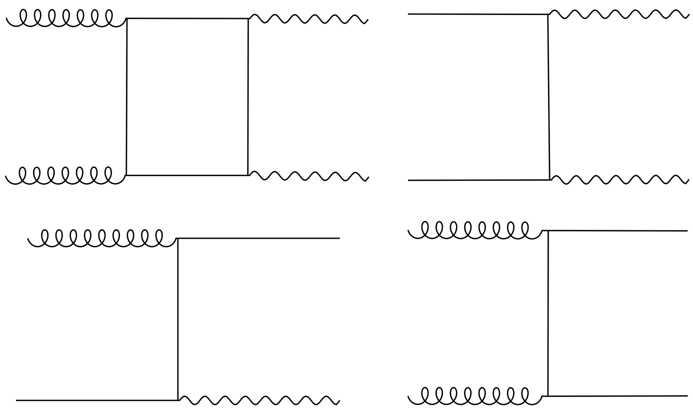

Figure 8.1: The Box (top left) and Born (top right) diphoton production, and the jet+γ (bottom left) and dijet (bottom right) production diagrams at the LHC.

originating from a heavy-flavour parton are tagged with the combined secondary vertex (CSVv2) algorithm [111]. A loose working point was chosen which has a high efficiency, around 80%, with a mistag rate of about 10% for light quarks and gluons.

Leptons with $\Delta R(\gamma, \text{lep}) < 0.5(1.0)$ for muons (electrons) are discarded. Photons are then removed from the jet collection, $\Delta R(\gamma, \text{jet}) < 0.4$, to avoid double counting them as jets. The full baseline selection for the objects, triggers and nonresonant photon suppression is summarized in Table 8.1.

The clustering algorithm that builds the pseudojets for the M_{T2} variable as described in Section 6.6 depends on the distance between the objects and the pseudojets. Since two photons coming from a Higgs decay will also come from the same decay chain of a supersymmetric particle, they should end up in the same hemisphere. To this end the two photons are individually removed from the event and then re-added as one *Higgs boson candidate* in the M_{T2} calculation. The thus defined M_{T2} variable further separates the resonant and nonresonant production of diphoton events. In case there is no further object in the event other than the diphoton pair (i.e. no jet, electron nor muon), the hemispheres cannot be built, and M_{T2} is not defined.

Since this analysis in not necessarily searching for SUSY in the tails of distributions, no minimal selection is applied to M_{T2}, but rather it is used to categorize events, as described in the next section.

Table 8.1: Summary of the baseline selection. Where the values differ between the 2016 and 2017 data samples, the 2017 value is given in brackets.

Trigger	$E_{\mathrm{T}}(\gamma_0)$>30 GeV, $E_{\mathrm{T}}(\gamma_1) > 18(22)$ GeV $R_9 > 0.85$ or $\sigma_{i\eta i\eta} < 0.015$ $H/E > 0.1$
Trigger eff.	$p_T(\gamma_0)/M_{\gamma\gamma} > 1/4$, $p_T(\gamma_1)/M_{\gamma\gamma} > 1/3$ $M_{\gamma\gamma} > 100$ GeV
Jet	$p_T > 30$ GeV, $\lvert\eta\rvert < 2.4$
B tagged jet	$p_T > 20$ GeV, $\lvert\eta\rvert < 2.4$
Muon	$p_T > 20$ GeV, $\lvert\eta\rvert < 2.4$
Electron	$p_T > 20$ GeV, $\lvert\eta\rvert < 2.4$
Nonres. γ suppression	$\lvert\eta\rvert < 1.44$ $\Delta R(\gamma, \mathrm{jet}) < 0.4$

8.2 Classification

The simplified models of SUSY were described in Section 3.4. They are built such that R parity is conserved, from which follows that there is always a pair of SUSY particles produced. Of the pair at least one is required to produce a Higgs boson which decays to two photons. Thus the neutralinos and charginos, since they have to couple to the Higgs boson, also have to couple to the W and Z bosons. All the models considered in this thesis have therefore either two Higgs bosons, or a Higgs and a Z or a W boson in the final state.

The first types of categories make use of the signatures of those bosons decaying to easily identifiable particles:

- $H \to bb$: Higgs boson decaying to two b-tagged jets
- $Z \to bb$: Z boson decaying to two b-tagged jets
- $Z \to l^+l^-$: Z boson decaying to two charged leptons (electrons or muons)
- $W \to l\nu$: W boson decaying to an electron or a muon with the corresponding neutrino

The second type of category makes use of the differences between the production and decay of SM and SUSY particles. Due to the heavy SUSY parent particle, initial state radiation (ISR) is enhanced compared to the SM resulting in additional jets. Furthermore b-tagged jets are produced in the cascade themselves. In particular for the case of the bottom squark production model two b-tagged jets are expected, one each from the decay of the bottom squark to a b quark and a $\tilde{\chi}_2^0$. The jet and b-tagged jet multiplicity are used to categorize the events that do not fall in the previously mentioned categories targeting the decays of the second boson.

These two types of categories are further split in $p_T^{H\gamma\gamma}/M_{\gamma\gamma}$ and M_{T2} to further improve the sensitivity. Since the Higgs boson produced in the SUSY cascade comes from a heavy particle, it receives in general more boost and thus a larger $p_T^{H\gamma\gamma}/M_{\gamma\gamma}$ than is the case for the SM production of a Higgs boson. The M_{T2} variable has been designed for signals with final states with two invisible particles, as is the case for the signals considered here. Thus the events are distinguished further in the M_{T2} dimension.

Figure 8.2 shows the simulation of the backgrounds at 35.9 fb^{-1} overlayed with the benchmarks signal points indicated on the figures. The distributions of M_{T2}, $p_T^{H\gamma\gamma}/M_{\gamma\gamma}$, N_{jets} and $N_{\mathrm{b-tags}}$ are shown after applying the baseline selection. The signal tends to have higher values in these variables than the backgrounds, although differences between the signal models exist, particularly in the $N_{\mathrm{b-tags}}$ dimension, where the electroweak models tend to have fewer b-tagged jets than the strong production models.

These two *kinematic* variables, M_{T2} and $p_T^{H\gamma\gamma}/M_{\gamma\gamma}$, divide the phase space where the statistical power of the regions allows it, as summarized in Table 8.2. In the following the selection criteria for the regions are described in the order of assignment. Then all the regions with their bin number, bin name and selection are listed in Tables 8.3 and 8.4.

<table>
<tr><td>$Z \to l^+l^-$</td><td>-</td><td>-</td></tr>
<tr><td>0 jets, ≥0 b-jets</td><td>-</td><td rowspan="2">$p_T^{H\gamma\gamma}/M_{\gamma\gamma} < 0.6$
or
$0.6 < p_T^{H\gamma\gamma}/M_{\gamma\gamma} \leq 1.0$
or
$p_T^{H\gamma\gamma}/M_{\gamma\gamma} > 1.0$</td></tr>
<tr><td>$Z \to bb$
$H \to bb$
$W(e\nu)$
$W(\mu\nu)$
1-3 jets, 0 b-jets
1-3 jets, 1 b-jets
1-3 jets, ≥2 b-jets
≥4 jets, 0 b-jets
≥4 jets, 1 b-jets
≥4 jets, ≥2 b-jets</td><td>$M_{\mathrm{T2}} < 30\,\mathrm{GeV}$
or
$M_{\mathrm{T2}} \geq 30\,\mathrm{GeV}$</td></tr>
</table>

Table 8.2: Summary of exclusive search regions. The symbol "-" means that the region is not further split.

$Z \to l^+l^-$ region

The $Z \to l^+l^-$ decays are selected with two opposite sign same flavor leptons, electrons or muons. Since the purity of this final state is already high a relatively

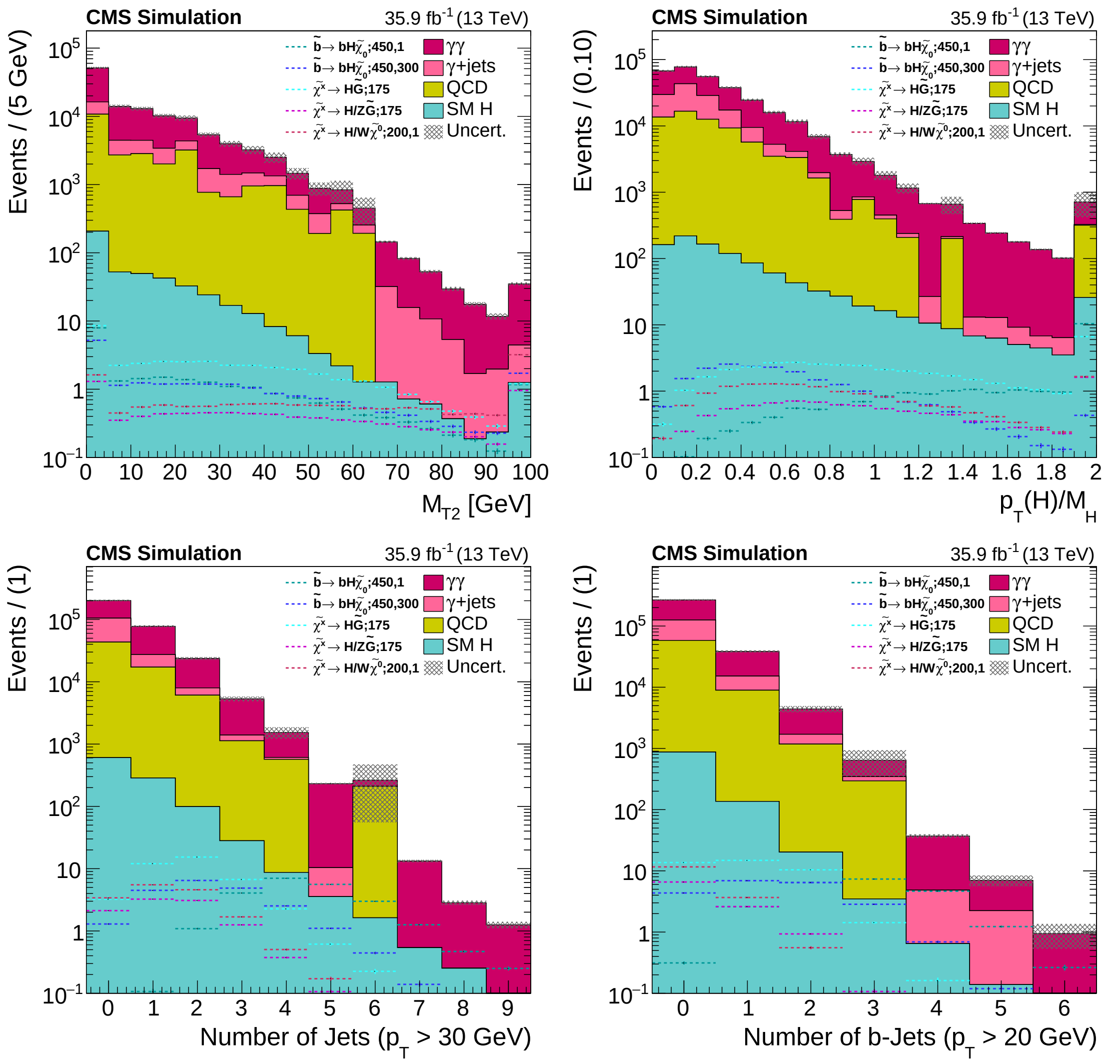

Figure 8.2: The 2016 simulation of the backgrounds and the signal after the baseline selection as a function of M_{T2} (top left), $p_T^{H\gamma\gamma}/M_{\gamma\gamma}$ (top right), N_{jets} (bottom left) and $N_{\mathrm{b-tags}}$ (bottom right). The nonresonant background of diphoton (magenta), γ+jets (pink) and QCD multijet (yellow) production and the resonant SM Higgs samples (cyan) are stacked and shown with the statistical uncertainty (grey hash) while the signals are overlayed as dashed lines: bottom squark pair production models with a bottom squark mass of 450 GeV and an LSP mass of either 1 GeV (turquoise) or 300 GeV (blue); higgsino-like chargino and neutralino production at an NLSP mass of 175 GeV with 100% branching fraction to $\tilde{\chi}_1^0 \to H\tilde{G}$ (cyan) and 50% branching fraction to $\tilde{\chi}_1^0 \to H\tilde{G}$ and $\tilde{\chi}_1^0 \to Z\tilde{G}$ each (purple); and wino-like chargino neutralino production at an NLSP mass of 200 GeV and an LSP mass of 1 GeV (magenta).

wide window around the Z boson mass, $|m_Z - m_{ll}| \leq 20\,\text{GeV}$, is chosen. If they fall outside of this mass window the event is not discarded but will end up in one of the single lepton regions. Due to the low event yield in this region, it is not further split.

$W \rightarrow l\nu$ regions

If there is an electron or muon present in the event, but it was not previously categorized as $Z \rightarrow l^+l^-$, it is labeled as $1e$ or 1μ, respectively. Should there be both an electron and a muon in the event, it is categorized by the higher p_T lepton. The statistical power of these two regions allows them to be split further in $p_T^{H\gamma\gamma}/M_{\gamma\gamma}$ and M_{T2}.

$Z \rightarrow bb$ and $H \rightarrow bb$ regions

The decays of a Z or H boson to two b-tagged jets yield resonance peaks slightly below the nominal boson mass as the momenta of the neutrinos in the bottom quark decays are not reconstructed. Their invariant mass is thus used to tag these events. First it is asserted that at least two b-tagged jets are present in the event. For all possible pairs i of b-tagged jets their invariant mass m_{bb}^i is computed and the following algorithm is applied:

- it is tagged as $H \rightarrow bb$ if any m_{bb}^i fulfils: $95\,\text{GeV} < m_{bb}^i < 140\,\text{GeV}$;
- else it is tagged as $Z \rightarrow bb$ if for any m_{bb}^i it holds that: $60\,\text{GeV} < m_{bb}^i < 95\,\text{GeV}$;
- else if none of the two conditions are fulfilled the event will be categorized into the jets and b-tagged jets bins.

The statistical power of $H \rightarrow bb$ and $Z \rightarrow bb$ regions allows them to be split further in $p_T^{H\gamma\gamma}/M_{\gamma\gamma}$ and M_{T2}.

Jet and b-tagged jet regions

All events that pass the baseline selection but were not categorized into the $Z \rightarrow l^+l^-$, $Z \rightarrow bb$, $H \rightarrow bb$ nor $W \rightarrow l\nu$ regions, are split according to their jet and b-tagged jet multiplicity. These multiplicities differ distinctively between the production modes considered. Electroweak SUSY production leads to generally fewer, and even zero, additional jets than is the case for the strong production of SUSY. On the other hand the strongly produced SUSY model considered for this analysis, where a pair of bottom squarks are produced, has minimally two b-tagged jets in the event from the decay of the sbottom quark. Furthermore there can be b-tagged jets from the decays of H, W and Z bosons. Taking into account the tagging efficiency and acceptance, not all b-tagged jets (and b-tagged jet pairs) will be tagged as such. Regions with 0 jets, 1-3 jets and at least 4 jets address the jet multiplicity, while the b-tagged jet multiplicity differences are accounted for in regions of 0, 1 and at least 2 b-tagged jets. All these regions are split in $p_T^{H\gamma\gamma}/M_{\gamma\gamma}$. Since the M_{T2} variable needs at least

Bin number	Bin name	Category	$p_T^{H\gamma\gamma}/M_{\gamma\gamma}$	M_{T2} (GeV)
SP 0	$Z_{\ell\ell}$	Two-Lepton	No req.	No req.
SP 1	$1\mu\ p_T^0,\ M_{\mathrm{T2}}^0$	Muon	0.0–0.6	0–30
SP 2	$1\mu\ p_T^0,\ M_{\mathrm{T2}}^{30}$	Muon	0.0–0.6	≥30
SP 3	$1\mu\ p_T^{75},\ M_{\mathrm{T2}}^0$	Muon	0.6–1.0	0–30
SP 4	$1\mu\ p_T^{75},\ M_{\mathrm{T2}}^{30}$	Muon	0.6–1.0	≥30
SP 5	$1\mu\ p_T^{125},\ M_{\mathrm{T2}}^0$	Muon	≥1.0	0–30
SP 6	$1\mu\ p_T^{125},\ M_{\mathrm{T2}}^{30}$	Muon	≥1.0	≥30
SP 7	$1e\ p_T^0,\ M_{\mathrm{T2}}^0$	Electron	0.0–0.6	0–30
SP 8	$1e\ p_T^0,\ M_{\mathrm{T2}}^{30}$	Electron	0.0–0.6	≥30
SP 9	$1e\ p_T^{75},\ M_{\mathrm{T2}}^0$	Electron	0.6–1.0	0–30
SP 10	$1e\ p_T^{75},\ M_{\mathrm{T2}}^{30}$	Electron	0.6–1.0	≥30
SP 11	$1e\ p_T^{125},\ M_{\mathrm{T2}}^0$	Electron	≥1.0	0–30
SP 12	$1e\ p_T^{125},\ M_{\mathrm{T2}}^{30}$	Electron	≥1.0	≥30
SP 13	$Zb\bar{b}\ p_T^0,\ M_{\mathrm{T2}}^0$	$Zb\bar{b}$	0.0–0.6	0–30
SP 14	$Zb\bar{b}\ p_T^{75},\ M_{\mathrm{T2}}^0$	$Zb\bar{b}$	0.6–1.0	0–30
SP 15	$Zb\bar{b}\ p_T^{125},\ M_{\mathrm{T2}}^0$	$Zb\bar{b}$	≥1.0	0–30
SP 16	$Zb\bar{b}\ p_T^0,\ M_{\mathrm{T2}}^{30}$	$Zb\bar{b}$	0.0–0.6	≥30
SP 17	$Zb\bar{b}\ p_T^{75},\ M_{\mathrm{T2}}^{30}$	$Zb\bar{b}$	0.6–1.0	≥30
SP 18	$Zb\bar{b}\ p_T^{125},\ M_{\mathrm{T2}}^{30}$	$Zb\bar{b}$	≥1.0	≥30
SP 19	$Hb\bar{b}\ p_T^0,\ M_{\mathrm{T2}}^0$	$Hb\bar{b}$	0.0–0.6	0–30
SP 20	$Hb\bar{b}\ p_T^{75},\ M_{\mathrm{T2}}^0$	$Hb\bar{b}$	0.6–1.0	0–30
SP 21	$Hb\bar{b}\ p_T^{125},\ M_{\mathrm{T2}}^0$	$Hb\bar{b}$	≥1.0	0–30
SP 22	$Hb\bar{b}\ p_T^0,\ M_{\mathrm{T2}}^{30}$	$Hb\bar{b}$	0.0–0.6	≥30
SP 23	$Hb\bar{b}\ p_T^{75},\ M_{\mathrm{T2}}^{30}$	$Hb\bar{b}$	0.6–1.0	≥30
SP 24	$Hb\bar{b}\ p_T^{125},\ M_{\mathrm{T2}}^{30}$	$Hb\bar{b}$	≥1.0	≥30

Table 8.3: Summary of the leptonic and H/Z boson to two b -tagged jets search regions. The bin number, name, general category along with the $p_T^{H\gamma\gamma}/M_{\gamma\gamma}$ and M_{T2} requirements are shown. For the Two-Lepton category, No req. means that no requirements are placed on the given observables.

two objects to construct the hemispheres, and in the case of the 0 jet bins exactly one object is present (the Higgs object), the 0 jet bins are not further split in M_{T2}.

Bin number	Bin name	Jets	b -tagged jets	$p_T^{H\gamma\gamma}/M_{\gamma\gamma}$	M_{T2} (GeV)
SP 25	0j, $\geq 0b$, p_T^0	0	No req.	0.0–0.6	No req.
SP 26	0j, $\geq 0b$, p_T^{75}	0	No req.	0.6–1.0	No req.
SP 27	0j, $\geq 0b$, p_T^{125}	0	No req.	$\geq$1.0	No req.
SP 28	1–3j, $0b$, p_T^0, M_{T2}^0	1–3	0	0.0–0.6	0–30
SP 29	1–3j, $0b$, p_T^0, M_{T2}^{30}	1–3	0	0.0–0.6	$\geq$30
SP 30	1–3j, $0b$, p_T^{75}, M_{T2}^0	1–3	0	0.6–1.0	0–30
SP 31	1–3j, $0b$, p_T^{75}, M_{T2}^{30}	1–3	0	0.6–1.0	$\geq$30
SP 32	1–3j, $0b$, p_T^{125}, M_{T2}^0	1–3	0	$\geq$1.0	0–30
SP 33	1–3j, $0b$, p_T^{125}, M_{T2}^{30}	1–3	0	$\geq$1.0	$\geq$30
SP 34	1–3j, $1b$, p_T^0, M_{T2}^0	1–3	1	0.0–0.6	0–30
SP 35	1–3j, $1b$, p_T^0, M_{T2}^{30}	1–3	1	0.0–0.6	$\geq$30
SP 36	1–3j, $1b$, p_T^{75}, M_{T2}^0	1–3	1	0.6–1.0	0–30
SP 37	1–3j, $1b$, p_T^{75}, M_{T2}^{30}	1–3	1	0.6–1.0	$\geq$30
SP 38	1–3j, $1b$, p_T^{125}, M_{T2}^0	1–3	1	$\geq$1.0	0–30
SP 39	1–3j, $1b$, p_T^{125}, M_{T2}^{30}	1–3	1	$\geq$1.0	$\geq$30
SP 40	1–3j, $\geq 2b$, p_T^0, M_{T2}^0	1–3	$\geq$2	0.0–0.6	0–30
SP 41	1–3j, $\geq 2b$, p_T^0, M_{T2}^{30}	1–3	$\geq$2	0.0–0.6	$\geq$30
SP 42	1–3j, $\geq 2b$, p_T^{75}, M_{T2}^0	1–3	$\geq$2	0.6–1.0	0–30
SP 43	1–3j, $\geq 2b$, p_T^{75}, M_{T2}^{30}	1–3	$\geq$2	0.6–1.0	$\geq$30
SP 44	1–3j, $\geq 2b$, p_T^{125}, M_{T2}^0	1–3	$\geq$2	$\geq$1.0	0–30
SP 45	1–3j, $\geq 2b$, p_T^{125}, M_{T2}^{30}	1–3	$\geq$2	$\geq$1.0	$\geq$30
SP 46	$\geq$4j, $0b$, p_T^0, M_{T2}^0	$\geq$4	0	0.0–0.6	0–30
SP 47	$\geq$4j, $0b$, p_T^0, M_{T2}^{30}	$\geq$4	0	0.0–0.6	$\geq$30
SP 48	$\geq$4j, $0b$, p_T^{75}, M_{T2}^0	$\geq$4	0	0.6–1.0	0–30
SP 49	$\geq$4j, $0b$, p_T^{75}, M_{T2}^{30}	$\geq$4	0	0.6–1.0	$\geq$30
SP 50	$\geq$4j, $0b$, p_T^{125}, M_{T2}^0	$\geq$4	0	$\geq$1.0	0–30
SP 51	$\geq$4j, $0b$, p_T^{125}, M_{T2}^{30}	$\geq$4	0	$\geq$1.0	$\geq$30
SP 52	$\geq$4j, $1b$, p_T^0, M_{T2}^0	$\geq$4	1	0.0–0.6	0–30
SP 53	$\geq$4j, $1b$, p_T^0, M_{T2}^{30}	$\geq$4	1	0.0–0.6	$\geq$30
SP 54	$\geq$4j, $1b$, p_T^{75}, M_{T2}^0	$\geq$4	1	0.6–1.0	0–30
SP 55	$\geq$4j, $1b$, p_T^{75}, M_{T2}^{30}	$\geq$4	1	0.6–1.0	$\geq$30
SP 56	$\geq$4j, $1b$, p_T^{125}, M_{T2}^0	$\geq$4	1	$\geq$1.0	0–30
SP 57	$\geq$4j, $1b$, p_T^{125}, M_{T2}^{30}	$\geq$4	1	$\geq$1.0	$\geq$30
SP 58	$\geq$4j, $\geq 2b$, p_T^0, M_{T2}^0	$\geq$4	$\geq$2	0.0–0.6	0–30
SP 59	$\geq$4j, $\geq 2b$, p_T^0, M_{T2}^{30}	$\geq$4	$\geq$2	0.0–0.6	$\geq$30
SP 60	$\geq$4j, $\geq 2b$, p_T^{75}, M_{T2}^0	$\geq$4	$\geq$2	0.6–1.0	0–30
SP 61	$\geq$4j, $\geq 2b$, p_T^{75}, M_{T2}^{30}	$\geq$4	$\geq$2	0.6–1.0	$\geq$30
SP 62	$\geq$4j, $\geq 2b$, p_T^{125}, M_{T2}^0	$\geq$4	$\geq$2	$\geq$1.0	0–30
SP 63	$\geq$4j, $\geq 2b$, p_T^{125}, M_{T2}^{30}	$\geq$4	$\geq$2	$\geq$1.0	$\geq$30

Table 8.4: Summary of the search region bins in the multijet and b-tagged jet categories, along with the requirements on $p_T^{H\gamma\gamma}/M_{\gamma\gamma}$ and M_{T2}. “No req.” means that no requirements are placed on the given observables.

8.3 Background estimation

There are several SM processes that can constitute a background for this search. They fall into two categories:

- a resonant background of Higgs bosons produced according to the SM
- a nonresonant background consisting of the misidentification of a jet as a photon

Both the signal processes and the resonant background have two photons from a Higgs boson decay, where the invariant mass of the diphoton system has a narrow peak at 125 GeV. Therefore this background has to be estimated directly from simulation.

The nonresonant background, on the other hand, has a steeply falling distribution in $M_{\gamma\gamma}$ that spans from the trigger threshold to the center of mass energy. A fit to this distribution in data allows to estimate the nonresonant contribution under the Higgs boson peak.

In the following I describe these two backgrounds and the methods to estimate them which are an extension of the those used in Ref. [103]. The nonresonant background fit is described in Section 8.3.1, while the resonant background is explained in Section 8.3.2. The statistical and systematic uncertainties that affect the backgrounds are described in Section 8.3.3.

8.3.1 Nonresonant background

The nonresonant background is a steeply falling distribution while the signal is a localized narrow peak around the mass of the Higgs boson at 125 GeV. Given that the signal peaks at M_H with a narrow distribution one can make use of the data to estimate the shape and normalization of the nonresonant background below the peak.

The events are classified as described in Section 8.2, and for each of those regions a functional form has to be found to describe the background. There is no assumption on the exact shape of the nonresonant background except that it is a falling distribution. Multiple functions are fit to the data in the window of $100 < M_{\gamma\gamma} < 180$ GeV and the ones that describe it reasonably well according to a χ^2 test are kept. Out of these functions the final fit is determined in the discrete profiling method, the so called *envelope* method, which is described in more detail in Ref. [112]. It was used in the measurement of the diphoton Higgs boson decay [103]. With this method the choice of the function is treated as a discrete nuisance parameter for the likelihood fit.

A set of functional forms is needed for the method to envelope all possible background shapes. The following four function groups, as used in Ref. [103], allow to cover the falling background contribution with different degrees of freedom (d.o.f.) p_i as the parameters of the fits:

- Sums of exponentials:
$$f_N(x) = \sum_{i=1}^{N} p_{2i} e^{p_{2i+1}x},$$
where p_{2i} and p_{2i+1} each count as one d.o.f.;
- Sums of polynomials in the Bernstein basis:
$$f_N(x) = \sum_{i=1}^{N} p_i b_{i,N} \qquad \text{with} \quad b_{i,N} = \binom{N}{i} x^i (1-x)^{N-i}$$
- Laurent series:
$$f_N(x) = \sum_{i=1}^{N} p_i x^{-4+\sum_{j=1}^{i}(-1)^j (j-1)}$$
- Sums of power-law functions:
$$f_N(x) = \sum_{i=1}^{N} p_{2i} x^{-p_{2i+1}},$$
where p_{2i} and p_{2i+1} each count as one d.o.f.

One could in principle have an arbitrarily large number of degrees of freedom for these functions by adding more and more parameters and thus obtaining an arbitrarily precise, but unphysical, description of the data. To avoid this overfitting of the shape, an F-test is used to determine which functions to pass to the likelihood fit.

Then a penalty is applied for each parameter of the fit N_b in the minimization of twice the negative logarithm of the likelihood ($2NLL$):

$$-2\ln \mathcal{L}_{b'} = -2\ln \mathcal{L} + N_b. \tag{8.1}$$

The set of functions with which to build the envelope is constructed by looking at $2\Delta NLL_{N+1} = 2(NLL_{N+1} - NNL_N)$, i.e. whether the higher order function with $N+1$ d.o.f. is supported by the data. As $2\Delta NLL_{N+1}$ should be distributed as a χ^2 distribution with M d.o.f., where M is the difference in d.o.f. between the N+1-th and N-th function, this is quantitatively expressed via a p-value:

$$\text{p-value} = P(2\Delta NLL_N > 2\Delta NLL_{N+1} | \chi^2(M)).$$

For a p-value smaller than 0.05, the N+1 function is supported by the data and the next order will be tested. Otherwise the function is too flexible and the N-th function is retained and no further higher degree is studied. In order to remove functions that pass this criteria but do not fit the data well, a goodness of fit test is set in place using a χ^2 test statistics. If the number of events is smaller than 5 in any given bin, toys are used instead of asymptotic approximations. The corresponding p-value is used to remove the function if the p-value is smaller than 0.01. Figure 8.3 shows the data and the fit candidates with which the envelope is built for two regions.

The discrete profile method constructs the envelope of $2NLL$ out of these functions when profiling for the parameter of interest μ, while taking into account the penalties of each function. Extensive tests of this method can be found in Ref. [112].

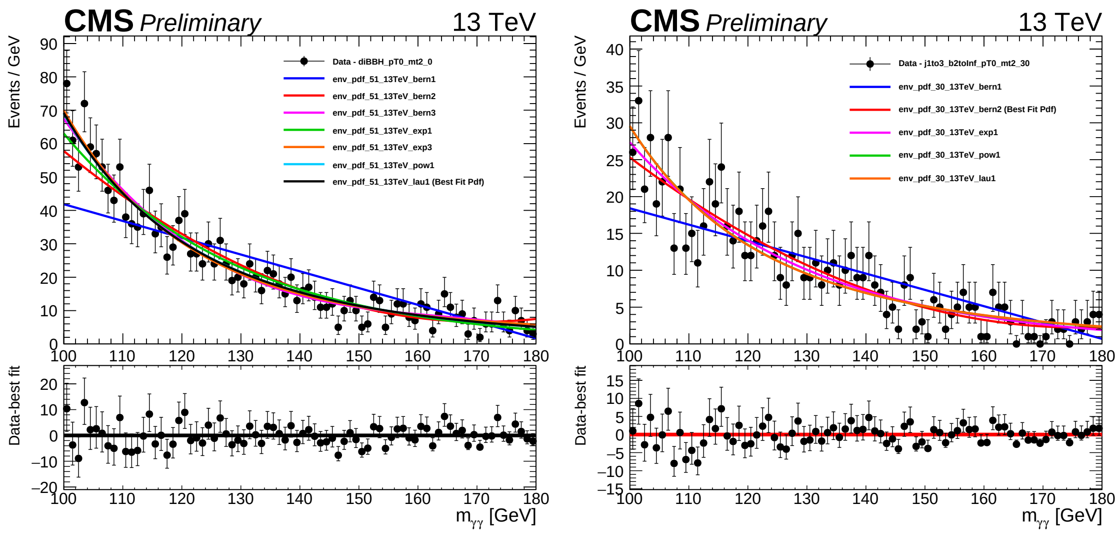

Figure 8.3: The data (black marker) and the fits to the nonresonant background (lines) for two example regions. The different colored lines represent the functions that the envelope of the region consists of.

8.3.2 Resonant background

The resonant background of Higgs bosons produced by the SM is obtained from simulation of the predominant production processes at a mass of 125 GeV via gluon-gluon fusion, vector boson fusion, associated production with a vector boson or a pair of top or bottom quarks (ggF, VBH, VH, ttH, bbH). For each category described in Section 8.2 a parametric model is constructed where the Higgs boson mass is allowed to float within 1% of its nominal mass. The only other floating parameter passed to the likelihood minimization is the normalization.

The parametric model is obtained by fitting the $M_{\gamma\gamma}$ distribution in simulation with up to four Gaussians. The model is defined through the relative contributions of the Gaussians, their mean and their width. If in a region an insufficient amount of events is present to construct a shape in a meaningful way, the shape of bin SP25 is taken while keeping the normalization of the problematic region. Figure 8.4 shows the fits with one to four Gaussians to the SM Higgs simulation of 2016 (left) and 2017 (right) in an example region.

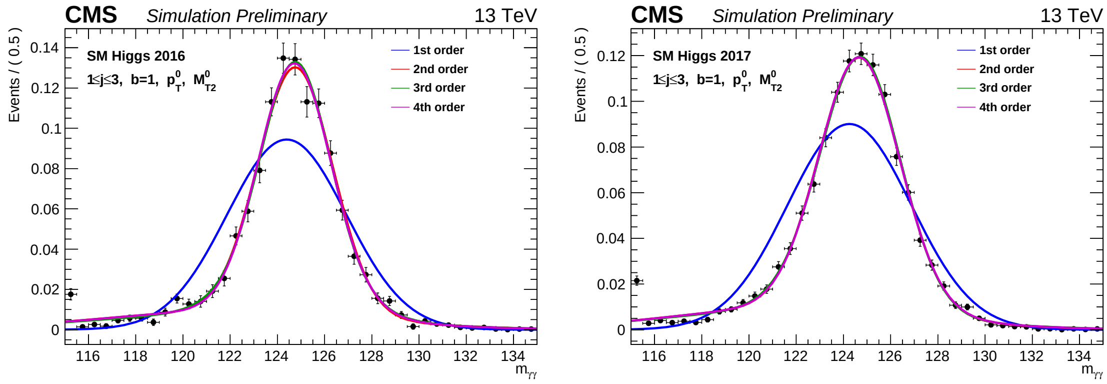

Figure 8.4: The simulation (black markers) fit by the sum of one to four Gaussians (1st to 4th order, solid lines).

8.3.3 Systematic and statistical uncertainties

The uncertainties on the normalization and shape of the nonresonant background are the dominant uncertainties in this search. The fit parameters are profiled in the final fit for the exclusion limits.

All uncertainties listed below, except the one on the Higgs boson mass, affect the yield of the SM Higgs boson production and are treated as log-normal uncertainties.

- Statistical uncertainty associated with the limited simulation statistics, taken separately for the simulations of the 2016 and 2017 conditions: 0-100%;
- integrated luminosity: 2.5% for the 2016 data taking [41] and 2.3% for the 2017 data taking period [113];
- the Higgs boson mass is allowed to float within a Gaussian uncertainty of 1% around the nominal value of 125 GeV due to the photon energy scale uncertainty;
- branching fraction of the Higgs boson decaying to two photons: 2% [114];
- photon trigger and selection efficiency: 3%;
- b-tagging efficiency: 4%;
- lepton efficiency: 4%;
- jet energy scale: 1-5%;
- the parton distribution function (PDF) uncertainty follows the LHC4PDF procedure [115] and the factorization and renormalization scales are varied between 0.5 and 2.0 according to the procedure in Ref. [116]: 10-30%.

Table 8.5: For each of the leptonic, $Zb\bar{b}$ and $Hb\bar{b}$ search regions the observed yield in data, nonresonant background as obtained from the fit and the SM Higgs boson background in the range $122 < M_{\gamma\gamma} < 129\,\mathrm{GeV}$ are listed.

Bin nr.	Search region	Observed data	Fitted nonres. bkg.	SM Higgs bkg.
SP 0	$Z_{\ell\ell}$	2	1.7 ± 0.2	0.84 ± 0.09
SP 1	$1\mu\ p_T^0,\ M_{\mathrm{T2}}^0$	24	20.0 ± 0.9	1.6 ± 0.1
SP 2	$1\mu\ p_T^0,\ M_{\mathrm{T2}}^{30}$	10	8.9 ± 1.4	1.1 ± 0.1
SP 3	$1\mu\ p_T^{75},\ M_{\mathrm{T2}}^0$	3	2.6 ± 0.5	0.89 ± 0.07
SP 4	$1\mu\ p_T^{75},\ M_{\mathrm{T2}}^{30}$	7	2.4 ± 0.4	0.79 ± 0.07
SP 5	$1\mu\ p_T^{125},\ M_{\mathrm{T2}}^0$	4	3.1 ± 0.4	1.0 ± 0.1
SP 6	$1\mu\ p_T^{125},\ M_{\mathrm{T2}}^{30}$	3	2.2 ± 0.4	1.1 ± 0.1
SP 7	$1e\ p_T^0,\ M_{\mathrm{T2}}^0$	93	87.2 ± 10.6	1.1 ± 0.1
SP 8	$1e\ p_T^0,\ M_{\mathrm{T2}}^{30}$	15	13.8 ± 0.9	0.59 ± 0.05
SP 9	$1e\ p_T^{75},\ M_{\mathrm{T2}}^0$	10	18.6 ± 3.0	0.74 ± 0.06
SP 10	$1e\ p_T^{75},\ M_{\mathrm{T2}}^{30}$	3	4.3 ± 0.3	0.48 ± 0.04
SP 11	$1e\ p_T^{125},\ M_{\mathrm{T2}}^0$	7	6.2 ± 0.4	1.1 ± 0.1
SP 12	$1e\ p_T^{125},\ M_{\mathrm{T2}}^{30}$	1	1.4 ± 0.2	0.89 ± 0.08
SP 13	$Zb\bar{b}\ p_T^0,\ M_{\mathrm{T2}}^0$	227	224 ± 17	4.4 ± 0.6
SP 14	$Zb\bar{b}\ p_T^{75},\ M_{\mathrm{T2}}^0$	33	42.2 ± 7.4	1.7 ± 0.2
SP 15	$Zb\bar{b}\ p_T^{125},\ M_{\mathrm{T2}}^0$	15	15.7 ± 3.6	2.9 ± 0.3
SP 16	$Zb\bar{b}\ p_T^0,\ M_{\mathrm{T2}}^{30}$	44	43.4 ± 7.5	0.83 ± 0.40
SP 17	$Zb\bar{b}\ p_T^{75},\ M_{\mathrm{T2}}^{30}$	13	10.8 ± 2.3	0.48 ± 0.13
SP 18	$Zb\bar{b}\ p_T^{125},\ M_{\mathrm{T2}}^{30}$	5	4.5 ± 0.4	0.82 ± 0.11
SP 19	$Hb\bar{b}\ p_T^0,\ M_{\mathrm{T2}}^0$	179	179 ± 15	3.4 ± 0.3
SP 20	$Hb\bar{b}\ p_T^{75},\ M_{\mathrm{T2}}^0$	45	41.2 ± 1.9	1.9 ± 0.2
SP 21	$Hb\bar{b}\ p_T^{125},\ M_{\mathrm{T2}}^0$	22	18.4 ± 1.8	3.0 ± 0.9
SP 22	$Hb\bar{b}\ p_T^0,\ M_{\mathrm{T2}}^{30}$	47	42.5 ± 7.4	0.93 ± 0.32
SP 23	$Hb\bar{b}\ p_T^{75},\ M_{\mathrm{T2}}^{30}$	13	12.1 ± 0.8	0.62 ± 0.06
SP 24	$Hb\bar{b}\ p_T^{125},\ M_{\mathrm{T2}}^{30}$	6	4.4 ± 0.7	1.3 ± 0.2

8.4 Results

8.4.1 Signal regions

In this section the data is compared to the resonant SM Higgs boson background as obtained from the parametric fit described in Section 8.3.2 and the best fit in the envelope of the nonresonant background 8.3.1. Tables 8.5 and 8.6 show the observed event yields in data, the fitted nonresonant background and the expected SM Higgs boson background for each of the search regions in the range of $122 < M_{\gamma\gamma} < 129\,\mathrm{GeV}$. The uncertainty includes all systematic uncertainties. The observed data agrees with the expected yield from the background estimates within the uncertainty ranges. No significant deviation from the SM is observed.

Table 8.6: For each of the all-hadronic search regions the observed yield in data, nonresonant background as obtained from the fit and the SM Higgs boson background in the range $122 < M_{\gamma\gamma} < 129\,\text{GeV}$ are listed.

Bin nr.	Search region	Observed data	Fitted nonres. bkg.	SM Higgs bkg.
SP 25	0j, $\geq 0b$, p_T^0	53 252	53 662 ± 104	973 ± 68
SP 26	0j, $\geq 0b$, p_T^{75}	586	574 ± 27	33.3 ± 4.1
SP 27	0j, $\geq 0b$, p_T^{125}	51	49.5 ± 8.0	7.4 ± 0.8
SP 28	1–3j, $0b$, p_T^0, M_{T2}^0	14 648	14 753 ± 138	308 ± 33
SP 29	1–3j, $0b$, p_T^0, M_{T2}^{30}	2732	2725 ± 10	125 ± 10
SP 30	1–3j, $0b$, p_T^{75}, M_{T2}^0	781	708 ± 30	101 ± 9
SP 31	1–3j, $0b$, p_T^{75}, M_{T2}^{30}	103	101 ± 11	0.90 ± 0.38
SP 32	1–3j, $0b$, p_T^{125}, M_{T2}^0	47	46.6 ± 7.7	0.95 ± 0.28
SP 33	1–3j, $0b$, p_T^{125}, M_{T2}^{30}	52	37.2 ± 6.9	3.9 ± 0.6
SP 34	1–3j, $1b$, p_T^0, M_{T2}^0	4184	4149 ± 7	78.4 ± 7.7
SP 35	1–3j, $1b$, p_T^0, M_{T2}^{30}	928	902 ± 34	35.3 ± 3.1
SP 36	1–3j, $1b$, p_T^{75}, M_{T2}^0	273	270 ± 19	36.4 ± 3.1
SP 37	1–3j, $1b$, p_T^{75}, M_{T2}^{30}	75	78.0 ± 10.0	1.3 ± 0.1
SP 38	1–3j, $1b$, p_T^{125}, M_{T2}^0	52	43.7 ± 7.5	0.97 ± 0.26
SP 39	1–3j, $1b$, p_T^{125}, M_{T2}^{30}	38	30.8 ± 6.3	3.7 ± 0.8
SP 40	1–3j, $\geq 2b$, p_T^0, M_{T2}^0	312	292 ± 19	5.6 ± 0.8
SP 41	1–3j, $\geq 2b$, p_T^0, M_{T2}^{30}	79	79.6 ± 10.1	3.0 ± 0.3
SP 42	1–3j, $\geq 2b$, p_T^{75}, M_{T2}^0	37	34.3 ± 6.6	4.5 ± 0.6
SP 43	1–3j, $\geq 2b$, p_T^{75}, M_{T2}^{30}	26	24.0 ± 5.6	0.57 ± 0.06
SP 44	1–3j, $\geq 2b$, p_T^{125}, M_{T2}^0	16	12.3 ± 0.8	0.54 ± 0.10
SP 45	1–3j, $\geq 2b$, p_T^{125}, M_{T2}^{30}	15	10.0 ± 0.8	1.7 ± 0.2
SP 46	$\geq$4j, $0b$, p_T^0, M_{T2}^0	2429	2426 ± 7	35.3 ± 2.6
SP 47	$\geq$4j, $0b$, p_T^0, M_{T2}^{30}	339	339 ± 21	12.9 ± 1.2
SP 48	$\geq$4j, $0b$, p_T^{75}, M_{T2}^0	118	97.8 ± 11.2	11.1 ± 2.2
SP 49	$\geq$4j, $0b$, p_T^{75}, M_{T2}^{30}	15	19.5 ± 3.1	0.16 ± 0.05
SP 50	$\geq$4j, $0b$, p_T^{125}, M_{T2}^0	13	10.0 ± 1.7	0.08 ± 1.76
SP 51	$\geq$4j, $0b$, p_T^{125}, M_{T2}^{30}	7	6.5 ± 0.6	0.73 ± 0.18
SP 52	$\geq$4j, $1b$, p_T^0, M_{T2}^0	833	800 ± 32	12.3 ± 2.5
SP 53	$\geq$4j, $1b$, p_T^0, M_{T2}^{30}	132	135 ± 13	4.6 ± 0.3
SP 54	$\geq$4j, $1b$, p_T^{75}, M_{T2}^0	33	42.5 ± 7.4	4.8 ± 0.7
SP 55	$\geq$4j, $1b$, p_T^{75}, M_{T2}^{30}	13	20.2 ± 5.1	0.35 ± 0.04
SP 56	$\geq$4j, $1b$, p_T^{125}, M_{T2}^0	10	11.4 ± 1.5	0.34 ± 0.04
SP 57	$\geq$4j, $1b$, p_T^{125}, M_{T2}^{30}	9	8.4 ± 0.6	0.97 ± 0.11
SP 58	$\geq$4j, $\geq 2b$, p_T^0, M_{T2}^0	90	88.4 ± 10.7	1.1 ± 0.3
SP 59	$\geq$4j, $\geq 2b$, p_T^0, M_{T2}^{30}	25	20.9 ± 4.6	0.52 ± 0.06
SP 60	$\geq$4j, $\geq 2b$, p_T^{75}, M_{T2}^0	11	8.7 ± 0.6	0.84 ± 0.17
SP 61	$\geq$4j, $\geq 2b$, p_T^{75}, M_{T2}^{30}	12	11.5 ± 3.7	0.26 ± 0.09
SP 62	$\geq$4j, $\geq 2b$, p_T^{125}, M_{T2}^0	6	3.7 ± 0.4	0.24 ± 0.08
SP 63	$\geq$4j, $\geq 2b$, p_T^{125}, M_{T2}^{30}	4	5.2 ± 1.1	0.69 ± 0.09

8.4.2 Interpretation in the context of simplified models of SUSY

No sign of new physics beyond the SM has been observed with the data presented above. Exclusion limits are set on the simplified models of SUSY with the method described in Appendix A. The signal yield and shape as well as the uncertainties are described here followed by the interpretation in the simplified models of SUSY using the background estimates as described above.

Systematic uncertainties on the signal

Similar uncertainties apply to the signal as for the SM Higgs boson background. They take into account the uncertainties from detector effects, simulation and theory. All uncertainties listed below affect the signal yield and are treated as log-normal uncertainties, except for the Higgs boson mass for which a Gaussian uncertainty is applied.

- Statistical uncertainty associated with the limited simulation statistics, taken separately for the simulations of the 2016 and 2017 conditions: 0-100%;
- integrated luminosity: 2.5% for the 2016 data taking [41] and 2.3% for the 2017 data taking period [113];
- the Higgs boson mass is allowed to float within a Gaussian uncertainty of 1% around the nominal value of 125 GeV due to the photon energy scale uncertainty described in Section 6.5;
- branching fraction of the Higgs boson decaying to two photons: 2% [114];
- photon trigger and selection efficiency: 3%;
- b-tagging efficiency: 4%;
- lepton efficiency: 4%;
- jet energy scale: 1-5%;
- PDF and QCD scale variations derived as for the SM Higgs background: 5-10% for the EW SUSY and 15-30% for the strong SUSY signal;
- ISR modeling as described in Section 8.1.2: 5-25%;
- modeling of $E_{\mathrm{T}}^{\mathrm{miss}}$ in the fast simulation: 3-16%.

Expected yield for the benchmark points

The signal shape is obtained with the same method as for the standard model Higgs background, described above in Section 8.3.2. In every region the sum of up to four Gaussians builds the parametric shape of the signal for said region.

Tables 8.7 and 8.8 list the expected signal yields at 77.5 fb^{-1} in the signal regions for benchmark points for the considered models. The benchmark points for each model were chosen to lie close to the expected exclusion boundary of Ref. [98] scale up to the integrated luminosity of 77.5 fb^{-1}: higgsino-like chargino and neutralino production at an NLSP mass of 175 GeV with 100% branching fraction to $\tilde{\chi}_1^0 \to H\tilde{G}$ (HH) and 50% branching fraction to $\tilde{\chi}_1^0 \to H\tilde{G}$ and $\tilde{\chi}_1^0 \to Z\tilde{G}$ each (HZ); wino-like chargino neutralino production (WH) at an NLSP mass of 200 GeV and an LSP mass of 1 GeV; bottom squark pair production models (T2bH) with a bottom squark mass of 450 GeV and an LSP mass of either 1 GeV or 300 GeV.

Upper limits on SUSY cross sections

Exclusion limits are set using profile likelihood ratio in the asymptotic approximation. Examples of fits to the background only (left) and to the signal and background (right) are shown in Figure 8.5.

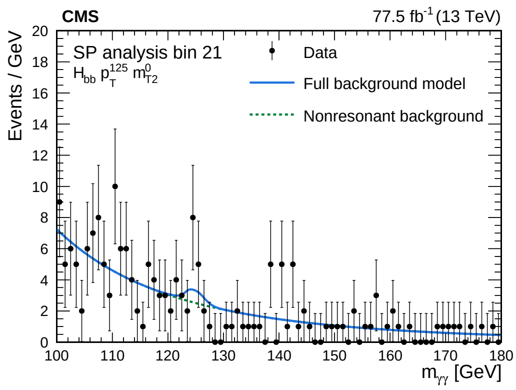

Figure 8.5: The diphoton mass distribution in data (black markers) is shown for the $H_{bb}\ p_T^{125},\ M_{\mathrm{T2}}^0$ category. Left: Nonresonant (green dotted line) and full background fit (blue solid line). Right: Signal plus background (green solid line), total background (blue dashed line) and the signal (red dotted line). The signal point shown is for bottom squark pair production with a bottom squark mass of $m_{\tilde{b}} = 500$ GeV and a neutralino mass of $m_{\tilde{\chi}_1^0} = 1$ GeV.

Figure 8.6 (left) shows the expected and observed exclusion limits for the bottom squark pair production model as a function of the mass of the $\tilde{\chi}_1^0$ and the bottom squark. For an LSP of 1 GeV bottom squark masses below 530 GeV are excluded.

In Figure 8.6 (right) the expected and observed exclusion limits are shown for the EW production of a wino-like chargino-neutralino pair as function of $m_{\tilde{\chi}_1^\pm}$ and $m_{\tilde{\chi}_1^0}$.

Table 8.7: Expected signal yield for the leptonic, $Zb\bar{b}$ and $Hb\bar{b}$ search regions. HH and HZ refer to the models at NLSP mass 175 GeV with higgsino-like chargino and neutralino production at 100% branching fraction to $\tilde{\chi}_1^0 \to H\tilde{G}$ and at 50% branching fraction to $\tilde{\chi}_1^0 \to H\tilde{G}$ and $\tilde{\chi}_1^0 \to Z\tilde{G}$ each, respectively. WH(200,1) corresponds to the wino-like neutralino chargino production with an NLSP mass of 200 GeV and an LSP mass of 1 GeV. T2bH are the bottom squark pair production model with a bottom squark mass of 450 GeV and an LSP mass of either 1 GeV or 300 GeV.

Search region	HH	HZ	WH (200,1)	T2bH (450, 1)	T2bH (450,300)
$Z_{\ell\bar{\ell}}$	0.15 ± 0.02	1.2 ± 0.2	0.0 ± 0.0	0.07 ± 0.01	0.10 ± 0.01
$Z_{b\bar{b}}\ p_T^{0},\ M_{\mathrm{T2}}^{0}$	1.3 ± 0.2	0.50 ± 0.08	0.09 ± 0.02	3.0 ± 0.2	0.29 ± 0.02
$Z_{b\bar{b}}\ p_T^{75},\ M_{\mathrm{T2}}^{0}$	1.3 ± 0.1	0.52 ± 0.06	0.05 ± 0.01	1.7 ± 0.1	0.63 ± 0.04
$Z_{b\bar{b}}\ p_T^{125},\ M_{\mathrm{T2}}^{0}$	2.9 ± 0.5	1.2 ± 0.2	0.11 ± 0.02	1.3 ± 0.1	5.1 ± 0.3
$Z_{b\bar{b}}\ p_T^{0},\ M_{\mathrm{T2}}^{30}$	1.1 ± 0.2	0.49 ± 0.08	0.12 ± 0.02	2.5 ± 0.3	0.13 ± 0.01
$Z_{b\bar{b}}\ p_T^{75},\ M_{\mathrm{T2}}^{30}$	1.1 ± 0.1	0.52 ± 0.07	0.13 ± 0.02	1.5 ± 0.1	0.31 ± 0.03
$Z_{b\bar{b}}\ p_T^{125},\ M_{\mathrm{T2}}^{30}$	2.3 ± 0.4	1.3 ± 0.2	0.25 ± 0.05	1.1 ± 0.1	2.2 ± 0.2
$H_{b\bar{b}}\ p_T^{0},\ M_{\mathrm{T2}}^{0}$	2.9 ± 0.5	0.81 ± 0.14	0.03 ± 0.01	5.9 ± 0.4	1.4 ± 0.1
$H_{b\bar{b}}\ p_T^{75},\ M_{\mathrm{T2}}^{0}$	3.3 ± 0.3	0.91 ± 0.13	0.04 ± 0.01	3.4 ± 0.3	2.6 ± 0.2
$H_{b\bar{b}}\ p_T^{125},\ M_{\mathrm{T2}}^{0}$	9.6 ± 1.8	2.6 ± 0.5	0.06 ± 0.01	3.0 ± 0.2	22.7 ± 1.7
$H_{b\bar{b}}\ p_T^{0},\ M_{\mathrm{T2}}^{30}$	2.5 ± 0.4	0.71 ± 0.10	0.10 ± 0.01	4.7 ± 0.5	0.49 ± 0.05
$H_{b\bar{b}}\ p_T^{75},\ M_{\mathrm{T2}}^{30}$	2.9 ± 0.3	0.82 ± 0.10	0.11 ± 0.02	3.0 ± 0.3	0.86 ± 0.08
$H_{b\bar{b}}\ p_T^{125},\ M_{\mathrm{T2}}^{30}$	8.2 ± 1.6	2.4 ± 0.4	0.15 ± 0.04	2.8 ± 0.2	8.7 ± 0.7
$1e\ p_T^{0},\ M_{\mathrm{T2}}^{0}$	0.43 ± 0.12	0.18 ± 0.03	0.41 ± 0.05	0.52 ± 0.04	0.06 ± 0.00
$1e\ p_T^{0},\ M_{\mathrm{T2}}^{30}$	0.43 ± 0.11	0.19 ± 0.04	0.78 ± 0.12	0.52 ± 0.03	0.05 ± 0.00
$1e\ p_T^{75},\ M_{\mathrm{T2}}^{0}$	0.45 ± 0.11	0.19 ± 0.02	0.30 ± 0.03	0.27 ± 0.02	0.12 ± 0.01
$1e\ p_T^{75},\ M_{\mathrm{T2}}^{30}$	0.48 ± 0.09	0.22 ± 0.02	0.66 ± 0.07	0.29 ± 0.02	0.12 ± 0.01
$1e\ p_T^{125},\ M_{\mathrm{T2}}^{0}$	1.3 ± 0.3	0.46 ± 0.09	0.60 ± 0.11	0.24 ± 0.02	0.87 ± 0.07
$1e\ p_T^{125},\ M_{\mathrm{T2}}^{30}$	1.5 ± 0.3	0.57 ± 0.09	1.4 ± 0.3	0.28 ± 0.02	1.1 ± 0.1
$1\mu\ p_T^{0},\ M_{\mathrm{T2}}^{0}$	0.67 ± 0.11	0.22 ± 0.04	0.63 ± 0.07	0.69 ± 0.06	0.10 ± 0.01
$1\mu\ p_T^{0},\ M_{\mathrm{T2}}^{30}$	0.59 ± 0.10	0.23 ± 0.04	1.1 ± 0.1	0.88 ± 0.07	0.09 ± 0.01
$1\mu\ p_T^{75},\ M_{\mathrm{T2}}^{0}$	0.68 ± 0.09	0.22 ± 0.03	0.44 ± 0.04	0.40 ± 0.03	0.17 ± 0.01
$1\mu\ p_T^{75},\ M_{\mathrm{T2}}^{30}$	0.74 ± 0.09	0.27 ± 0.03	1.0 ± 0.1	0.45 ± 0.04	0.18 ± 0.01
$1\mu\ p_T^{125},\ M_{\mathrm{T2}}^{0}$	1.6 ± 0.3	0.51 ± 0.08	0.72 ± 0.14	0.24 ± 0.02	1.2 ± 0.1
$1\mu\ p_T^{125},\ M_{\mathrm{T2}}^{30}$	1.7 ± 0.3	0.58 ± 0.10	1.7 ± 0.3	0.32 ± 0.03	1.6 ± 0.1

Table 8.8: The expected signal yields for the SUSY simplified model signals considered are shown for each search region bin in the all-hadronic categories of the analysis. The model points are as listed in Table 8.7.

Search region	HH	HZ	WH (200,1)	T2bH (450, 1)	T2bH (450,300)
0j, $\geq 0b$, p_T^0	3.9 ± 0.6	2.9 ± 0.5	2.6 ± 0.3	2.7 ± 0.1	0.0 ± 0.0
0j, $\geq 0b$, p_T^{75}	2.4 ± 0.3	2.1 ± 0.2	1.8 ± 0.2	0.54 ± 0.02	0.0 ± 0.0
0j, $\geq 0b$, p_T^{125}	1.7 ± 0.2	2.7 ± 0.4	1.7 ± 0.2	0.15 ± 0.01	0.01 ± 0.00
1–3j, $0b$, p_T^0, M_{T2}^0	4.7 ± 0.8	2.7 ± 0.4	2.9 ± 0.3	4.2 ± 0.5	0.03 ± 0.00
1–3j, $0b$, p_T^0, M_{T2}^{30}	4.7 ± 0.5	2.6 ± 0.3	2.1 ± 0.2	1.6 ± 0.3	0.03 ± 0.01
1–3j, $0b$, p_T^{75}, M_{T2}^0	9.0 ± 1.5	5.1 ± 0.9	3.1 ± 0.6	0.73 ± 0.15	0.27 ± 0.05
1–3j, $0b$, p_T^{75}, M_{T2}^{30}	0.21 ± 0.04	0.10 ± 0.02	0.10 ± 0.01	0.34 ± 0.09	0.04 ± 0.01
1–3j, $0b$, p_T^{125}, M_{T2}^0	0.18 ± 0.02	0.10 ± 0.01	0.07 ± 0.01	0.15 ± 0.04	0.05 ± 0.01
1–3j, $0b$, p_T^{125}, M_{T2}^{30}	0.66 ± 0.14	0.35 ± 0.07	0.19 ± 0.04	0.14 ± 0.03	0.35 ± 0.07
1–3j, $1b$, p_T^0, M_{T2}^0	6.1 ± 0.9	2.2 ± 0.3	1.1 ± 0.1	7.1 ± 1.0	0.12 ± 0.02
1–3j, $1b$, p_T^0, M_{T2}^{30}	6.6 ± 0.6	2.4 ± 0.2	0.81 ± 0.06	3.4 ± 0.3	0.20 ± 0.02
1–3j, $1b$, p_T^{75}, M_{T2}^0	13.7 ± 2.1	5.1 ± 0.9	1.4 ± 0.2	2.2 ± 0.3	1.7 ± 0.2
1–3j, $1b$, p_T^{75}, M_{T2}^{30}	0.23 ± 0.03	0.09 ± 0.01	0.08 ± 0.01	0.82 ± 0.13	0.27 ± 0.04
1–3j, $1b$, p_T^{125}, M_{T2}^0	0.36 ± 0.04	0.13 ± 0.01	0.07 ± 0.00	0.39 ± 0.06	0.59 ± 0.08
1–3j, $1b$, p_T^{125}, M_{T2}^{30}	1.2 ± 0.2	0.47 ± 0.09	0.18 ± 0.03	0.37 ± 0.05	3.5 ± 0.5
1–3j, $\geq 2b$, p_T^0, M_{T2}^0	0.60 ± 0.09	0.21 ± 0.04	0.08 ± 0.01	1.9 ± 0.2	0.43 ± 0.05
1–3j, $\geq 2b$, p_T^0, M_{T2}^{30}	0.81 ± 0.07	0.27 ± 0.02	0.07 ± 0.01	1.2 ± 0.1	0.69 ± 0.07
1–3j, $\geq 2b$, p_T^{75}, M_{T2}^0	2.0 ± 0.4	0.67 ± 0.11	0.09 ± 0.03	0.98 ± 0.12	5.0 ± 0.6
1–3j, $\geq 2b$, p_T^{75}, M_{T2}^{30}	0.08 ± 0.01	0.03 ± 0.01	0.02 ± 0.01	0.38 ± 0.04	1.3 ± 0.1
1–3j, $\geq 2b$, p_T^{125}, M_{T2}^0	0.11 ± 0.03	0.04 ± 0.00	0.03 ± 0.00	0.28 ± 0.03	2.2 ± 0.2
1–3j, $\geq 2b$, p_T^{125}, M_{T2}^{30}	0.44 ± 0.10	0.16 ± 0.03	0.05 ± 0.03	0.37 ± 0.03	15.5 ± 1.3
≥ 4j, $0b$, p_T^0, M_{T2}^0	3.9 ± 0.6	3.1 ± 0.5	6.6 ± 0.7	3.3 ± 0.8	0.01 ± 0.00
≥ 4j, $0b$, p_T^0, M_{T2}^{30}	4.2 ± 0.5	3.4 ± 0.4	5.6 ± 0.5	1.2 ± 0.2	0.03 ± 0.01
≥ 4j, $0b$, p_T^{75}, M_{T2}^0	7.5 ± 1.2	6.9 ± 1.2	8.0 ± 1.4	0.56 ± 0.11	0.13 ± 0.03
≥ 4j, $0b$, p_T^{75}, M_{T2}^{30}	0.14 ± 0.02	0.10 ± 0.01	0.19 ± 0.02	0.52 ± 0.11	0.02 ± 0.00
≥ 4j, $0b$, p_T^{125}, M_{T2}^0	0.16 ± 0.02	0.13 ± 0.02	0.19 ± 0.02	0.25 ± 0.05	0.02 ± 0.00
≥ 4j, $0b$, p_T^{125}, M_{T2}^{30}	0.81 ± 0.18	0.50 ± 0.11	0.51 ± 0.11	0.27 ± 0.05	0.16 ± 0.03
≥ 4j, $1b$, p_T^0, M_{T2}^0	5.0 ± 0.8	2.3 ± 0.3	2.5 ± 0.3	5.1 ± 0.9	0.08 ± 0.01
≥ 4j, $1b$, p_T^0, M_{T2}^{30}	5.4 ± 0.6	2.5 ± 0.2	2.1 ± 0.2	2.3 ± 0.2	0.15 ± 0.02
≥ 4j, $1b$, p_T^{75}, M_{T2}^0	11.4 ± 1.8	5.5 ± 0.9	3.5 ± 0.6	1.4 ± 0.2	1.1 ± 0.1
≥ 4j, $1b$, p_T^{75}, M_{T2}^{30}	0.27 ± 0.03	0.14 ± 0.02	0.18 ± 0.02	1.2 ± 0.2	0.11 ± 0.01
≥ 4j, $1b$, p_T^{125}, M_{T2}^0	0.33 ± 0.03	0.14 ± 0.01	0.17 ± 0.01	0.81 ± 0.13	0.15 ± 0.03
≥ 4j, $1b$, p_T^{125}, M_{T2}^{30}	1.4 ± 0.3	0.65 ± 0.12	0.42 ± 0.09	0.76 ± 0.12	1.5 ± 0.2
≥ 4j, $\geq 2b$, p_T^0, M_{T2}^0	0.42 ± 0.06	0.18 ± 0.03	0.16 ± 0.03	1.4 ± 0.1	0.18 ± 0.02
≥ 4j, $\geq 2b$, p_T^0, M_{T2}^{30}	0.65 ± 0.07	0.26 ± 0.03	0.13 ± 0.02	0.86 ± 0.08	0.35 ± 0.03
≥ 4j, $\geq 2b$, p_T^{75}, M_{T2}^0	1.6 ± 0.3	0.67 ± 0.11	0.24 ± 0.07	0.71 ± 0.08	2.4 ± 0.3
≥ 4j, $\geq 2b$, p_T^{75}, M_{T2}^{30}	0.08 ± 0.02	0.03 ± 0.00	0.03 ± 0.01	0.73 ± 0.07	0.44 ± 0.04
≥ 4j, $\geq 2b$, p_T^{125}, M_{T2}^0	0.14 ± 0.03	0.05 ± 0.02	0.03 ± 0.00	0.53 ± 0.06	0.82 ± 0.09
≥ 4j, $\geq 2b$, p_T^{125}, M_{T2}^{30}	0.51 ± 0.11	0.20 ± 0.06	0.11 ± 0.03	0.57 ± 0.05	6.4 ± 0.6

For a LSP mass of 1 GeV NLSP masses below 220 GeV are excluded.

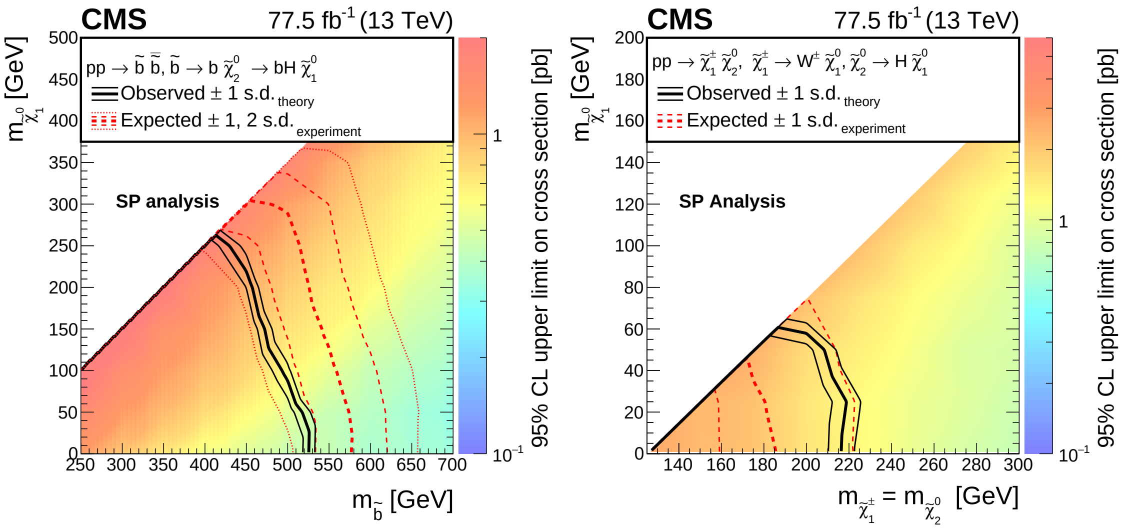

Figure 8.6: The observed and expected upper limits on the production cross section of bottom squark pair production (left) and chargino-neutralino production (right) are shown. The black solid lines correspond to the observed exclusion limit and its ± 1 uncertainty band. The red solid and dashed lines represent the expected excluded region and the corresponding ± 1 and ± 2 standard deviation bands.

Figure 8.7 shows the expected and observed upper limits on the cross section for the higgsino-like chargino-neutralino production models as a function of the neutralino mass. The two models with 100% branching fraction to $\tilde{\chi}_1^0 \to H\tilde{G}$ (Figure 8.7 left) and 50% branching fraction to $\tilde{\chi}_1^0 \to H\tilde{G}$ and $\tilde{\chi}_1^0 \to Z\tilde{G}$ each (Figure 8.7 right) are shown. Charginos and neutralinos up to masses of 275 GeV and 190 GeV for a $\tilde{G}$ mass of 1 GeV are excluded for the two models, respectively.

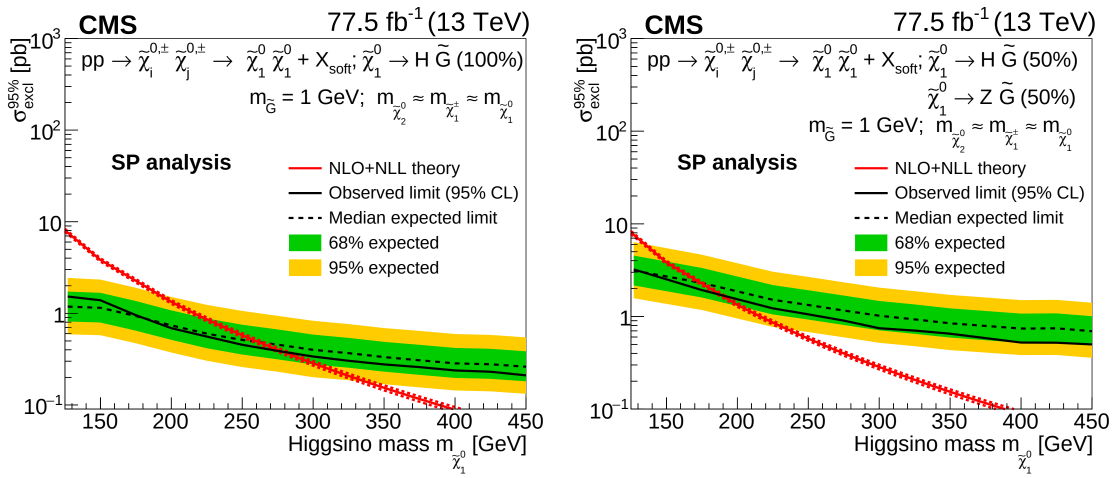

Figure 8.7: The upper limits for electroweak production of a higgsino-like chargino-neutralino pair are shown, for the model with 100% branching fraction to $\tilde{\chi}_1^0 \to H\tilde{G}$ (left) and 50% branching fraction to $\tilde{\chi}_1^0 \to H\tilde{G}$ and $\tilde{\chi}_1^0 \to Z\tilde{G}$ each (right). The solid and dotted black lines correspond to the observed and expected upper limits, with the green and yellow bands representing the corresponding ± 1 and ± 2 standard deviations, respectively. The solid and dotted red curves represent the theoretical cross section and its uncertainty band.

8.5 Conclusion

I presented a search for supersymmetry in the final state with a Higgs boson decaying to two photons with data collected by the CMS detector during the years 2016 and 2017, corresponding to an integrated luminosity of 77.5 fb^{-1}. The final state with two photons allows to probe a phase space generally not accessible to most searches for SUSY at the LHC, namely with no lower limit on the missing transverse energy of the event.

The two strategies presented in Ref. [100], optimized for the strong and electroweak production of SUSY, make use of the M_{T2} and Razor variables as a way to suppress the SM backgrounds, respectively.

For the analysis using the M_{T2} variable, described in this work, methods of the SM measurement of the Higgs boson properties are applied to estimate the backgrounds. For the nonresonant background the *envelope method* permits to eliminate the explicit choice of the functional form of the background. Instead multiple functions that are a good description of the data are passed to the final likelihood fit, where each degree of freedom results in a penalty on the likelihood.

Four scenarios of SUSY production have been tested: strong production of a bottom squark pair; EW production of wino-like chargino-neutralino pairs as well as higgsino-like chargino-neutralino production with either 100% branching fraction to $\tilde{\chi}_1^0 \rightarrow H\tilde{G}$ or 50% branching fraction to $\tilde{\chi}_1^0 \rightarrow H\tilde{G}$ and $\tilde{\chi}_1^0 \rightarrow Z\tilde{G}$ each. For the first model bottom squark masses below 530 GeV are excluded for an LSP mass of 1 GeV. For the second model neutralino-chargino masses below 220 GeV are excluded for an LSP mass of 1 GeV. And finally chargino-neutralino masses up to 275 GeV and 190 GeV for a $\tilde{G}$ mass of 1 GeV are excluded for the last two models, respectively.

The M_{T2} and Razor analysis together improve the previous limits of Ref. [98, 99] by 100 GeV for the bottom squark production model and by 50 GeV for the chargino-neutralino production.

9 Conclusion

I have presented two searches for SUSY that test and exclude part of the phase space accessible at the LHC. The two searches target different signatures of SUSY in the fully hadronic and the diphoton final states. They analyze proton-proton collisions at a center of mass energy of 13 TeV collected with the CMS experiment corresponding to an integrated luminosity of 35.9 fb^{-1} and 77.5 fb^{-1}, respectively.

The search for SUSY in the fully hadronic final state uses the stransverse mass, M_{T2}, to suppress SM production of multijet events and for categorization. The backgrounds from $Z \to \nu\nu$, tt+jets, $W +$ jets and QCD multijet production are estimated from data. The dilepton data control region is used for the estimate of the $Z \to \nu\nu$ and the single lepton data control region is used for the tt+jets and $W +$ jets background estimate. For the multijet background events with a small angular separation of the jets and missing transverse energy ($E_{\mathrm{T}}^{\mathrm{miss}}$) are used to estimate the contribution of instrumental $E_{\mathrm{T}}^{\mathrm{miss}}$ in the signal regions. Simplified models of strong SUSY production were tested and gluino masses up to 2 TeV and squark masses up to 1 TeV(1.6 TeV) for one (four) light squark type(s) for a massless LSP are excluded.

The search for SUSY with the Higgs boson to diphoton final state makes use of the narrow peak in the invariant mass spectrum of the two photons to suppress the SM backgrounds. The SM Higgs boson background is taken from simulation while the nonresonant background is fit with multiple functional forms on the data. The likelihood minimization takes into account the penalties for each degree of freedom a given function has, treating the choice of the function as a discrete nuisance parameter. For the strong production of a bottom squark pair bottom squark masses up to 530 GeV are excluded for a massless $\tilde{\chi}_1^0$. In the case of wino-like chargino-neutralino pair production masses below 220 GeV for a gravitino mass of 1 GeV are excluded. Finally for the two cases of higgsino-like chargino-neutralino production masses up to 275 GeV and 190 GeV are excluded for a gravitino mass of 1 GeV for the case with 100% branching fraction to $\tilde{\chi}_1^0 \to H\tilde{G}$ and the case with 50% branching fraction to $\tilde{\chi}_1^0 \to H\tilde{G}$ and $\tilde{\chi}_1^0 \to Z\tilde{G}$, respectively.

While it might seem like SUSY has been pushed to a corner, a large area of masses and couplings has yet to be probed. It remains a compelling theory that, at the current mass limits, could still solve the hierarchy problem in a natural way. The amount of unanswered questions and their importance in explaining the universe around us give a compelling reason to search for physics beyond the SM. If nature chose SUSY or a different model can only be determined with future measurements.

A Statistical method for signal extraction

Searches for new particles in the age of large scale accelerators are often compared to the search for a needle in a haystack. One has tailored a selection for a specific model, corresponding to just a small percentage of the total pp cross section. Fluctuations up and down of event yields are the norm, not the exception. Common tools to quantify these deviations are introduced in this chapter, along with their specific form as used for the two analyses.

The analyses presented in this thesis make use of multiple categories to increase the signal sensitivity as well as the sensitivity to different signal models. The second analysis furthermore uses parametric shapes for the signal and backgrounds in each category.

In both cases these categories are combined and tested with a modified frequentist approach, where the profile likelihood ratio is used as test statistic in combination with the asymptotic approximation and the CL$_s$ criterion [117–120].

A.1 Likelihood

The measure to qualify the goodness of fit of a signal model to the observations $n_1, ..., n_N$ for the N signal regions is the likelihood $\mathcal{L}$. The n_k are random variables with a probability density function (pdf) that incorporates the uncertainties from theory and experiment.

In the case of the first binned analysis $\mathcal{L}$ is constructed of the product of the Poisson probabilities of the regions:

$$\mathcal{L} = \prod_{k=1}^{N_{SR}} \frac{\lambda_k^{n_k} e^{-\lambda_k}}{n_k!} \tag{A.1}$$

where λ_k and n_k are the expected and observed number of events for the signal region k, of which a total of N_{SR} are considered. The predicted yield λ_k consists of the expected signal yield s times the signal strength modifier μ and the sum of the expected backgrounds b:

$$\lambda_k = \mu \cdot s_k + \sum_{j=1}^{N_B} b_{kj}. \tag{A.2}$$

For the second analysis parametric shapes are used for the signal and backgrounds. The corresponding likelihood function for k events of an observable x in a signal region c is :

$$\mathcal{L}_{cat} = \prod_{i=1}^{N_{Ec}} \frac{1}{k_c} (\mu S_c f_{Sc}(x_i) + B_c f_{Bc}(x_i)) \cdot e^{-(\mu S_c + B_c)} \tag{A.3}$$

Here the expected signal and backgrounds yields S_c and B_c are multiplied by their probability density functions (pdf) $f_S(x)$ and $f_B(x)$, respectively. The notation B again encapsulates all the background sources. The likelihood in the category is the product over all the events in the category N_{Ec} and the total likelihood is the product over the categories c to N_c.

A.2 Nuisance parameters

Above mentioned uncertainties are taken into account for the likelihood via nuisance parameters θ_i for each source i of an uncertainty, that applies to either b, s or both. Each of them is taken to be fully correlated, anti-correlated or uncorrelated between the categories, depending on which is the most appropriate or conservative choice. The nuisance parameters are incorporated into the likelihood function in the following way:

$$\mathcal{L}(n_{obs}|\mu, \theta) = \text{Poisson}(n_{obs}|\mu \cdot s(\theta) + b(\theta)) \cdot p(\theta), \tag{A.4}$$

where $p(\theta)$ is the pdf appropriate for the uncertainty and Poisson is the likelihood function as mentioned above for either the binned or unbinned case.

Three types of pdfs are used in this analysis.

- *Gaussian pdf:* This distribution is a good choice for parameters that can go both positive and negative.

$$\rho(\theta) = \frac{1}{\sqrt{2\pi}\sigma} \cdot \exp\left(\frac{(\theta - \bar{\theta})^2}{2\sigma}\right) \tag{A.5}$$

  Here σ stands for the Gaussian uncertainty, $\bar{\theta}$ is the best estimate, normally the mean value, of the nuisance parameter θ. Since this pdf can also be negative it is not suited for positively definite observables. For those cases the next pdf type is used.

- *Log-normal pdf:*

$$\rho(\theta) = \frac{1}{\sqrt{2\pi}\ln(\kappa)} \cdot \frac{1}{\theta} \cdot \exp\left(-\frac{\ln^2(\theta/\bar{\theta})}{2(\ln(\kappa))^2}\right), \tag{A.6}$$

  where θ and $\bar{\theta}$ are as define above and κ is the width of the distribution: $\kappa = 1 + \sigma_\theta/\theta$, which normalizes the uncertainty σ_θ by the nuisance parameter.

- *Gamma distribution:* This pdf is used for the statistical uncertainty associated with the number of observed events N in a control region in data or simulation. The Γ distribution is described by the number of events n in the signal region, that is connected to the control region yield N via a transfer factor α: $n = \alpha N$. The uncertainty on α is taken care of separately with a log-normal pdf. The uncertainty of the control region statistics then reads:

$$\rho(n) = \frac{1}{\alpha} \cdot \frac{(n/\alpha)^N}{N!} \cdot \exp(-n/\alpha) \tag{A.7}$$

A.3 Test statistic and CL_s method

The data is tested for its compatibility with the background-only and the signal+background hypothesis. The test statistic q_μ used for this is based on the profile likelihood ratio:

$$q_\mu = -2\ln\frac{\mathcal{L}(n|\mu,\hat{\theta}_\mu)}{\mathcal{L}(n|\hat{\mu},\hat{\theta})}, \quad \text{with } \ 0 \leq \hat{\mu} \leq \mu, \tag{A.8}$$

where n is the data yield or the pseudo data in the case of the Asimov data set, where all the parameters as set to their expected value. The hat above the variables denotes the value where the maximum of the likelihood is achieved: in the denominator both μ and θ are left floating simultaneously, while in the numerator the maximum of the likelihood is obtained at θ_μ for the fixed value of μ. Negative values of $\hat{\mu}$, i.e. negative signal, is not allowed. Furthermore is $\hat{\mu}$ constraint from above by μ, which means that upwards fluctuations are not counted as evidence against the signal model. This also results in one sided confidence interval. The test statistic is called q_μ^{obs} if n is the observed data yield. Asymptotic approximations [119] of the PDFs, test statistics and probability values are used. The probability values (p-values) are defined as the probability of obtaining a result at least as extreme as the one observed given a hypothesis H.

The test statistic is then used to obtain the probabilities P (p-values) given the observed data for the *background only* $(H_0, \mu = 0)$ and the *background+signal* $(H_1, \mu > 0)$ hypotheses:

$$\begin{aligned} \mathrm{CL}_{s+b} &= P(q_\mu \geq q_\mu^{obs}|H_1) \\ \mathrm{CL}_b &= P(q_\mu \geq q_\mu^{obs}|H_0) \end{aligned} \tag{A.9}$$

The modified frequentist statistic CL_s is defined as the ratio of these two probabilities:

$$\mathrm{CL}_s = \frac{\mathrm{CL}_{s+b}}{\mathrm{CL}_b}. \tag{A.10}$$

In this modified frequentist approach $\mathrm{CL}_s \leq \alpha$ is needed to claim "$1-\alpha$" confidence level (CL) exclusion for the signal hypothesis. To set 95% CL, one needs thus $\mathrm{CL}_s = 0.05$, which is reached at the upper limit value of μ_{UL}. Cross sections larger than μ_{UL} are excluded at 95% CL. The CL_s procedure is a conservative approach since $1-\mathrm{CL}_s \leq$CL.

Pseudo experiments are simulated to obtain the distribution of q_μ under the H_0 and H_1 hypotheses. The pseudo data for this is generated by varying the nuisance parameters by their corresponding pdf as mentioned above. From these the p-values and thus the observed CL_s is obtained in the asymptotic approximation. The expected limit is obtained by using the median value of the distribution of the test-statistic.

B Additional material on the search for SUSY in the fully hadronic final state

B.1 Alternative representation of results

The results are shown in alternative form in Tables B.1 to B.6, they list for each of the monojet and H_{T} regions the bins in N_{jets} and $N_{\mathrm{b-tags}}$ in the first column and M_{T2} in the second column, and their respective yield for the $Z \to \nu\nu$, lost lepton and QCD multijet backgrounds with their statistical and systematic uncertainty, and in the last column the data.

The background estimates are compared to the data in the signal regions, after fitting the estimates to the background only hypothesis. For a general overview of the results, Figure B.7 shows the comparison in the topological regions, i.e. in each bin of (H_{T}, N_{jets}, $N_{\mathrm{b-tags}}$) integrated over the M_{T2} dimension. Then all of the bins are shown for the monojet and each of the H_{T} regions separately in Figures B.8 to B.13. The data (black marker) is compared to the sum of the background estimates: QCD multijet (yellow), lost lepton (blue) and $Z \to \nu\nu$ (green). The uncertainty band (grey hash) includes the statistical and systematic uncertainties. They are propagated to the bottom panel where the ratio of the data over the sum of the estimates is shown.

$N_{\mathrm{j}} = 1$						
N_{j}, N_{b}	$p_{\mathrm{T}}^{\mathrm{jet1}}$ [GeV]	$Z \to \nu\bar{\nu}$	Lost lepton	Multijet	Total background	Data
1j, 0b	250 – 350	$42900\ ^{+497}_{-491}$(stat) ±2370(syst)	$19500\ ^{+135}_{-134}$(stat) ±1240(syst)	853 ± 14(stat) ±118(syst)	$63253\ ^{+515}_{-509}$(stat) ±2677(syst)	67052
	350 – 450	$9840\ ^{+221}_{-216}$(stat) ±549(syst)	3630 ± 42(stat) ±233(syst)	$209\ ^{+6}_{-5}$(stat) ±35(syst)	$13679\ ^{+225}_{-220}$(stat) ±597(syst)	14301
	450 – 575	$2730\ ^{+114}_{-110}$(stat) ±154(syst)	780 ± 18(stat) ±52(syst)	34 ± 2(stat) ±12(syst)	$3544\ ^{+115}_{-111}$(stat) ±163(syst)	3590
	575 – 700	$667\ ^{+54}_{-50}$(stat) ±38(syst)	$153\ ^{+9}_{-8}$(stat) ±13(syst)	2.7 ± 0.3(stat) ±2.7(syst)	$823\ ^{+55}_{-51}$(stat) ±40(syst)	869
	700 – 1000	$278\ ^{+37}_{-33}$(stat) ±17(syst)	$43\ ^{+6}_{-5}$(stat) ±6(syst)	$2.0\ ^{+0.5}_{-0.4}$(stat) ±1.8(syst)	$323\ ^{+38}_{-33}$(stat) ±18(syst)	336
	1000 – 1200	$41\ ^{+18}_{-13}$(stat) ±8(syst)	$0.7\ ^{+1.7}_{-0.6}$(stat) ±0.7(syst)	0.1 ± 0.1(stat) ±0.1(syst)	$42\ ^{+18}_{-13}$(stat) ±8(syst)	15
	> 1200	$12\ ^{+12}_{-7}$(stat) ±8(syst)	$2.1\ ^{+4.9}_{-1.8}$(stat) ±2.1(syst)	< 0.01	$15\ ^{+13}_{-7}$(stat) ±8(syst)	7
1j, ≥ 1b	250 – 350	$2300\ ^{+110}_{-105}$(stat) ±143(syst)	$992\ ^{+31}_{-30}$(stat) ±70(syst)	$110\ ^{+6}_{-5}$(stat) ±44(syst)	$3402\ ^{+114}_{-109}$(stat) ±165(syst)	3521
	350 – 450	$517\ ^{+50}_{-46}$(stat) ±36(syst)	$219\ ^{+11}_{-10}$(stat) ±17(syst)	35 ± 3(stat) ±14(syst)	$771\ ^{+51}_{-47}$(stat) ±43(syst)	845
	450 – 575	$172\ ^{+31}_{-27}$(stat) ±14(syst)	$45\ ^{+5}_{-4}$(stat) ±5(syst)	2.7 ± 0.4(stat) ±2.7(syst)	$219\ ^{+32}_{-27}$(stat) ±15(syst)	215
	575 – 700	$87\ ^{+25}_{-20}$(stat) ±10(syst)	10 ± 2(stat) ±2(syst)	< 0.01	$97\ ^{+25}_{-20}$(stat) ±11(syst)	62
	> 700	$17\ ^{+12}_{-7}$(stat) ±6(syst)	$3.8\ ^{+2.0}_{-1.4}$(stat) ±1.5(syst)	< 0.01	$21\ ^{+12}_{-8}$(stat) ±7(syst)	38

Figure B.1: The results for the monojet region: The first column lists the N_{jets} and $N_{\mathrm{b-tags}}$ requirements, followed by the p_T^{jet1} bins, the estimates for the $Z \to \nu\nu$, lost lepton and QCD multijet background and finally the data. The uncertainties are given split into the statistical (stat.) and systematic (syst.) contributions.

$250 < H_{\mathrm{T}} < 450$ GeV						
N_{j}, N_{b}	M_{T2} [GeV]	$Z \to \nu\bar{\nu}$	Lost lepton	Multijet	Total background	Data
$2-3$j, 0b	$200-300$	$41000\ ^{+440}_{-436}$(stat) ± 2980(syst)	$19300\ ^{+169}_{-167}$(stat) ± 1240(syst)	24 ± 0(stat) $^{+33}_{-24}$(syst)	$60324\ ^{+471}_{-467}$(stat) ± 3228(syst)	63791
	$300-400$	$8030\ ^{+86}_{-85}$(stat) ± 615(syst)	$3420\ ^{+82}_{-80}$(stat) ± 247(syst)	1.4 ± 0.1(stat) $^{+2.5}_{-1.4}$(syst)	$11451\ ^{+119}_{-117}$(stat) ± 663(syst)	11758
	> 400	397 ± 4(stat) ± 53(syst)	143 ± 3(stat) ± 59(syst)	0.02 ± 0.01(stat) $^{+0.04}_{-0.02}$(syst)	540 ± 5(stat) ± 79(syst)	541
$2-3$j, 1b	$200-300$	$4520\ ^{+145}_{-140}$(stat) ± 339(syst)	$2950\ ^{+60}_{-59}$(stat) ± 200(syst)	9 ± 0(stat) $^{+13}_{-9}$(syst)	$7479\ ^{+157}_{-152}$(stat) ± 394(syst)	7814
	$300-400$	886 ± 28(stat) ± 70(syst)	$587\ ^{+33}_{-31}$(stat) ± 54(syst)	0.5 ± 0.0(stat) $^{+1.0}_{-0.5}$(syst)	$1474\ ^{+44}_{-42}$(stat) ± 88(syst)	1477
	> 400	44 ± 1(stat) ± 6(syst)	22 ± 1(stat) ± 10(syst)	0.01 ± 0.00(stat) ± 0.01(syst)	66 ± 2(stat) ± 11(syst)	70
$2-3$j, 2b	$200-300$	$556\ ^{+52}_{-48}$(stat) ± 51(syst)	$426\ ^{+21}_{-20}$(stat) ± 40(syst)	1.4 ± 0.0(stat) $^{+2.0}_{-1.4}$(syst)	$983\ ^{+56}_{-52}$(stat) ± 65(syst)	960
	$300-400$	$109\ ^{+10}_{-9}$(stat) ± 10(syst)	79 ± 4(stat) ± 17(syst)	0.1 ± 0.0(stat) $^{+0.2}_{-0.1}$(syst)	$188\ ^{+11}_{-10}$(stat) ± 20(syst)	177
	> 400	5.4 ± 0.5(stat) ± 0.8(syst)	3.0 ± 0.1(stat) ± 1.4(syst)	< 0.01	8.4 ± 0.5(stat) ± 1.6(syst)	6
≥ 4j, 0b	$200-300$	$5370\ ^{+162}_{-157}$(stat) ± 432(syst)	$3410\ ^{+69}_{-68}$(stat) ± 232(syst)	44 ± 1(stat) $^{+60}_{-44}$(syst)	$8824\ ^{+176}_{-171}$(stat) ± 494(syst)	8901
	$300-400$	$1290\ ^{+39}_{-38}$(stat) ± 129(syst)	$513\ ^{+31}_{-29}$(stat) ± 49(syst)	2.6 ± 0.1(stat) $^{+4.7}_{-2.6}$(syst)	$1806\ ^{+50}_{-48}$(stat) ± 138(syst)	1763
	> 400	48 ± 1(stat) ± 20(syst)	12 ± 1(stat) ± 5(syst)	0.0 ± 0.0(stat) $^{+0.1}_{-0.0}$(syst)	60 ± 2(stat) ± 20(syst)	61
≥ 4j, 1b	$200-300$	$997\ ^{+69}_{-64}$(stat) ± 88(syst)	$1440\ ^{+42}_{-40}$(stat) ± 103(syst)	24 ± 0(stat) $^{+33}_{-24}$(syst)	$2461\ ^{+80}_{-76}$(stat) ± 139(syst)	2537
	$300-400$	$240\ ^{+17}_{-16}$(stat) ± 25(syst)	$195\ ^{+19}_{-17}$(stat) ± 24(syst)	1.4 ± 0.1(stat) $^{+2.5}_{-1.4}$(syst)	$436\ ^{+25}_{-23}$(stat) ± 35(syst)	419
	> 400	8.9 ± 0.6(stat) ± 3.7(syst)	1.9 ± 0.2(stat) ± 0.9(syst)	0.02 ± 0.01(stat) $^{+0.04}_{-0.02}$(syst)	11 ± 1(stat) ± 4(syst)	8
≥ 4j, 2b	$200-300$	$162\ ^{+31}_{-26}$(stat) ± 19(syst)	$522\ ^{+25}_{-24}$(stat) ± 44(syst)	7 ± 0(stat) $^{+10}_{-7}$(syst)	$691\ ^{+40}_{-36}$(stat) ± 49(syst)	747
	$300-400$	$39\ ^{+8}_{-6}$(stat) ± 5(syst)	$53\ ^{+3}_{-2}$(stat) ± 12(syst)	0.4 ± 0.0(stat) $^{+0.8}_{-0.4}$(syst)	$93\ ^{+8}_{-7}$(stat) ± 13(syst)	102
	> 400	$1.4\ ^{+0.3}_{-0.2}$(stat) ± 0.6(syst)	0.9 ± 0.0(stat) ± 0.6(syst)	0.01 ± 0.00(stat) ± 0.01(syst)	$2.4\ ^{+0.3}_{-0.2}$(stat) ± 0.8(syst)	3
≥ 2j, ≥ 3b	$200-300$	$33\ ^{+18}_{-12}$(stat) ± 11(syst)	$68\ ^{+10}_{-9}$(stat) ± 11(syst)	1.6 ± 0.0(stat) $^{+2.5}_{-1.6}$(syst)	$102\ ^{+20}_{-15}$(stat) ± 15(syst)	123
	$300-400$	$7.8\ ^{+4.2}_{-2.9}$(stat) ± 2.6(syst)	$8.0\ ^{+1.2}_{-1.0}$(stat) ± 2.2(syst)	0.1 ± 0.0(stat) $^{+0.2}_{-0.1}$(syst)	$16\ ^{+4}_{-3}$(stat) ± 3(syst)	22
	> 400	$0.3\ ^{+0.2}_{-0.1}$(stat) ± 0.1(syst)	0.1 ± 0.0(stat) ± 0.1(syst)	< 0.01	$0.4\ ^{+0.2}_{-0.1}$(stat) ± 0.2(syst)	0

Figure B.2: The results for the very low H_{T} region: The first column lists the N_{jets} and $N_{\mathrm{b-tags}}$ requirements, followed by the M_{T2} bins, the estimates for the $Z \to \nu\nu$, lost lepton and QCD multijet background and finally the data. The uncertainties are given split into the statistical (stat.) and systematic (syst.) contributions.

$450 < H_T < 575$ GeV						
N_j, N_b	M_{T2} [GeV]	$Z \to \nu\bar{\nu}$	Lost lepton	Multijet	Total background	Data
$2-3$j, 0b	$200-300$	5200^{+121}_{-119}(stat) ±330(syst)	2230^{+40}_{-40}(stat) ±150(syst)	10 ± 0(stat) ±8(syst)	7440^{+128}_{-125}(stat) ±363(syst)	7487
	$300-400$	3000^{+70}_{-68}(stat) ±204(syst)	1060^{+30}_{-30}(stat) ±77(syst)	0.4 ± 0.0(stat) ±0.4(syst)	4060^{+76}_{-75}(stat) ±218(syst)	4061
	$400-500$	1220^{+28}_{-28}(stat) ±117(syst)	351^{+22}_{-20}(stat) ±37(syst)	0.03 ± 0.00(stat) $^{+0.04}_{-0.03}$(syst)	1571^{+36}_{-35}(stat) ±123(syst)	1763
	> 500	164 ± 4(stat) ±67(syst)	38 ± 2(stat) ±16(syst)	< 0.01	202^{+5}_{-4}(stat) ±69(syst)	201
$2-3$j, 1b	$200-300$	737^{+45}_{-43}(stat) ±50(syst)	303 ± 13(stat) ±26(syst)	3.9 ± 0.1(stat) ±3.0(syst)	1044^{+47}_{-45}(stat) ±56(syst)	968
	$300-400$	425^{+26}_{-25}(stat) ±30(syst)	154^{+10}_{-9}(stat) ±22(syst)	0.1 ± 0.0(stat) ±0.1(syst)	579^{+28}_{-26}(stat) ±38(syst)	547
	$400-500$	173^{+11}_{-10}(stat) ±17(syst)	68 ± 4(stat) ±16(syst)	0.01 ± 0.00(stat) ±0.01(syst)	241 ± 11(stat) ±23(syst)	247
	> 500	23 ± 1(stat) ±10(syst)	$5.7^{+0.4}_{-0.3}$(stat) ±2.6(syst)	< 0.01	29 ± 1(stat) ±10(syst)	33
$2-3$j, 2b	$200-300$	50^{+13}_{-11}(stat) ±6(syst)	41^{+4}_{-3}(stat) ±8(syst)	0.6 ± 0.0(stat) ±0.5(syst)	92^{+14}_{-11}(stat) ±10(syst)	113
	$300-400$	29^{+8}_{-6}(stat) ±4(syst)	27 ± 2(stat) ±5(syst)	0.02 ± 0.00(stat) ±0.02(syst)	56^{+8}_{-7}(stat) ±6(syst)	61
	$400-500$	12 ± 3(stat) ±2(syst)	10 ± 1(stat) ±3(syst)	< 0.01	22 ± 3(stat) ±4(syst)	34
	> 500	$1.6^{+0.4}_{-0.3}$(stat) ±0.7(syst)	0.3 ± 0.0(stat) ±0.2(syst)	< 0.01	$1.9^{+0.4}_{-0.3}$(stat) ±0.7(syst)	6
$4-6$j, 0b	$200-300$	2050^{+81}_{-78}(stat) ±154(syst)	1470^{+35}_{-34}(stat) ±102(syst)	25 ± 1(stat) ±17(syst)	3545^{+89}_{-86}(stat) ±186(syst)	3994
	$300-400$	1170^{+46}_{-44}(stat) ±97(syst)	618^{+25}_{-24}(stat) ±49(syst)	0.9 ± 0.0(stat) ±0.9(syst)	1789^{+53}_{-51}(stat) ±109(syst)	1726
	$400-500$	356 ± 14(stat) ±46(syst)	110^{+13}_{-12}(stat) ±16(syst)	0.1 ± 0.0(stat) ±0.1(syst)	466^{+19}_{-18}(stat) ±48(syst)	462
	> 500	31 ± 1(stat) ±13(syst)	$7.6^{+0.9}_{-0.8}$(stat) ±3.5(syst)	< 0.01	38^{+2}_{-1}(stat) ±13(syst)	25
$4-6$j, 1b	$200-300$	458^{+39}_{-36}(stat) ±37(syst)	654^{+22}_{-21}(stat) ±48(syst)	13 ± 0(stat) ±9(syst)	1125^{+45}_{-42}(stat) ±62(syst)	1159
	$300-400$	260^{+22}_{-20}(stat) ±23(syst)	247^{+14}_{-13}(stat) ±24(syst)	0.5 ± 0.0(stat) ±0.5(syst)	507^{+26}_{-24}(stat) ±33(syst)	477
	$400-500$	80^{+7}_{-6}(stat) ±10(syst)	40 ± 2(stat) ±9(syst)	0.04 ± 0.00(stat) $^{+0.05}_{-0.04}$(syst)	119 ± 7(stat) ±14(syst)	106
	> 500	$6.8^{+0.6}_{-0.5}$(stat) ±2.9(syst)	1.1 ± 0.1(stat) ±0.6(syst)	< 0.01	$7.9^{+0.6}_{-0.5}$(stat) ±2.9(syst)	10
$4-6$j, 2b	$200-300$	79^{+17}_{-14}(stat) ±10(syst)	270 ± 14(stat) ±23(syst)	3.3 ± 0.1(stat) ±2.5(syst)	352^{+22}_{-20}(stat) ±25(syst)	384
	$300-400$	45^{+10}_{-8}(stat) ±6(syst)	72^{+9}_{-8}(stat) ±10(syst)	0.1 ± 0.0(stat) ±0.1(syst)	117^{+13}_{-12}(stat) ±12(syst)	109
	$400-500$	14^{+3}_{-2}(stat) ±2(syst)	$7.8^{+1.0}_{-0.9}$(stat) ±2.1(syst)	0.01 ± 0.00(stat) ±0.01(syst)	22 ± 3(stat) ±3(syst)	33
	> 500	$1.2^{+0.3}_{-0.2}$(stat) ±0.5(syst)	0.4 ± 0.1(stat) ±0.3(syst)	< 0.01	$1.6^{+0.3}_{-0.2}$(stat) ±0.6(syst)	3
≥ 7j, 0b	$200-300$	29^{+16}_{-11}(stat) ±15(syst)	41^{+8}_{-7}(stat) ±8(syst)	1.4 ± 0.0(stat) ±1.1(syst)	72^{+17}_{-13}(stat) ±18(syst)	93
	$300-400$	10^{+5}_{-4}(stat) ±5(syst)	11 ± 2(stat) ±3(syst)	0.1 ± 0.0(stat) ±0.1(syst)	20^{+6}_{-4}(stat) ±6(syst)	25
	> 400	$1.5^{+0.8}_{-0.6}$(stat) ±1.0(syst)	0.4 ± 0.1(stat) ±0.3(syst)	< 0.01	$1.9^{+0.8}_{-0.6}$(stat) ±1.0(syst)	0
≥ 7j, 1b	$200-300$	17^{+13}_{-8}(stat) ±11(syst)	50^{+7}_{-6}(stat) ±8(syst)	0.9 ± 0.0(stat) ±0.8(syst)	68^{+15}_{-10}(stat) ±13(syst)	76
	$300-400$	$5.4^{+4.3}_{-2.6}$(stat) ±3.8(syst)	$8.9^{+1.2}_{-1.1}$(stat) ±2.3(syst)	0.03 ± 0.00(stat) $^{+0.04}_{-0.03}$(syst)	14^{+4}_{-3}(stat) ±4(syst)	20
	> 400	$0.9^{+0.7}_{-0.4}$(stat) ±0.7(syst)	0.3 ± 0.0(stat) ±0.2(syst)	< 0.01	$1.2^{+0.7}_{-0.4}$(stat) ±0.7(syst)	1
≥ 7j, 2b	$200-300$	$5.5^{+4.3}_{-2.6}$(stat) ±3.9(syst)	30 ± 4(stat) ±5(syst)	0.4 ± 0.0(stat) ±0.3(syst)	36^{+6}_{-4}(stat) ±6(syst)	45
	$300-400$	$1.8^{+1.4}_{-0.9}$(stat) ±1.3(syst)	$4.3^{+0.6}_{-0.5}$(stat) ±1.2(syst)	0.01 ± 0.00(stat) $^{+0.02}_{-0.01}$(syst)	$6.1^{+1.5}_{-1.0}$(stat) ±1.8(syst)	8
	> 400	$0.3^{+0.2}_{-0.1}$(stat) ±0.2(syst)	0.1 ± 0.0(stat) ±0.1(syst)	< 0.01	$0.4^{+0.2}_{-0.1}$(stat) ±0.2(syst)	1
$2-6$j, ≥ 3b	$200-300$	24^{+13}_{-9}(stat) ±8(syst)	45^{+6}_{-5}(stat) ±7(syst)	0.7 ± 0.0(stat) ±0.7(syst)	70^{+14}_{-10}(stat) ±10(syst)	57
	$300-400$	$9.4^{+5.0}_{-3.5}$(stat) ±3.0(syst)	12^{+2}_{-1}(stat) ±3(syst)	0.03 ± 0.00(stat) ±0.03(syst)	21^{+5}_{-4}(stat) ±4(syst)	10
	$400-500$	$3.3^{+1.8}_{-1.2}$(stat) ±1.1(syst)	1.7 ± 0.2(stat) ±0.7(syst)	< 0.01	$5.0^{+1.8}_{-1.2}$(stat) ±1.3(syst)	2
	> 500	0.3 ± 0.1(stat) ±0.1(syst)	0.2 ± 0.0(stat) ±0.1(syst)	< 0.01	0.4 ± 0.1(stat) ±0.2(syst)	0
≥ 7j, ≥ 3b	$200-300$	$1.3^{+1.0}_{-0.6}$(stat) ±1.2(syst)	$6.2^{+0.8}_{-0.7}$(stat) ±1.1(syst)	0.1 ± 0.0(stat) ±0.1(syst)	$7.6^{+1.3}_{-1.0}$(stat) ±1.7(syst)	8
	$300-400$	$0.4^{+0.3}_{-0.2}$(stat) ±0.4(syst)	0.8 ± 0.1(stat) ±0.3(syst)	< 0.01	$1.2^{+0.4}_{-0.2}$(stat) ±0.5(syst)	2
	> 400	$0.1^{+0.1}_{-0.0}$(stat) ±0.1(syst)	< 0.01	< 0.01	$0.1^{+0.1}_{-0.0}$(stat) ±0.1(syst)	0

Figure B.3: The results for the low H_T region: The first column lists the N_{jets} and $N_{\text{b-tags}}$ requirements, followed by the M_{T2} bins, the estimates for the $Z \to \nu\nu$, lost lepton and QCD multijet background and finally the data. The uncertainties are given split into the statistical (stat.) and systematic (syst.) contributions.

$575 < H_T < 1000$ GeV						
N_j, N_b	M_{T2} [GeV]	$Z \to \nu\bar{\nu}$	Lost lepton	Multijet	Total background	Data
2 – 3j, 0b	200 – 300	2700^{+74}_{-72}(stat) ±186(syst)	1250 ±27(stat) ±85(syst)	27 ±0(stat) ±13(syst)	3977^{+79}_{-77}(stat) ±205(syst)	4163
	300 – 400	1840^{+51}_{-49}(stat) ±134(syst)	598^{+20}_{-19}(stat) ±43(syst)	2.5 ±0.1(stat) ±1.4(syst)	2441^{+54}_{-53}(stat) ±141(syst)	2442
	400 – 600	1630^{+45}_{-44}(stat) ±121(syst)	383^{+18}_{-17}(stat) ±31(syst)	0.1 ±0.0(stat) ±0.1(syst)	2013^{+48}_{-47}(stat) ±125(syst)	1940
	600 – 800	272 ±7(stat) ±37(syst)	50^{+8}_{-7}(stat) ±8(syst)	< 0.01	322^{+11}_{-10}(stat) ±38(syst)	302
	> 800	26 ±1(stat) ±11(syst)	3.8 ±0.6(stat) ±1.7(syst)	< 0.01	30 ±1(stat) ±11(syst)	25
2 – 3j, 1b	200 – 300	298^{+24}_{-22}(stat) ±22(syst)	199 ±10(stat) ±17(syst)	10 ±0(stat) ±5(syst)	507^{+26}_{-24}(stat) ±28(syst)	612
	300 – 400	203^{+17}_{-15}(stat) ±15(syst)	96^{+8}_{-7}(stat) ±10(syst)	1.0 ±0.0(stat) ±0.6(syst)	299^{+18}_{-17}(stat) ±18(syst)	323
	400 – 600	180^{+15}_{-14}(stat) ±14(syst)	63 ±7(stat) ±8(syst)	0.04 ±0.00(stat) ±0.03(syst)	243^{+16}_{-15}(stat) ±16(syst)	253
	600 – 800	30 ±2(stat) ±4(syst)	$9.4^{+1.1}_{-1.0}$(stat) ±2.4(syst)	< 0.01	39^{+3}_{-2}(stat) ±5(syst)	44
	> 800	2.8 ±0.2(stat) ±1.2(syst)	0.5 ±0.1(stat) ±0.3(syst)	< 0.01	3.4 ±0.2(stat) ±1.2(syst)	1
2 – 3j, 2b	200 – 300	51^{+12}_{-10}(stat) ±5(syst)	22 ±2(stat) ±4(syst)	1.6 ±0.0(stat) ±1.0(syst)	75^{+12}_{-10}(stat) ±7(syst)	71
	300 – 400	35^{+8}_{-7}(stat) ±4(syst)	9.4 ±1.0(stat) ±1.7(syst)	0.2 ±0.0(stat) ±0.1(syst)	44^{+8}_{-7}(stat) ±4(syst)	34
	400 – 600	31^{+7}_{-6}(stat) ±3(syst)	7.5 ±0.8(stat) ±1.9(syst)	< 0.01	38^{+7}_{-6}(stat) ±4(syst)	24
	600 – 800	$5.1^{+1.2}_{-1.0}$(stat) ±0.8(syst)	0.9 ±0.1(stat) ±0.4(syst)	< 0.01	$6.0^{+1.2}_{-1.0}$(stat) ±0.9(syst)	6
	> 800	0.5 ±0.1(stat) ±0.2(syst)	0.1 ±0.0(stat) ±0.1(syst)	< 0.01	0.5 ±0.1(stat) ±0.2(syst)	0
4 – 6j, 0b	200 – 300	2170^{+77}_{-75}(stat) ±156(syst)	1550 ±32(stat) ±104(syst)	108 ±2(stat) ±44(syst)	3828^{+84}_{-81}(stat) ±193(syst)	3718
	300 – 400	1200^{+43}_{-41}(stat) ±96(syst)	651^{+21}_{-20}(stat) ±47(syst)	10 ±0(stat) ±5(syst)	1861^{+47}_{-46}(stat) ±107(syst)	1939
	400 – 600	757^{+27}_{-26}(stat) ±68(syst)	266 ±13(stat) ±23(syst)	0.4 ±0.0(stat) ±0.3(syst)	1023^{+30}_{-29}(stat) ±71(syst)	1180
	600 – 800	108 ±4(stat) ±22(syst)	29 ±1(stat) ±6(syst)	< 0.01	137 ±4(stat) ±23(syst)	140
	> 800	7.6 ±0.3(stat) ±3.4(syst)	1.7 ±0.1(stat) ±0.7(syst)	< 0.01	9.3 ±0.3(stat) ±3.5(syst)	7
4 – 6j, 1b	200 – 300	468^{+36}_{-33}(stat) ±35(syst)	665^{+20}_{-19}(stat) ±47(syst)	55 ±1(stat) ±25(syst)	1188^{+41}_{-38}(stat) ±64(syst)	1183
	300 – 400	258^{+20}_{-18}(stat) ±21(syst)	240^{+12}_{-11}(stat) ±20(syst)	5.2 ±0.1(stat) ±2.8(syst)	503^{+23}_{-21}(stat) ±29(syst)	616
	400 – 600	163 ±12(stat) ±15(syst)	90^{+8}_{-7}(stat) ±10(syst)	0.2 ±0.0(stat) ±0.2(syst)	254^{+15}_{-14}(stat) ±18(syst)	277
	600 – 800	23 ±2(stat) ±5(syst)	6.9 ±0.6(stat) ±1.7(syst)	< 0.01	30 ±2(stat) ±5(syst)	31
	> 800	1.6 ±0.1(stat) ±0.7(syst)	0.1 ±0.0(stat) ±0.1(syst)	< 0.01	1.8 ±0.1(stat) ±0.7(syst)	2
4 – 6j, 2b	200 – 300	71^{+15}_{-12}(stat) ±10(syst)	275 ±12(stat) ±22(syst)	14 ±0(stat) ±8(syst)	360^{+19}_{-17}(stat) ±25(syst)	366
	300 – 400	39^{+8}_{-7}(stat) ±5(syst)	103^{+8}_{-7}(stat) ±11(syst)	1.3 ±0.0(stat) ±0.8(syst)	144^{+11}_{-10}(stat) ±12(syst)	147
	400 – 600	25^{+5}_{-4}(stat) ±4(syst)	44^{+6}_{-5}(stat) ±7(syst)	0.1 ±0.0(stat) ±0.0(syst)	69^{+8}_{-7}(stat) ±7(syst)	72
	600 – 800	$3.5^{+0.7}_{-0.6}$(stat) ±0.8(syst)	3.2 ±0.4(stat) ±0.9(syst)	< 0.01	$6.7^{+0.8}_{-0.7}$(stat) ±1.2(syst)	5
	> 800	$0.2^{+0.1}_{-0.0}$(stat) ±0.1(syst)	0.2 ±0.0(stat) ±0.1(syst)	< 0.01	$0.4^{+0.1}_{-0.0}$(stat) ±0.2(syst)	2
≥ 7j, 0b	200 – 300	106^{+22}_{-18}(stat) ±21(syst)	124^{+12}_{-11}(stat) ±14(syst)	9.4 ±0.1(stat) ±4.4(syst)	239^{+24}_{-21}(stat) ±26(syst)	290
	300 – 400	56^{+11}_{-10}(stat) ±11(syst)	49^{+7}_{-6}(stat) ±8(syst)	0.9 ±0.0(stat) ±0.5(syst)	106^{+13}_{-11}(stat) ±13(syst)	130
	400 – 600	29^{+6}_{-5}(stat) ±8(syst)	16 ±2(stat) ±3(syst)	0.04 ±0.00(stat) ±0.03(syst)	45^{+6}_{-5}(stat) ±8(syst)	47
	600 – 800	$2.9^{+0.6}_{-0.5}$(stat) ±1.0(syst)	1.0 ±0.1(stat) ±0.4(syst)	< 0.01	$3.9^{+0.6}_{-0.5}$(stat) ±1.1(syst)	2
	> 800	0.1 ±0.0(stat) ±0.1(syst)	< 0.01	< 0.01	0.1 ±0.0(stat) ±0.1(syst)	0
≥ 7j, 1b	200 – 300	39^{+11}_{-9}(stat) ±10(syst)	173^{+10}_{-9}(stat) ±15(syst)	6.2 ±0.1(stat) ±3.1(syst)	219^{+15}_{-13}(stat) ±19(syst)	223
	300 – 400	21^{+6}_{-5}(stat) ±5(syst)	60 ±5(stat) ±8(syst)	0.6 ±0.0(stat) ±0.3(syst)	81^{+8}_{-7}(stat) ±9(syst)	74
	400 – 600	11^{+3}_{-2}(stat) ±4(syst)	17^{+2}_{-1}(stat) ±4(syst)	0.02 ±0.00(stat) ±0.02(syst)	28 ±3(stat) ±5(syst)	20
	> 600	1.1 ±0.3(stat) ±0.5(syst)	0.8 ±0.1(stat) ±0.4(syst)	< 0.01	2.0 ±0.3(stat) ±0.7(syst)	1
≥ 7j, 2b	200 – 300	10^{+3}_{-2}(stat) ±3(syst)	113 ±6(stat) ±10(syst)	2.5 ±0.0(stat) ±1.5(syst)	125^{+7}_{-6}(stat) ±11(syst)	132
	300 – 400	$5.1^{+1.5}_{-1.1}$(stat) ±1.3(syst)	38 ±3(stat) ±5(syst)	0.2 ±0.0(stat) ±0.2(syst)	44^{+4}_{-3}(stat) ±5(syst)	41
	400 – 600	$2.7^{+0.8}_{-0.6}$(stat) ±0.9(syst)	$9.2^{+0.8}_{-0.7}$(stat) ±2.2(syst)	0.01 ±0.00(stat) ±0.01(syst)	12 ±1(stat) ±2(syst)	7
	> 600	0.3 ±0.1(stat) ±0.1(syst)	0.2 ±0.0(stat) ±0.1(syst)	< 0.01	0.5 ±0.1(stat) ±0.1(syst)	0
2 – 6j, ≥ 3b	200 – 300	15^{+8}_{-5}(stat) ±5(syst)	51^{+5}_{-4}(stat) ±7(syst)	2.7 ±0.0(stat) ±2.1(syst)	69^{+9}_{-7}(stat) ±9(syst)	53
	300 – 400	$9.4^{+4.6}_{-3.2}$(stat) ±2.8(syst)	17^{+2}_{-1}(stat) ±3(syst)	0.2 ±0.0(stat) ±0.2(syst)	27^{+5}_{-4}(stat) ±4(syst)	24
	400 – 600	$6.7^{+3.3}_{-2.3}$(stat) ±2.0(syst)	$6.4^{+0.6}_{-0.5}$(stat) ±2.0(syst)	0.01 ±0.00(stat) ±0.01(syst)	13^{+3}_{-2}(stat) ±3(syst)	5
	> 600	$1.3^{+0.6}_{-0.4}$(stat) ±1.3(syst)	0.2 ±0.0(stat) ±0.1(syst)	< 0.01	$1.4^{+0.6}_{-0.4}$(stat) ±1.3(syst)	0
≥ 7j, ≥ 3b	200 – 300	$1.9^{+0.5}_{-0.4}$(stat) ±0.5(syst)	27^{+2}_{-1}(stat) ±3(syst)	0.6 ±0.0(stat) ±0.5(syst)	30^{+2}_{-1}(stat) ±3(syst)	45
	300 – 400	$1.0^{+0.3}_{-0.2}$(stat) ±0.3(syst)	10 ±1(stat) ±2(syst)	0.1 ±0.0(stat) ±0.0(syst)	11 ±1(stat) ±2(syst)	14
	400 – 600	0.5 ±0.1(stat) ±0.2(syst)	2.3 ±0.2(stat) ±0.7(syst)	< 0.01	2.8 ±0.2(stat) ±0.7(syst)	2
	> 600	0.1 ±0.0(stat) ±0.0(syst)	0.1 ±0.0(stat) ±0.1(syst)	< 0.01	0.2 ±0.0(stat) ±0.1(syst)	0

Figure B.4: The results for the medium H_T region: The first column lists the N_{jets} and N_{b-tags} requirements, followed by the M_{T2} bins, the estimates for the $Z \to \nu\nu$, lost lepton and QCD multijet background and finally the data. The uncertainties are given split into the statistical (stat.) and systematic (syst.) contributions.

$1000 < H_{\mathrm{T}} < 1500$ GeV						
$N_{\mathrm{j}}, N_{\mathrm{b}}$	M_{T2} [GeV]	$Z \to \nu\bar{\nu}$	Lost lepton	Multijet	Total background	Data
$2-3$j, 0b	$200-400$	489 $^{+45}_{-41}$(stat) ±53(syst)	225 $^{+12}_{-11}$(stat) ±19(syst)	29 ±1(stat) ±10(syst)	743 $^{+47}_{-43}$(stat) ±57(syst)	766
	$400-600$	74 $^{+7}_{-6}$(stat) ±17(syst)	36 $^{+5}_{-4}$(stat) ±6(syst)	0.3 ±0.0(stat) ±0.1(syst)	110 $^{+8}_{-7}$(stat) ±18(syst)	159
	$600-800$	30 ±3(stat) ±7(syst)	10 ±1(stat) ±2(syst)	< 0.01	40 ±3(stat) ±7(syst)	64
	$800-1000$	15 ±1(stat) ±4(syst)	5.1 $^{+0.7}_{-0.6}$(stat) ±1.5(syst)	< 0.01	20 $^{+2}_{-1}$(stat) ±5(syst)	24
	$1000-1200$	6.3 $^{+0.6}_{-0.5}$(stat) ±2.3(syst)	1.2 $^{+0.2}_{-0.1}$(stat) ±0.6(syst)	< 0.01	7.5 $^{+0.6}_{-0.5}$(stat) ±2.3(syst)	10
	> 1200	1.0 ±0.1(stat) ±0.4(syst)	0.2 ±0.0(stat) ±0.2(syst)	< 0.01	1.2 ±0.1(stat) ±0.5(syst)	2
$2-3$j, 1b	$200-400$	95 $^{+22}_{-18}$(stat) ±11(syst)	46 $^{+5}_{-4}$(stat) ±6(syst)	11 ±0(stat) ±4(syst)	153 $^{+23}_{-19}$(stat) ±14(syst)	130
	$400-600$	14 ±3(stat) ±3(syst)	6.7 $^{+0.7}_{-0.6}$(stat) ±1.3(syst)	0.1 ±0.0(stat) ±0.1(syst)	21 ±3(stat) ±4(syst)	26
	$600-800$	5.9 $^{+1.4}_{-1.1}$(stat) ±1.3(syst)	1.7 ±0.2(stat) ±0.5(syst)	< 0.01	7.6 $^{+1.4}_{-1.1}$(stat) ±1.4(syst)	10
	$800-1000$	2.9 $^{+0.7}_{-0.6}$(stat) ±0.8(syst)	1.0 ±0.1(stat) ±0.5(syst)	< 0.01	4.0 $^{+0.7}_{-0.6}$(stat) ±1.0(syst)	4
	$1000-1200$	1.2 $^{+0.3}_{-0.2}$(stat) ±0.4(syst)	0.4 ±0.0(stat) ±0.3(syst)	< 0.01	1.6 $^{+0.3}_{-0.2}$(stat) ±0.5(syst)	1
	> 1200	0.2 ±0.0(stat) ±0.1(syst)	< 0.01	< 0.01	0.2 ±0.0(stat) ±0.1(syst)	1
$2-3$j, 2b	$200-400$	7.0 $^{+6.8}_{-3.8}$(stat) ±4.3(syst)	3.5 $^{+1.6}_{-1.2}$(stat) ±1.4(syst)	1.7 ±0.0(stat) ±0.8(syst)	12 $^{+7}_{-4}$(stat) ±5(syst)	14
	$400-600$	1.0 $^{+1.0}_{-0.6}$(stat) ±0.7(syst)	0.4 $^{+0.2}_{-0.1}$(stat) ±0.2(syst)	0.02 ±0.00(stat) ±0.01(syst)	1.4 $^{+1.0}_{-0.6}$(stat) ±0.7(syst)	2
	$600-800$	0.4 $^{+0.4}_{-0.2}$(stat) ±0.3(syst)	0.03 ±0.01(stat) ±0.03(syst)	< 0.01	0.5 $^{+0.4}_{-0.2}$(stat) ±0.3(syst)	2
	$800-1000$	0.2 $^{+0.2}_{-0.1}$(stat) ±0.2(syst)	0.1 ±0.0(stat) ±0.1(syst)	< 0.01	0.3 $^{+0.2}_{-0.1}$(stat) ±0.2(syst)	0
	> 1000	0.1 ±0.1(stat) ±0.1(syst)	0.2 ±0.1(stat) $^{+0.3}_{-0.2}$(syst)	< 0.01	0.3 ±0.1(stat) ±0.3(syst)	0
$4-6$j, 0b	$200-400$	578 $^{+48}_{-45}$(stat) ±59(syst)	434 $^{+17}_{-16}$(stat) ±33(syst)	194 ±3(stat) ±44(syst)	1206 $^{+51}_{-48}$(stat) ±80(syst)	1166
	$400-600$	132 $^{+11}_{-10}$(stat) ±23(syst)	49 ±4(stat) ±6(syst)	2.1 ±0.1(stat) ±0.8(syst)	183 $^{+12}_{-11}$(stat) ±24(syst)	221
	$600-800$	50 ±4(stat) ±9(syst)	13 ±1(stat) ±2(syst)	0.03 ±0.01(stat) $^{+0.04}_{-0.03}$(syst)	63 ±4(stat) ±9(syst)	57
	$800-1000$	21 ±2(stat) ±5(syst)	4.2 ±0.4(stat) ±1.1(syst)	0.00 ±0.00(stat) $^{+0.01}_{-0.00}$(syst)	25 ±2(stat) ±5(syst)	19
	$1000-1200$	5.6 $^{+0.5}_{-0.4}$(stat) ±1.9(syst)	1.2 ±0.1(stat) ±0.6(syst)	< 0.01	6.8 $^{+0.5}_{-0.4}$(stat) ±2.0(syst)	6
	> 1200	0.7 ±0.1(stat) ±0.3(syst)	0.3 ±0.0(stat) ±0.3(syst)	< 0.01	1.0 ±0.1(stat) ±0.4(syst)	1
$4-6$j, 1b	$200-400$	156 $^{+28}_{-24}$(stat) ±17(syst)	188 $^{+10}_{-9}$(stat) ±16(syst)	100 ±2(stat) ±29(syst)	444 $^{+30}_{-26}$(stat) ±37(syst)	396
	$400-600$	36 $^{+6}_{-5}$(stat) ±6(syst)	25 $^{+4}_{-3}$(stat) ±4(syst)	1.1 ±0.1(stat) ±0.4(syst)	62 $^{+7}_{-6}$(stat) ±8(syst)	51
	$600-800$	14 ±2(stat) ±2(syst)	5.9 $^{+0.9}_{-0.8}$(stat) ±1.4(syst)	0.01 ±0.00(stat) $^{+0.02}_{-0.01}$(syst)	19 $^{+3}_{-2}$(stat) ±3(syst)	18
	$800-1000$	5.5 $^{+1.0}_{-0.9}$(stat) ±1.4(syst)	1.9 $^{+0.3}_{-0.2}$(stat) ±0.7(syst)	< 0.01	7.5 $^{+1.0}_{-0.9}$(stat) ±1.6(syst)	7
	$1000-1200$	1.5 $^{+0.3}_{-0.2}$(stat) ±0.5(syst)	0.1 ±0.0(stat) ±0.1(syst)	< 0.01	1.7 $^{+0.3}_{-0.2}$(stat) ±0.5(syst)	0
	> 1200	0.2 ±0.0(stat) ±0.1(syst)	0.3 ±0.0(stat) ±0.3(syst)	< 0.01	0.4 $^{+0.1}_{-0.0}$(stat) ±0.3(syst)	1
$4-6$j, 2b	$200-400$	42 $^{+17}_{-12}$(stat) ±8(syst)	65 ±5(stat) ±7(syst)	26 ±0(stat) ±10(syst)	133 $^{+18}_{-13}$(stat) ±15(syst)	128
	$400-600$	10 $^{+4}_{-3}$(stat) ±2(syst)	7.1 $^{+0.6}_{-0.5}$(stat) ±1.3(syst)	0.3 ±0.0(stat) ±0.1(syst)	17 $^{+4}_{-3}$(stat) ±3(syst)	16
	$600-800$	3.6 $^{+1.5}_{-1.1}$(stat) ±0.9(syst)	1.7 ±0.1(stat) ±0.5(syst)	< 0.01	5.3 $^{+1.5}_{-1.1}$(stat) ±1.1(syst)	5
	$800-1000$	1.5 $^{+0.6}_{-0.4}$(stat) ±0.5(syst)	0.6 $^{+0.1}_{-0.0}$(stat) ±0.3(syst)	< 0.01	2.1 $^{+0.6}_{-0.4}$(stat) ±0.6(syst)	2
	> 1000	0.5 $^{+0.2}_{-0.1}$(stat) ±0.2(syst)	0.2 ±0.0(stat) ±0.2(syst)	< 0.01	0.7 $^{+0.2}_{-0.1}$(stat) ±0.3(syst)	0
≥ 7j, 0b	$200-400$	83 $^{+24}_{-19}$(stat) ±21(syst)	80 $^{+8}_{-7}$(stat) ±9(syst)	49 ±1(stat) ±14(syst)	213 $^{+25}_{-20}$(stat) ±27(syst)	201
	$400-600$	19 $^{+5}_{-4}$(stat) ±5(syst)	10 ±1(stat) ±2(syst)	0.5 ±0.0(stat) ±0.2(syst)	29 $^{+5}_{-4}$(stat) ±5(syst)	19
	$600-800$	5.3 $^{+1.5}_{-1.2}$(stat) ±1.7(syst)	2.1 ±0.2(stat) ±0.6(syst)	< 0.01	7.4 $^{+1.5}_{-1.2}$(stat) ±1.8(syst)	6
	$800-1000$	1.1 ±0.3(stat) ±0.4(syst)	0.3 ±0.0(stat) ±0.2(syst)	< 0.01	1.4 ±0.3(stat) ±0.5(syst)	1
	> 1000	0.2 ±0.1(stat) ±0.1(syst)	0.03 ±0.00(stat) ±0.03(syst)	< 0.01	0.3 ±0.1(stat) ±0.1(syst)	0
≥ 7j, 1b	$200-400$	36 $^{+15}_{-11}$(stat) ±11(syst)	104 ±6(stat) ±10(syst)	32 ±1(stat) ±11(syst)	172 $^{+17}_{-13}$(stat) ±18(syst)	153
	$400-600$	8.0 $^{+3.4}_{-2.5}$(stat) ±2.6(syst)	12 ±1(stat) ±2(syst)	0.4 ±0.0(stat) ±0.2(syst)	20 ±3(stat) ±3(syst)	15
	$600-800$	2.3 $^{+1.0}_{-0.7}$(stat) ±0.9(syst)	1.4 ±0.1(stat) ±0.5(syst)	< 0.01	3.7 $^{+1.0}_{-0.7}$(stat) ±1.0(syst)	3
	> 800	0.6 ±0.2(stat) ±0.3(syst)	0.1 ±0.0(stat) ±0.1(syst)	< 0.01	0.7 ±0.2(stat) ±0.3(syst)	1
≥ 7j, 2b	$200-400$	9.4 $^{+4.0}_{-2.9}$(stat) ±2.9(syst)	74 ±4(stat) ±7(syst)	13 ±0(stat) ±6(syst)	97 $^{+6}_{-5}$(stat) ±10(syst)	84
	$400-600$	2.1 $^{+0.9}_{-0.7}$(stat) ±0.7(syst)	6.2 ±0.4(stat) ±1.2(syst)	0.1 ±0.0(stat) ±0.1(syst)	8.4 $^{+1.0}_{-0.7}$(stat) ±1.4(syst)	9
	$600-800$	0.6 $^{+0.3}_{-0.2}$(stat) ±0.2(syst)	0.8 ±0.0(stat) ±0.3(syst)	< 0.01	1.4 $^{+0.3}_{-0.2}$(stat) ±0.4(syst)	1
	> 800	0.2 $^{+0.1}_{-0.0}$(stat) ±0.1(syst)	0.3 ±0.0(stat) ±0.3(syst)	< 0.01	0.5 ±0.1(stat) ±0.3(syst)	1
$2-6$j, ≥ 3b	$200-400$	3.1 $^{+7.2}_{-2.6}$(stat) $^{+3.2}_{-3.1}$(syst)	14 ±3(stat) ±3(syst)	4.4 ±0.1(stat) ±3.2(syst)	22 $^{+8}_{-4}$(stat) ±6(syst)	26
	$400-600$	0.7 $^{+1.6}_{-0.6}$(stat) ±0.7(syst)	1.1 ±0.2(stat) ±0.4(syst)	0.05 ±0.00(stat) ±0.04(syst)	1.9 $^{+1.6}_{-0.6}$(stat) ±0.8(syst)	2
	> 600	0.3 $^{+0.8}_{-0.3}$(stat) $^{+0.5}_{-0.3}$(syst)	0.2 ±0.0(stat) ±0.1(syst)	< 0.01	0.6 $^{+0.8}_{-0.3}$(stat) ±0.5(syst)	0
≥ 7j, ≥ 3b	$200-400$	1.4 $^{+0.6}_{-0.4}$(stat) ±0.5(syst)	23 ±1(stat) ±3(syst)	3.1 ±0.1(stat) ±2.3(syst)	27 ±1(stat) ±4(syst)	26
	$400-600$	0.3 ±0.1(stat) ±0.1(syst)	2.3 ±0.1(stat) ±0.6(syst)	0.03 ±0.00(stat) ±0.03(syst)	2.6 ±0.2(stat) ±0.7(syst)	3
	> 600	0.1 ±0.0(stat) ±0.1(syst)	0.3 ±0.0(stat) ±0.3(syst)	< 0.01	0.5 $^{+0.1}_{-0.0}$(stat) ±0.3(syst)	1

Figure B.5: The results for the high H_{T} region: The first column lists the N_{jets} and $N_{\mathrm{b-tags}}$ requirements, followed by the M_{T2} bins, the estimates for the $Z \to \nu\nu$, lost lepton and QCD multijet background and finally the data. The uncertainties are given split into the statistical (stat.) and systematic (syst.) contributions.

$H_{\mathrm{T}} > 1500$ GeV						
$N_{\mathrm{j}}, N_{\mathrm{b}}$	M_{T2} [GeV]	$Z \to \nu\bar{\nu}$	Lost lepton	Multijet	Total background	Data
$2-3$j, 0b	$400-600$	$31\,^{+7}_{-6}$(stat) ±7(syst)	$7.0\,^{+0.8}_{-0.7}$(stat) ±1.5(syst)	0.3 ± 0.0(stat) ±0.2(syst)	$39\,^{+7}_{-6}$(stat) ±8(syst)	35
	$600-800$	$12\,^{+3}_{-2}$(stat) ±3(syst)	$2.2\,^{+0.3}_{-0.2}$(stat) ±0.8(syst)	0.02 ± 0.01(stat) ±0.01(syst)	$14\,^{+3}_{-2}$(stat) ±3(syst)	8
	$800-1000$	$5.1\,^{+1.1}_{-0.9}$(stat) ±1.5(syst)	0.6 ± 0.1(stat) ±0.4(syst)	< 0.01	$5.7\,^{+1.1}_{-0.9}$(stat) ±1.5(syst)	4
	$1000-1400$	$4.0\,^{+0.9}_{-0.7}$(stat) ±1.5(syst)	1.2 ± 0.1(stat) ±0.6(syst)	< 0.01	$5.2\,^{+0.9}_{-0.8}$(stat) ±1.6(syst)	3
	> 1400	1.0 ± 0.2(stat) ±0.5(syst)	0.4 ± 0.0(stat) ±0.3(syst)	< 0.01	1.4 ± 0.2(stat) ±0.6(syst)	2
$2-3$j, 1b	$400-600$	$8.2\,^{+4.1}_{-2.8}$(stat) ±2.9(syst)	$1.8\,^{+0.5}_{-0.4}$(stat) ±0.8(syst)	0.1 ± 0.0(stat) ±0.1(syst)	$10\,^{+4}_{-3}$(stat) ±3(syst)	2
	$600-800$	$3.1\,^{+1.5}_{-1.1}$(stat) ±1.0(syst)	0.3 ± 0.1(stat) ±0.3(syst)	< 0.01	$3.4\,^{+1.5}_{-1.1}$(stat) ±1.1(syst)	2
	$800-1000$	$1.3\,^{+0.7}_{-0.5}$(stat) ±0.5(syst)	0.2 ± 0.1(stat) ±0.2(syst)	< 0.01	$1.6\,^{+0.7}_{-0.5}$(stat) ±0.6(syst)	0
	> 1000	$1.4\,^{+0.7}_{-0.5}$(stat) ±0.7(syst)	$0.2\,^{+0.1}_{-0.0}$(stat) ±0.2(syst)	< 0.01	$1.6\,^{+0.7}_{-0.5}$(stat) ±0.7(syst)	2
$2-3$j, 2b	> 400	$0.0\,^{+2.0}_{-0.0}$(stat) ±0.0(syst)	$0.0\,^{+0.7}_{-0.0}$(stat) ±0.0(syst)	0.02 ± 0.00(stat) ±0.01(syst)	$0.0\,^{+2.1}_{-0.0}$(stat) ±0.0(syst)	1
$4-6$j, 0b	$400-600$	$32\,^{+7}_{-6}$(stat) ±7(syst)	$7.2\,^{+1.8}_{-1.5}$(stat) ±1.9(syst)	$2.9\,^{+0.4}_{-0.3}$(stat) ±1.2(syst)	$42\,^{+7}_{-6}$(stat) ±8(syst)	47
	$600-800$	$12\,^{+3}_{-2}$(stat) ±3(syst)	$1.2\,^{+0.3}_{-0.2}$(stat) ±0.4(syst)	0.2 ± 0.1(stat) ±0.1(syst)	$13\,^{+3}_{-2}$(stat) ±3(syst)	17
	$800-1000$	$5.2\,^{+1.1}_{-1.0}$(stat) ±1.5(syst)	$1.2\,^{+0.3}_{-0.2}$(stat) ±0.5(syst)	$0.02\,^{+0.02}_{-0.01}$(stat) $^{+0.03}_{-0.02}$(syst)	$6.4\,^{+1.2}_{-1.0}$(stat) ±1.5(syst)	6
	$1000-1400$	$4.1\,^{+0.9}_{-0.7}$(stat) ±1.5(syst)	$0.2\,^{+0.1}_{-0.0}$(stat) ±0.2(syst)	$0.01\,^{+0.02}_{-0.01}$(stat) $^{+0.02}_{-0.01}$(syst)	$4.4\,^{+0.9}_{-0.7}$(stat) ±1.5(syst)	8
	> 1400	1.0 ± 0.2(stat) ±0.5(syst)	0.1 ± 0.0(stat) ±0.1(syst)	< 0.01	1.2 ± 0.2(stat) ±0.5(syst)	1
$4-6$j, 1b	$400-600$	$16\,^{+5}_{-4}$(stat) ±4(syst)	$4.5\,^{+0.6}_{-0.5}$(stat) ±1.1(syst)	1.5 ± 0.2(stat) ±0.7(syst)	$22\,^{+5}_{-4}$(stat) ±4(syst)	18
	$600-800$	$6.0\,^{+2.1}_{-1.6}$(stat) ±1.5(syst)	1.0 ± 0.1(stat) ±0.4(syst)	0.1 ± 0.0(stat) ±0.1(syst)	$7.1\,^{+2.1}_{-1.6}$(stat) ±1.6(syst)	8
	$800-1000$	$2.6\,^{+0.9}_{-0.7}$(stat) ±0.8(syst)	0.2 ± 0.0(stat) ±0.2(syst)	$0.01\,^{+0.01}_{-0.00}$(stat) ±0.01(syst)	$2.8\,^{+0.9}_{-0.7}$(stat) ±0.8(syst)	3
	$1000-1400$	$2.0\,^{+0.7}_{-0.5}$(stat) ±0.8(syst)	0.2 ± 0.0(stat) ±0.2(syst)	$0.01\,^{+0.01}_{-0.00}$(stat) ±0.01(syst)	$2.3\,^{+0.7}_{-0.5}$(stat) ±0.8(syst)	0
	> 1400	$0.5\,^{+0.2}_{-0.1}$(stat) ±0.2(syst)	< 0.01	< 0.01	$0.5\,^{+0.2}_{-0.1}$(stat) ±0.2(syst)	1
$4-6$j, 2b	$400-600$	$3.4\,^{+2.7}_{-1.6}$(stat) ±1.8(syst)	2.4 ± 0.4(stat) ±0.8(syst)	$0.4\,^{+0.1}_{-0.0}$(stat) ±0.2(syst)	$6.3\,^{+2.8}_{-1.7}$(stat) ±1.9(syst)	5
	$600-800$	$1.3\,^{+1.0}_{-0.6}$(stat) ±0.7(syst)	0.5 ± 0.1(stat) ±0.3(syst)	0.03 ± 0.01(stat) ±0.02(syst)	$1.8\,^{+1.0}_{-0.6}$(stat) ±0.7(syst)	1
	> 800	$1.1\,^{+0.9}_{-0.5}$(stat) ±0.7(syst)	0.6 ± 0.1(stat) ±0.5(syst)	< 0.01	$1.8\,^{+0.9}_{-0.5}$(stat) ±0.8(syst)	0
≥ 7j, 0b	$400-600$	$5.4\,^{+3.7}_{-2.3}$(stat) ±2.4(syst)	$4.8\,^{+0.8}_{-0.7}$(stat) ±1.3(syst)	$1.2\,^{+0.2}_{-0.1}$(stat) ±0.5(syst)	$11\,^{+4}_{-2}$(stat) ±3(syst)	4
	$600-800$	$2.0\,^{+1.4}_{-0.9}$(stat) ±0.9(syst)	1.4 ± 0.2(stat) ±0.6(syst)	0.1 ± 0.0(stat) ±0.1(syst)	$3.5\,^{+1.4}_{-0.9}$(stat) ±1.1(syst)	3
	$800-1000$	$0.9\,^{+0.6}_{-0.4}$(stat) ±0.4(syst)	0.03 ± 0.00(stat) ±0.01(syst)	$0.01\,^{+0.01}_{-0.00}$(stat) ±0.01(syst)	$0.9\,^{+0.6}_{-0.4}$(stat) ±0.4(syst)	1
	> 1000	$0.9\,^{+0.6}_{-0.4}$(stat) ±0.5(syst)	0.01 ± 0.00(stat) ±0.01(syst)	< 0.01	$0.9\,^{+0.6}_{-0.4}$(stat) ±0.5(syst)	2
≥ 7j, 1b	$400-600$	$1.8\,^{+1.7}_{-1.0}$(stat) ±1.2(syst)	3.6 ± 0.4(stat) ±0.9(syst)	0.8 ± 0.1(stat) ±0.4(syst)	$6.1\,^{+1.8}_{-1.0}$(stat) ±1.6(syst)	7
	$600-800$	$0.7\,^{+0.6}_{-0.4}$(stat) ±0.4(syst)	1.0 ± 0.1(stat) ±0.5(syst)	0.1 ± 0.0(stat) ±0.0(syst)	$1.7\,^{+0.7}_{-0.4}$(stat) ±0.7(syst)	4
	> 800	$0.6\,^{+0.6}_{-0.3}$(stat) ±0.4(syst)	0.6 ± 0.1(stat) ±0.4(syst)	< 0.01	$1.2\,^{+0.6}_{-0.3}$(stat) ±0.6(syst)	2
≥ 7j, 2b	$400-600$	$0.5\,^{+0.5}_{-0.3}$(stat) ±0.3(syst)	$2.1\,^{+0.3}_{-0.2}$(stat) ±0.5(syst)	0.3 ± 0.0(stat) ±0.2(syst)	$2.9\,^{+0.5}_{-0.4}$(stat) ±0.7(syst)	8
	$600-800$	$0.2\,^{+0.2}_{-0.1}$(stat) ±0.1(syst)	0.8 ± 0.1(stat) ±0.4(syst)	0.02 ± 0.01(stat) ±0.02(syst)	$1.0\,^{+0.2}_{-0.1}$(stat) ±0.4(syst)	2
	> 800	$0.2\,^{+0.2}_{-0.1}$(stat) ±0.1(syst)	0.01 ± 0.00(stat) ±0.01(syst)	< 0.01	$0.2\,^{+0.2}_{-0.1}$(stat) ±0.1(syst)	0
$2-6$j, ≥ 3b	$400-600$	$1.3\,^{+3.1}_{-1.1}$(stat) $^{+1.5}_{-1.3}$(syst)	$0.3\,^{+0.2}_{-0.1}$(stat) ±0.2(syst)	0.1 ± 0.0(stat) ±0.1(syst)	$1.7\,^{+3.1}_{-1.1}$(stat) ±1.5(syst)	2
	> 600	$0.9\,^{+2.2}_{-0.8}$(stat) $^{+1.1}_{-0.9}$(syst)	0.01 ± 0.01(stat) ±0.01(syst)	< 0.01	$1.0\,^{+2.2}_{-0.8}$(stat) $^{+1.1}_{-1.0}$(syst)	1
≥ 7j, ≥ 3b	> 400	$0.2\,^{+0.2}_{-0.1}$(stat) ±0.2(syst)	0.7 ± 0.1(stat) ±0.4(syst)	0.1 ± 0.0(stat) ±0.1(syst)	$1.0\,^{+0.2}_{-0.1}$(stat) ±0.4(syst)	1

Figure B.6: The results for the ultra high H_{T} region: The first column lists the N_{jets} and $N_{\mathrm{b-tags}}$ requirements, followed by the M_{T2} bins, the estimates for the $Z \to \nu\nu$, lost lepton and QCD multijet background and finally the data. The uncertainties are given split into the statistical (stat.) and systematic (syst.) contributions.

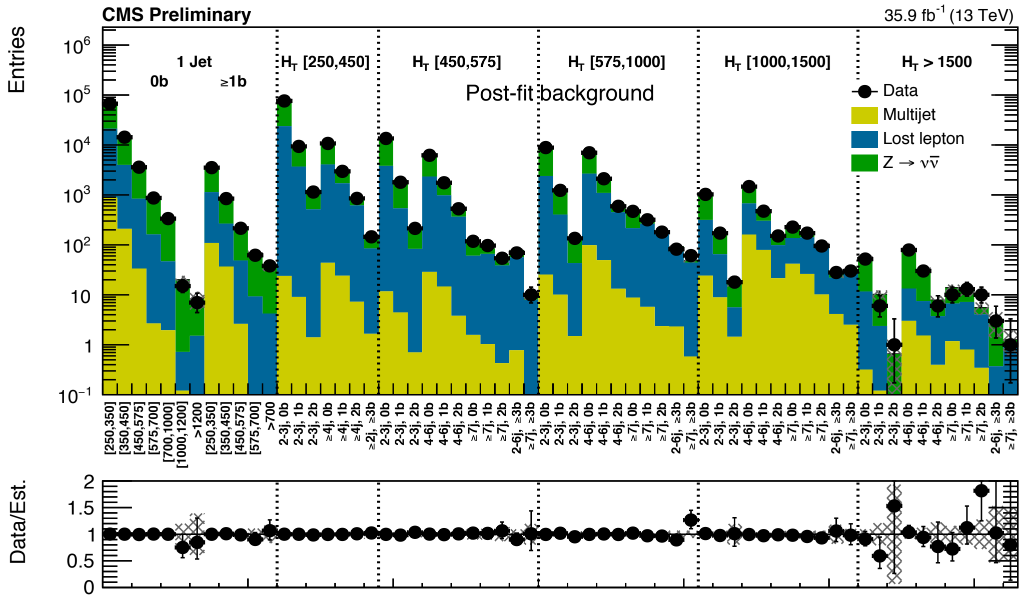

Figure B.7: The data are compared to the background estimates for all of the kinematic bins, for $N_{\text{jets}} = 0$ each of the jet p_T bins is show, while for the multijet regions, the bins are integrated along the M_{T2} dimension. The N_{jets} and $N_{\text{b-tags}}$ bins are indicated by the labels j and b, respectively. The hatched band corresponds to the full uncertainty.

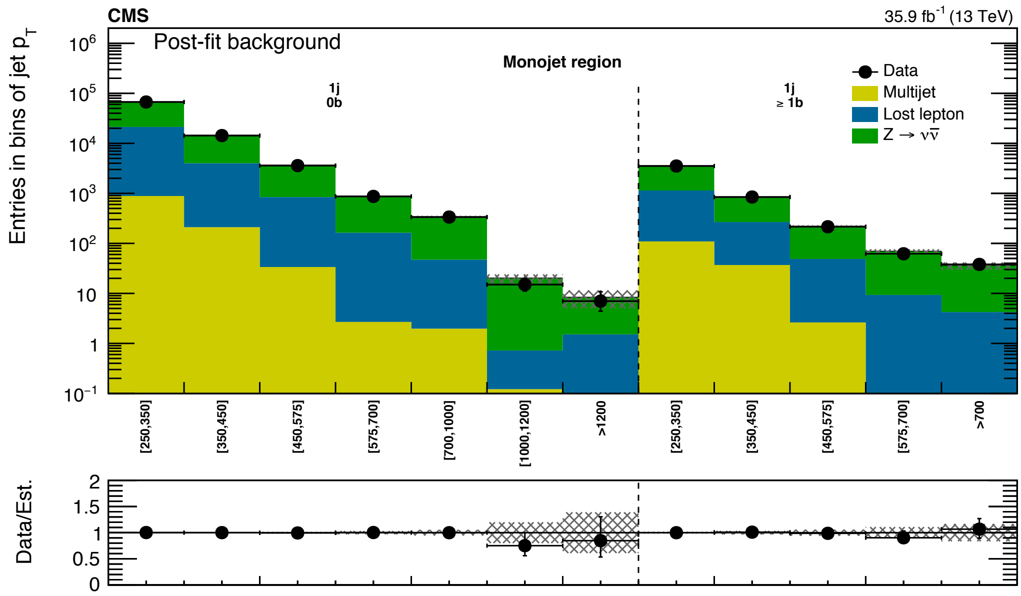

Figure B.8: The data are compared to the background estimates post-fit for the monojet region. The N_{jets} and $N_{\text{b-tags}}$ bins are indicated by the labels j and b, respectively. The hatched band corresponds to the full uncertainty.

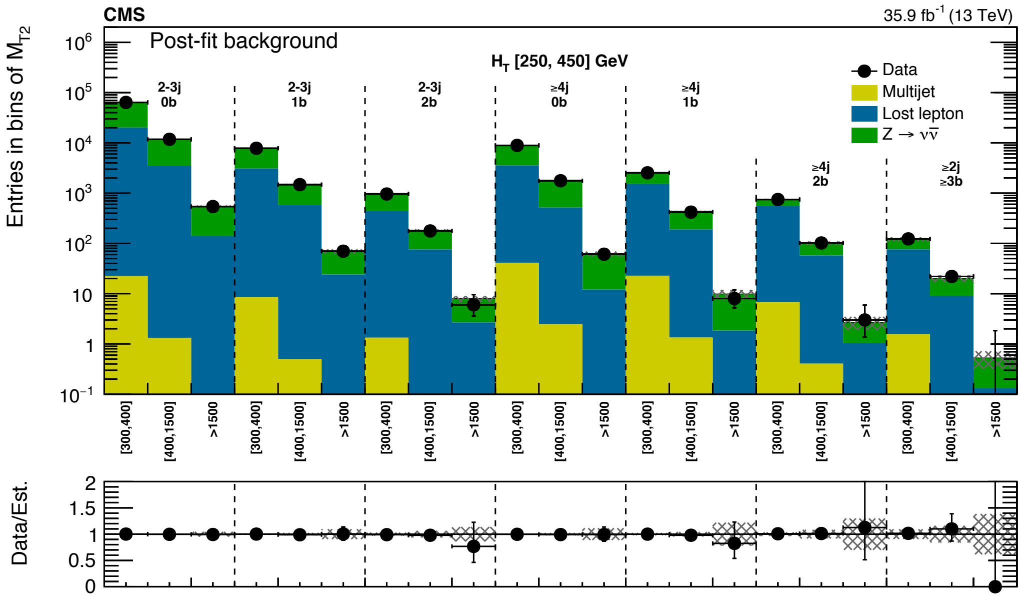

Figure B.9: The data are compared to the background estimates post-fit for the $250 < H_{\mathrm{T}} < 450\,\mathrm{GeV}$ region. The N_{jets} and $N_{\mathrm{b-tags}}$ bins are indicated by the labels j and b, respectively. The hatched band corresponds to the full uncertainty.

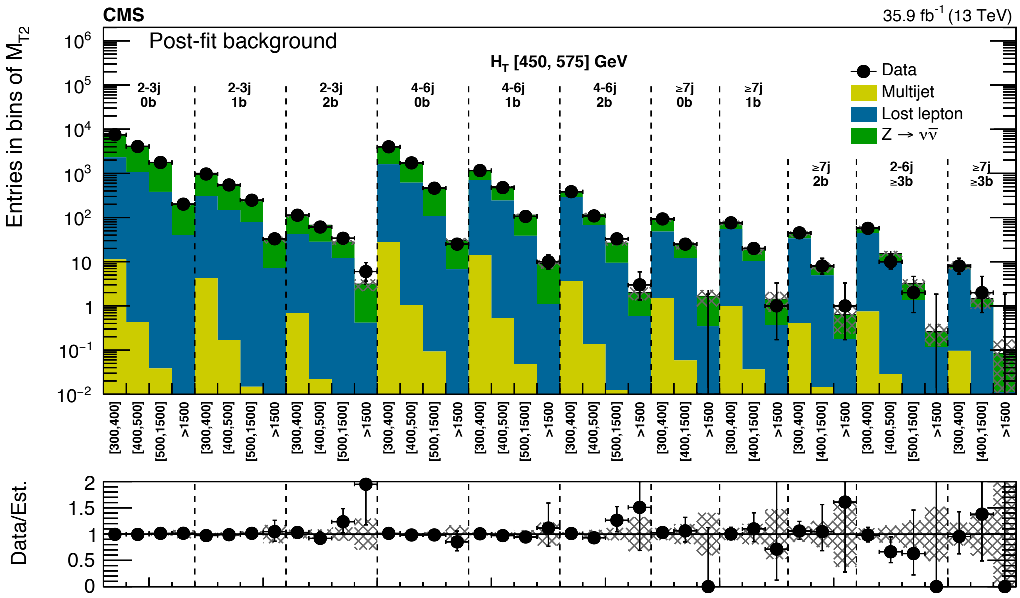

Figure B.10: The data are compared to the background estimates post-fit for the $450 < H_{\mathrm{T}} < 575\,\mathrm{GeV}$ region. The N_{jets} and $N_{\mathrm{b-tags}}$ bins are indicated by the labels j and b, respectively. The hatched band corresponds to the full uncertainty.

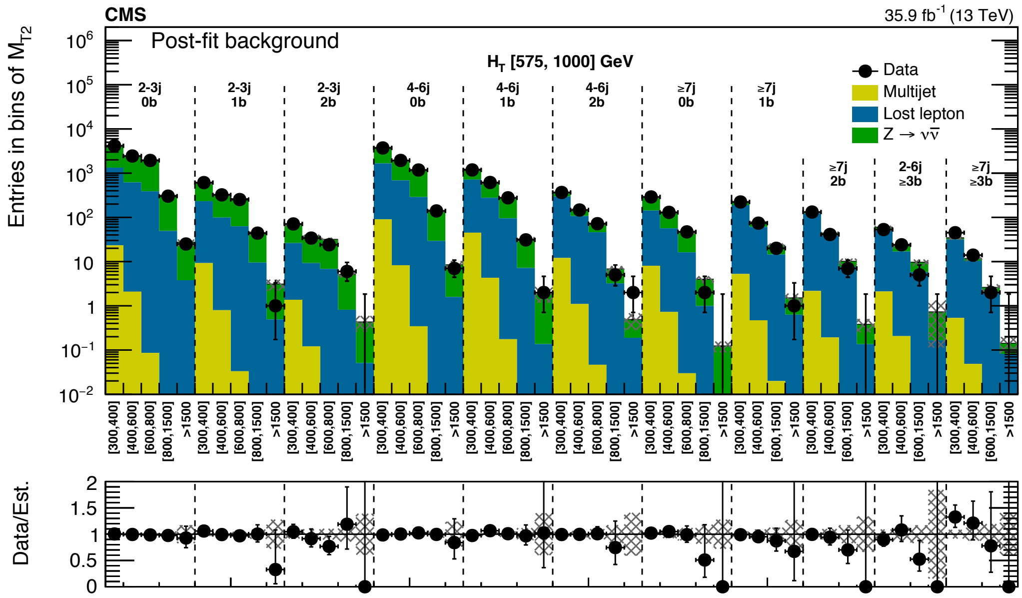

Figure B.11: The data are compared to the background estimates post-fit for the $575 < H_\mathrm{T} < 1000$ GeV region. The N_jets and $N_\mathrm{b-tags}$ bins are indicated by the labels j and b, respectively. The hatched band corresponds to the full uncertainty.

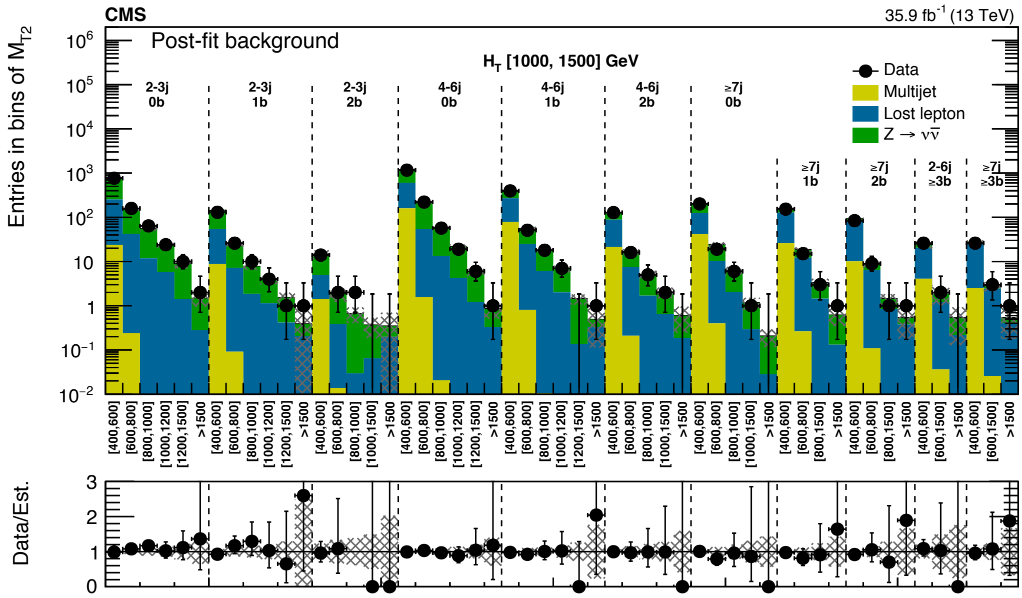

Figure B.12: The data are compared to the background estimates post-fit for the $1000 < H_\mathrm{T} < 1500$ GeV region. The N_jets and $N_\mathrm{b-tags}$ bins are indicated by the labels j and b, respectively. The hatched band corresponds to the full uncertainty.

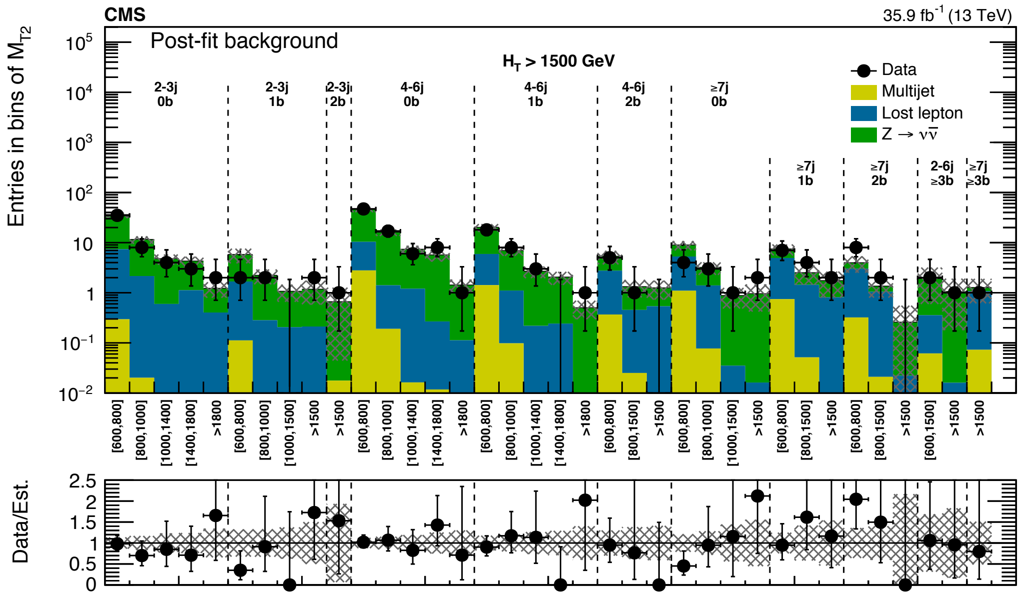

Figure B.13: The data are compared to the background estimates post-fit for the $H_{\mathrm{T}} > 1500\,\mathrm{GeV}$ region. The N_{jets} and $N_{\mathrm{b-tags}}$ bins are indicated by the labels j and b, respectively. The hatched band corresponds to the full uncertainty.

B.2 Event display

Figure B.14 shows an event, with $M_{\mathrm{T2}} = 404\,\mathrm{GeV}$, $H_{\mathrm{T}} = 2066\,\mathrm{GeV}$, $E_{\mathrm{T}}^{\mathrm{miss}} = 541\,\mathrm{GeV}$, $N_{\mathrm{jets}} = 6$ and $N_{\mathrm{b-tags}} = 2$, passing the analysis selection.

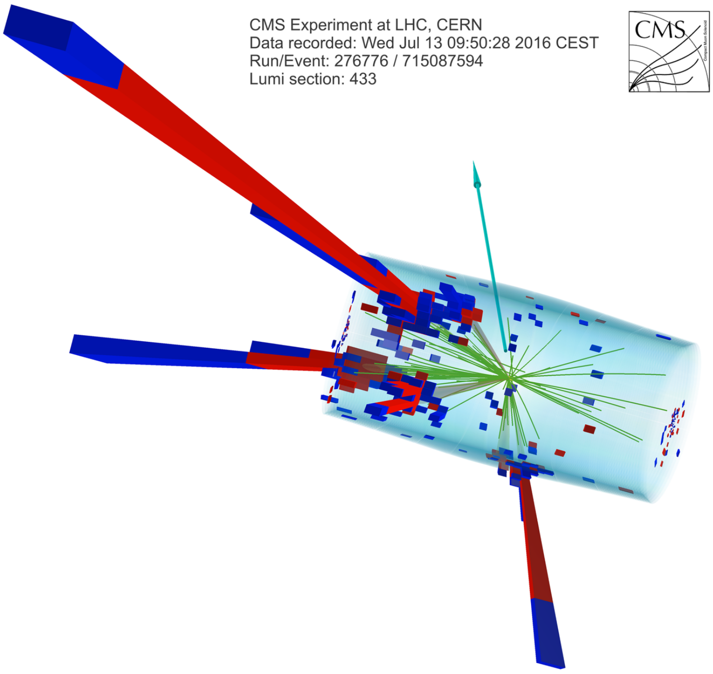

Figure B.14: Event showing a candidate event with $M_{\mathrm{T2}} = 404\,\mathrm{GeV}$, $H_{\mathrm{T}} = 2066\,\mathrm{GeV}$, $E_{\mathrm{T}}^{\mathrm{miss}} = 541\,\mathrm{GeV}$, $N_{\mathrm{jets}} = 6$ and $N_{\mathrm{b-tags}} = 2$ [121].

C Additional material of the search for SUSY in the diphoton final state

C.1 Distribution of the kinematic variables

Figure C.1 shows the simulation of the backgrounds at 41.5 fb^{-1} overlayed with the benchmarks signal points indicated on the figures. The distributions of M_{T2}, $p_T^{H\gamma\gamma}/M_{\gamma\gamma}$, N_{jets} and $N_{\mathrm{b-tags}}$ are shown after applying the baseline selection.

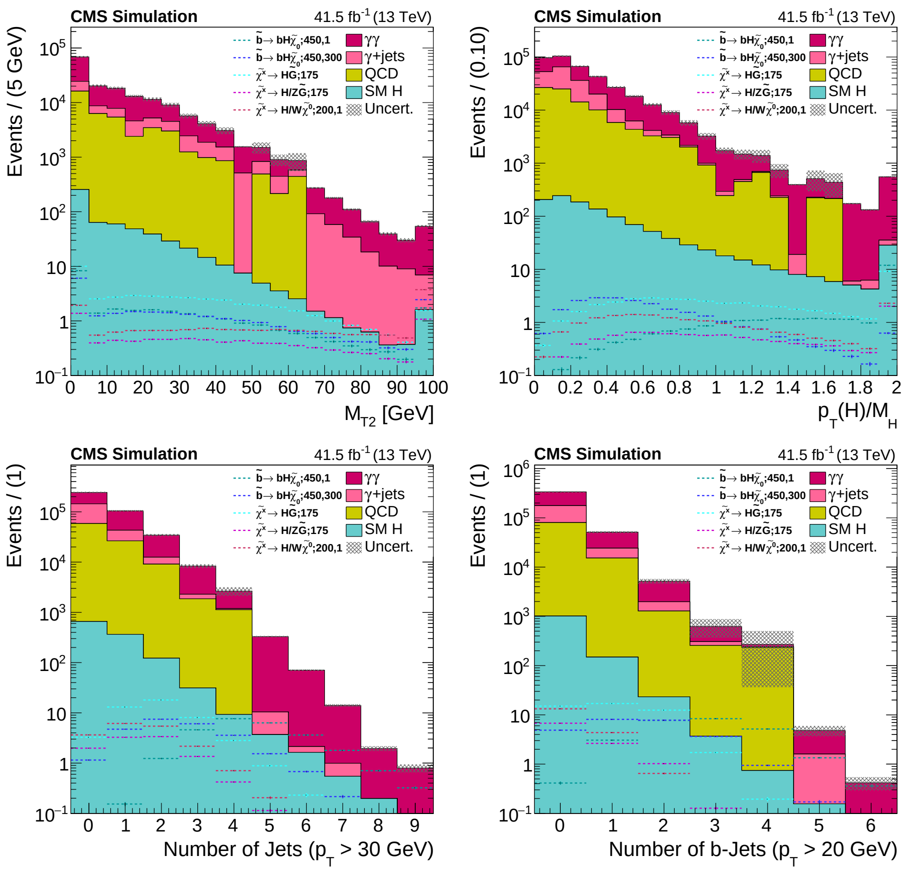

Figure C.1: The 2017 simulation of the backgrounds and the signal after the baseline selection as a function of M_{T2} (top left), $p_T^{H\gamma\gamma}/M_{\gamma\gamma}$ (top right), N_{jets} (bottom left) and $N_{\mathrm{b-tags}}$ (bottom right). The nonresonant background of diphoton (magenta), γ+jets (pink) and QCD multijet (yellow) production and the resonant SM Higgs samples (cyan) are stacked and shown with the statistical uncertainty (grey hash) while the signals are overlayed as dashed lines.

C.2 Nonresonant background fits

Tables C.2 to C.12 show the data and the fits to the nonresonant background as described in Section 8.3.1 in all the search regions.

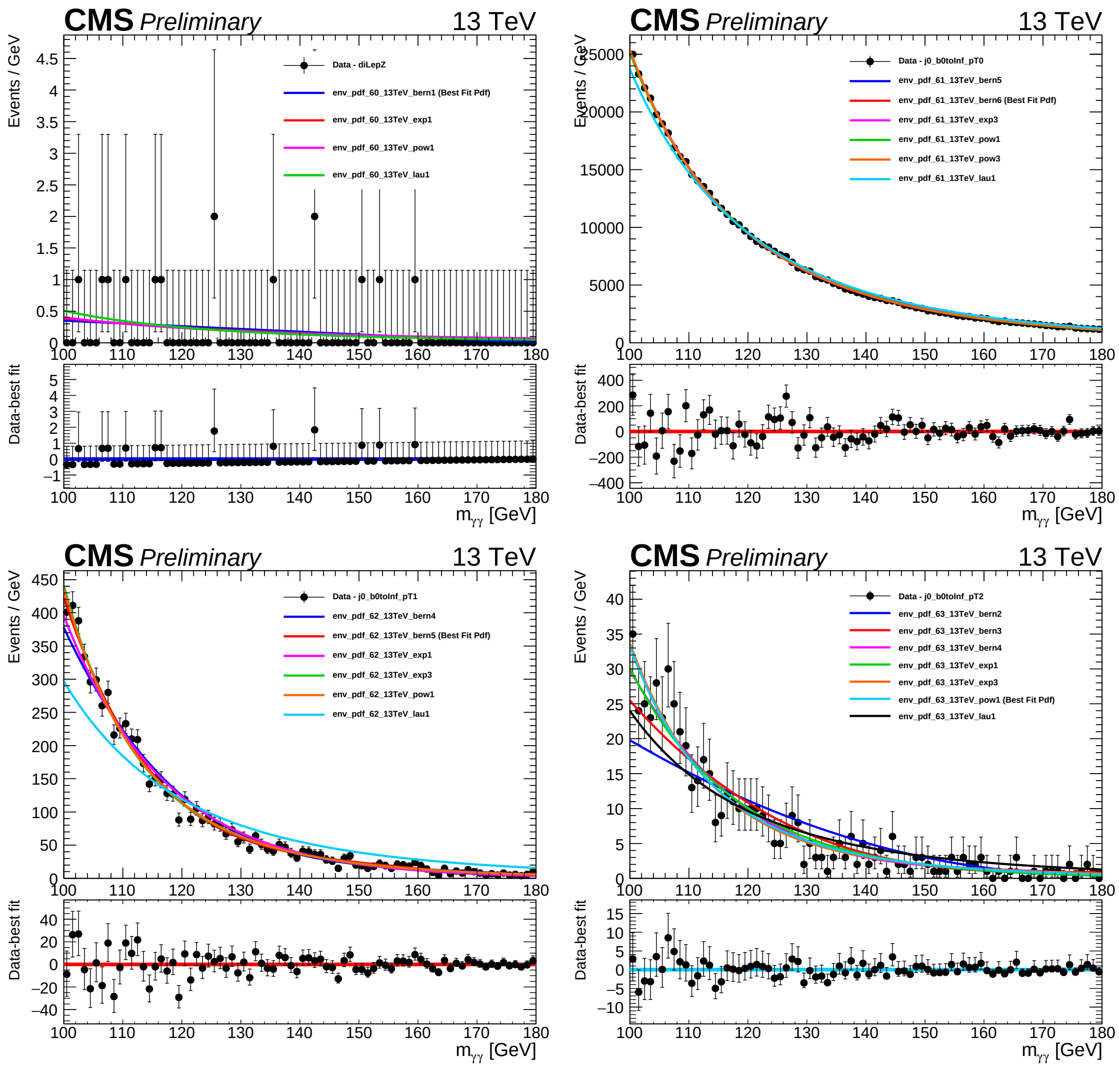

Figure C.2: The data (black marker) and the fits to the nonresonant background (lines) for the $Z \to l^+l^-$ and the zero jet regions. The different colored lines represent the functions that the envelope of the region consists of.

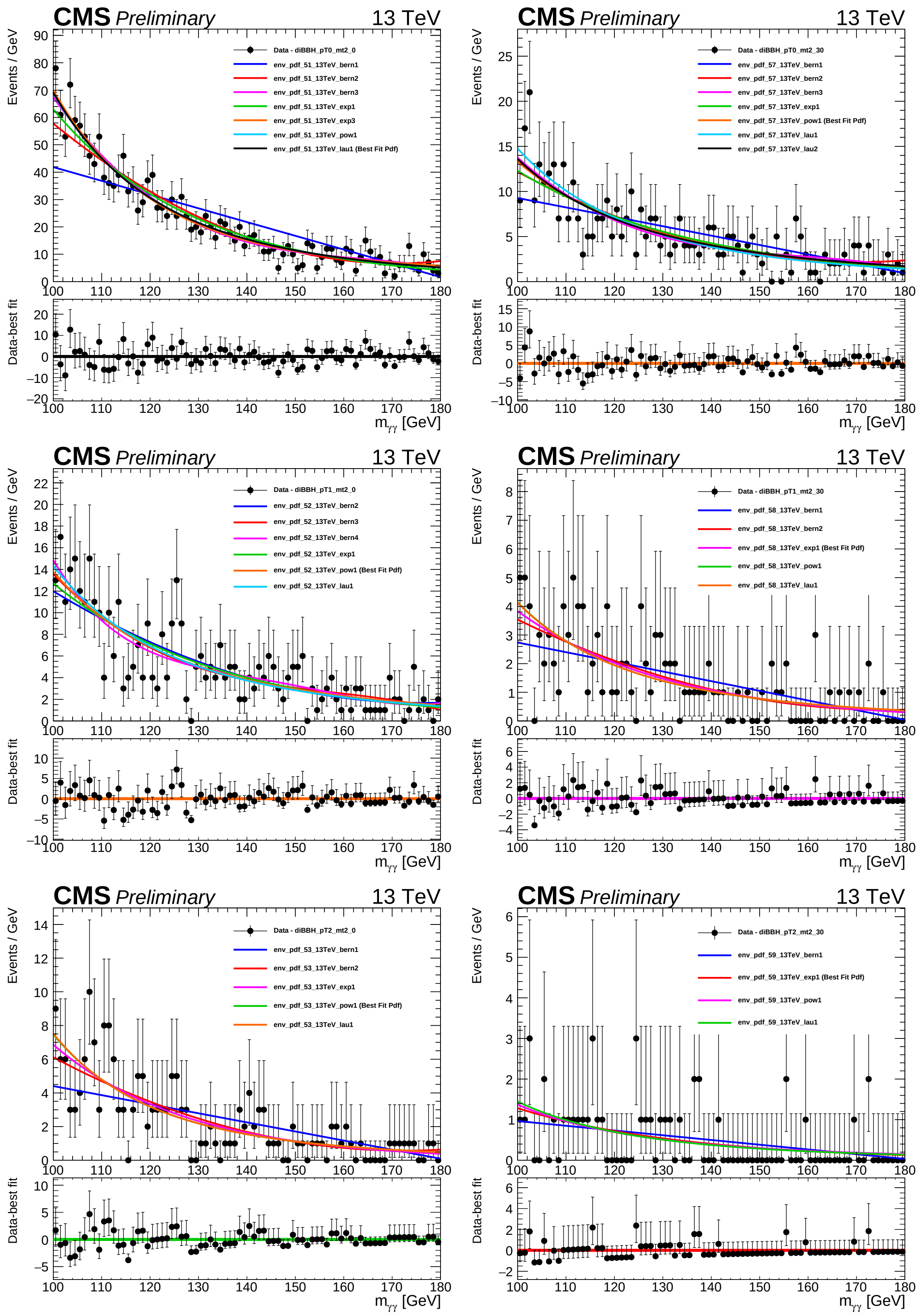

Figure C.3: The data (black marker) and the fits to the nonresonant background (lines) for the $H \to bb$ regions. The different colored lines represent the functions that the envelope of the region consists of.

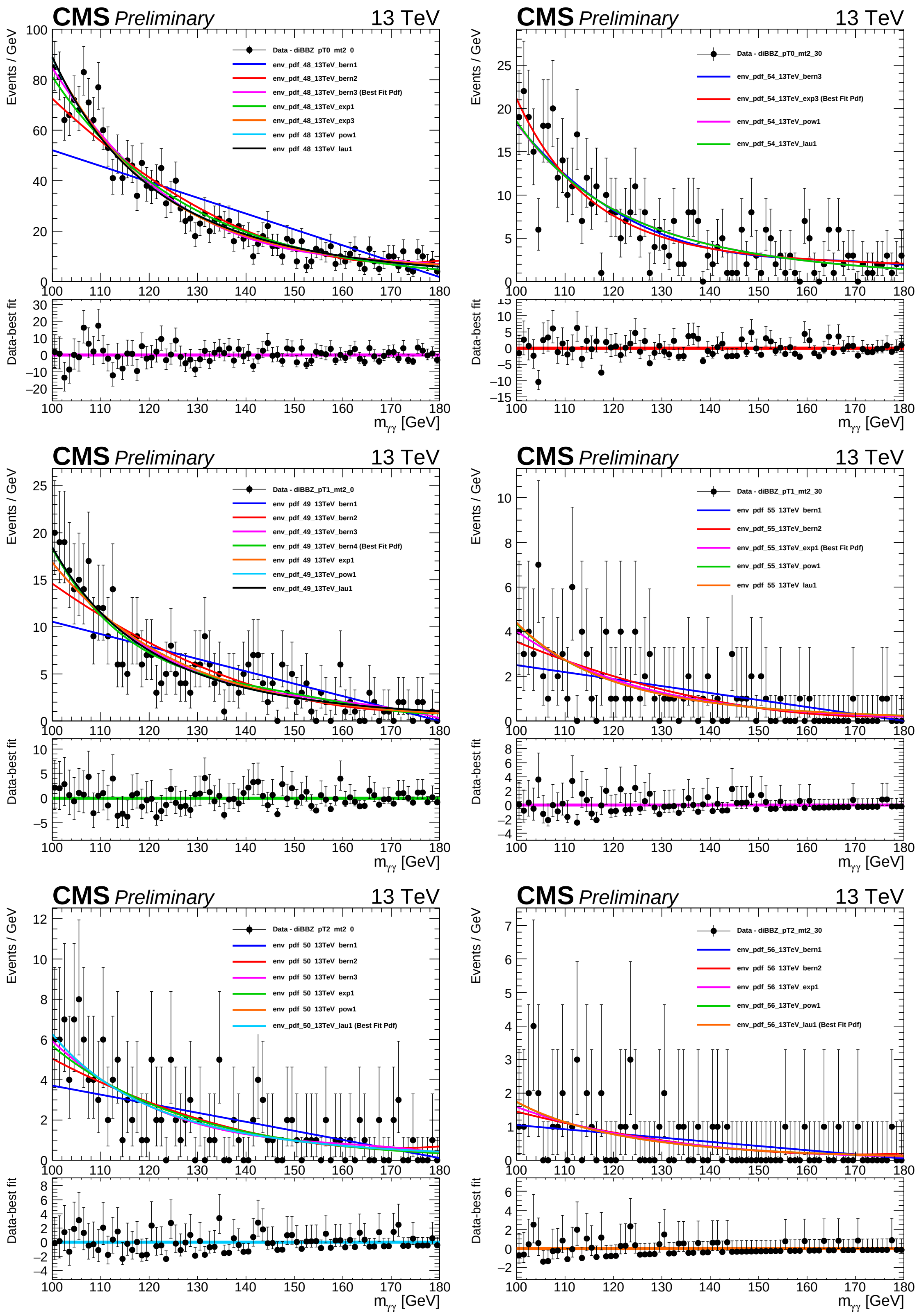

Figure C.4: The data (black marker) and the fits to the nonresonant background (lines) for the $Z \to bb$ regions. The different colored lines represent the functions that the envelope of the region consists of.

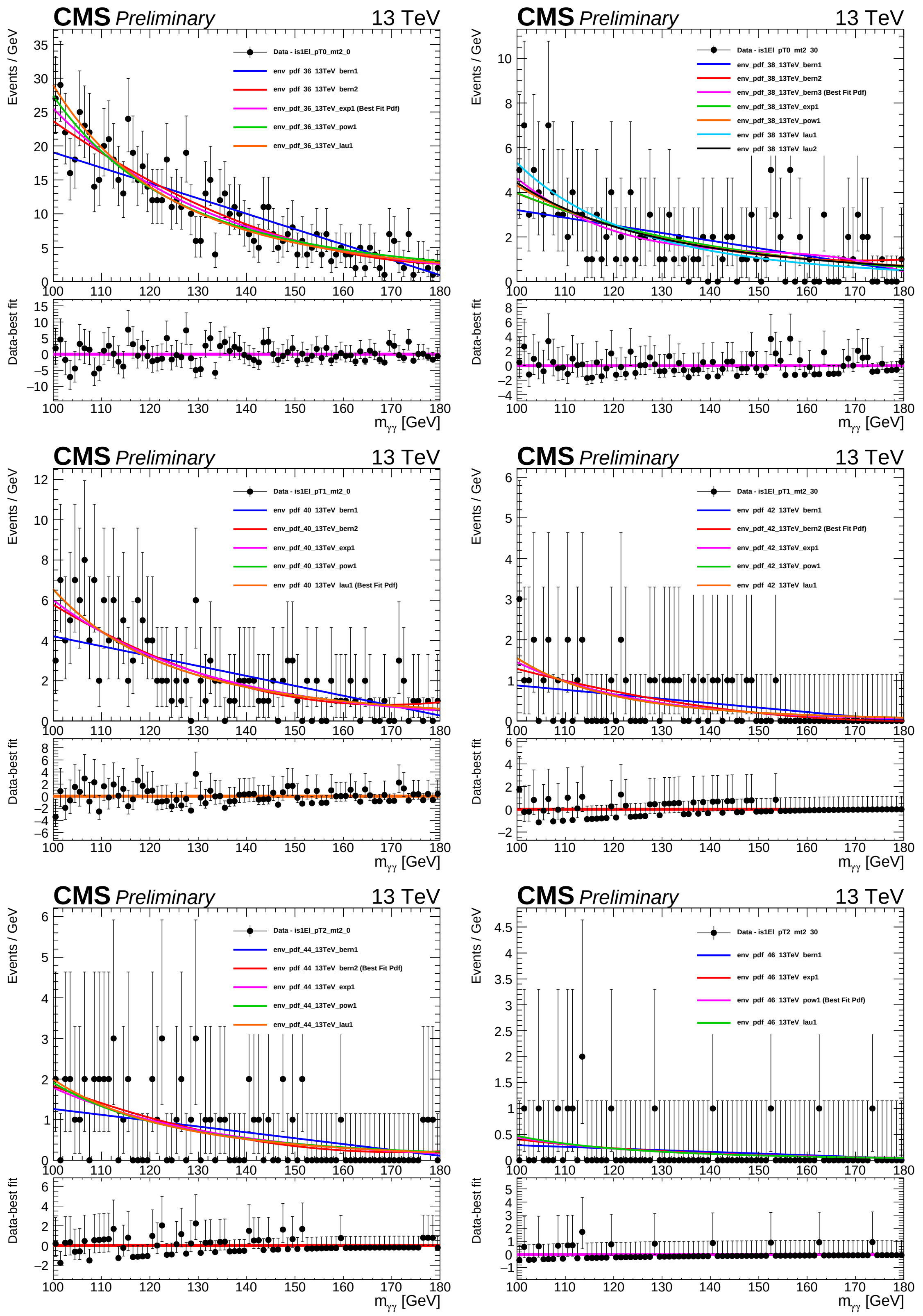

Figure C.5: The data (black marker) and the fits to the nonresonant background (lines) for the single electron regions. The different colored lines represent the functions that the envelope of the region consists of.

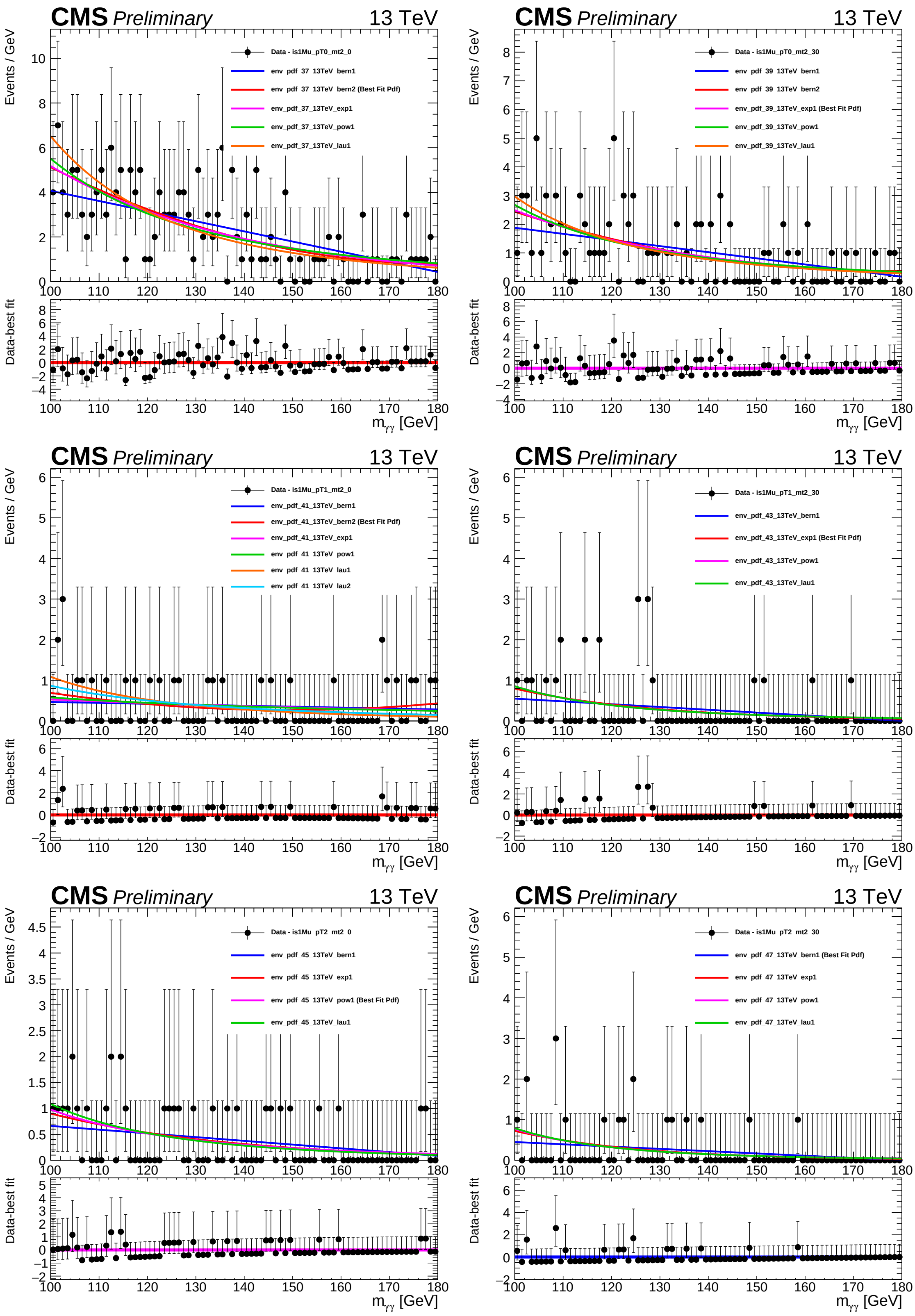

Figure C.6: The data (black marker) and the fits to the nonresonant background (lines) for the single muon regions. The different colored lines represent the functions that the envelope of the region consists of.

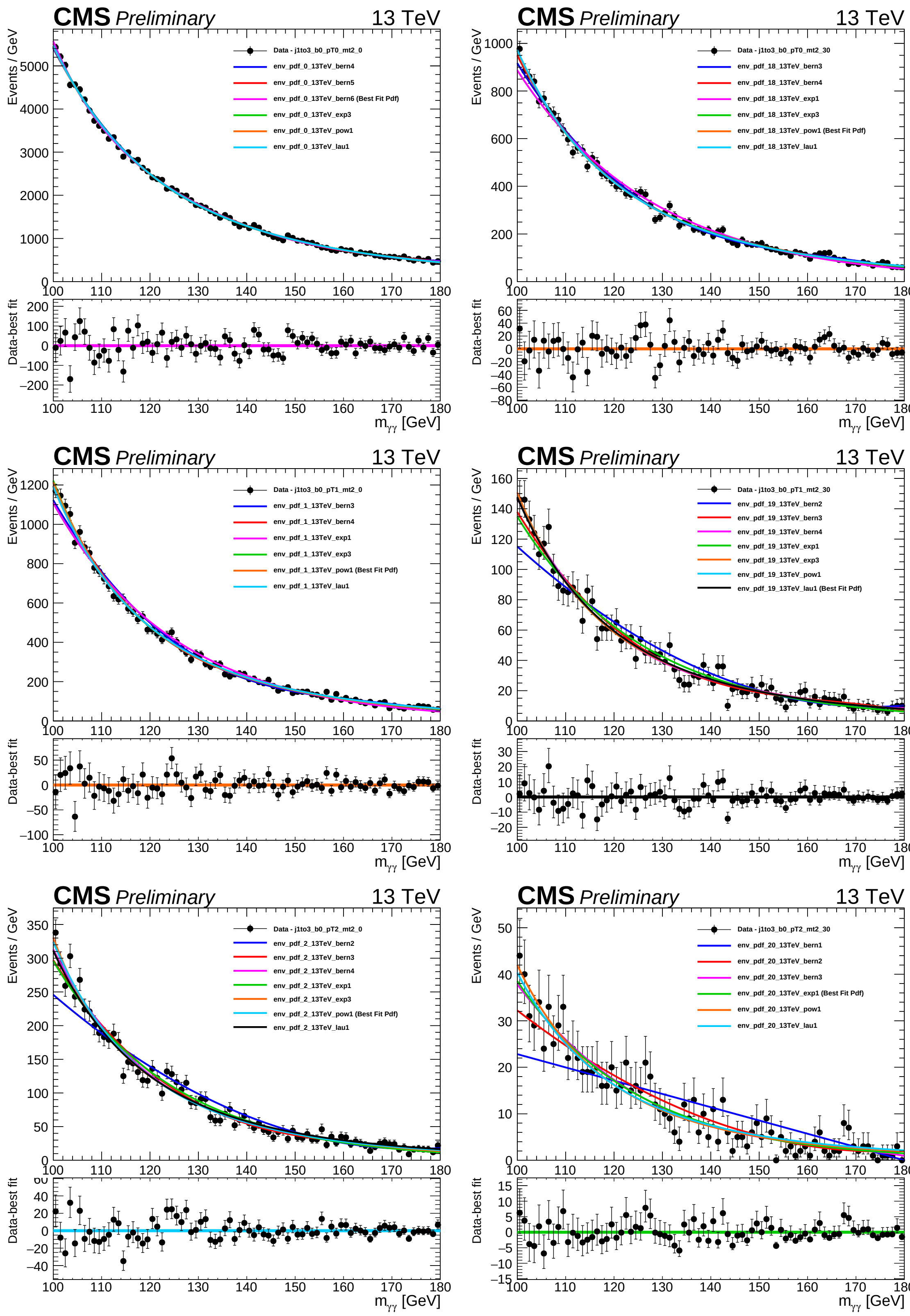

Figure C.7: The data (black marker) and the fits to the nonresonant background (lines) for the 1-3 jets and 0 b-tagged jet regions. The different colored lines represent the functions that the envelope of the region consists of.

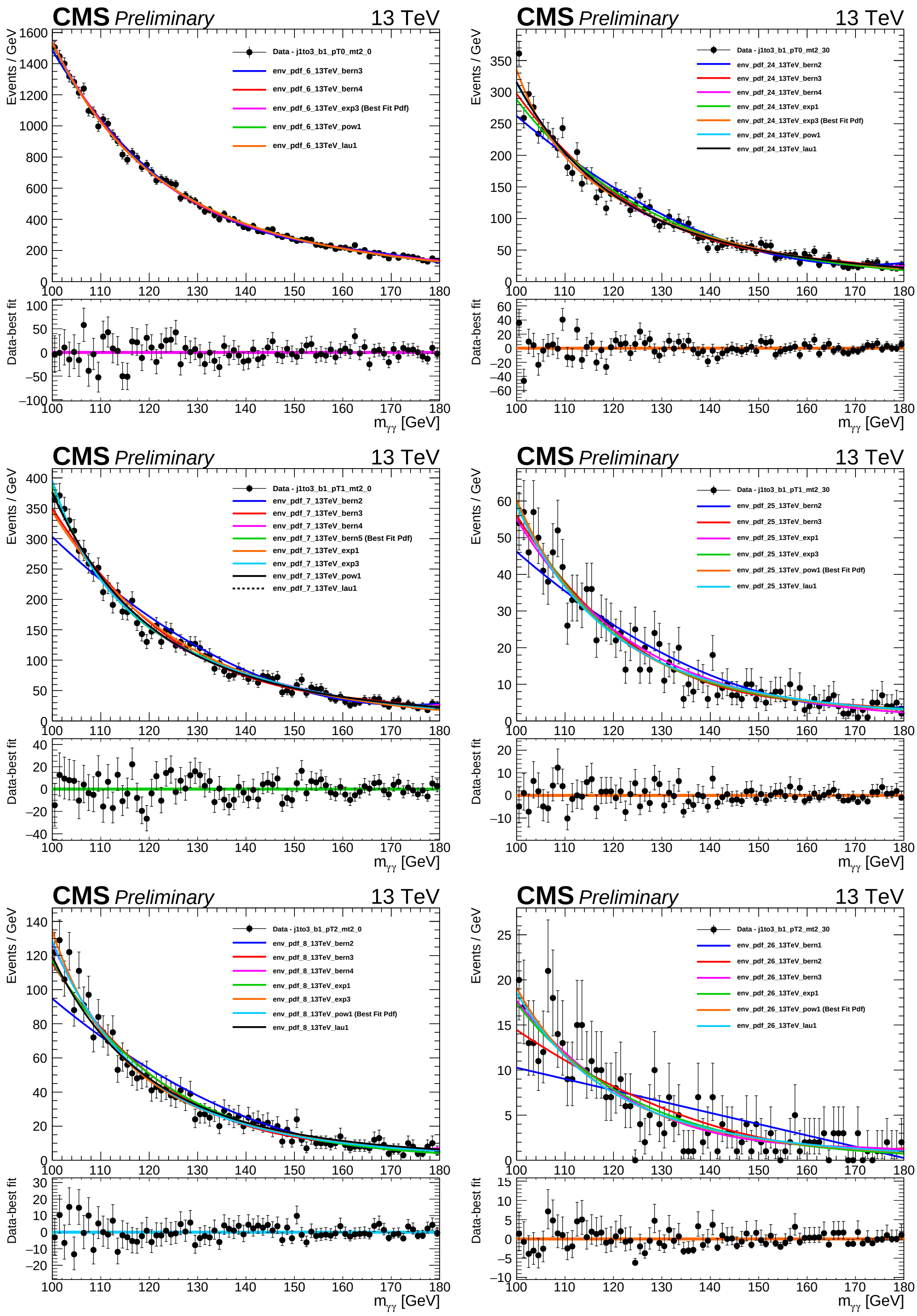

Figure C.8: The data (black marker) and the fits to the nonresonant background (lines) for the 1-3 jets and 1 b-tagged jets regions. The different colored lines represent the functions that the envelope of the region consists of.

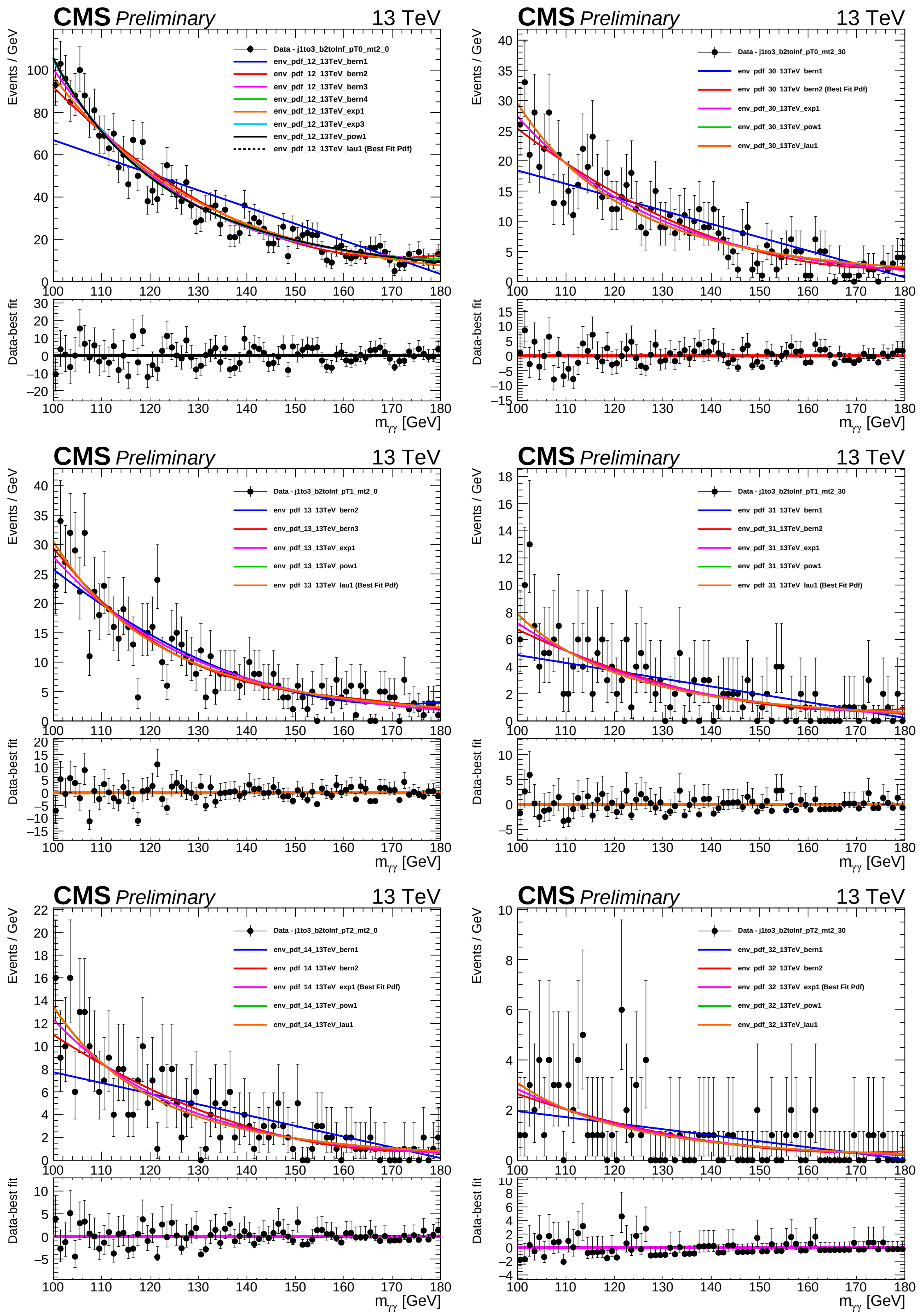

Figure C.9: The data (black marker) and the fits to the nonresonant background (lines) for the 1-3 jets and at least 2 b-tagged jets regions. The different colored lines represent the functions that the envelope of the region consists of.

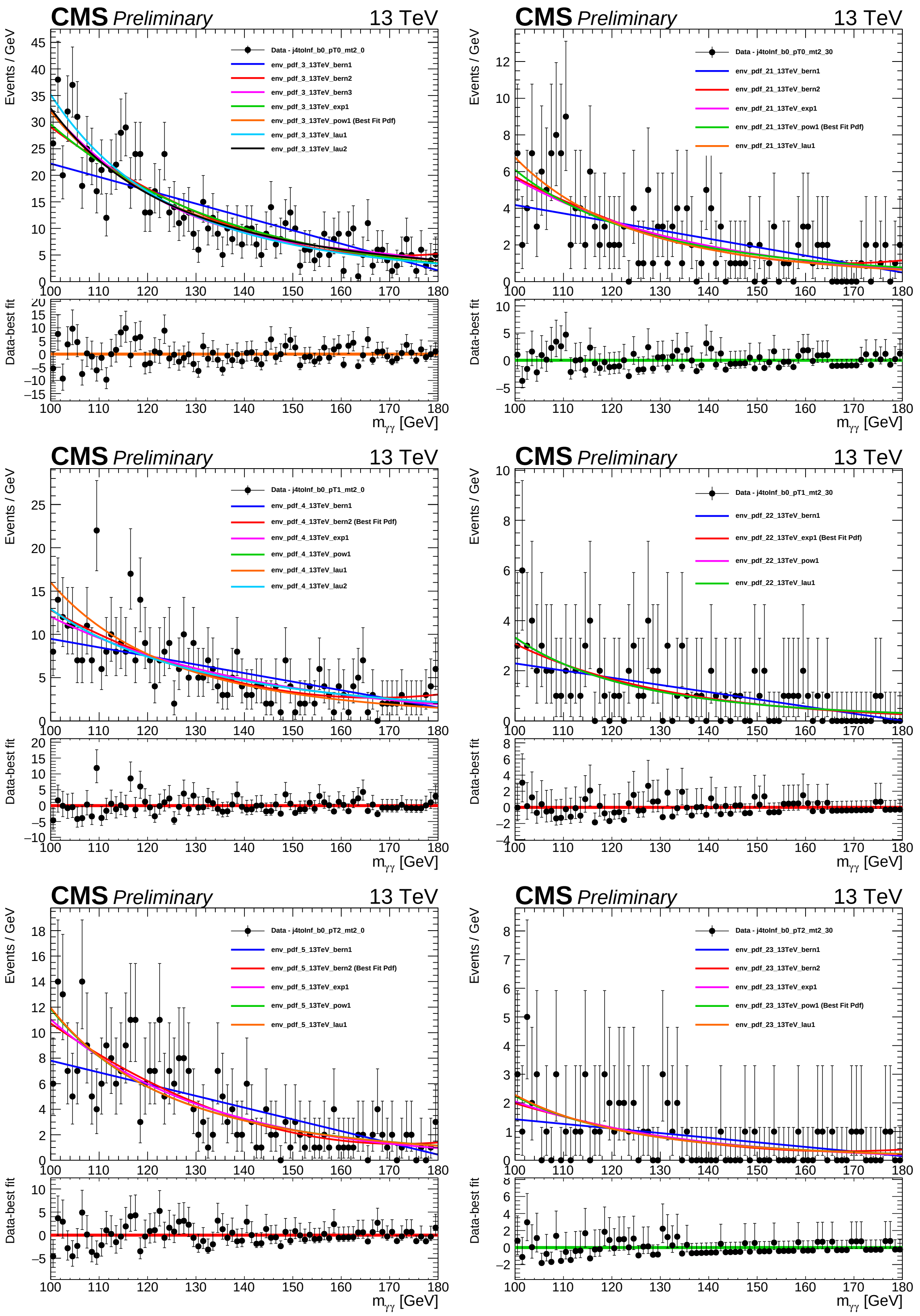

Figure C.10: The data (black marker) and the fits to the nonresonant background (lines) for the at least 4 jets and 0 b-tagged jets regions. The different colored lines represent the functions that the envelope of the region consists of.

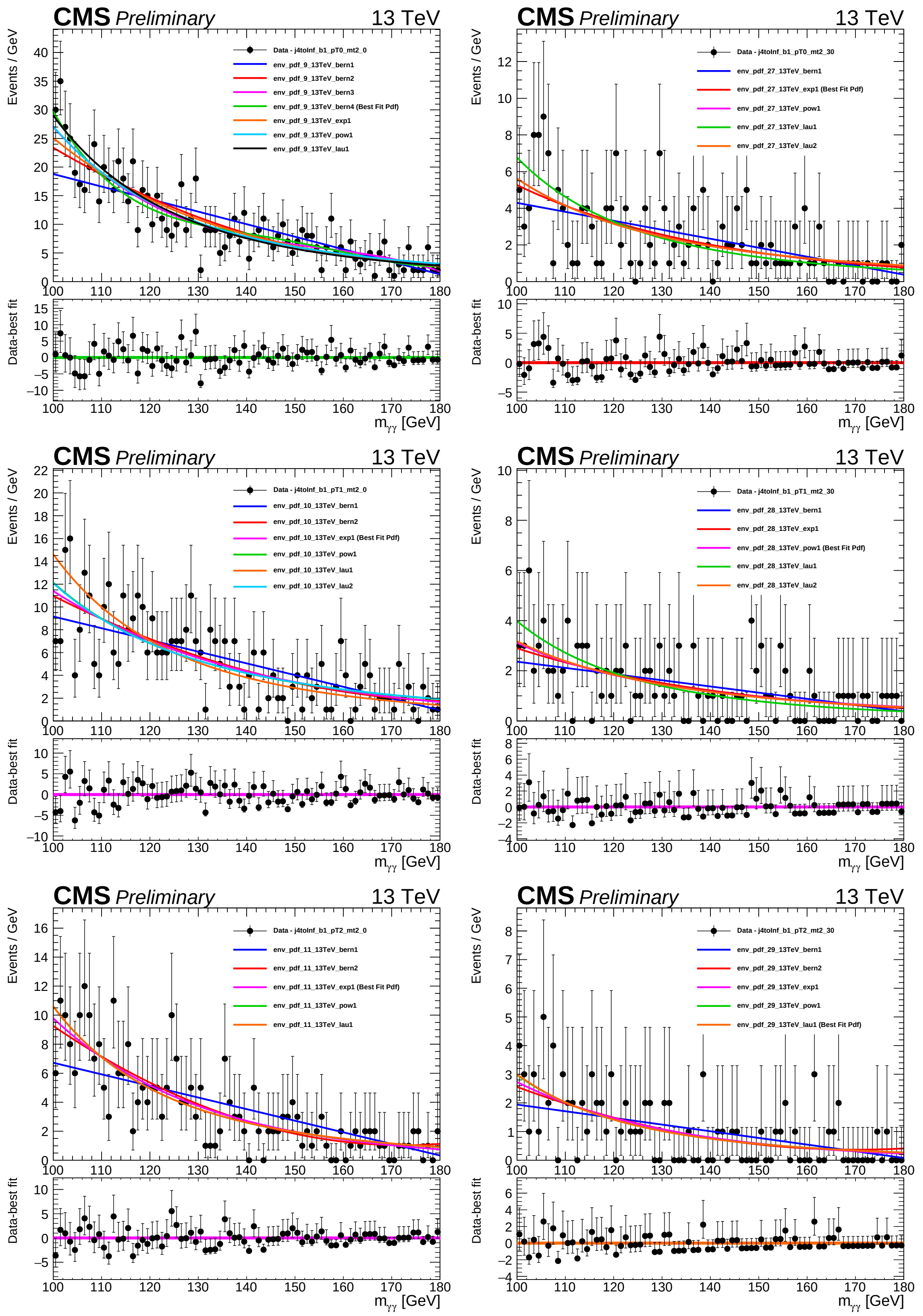

Figure C.11: The data (black marker) and the fits to the nonresonant background (lines) for the at least 4 jets and 1 b-tagged jets regions. The different colored lines represent the functions that the envelope of the region consists of.

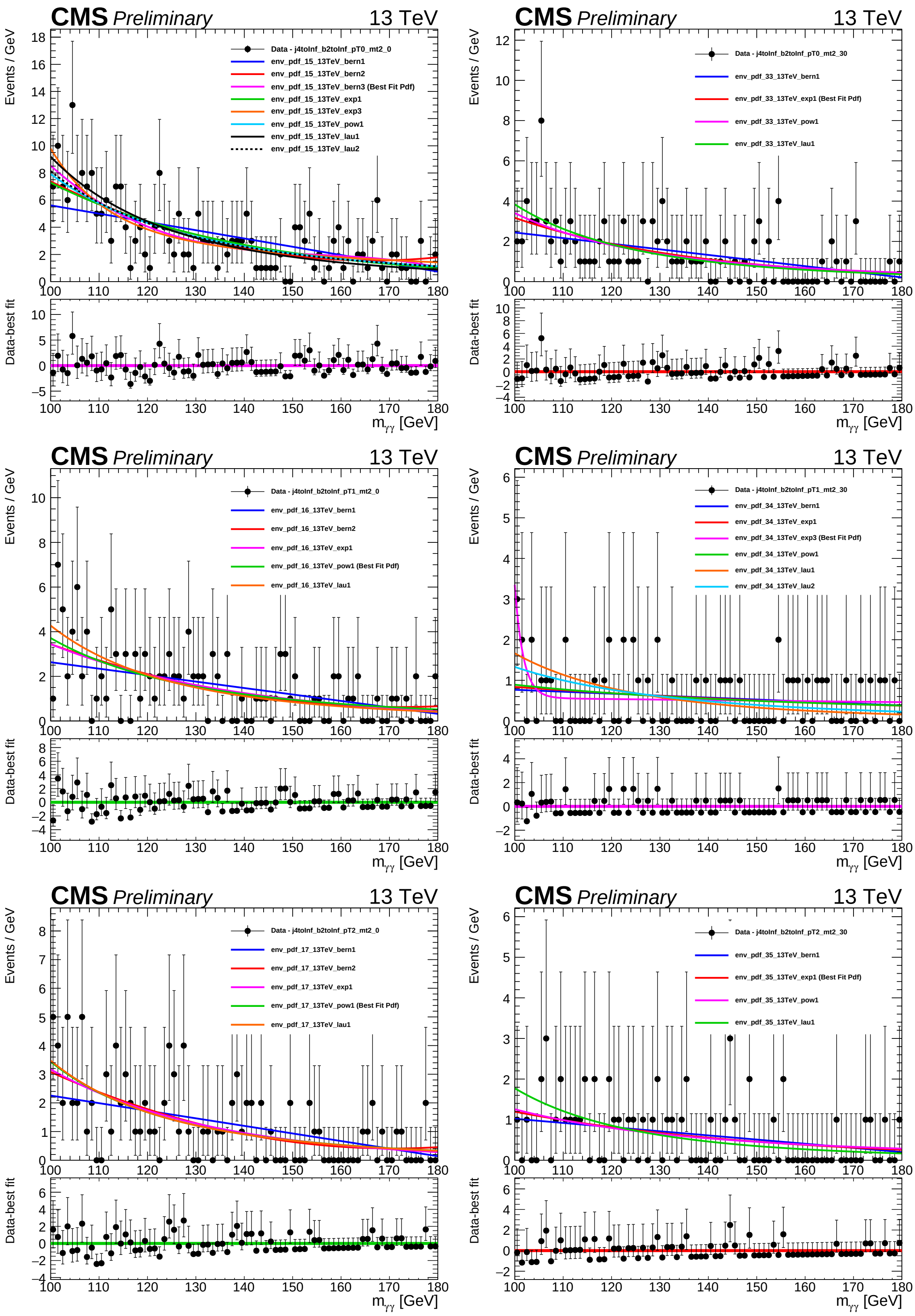

Figure C.12: The data (black marker) and the fits to the nonresonant background (lines) for the at least 4 jets and at least 2 b-tagged jets regions. The different colored lines represent the functions that the envelope of the region consists of.

C.3 Event display

Figure C.13 shows an event with two photons and two muons with an invariant mass compatible with a Z boson.

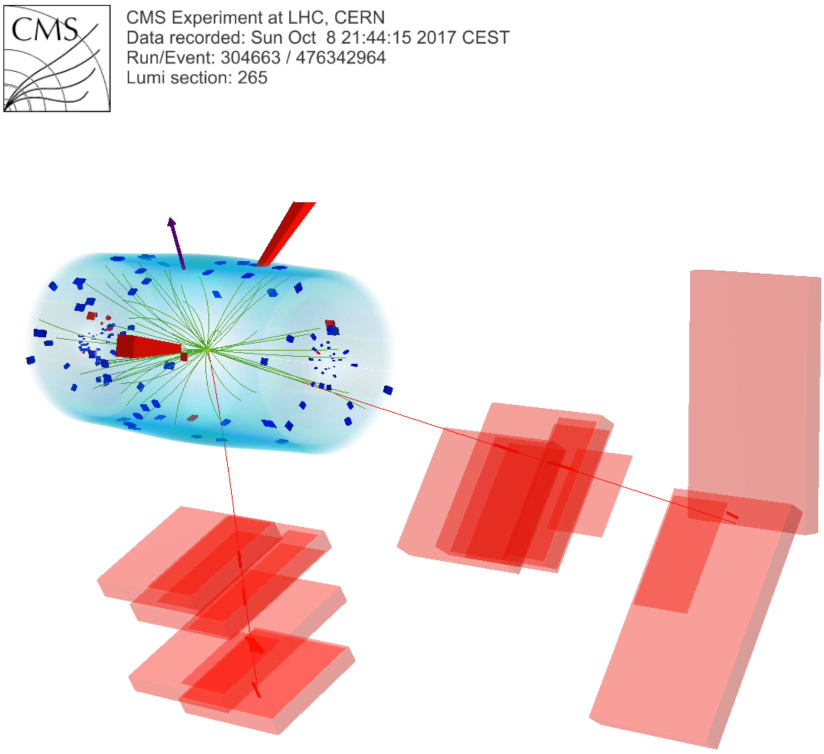

Figure C.13: Event showing a candidate for a Higgs decaying to two photons and a Z-boson decaying to two muons.

D Bibliography

[1] Michael E. Peskin. Lectures on the Theory of the Weak Interaction. Lectures on the Theory of the Weak Interaction. (SLAC-PUB-17142. SLAC-PUB-17142):1–70. 96 p, Aug 2017. doi: 10.23730/CYRSP-2017-005.1. URL https://cds.cern.ch/record/2300399.

[2] B.C. Allanach. Beyond the Standard Model Lectures for the 2016 European School of High-Energy Physics. (arXiv:1609.02015):30 p, Sep 2016. doi: 10.23730/CYRSP-2017-005.123. URL https://cds.cern.ch/record/2214349.

[3] R. P. Feynman: Elementary Particles and the Laws of Physics (1986 Dirac memorial lecture) III. URL https://youtu.be/p0eYf4PA2O8?t=323.

[4] M. Tanabashi et al. Review of particle physics. *Phys. Rev. D*, 98:030001, Aug 2018. doi: 10.1103/PhysRevD.98.030001. URL https://link.aps.org/doi/10.1103/PhysRevD.98.030001.

[5] E. Noether. Invariante Variationsprobleme. *Nachrichten von der Gesellschaft der Wissenschaften zu Göttingen, Mathematisch-Physikalische Klasse*, 1918: 235–257, 1918. URL http://eudml.org/doc/59024.

[6] David J. Gross and Frank Wilczek. Ultraviolet behavior of non-abelian gauge theories. *Phys. Rev. Lett.*, 30:1343–1346, Jun 1973. doi: 10.1103/PhysRevLett.30.1343. URL https://link.aps.org/doi/10.1103/PhysRevLett.30.1343.

[7] F. Englert and R. Brout. Broken symmetry and the mass of gauge vector mesons. *Phys. Rev. Lett.*, 13:321–323, Aug 1964. doi: 10.1103/PhysRevLett.13.321. URL https://link.aps.org/doi/10.1103/PhysRevLett.13.321.

[8] Peter W. Higgs. Broken symmetries and the masses of gauge bosons. *Phys. Rev. Lett.*, 13:508–509, Oct 1964. doi: 10.1103/PhysRevLett.13.508. URL https://link.aps.org/doi/10.1103/PhysRevLett.13.508.

[9] G. S. Guralnik, C. R. Hagen, and T. W. B. Kibble. Global conservation laws and massless particles. *Phys. Rev. Lett.*, 13:585–587, Nov 1964. doi: 10.1103/PhysRevLett.13.585. URL https://link.aps.org/doi/10.1103/PhysRevLett.13.585.

[10] F. Quevedo, S. Krippendorf, and O. Schlotterer. Cambridge Lectures on Supersymmetry and Extra Dimensions. 2010. URL http://arxiv.org/abs/arXiv:1011.1491.

[11] ATLAS and CMS Collaborations. Measurements of the Higgs boson production and decay rates and constraints on its couplings from a combined ATLAS and CMS analysis of the LHC pp collision data at $\sqrt{s} = 7$ and 8 TeV. *JHEP*, 08:045, 2016. doi: 10.1007/JHEP08(2016)045. URL https://doi.org/10.1007/JHEP08(2016)045.

[12] S Dittmaier et al. *Handbook of LHC Higgs Cross Sections: 1. Inclusive Observables*. CERN Yellow Reports: Monographs. CERN, Geneva, 2011. doi: 10.5170/CERN-2011-002. URL https://cds.cern.ch/record/1318996.

[13] A. Denner et al. Standard Model Higgs-Boson Branching Ratios with Uncertainties. *Eur. Phys. J.*, C71:1753, 2011. doi: 10.1140/epjc/s10052-011-1753-8. URL https://doi.org/10.1140/epjc/s10052-011-1753-8.

[14] CMS Collaboration. Summaries of CMS cross section measurements. URL https://twiki.cern.ch/twiki/bin/view/CMSPublic/PhysicsResultsCombined.

[15] LIGO Scientific Collaboration and Virgo Collaboration. Observation of gravitational waves from a binary black hole merger. *Phys. Rev. Lett.*, 116:061102, Feb 2016. doi: 10.1103/PhysRevLett.116.061102. URL https://link.aps.org/doi/10.1103/PhysRevLett.116.061102.

[16] Planck Collaboration, Ade, P. A. R., et al. Planck 2015 results - xiii. cosmological parameters. *A&A*, 594:A13, 2016. doi: 10.1051/0004-6361/201525830. URL https://doi.org/10.1051/0004-6361/201525830.

[17] Steven Weinberg. The cosmological constant problem. *Rev. Mod. Phys.*, 61:1–23, Jan 1989. doi: 10.1103/RevModPhys.61.1. URL https://link.aps.org/doi/10.1103/RevModPhys.61.1.

[18] Y. Fukuda et al. Evidence for oscillation of atmospheric neutrinos. *Phys. Rev. Lett.*, 81:1562–1567, 1998. doi: 10.1103/PhysRevLett.81.1562. URL https://link.aps.org/doi/10.1103/PhysRevLett.81.1562.

[19] N. Agafonova et al. Observation of a first ν_τ candidate event in the opera experiment in the cngs beam. *Physics Letters B*, 691(3):138 – 145, 2010. ISSN 0370-2693. doi: https://doi.org/10.1016/j.physletb.2010.06.022. URL http://www.sciencedirect.com/science/article/pii/S0370269310007537.

[20] Stephen P. Martin. *A Supersymmetry Primer*, pages 1–153. doi: 10.1142/9789814307505_0001. URL https://www.worldscientific.com/doi/abs/10.1142/9789814307505_0001.

[21] Super-Kamiokande Collaboration. Search for proton decay via $p \to e^+\pi^0$ and $p \to \mu^+\pi^0$ in 0.31 megaton·years exposure of the Super-Kamiokande water Cherenkov detector. *Phys. Rev.*, D95(1):012004, 2017. doi: 10.1103/

PhysRevD.95.012004. URL https://link.aps.org/doi/10.1103/PhysRevD.95.012004.

[22] R. Franceschini and R. N. Mohapatra. New Patterns of Natural R-Parity Violation with Supersymmetric Gauged Flavor. *JHEP*, 04:098, 2013. doi: 10.1007/JHEP04(2013)098. URL https://doi.org/10.1007/JHEP04(2013)098.

[23] Johan Alwall, My-Phuong Le, Mariangela Lisanti, and Jay G. Wacker. Model-independent jets plus missing energy searches. *Phys. Rev. D*, 79:015005, Jan 2009. doi: 10.1103/PhysRevD.79.015005. URL https://link.aps.org/doi/10.1103/PhysRevD.79.015005.

[24] Daniele Alves and other. Simplified models for LHC new physics searches. *Journal of Physics G: Nuclear and Particle Physics*, 39(10):105005, sep 2012. doi: 10.1088/0954-3899/39/10/105005. URL https://doi.org/10.1088%2F0954-3899%2F39%2F10%2F105005.

[25] CMS Collaboration. Interpretation of searches for supersymmetry with simplified models. *Phys. Rev. D*, 88:052017, Sep 2013. doi: 10.1103/PhysRevD.88.052017. URL https://link.aps.org/doi/10.1103/PhysRevD.88.052017.

[26] N. Arkani-Hamed et al. MARMOSET: The Path from LHC Data to the New Standard Model via On-Shell Effective Theories. 2007. URL http://arxiv.org/abs/hep-ph/0703088.

[27] Johan Alwall, Philip C. Schuster, and Natalia Toro. Simplified models for a first characterization of new physics at the lhc. *Phys. Rev. D*, 79:075020, Apr 2009. doi: 10.1103/PhysRevD.79.075020. URL https://link.aps.org/doi/10.1103/PhysRevD.79.075020.

[28] https://twiki.cern.ch/twiki/bin/view/lhcphysics/susycrosssections. URL https://twiki.cern.ch/twiki/bin/view/LHCPhysics/SUSYCrossSections.

[29] ATLAS Collaboration. Search for top squark pair production in final states with one isolated lepton, jets, and missing transverse momentum in $\sqrt{s} = 8$ TeV *pp* collisions with the ATLAS detector. *JHEP*, 11(CERN-PH-EP-2014-143. arXiv:1407.0583):118. 94 p, Jul 2014. doi: 10.1007/JHEP11(2014)118. URL https://cds.cern.ch/record/1714148.

[30] W. Beenakker, M. Klasen, M. Krämer, T. Plehn, M. Spira, and P. M. Zerwas. Production of charginos, neutralinos, and sleptons at hadron colliders. *Phys. Rev. Lett.*, 83:3780, 1999. doi: 10.1103/PhysRevLett.83.3780. [Erratum: 10.1103/PhysRevLett.100.029901].

[31] Benjamin Fuks, Michael Klasen, David R. Lamprea, and Marcel Rothering. Gaugino production in proton-proton collisions at a center-of-mass energy of 8 TeV. *JHEP*, 10:081, 2012. doi: 10.1007/JHEP10(2012)081. URL https://doi.org/10.1007/JHEP10(2012)081.

[32] Benjamin Fuks, Michael Klasen, David R. Lamprea, and Marcel Rothering. Precision predictions for electroweak superpartner production at hadron colliders with Resummino. *Eur. Phys. J. C*, 73:2480, 2013. doi: 10.1140/epjc/s10052-013-2480-0. URL https://doi.org/10.1140/epjc/s10052-013-2480-0.

[33] Savas Dimopoulos, Michael Dine, Stuart Raby, and Scott D. Thomas. Experimental signatures of low-energy gauge mediated supersymmetry breaking. *Phys. Rev. Lett.*, 76:3494, 1996. doi: 10.1103/PhysRevLett.76.3494. URL http://dx.doi.org/10.1103/PhysRevLett.76.3494.

[34] Konstantin T. Matchev and Scott D. Thomas. Higgs and Z boson signatures of supersymmetry. *Phys. Rev. D*, 62:077702, 2000. doi: 10.1103/PhysRevD.62.077702. URL https://link.aps.org/doi/10.1103/PhysRevD.62.077702.

[35] Lyndon Evans and Philip Bryant. LHC machine. *Journal of Instrumentation*, 3(08):S08001–S08001, aug 2008. doi: 10.1088/1748-0221/3/08/s08001. URL https://doi.org/10.1088%2F1748-0221%2F3%2F08%2Fs08001.

[36] ATLAS Collaboration. The ATLAS Experiment at the CERN Large Hadron Collider. *Journal of Instrumentation*, 3(08):S08003, 2008. URL http://stacks.iop.org/1748-0221/3/i=08/a=S08003.

[37] CMS Collaboration. The CMS experiment at the CERN LHC. *Journal of Instrumentation*, 3(08):S08004, 2008. URL http://stacks.iop.org/1748-0221/3/i=08/a=S08004.

[38] ALICE Collaboration. The ALICE experiment at the CERN LHC. *Journal of Instrumentation*, 3(08):S08002, 2008. URL http://stacks.iop.org/1748-0221/3/i=08/a=S08002.

[39] LHCb Collaboration. The LHCb Detector at the LHC. *Journal of Instrumentation*, 3(08):S08005, 2008. URL http://stacks.iop.org/1748-0221/3/i=08/a=S08005.

[40] E. Mobs. The CERN accelerator complex. Complexe des accélérateurs du CERN. Jul 2016. URL https://cds.cern.ch/record/2197559. General Photo.

[41] CMS Luminosity Measurements for the 2016 Data Taking Period. Technical Report CMS-PAS-LUM-17-001, CERN, Geneva, 2017. URL https://cds.cern.ch/record/2257069.

[42] CMS Collaboration . CMS Luminosity - Public results. URL https://twiki.cern.ch/twiki/bin/view/CMSPublic/LumiPublicResults.

[43] I. Neutelings. How to draw diagrams in LaTeX with TikZ. URL https://wiki.physik.uzh.ch/cms/latex:tikz.

[44] CMS Collaboration. CMS Physics Technical Design Report, Volume I: Detector Performance and Software. Technical report, Geneva, 2006. URL http://cds.cern.ch/record/922757.

[45] K. Klein. The Phase-1 Upgrade of the CMS pixel detector. Technical Report CMS-CR-2016-036, CERN, Geneva, Mar 2016. URL https://cds.cern.ch/record/2140071.

[46] CMS Collaboration. *The CMS electromagnetic calorimeter project: Technical Design Report*. Technical Design Report CMS. CERN, Geneva, 1997. URL https://cds.cern.ch/record/349375.

[47] CMS Collaboration. Energy resolution of the barrel of the CMS electromagnetic calorimeter. *Journal of Instrumentation*, 2(04):P04004–P04004, apr 2007. doi: 10.1088/1748-0221/2/04/p04004. URL https://doi.org/10.1088%2F1748-0221%2F2%2F04%2Fp04004.

[48] CMS Collaboration. Performance of the CMS hadron calorimeter with cosmic ray muons and LHC beam data. *Journal of Instrumentation*, 5(03):T03012–T03012, mar 2010. doi: 10.1088/1748-0221/5/03/t03012. URL https://doi.org/10.1088%2F1748-0221%2F5%2F03%2Ft03012.

[49] CMS Collaboration. Precise mapping of the magnetic field in the CMS barrel yoke using cosmic rays. *Journal of Instrumentation*, 5(03):T03021–T03021, mar 2010. doi: 10.1088/1748-0221/5/03/t03021. URL https://doi.org/10.1088%2F1748-0221%2F5%2F03%2Ft03021.

[50] CMS Collaboration. Performance of the CMS muon detector and muon reconstruction with proton-proton collisions at $\sqrt{s}$=13 TeV. *Journal of Instrumentation*, 13(06):P06015–P06015, jun 2018. doi: 10.1088/1748-0221/13/06/p06015. URL https://doi.org/10.1088%2F1748-0221%2F13%2F06%2Fp06015.

[51] CMS Collaboration. *CMS. The TriDAS project. Technical design report, vol. 1: The trigger systems*. Technical Design Report CMS. CERN, Geneva, 2000. URL https://cds.cern.ch/record/706847.

[52] CMS Collaboration. *CMS The TriDAS Project: Technical Design Report, Volume 2: Data Acquisition and High-Level Trigger. CMS trigger and data-acquisition project*. Technical Design Report CMS. CERN, Geneva, 2002. URL http://cds.cern.ch/record/578006.

[53] CMS Collaboration. Cms tracking performance results from early lhc operation. *Eur. Phys. J.*, 70(4):1165–1192, Dec 2010. ISSN 1434-6052. doi: 10.1140/epjc/s10052-010-1491-3. URL https://doi.org/10.1140/epjc/s10052-010-1491-3.

[54] R. Frühwirth. Application of Kalman filtering to track and vertex fitting. *Nuclear Instruments and Methods in Physics Research Section A: Accelerators, Spectrometers, Detectors and Associated Equipment*, 262(2):444 – 450, 1987. ISSN 0168-9002. doi: 10.1016/0168-9002(87)90887-4. URL https://doi.org/10.1016/0168-9002(87)90887-4.

[55] K. Rose. Deterministic annealing for clustering, compression, classification, regression, and related optimization problems. *Proceedings of the IEEE*, 86 (11):2210–2239, Nov 1998. doi: 10.1109/5.726788. URL https://doi.org/10.1109/5.726788.

[56] W. Waltenberger et al. Adaptive vertex fitting. *Journal of Physics G: Nuclear and Particle Physics*, 34(12):N343–N356, nov 2007. doi: 10.1088/0954-3899/34/12/n01. URL https://doi.org/10.1088%2F0954-3899%2F34%2F12%2Fn01.

[57] CMS Collaboration. Description and performance of track and primary-vertex reconstruction with the CMS tracker. *Journal of Instrumentation*, 9(10): P10009–P10009, oct 2014. doi: 10.1088/1748-0221/9/10/p10009. URL https://doi.org/10.1088%2F1748-0221%2F9%2F10%2Fp10009.

[58] CMS Collaboration. Particle-flow reconstruction and global event description with the CMS detector. *Journal of Instrumentation*, 12(10):P10003–P10003, oct 2017. doi: 10.1088/1748-0221/12/10/p10003. URL https://doi.org/10.1088%2F1748-0221%2F12%2F10%2Fp10003.

[59] CMS Collaboration. Interactive Slice of the CMS detector. URL https://cms-docdb.cern.ch/cgi-bin/DocDB/ShowDocument?docid=4172.

[60] CMS Collaboration. Performance of CMS muon reconstruction in pp collision events at $\sqrt{s} = 7$TeV. *Journal of Instrumentation*, 7(10):P10002–P10002, oct 2012. doi: 10.1088/1748-0221/7/10/p10002. URL https://doi.org/10.1088%2F1748-0221%2F7%2F10%2Fp10002.

[61] W Adam, R Frühwirth, A Strandlie, and T Todorov. Reconstruction of electrons with the gaussian-sum filter in the CMS tracker at the LHC. *Journal of Physics G: Nuclear and Particle Physics*, 31(9):N9–N20, jul 2005. doi: 10.1088/0954-3899/31/9/n01. URL https://doi.org/10.1088%2F0954-3899%2F31%2F9%2Fn01.

[62] CMS Collaboration. Performance of electron reconstruction and selection with the CMS detector in proton-proton collisions at $\sqrt{s}$= 8 TeV. *Journal of Instrumentation*, 10(06):P06005–P06005, jun 2015. doi: 10.1088/1748-0221/

10/06/p06005. URL https://doi.org/10.1088%2F1748-0221%2F10%2F06%2Fp06005.

[63] CMS Collaboration. Energy calibration and resolution of the CMS electromagnetic calorimeter in pp collisions at $\sqrt{s}$= 7 TeV. *Journal of Instrumentation*, 8(09):P09009–P09009, sep 2013. doi: 10.1088/1748-0221/8/09/p09009. URL https://doi.org/10.1088%2F1748-0221%2F8%2F09%2Fp09009.

[64] M. Cacciari, Gavin P. Salam, and G. Soyez. The anti-k_t jet clustering algorithm. *JHEP*, 04:063, 2008. doi: 10.1088/1126-6708/2008/04/063. URL https://doi.org/10.1088/1126-6708/2008/04/063.

[65] CMS Collaboration. Jet performance in pp collisions at $\sqrt{s}$=7 TeV. CMS Physics Analysis Summary CMS-PAS-JME-10-003, 2010. URL http://cdsweb.cern.ch/record/1279362.

[66] CMS Collaboration. Pileup mitigation at CMS in 13 TeV data. Technical Report CMS-PAS-JME-18-001, CERN, Geneva, 2019. URL https://cds.cern.ch/record/2683784.

[67] CMS Collaboration. Identification of heavy-flavour jets with the CMS detector in pp collisions at 13 TeV. *Journal of Instrumentation*, 13(05):P05011–P05011, may 2018. doi: 10.1088/1748-0221/13/05/p05011. URL https://doi.org/10.1088%2F1748-0221%2F13%2F05%2Fp05011.

[68] CMS Collaboration. Performance of missing transverse momentum reconstruction in proton-proton collisions at $\sqrt{s}$ = 13 TeV using the CMS detector. *JINST*, 14(07):P07004, 2019. doi: 10.1088/1748-0221/14/07/P07004. URL https://doi.org/10.1088%2F1748-0221%2F14%2F07%2Fp07004.

[69] C.G. Lester and D.J. Summers. Measuring masses of semiinvisibly decaying particles pair produced at hadron colliders. *Phys. Lett. B*, 463:99, 1999. doi: 10.1016/S0370-2693(99)00945-4. URL https://doi.org/10.1016/S0370-2693(99)00945-4.

[70] CMS Collaboration. CMS physics technical design report, volume II: Physics performance. *J. Phys. G*, 34:995–1579, 2007. doi: 10.1088/0954-3899/34/6/S01. URL https://doi.org/10.1088%2F0954-3899%2F34%2F6%2Fs01.

[71] T. Sjöstrand et al. PYTHIA 6.4 physics and manual. *JHEP*, 05:026, 2006. doi: 10.1088/1126-6708/2006/05/026. URL https://doi.org/10.1088%2F1126-6708%2F2006%2F05%2F026.

[72] CMS Collaboration. Search for supersymmetry in hadronic final states with missing transverse energy using the variables α_T and b-quark multiplicity in pp collisions at $\sqrt{s}$ = 8 TeV. *Eur. Phys. J.*, 73(9):2568, Sep 2013. ISSN 1434-6052. doi: 10.1140/epjc/s10052-013-2568-6. URL https://doi.org/10.1140/epjc/s10052-013-2568-6.

[73] CMS Collaboration. Search for new physics in the multijet and missing transverse momentum final state in proton-proton collisions at $\sqrt{s}$= 8 TeV. *Journal of High Energy Physics*, 2014(6):55, Jun 2014. ISSN 1029-8479. doi: 10.1007/JHEP06(2014)055. URL https://doi.org/10.1007/JHEP06(2014)055.

[74] CMS Collaboration. Search for Gluino Mediated Bottom- and Top-Squark Production in Multijet Final States in *pp* Collisions at 8 TeV. *Phys. Lett.*, B725:243–270, 2013. doi: 10.1016/j.physletb.2013.06.058. URL https://cds.cern.ch/record/1546693.

[75] ATLAS Collaboration. Search for new phenomena in final states with an energetic jet and large missing transverse momentum in *pp* collisions at $\sqrt{s} = 13$ TeV using the ATLAS detector. *Phys. Rev. D*, 94:032005, Aug 2016. doi: 10.1103/PhysRevD.94.032005. URL https://link.aps.org/doi/10.1103/PhysRevD.94.032005.

[76] ATLAS Collaboration. Search for new phenomena in final states with large jet multiplicities and missing transverse momentum with ATLAS using $\sqrt{s} = 13$ TeV proton–proton collisions. *Physics Letters B*, 757:334 – 355, 2016. ISSN 0370-2693. doi: https://doi.org/10.1016/j.physletb.2016.04.005. URL http://www.sciencedirect.com/science/article/pii/S0370269316300752.

[77] ATLAS Collaboration. Search for squarks and gluinos in final states with jets and missing transverse momentum at $\sqrt{s} = 13$ TeV with the atlas detector. *Eur. Phys. J.*, 76(7):392, Jul 2016. ISSN 1434-6052. doi: 10.1140/epjc/s10052-016-4184-8. URL https://doi.org/10.1140/epjc/s10052-016-4184-8.

[78] ATLAS Collaboration. Search for pair production of gluinos decaying via stop and sbottom in events with b-jets and large missing transverse momentum in *pp* collisions at $\sqrt{s} = 13$ TeV with the atlas detector. *Phys. Rev. D*, 94:032003, Aug 2016. doi: 10.1103/PhysRevD.94.032003. URL https://link.aps.org/doi/10.1103/PhysRevD.94.032003.

[79] ATLAS Collaboration. Search for bottom squark pair production in proton–proton collisions at $\sqrt{s} = 13$ TeV with the atlas detector. *Eur. Phys. J.*, 76(10):547, Oct 2016. ISSN 1434-6052. doi: 10.1140/epjc/s10052-016-4382-4. URL https://doi.org/10.1140/epjc/s10052-016-4382-4.

[80] CMS Collaboration. Searches for supersymmetry using the MT2 variable in hadronic events produced in pp collisions at 8 TeV. *Journal of High Energy Physics*, 2015(5):78, May 2015. ISSN 1029-8479. doi: 10.1007/JHEP05(2015)078. URL https://doi.org/10.1007/JHEP05(2015)078.

[81] CMS Collaboration. Search for new physics with the MT2 variable in all-jets final states produced in pp collisions at $\sqrt{s}$=13 TeV. *Journal of High Energy*

Physics, 2016(10):6, Oct 2016. ISSN 1029-8479. doi: 10.1007/JHEP10(2016)006. URL https://doi.org/10.1007/JHEP10(2016)006.

[82] CMS Collaboration. Search for new phenomena with the MT2 variable in the all-hadronic final state produced in proton–proton collisions at $\sqrt{s}$ = 13 TeV. *Eur. Phys. J.*, 77(10):710, Oct 2017. ISSN 1434-6052. doi: 10.1140/epjc/s10052-017-5267-x. URL https://doi.org/10.1140/epjc/s10052-017-5267-x.

[83] J. Alwall et al. The automated computation of tree-level and next-to-leading order differential cross sections, and their matching to parton shower simulations. *Journal of High Energy Physics*, 2014(7):79, Jul 2014. ISSN 1029-8479. doi: 10.1007/JHEP07(2014)079. URL https://doi.org/10.1007/JHEP07(2014)079.

[84] J. Alwall et al. Comparative study of various algorithms for the merging of parton showers and matrix elements in hadronic collisions. *Eur. Phys. J.*, 53 (3):473–500, Feb 2008. ISSN 1434-6052. doi: 10.1140/epjc/s10052-007-0490-5. URL https://doi.org/10.1140/epjc/s10052-007-0490-5.

[85] T. Sjostrand et al. A Brief Introduction to PYTHIA 8.1. *Comput. Phys. Commun.*, 178:852–867, 2008. doi: 10.1016/j.cpc.2008.01.036. URL https://cds.cern.ch/record/1064095.

[86] S. Alioli et al. NLO single-top production matched with shower in POWHEG:s- and t-channel contributions. *Journal of High Energy Physics*, 2009(09):111–111, sep 2009. doi: 10.1088/1126-6708/2009/09/111. URL https://doi.org/10.1088%2F1126-6708%2F2009%2F09%2F111.

[87] Emanuele Re. Single-top wt-channel production matched with parton showers using the powheg method. *Eur. Phys. J.*, 71(2):1547, Feb 2011. ISSN 1434-6052. doi: 10.1140/epjc/s10052-011-1547-z. URL https://doi.org/10.1140/epjc/s10052-011-1547-z.

[88] S. Agostinelli et al. GEANT4—a simulation toolkit. *Nucl. Instrum. Meth. A*, 506:250, 2003. doi: 10.1016/S0168-9002(03)01368-8. URL https://doi.org/10.1016/S0168-9002(03)01368-8.

[89] S. Abdullin et al. The fast simulation of the CMS detector at LHC. *J. Phys. Conf. Ser.*, 331:032049, 2011. doi: 10.1088/1742-6596/331/3/032049. URL https://doi.org/10.1088%2F1742-6596%2F331%2F3%2F032049.

[90] A. Giammanco. The fast simulation of the CMS experiment. *J. Phys. Conf. Ser.*, 513:022012, 2014. doi: 10.1088/1742-6596/513/2/022012. URL https://doi.org/10.1088%2F1742-6596%2F513%2F2%2F022012.

[91] R. Gavin et al. Fewz 2.0: A code for hadronic z production at next-to-next-to-leading order. *Computer Physics Communications*, 182(11):2388 – 2403, 2011. ISSN 0010-4655. doi: https://doi.org/10.1016/j.cpc.2011.06.008. URL http://www.sciencedirect.com/science/article/pii/S0010465511002189.

[92] S. Quackenbush et al. W physics at the LHC with fewz 2.1. *Computer Physics Communications*, 184(1):209 – 214, 2013. ISSN 0010-4655. doi: https://doi.org/10.1016/j.cpc.2012.09.005. URL http://www.sciencedirect.com/science/article/pii/S0010465512002913.

[93] M. Czakon and A. Mitov. Top++: A program for the calculation of the top-pair cross-section at hadron colliders. *Computer Physics Communications*, 185(11):2930 – 2938, 2014. ISSN 0010-4655. doi: https://doi.org/10.1016/j.cpc.2014.06.021. URL http://www.sciencedirect.com/science/article/pii/S0010465514002264.

[94] C. Borschensky et al. Squark and gluino production cross sections in pp collisions at $\sqrt{s}$ = 13, 14, 33 and 100TeV. *Eur. Phys. J.*, 74(12):3174, Dec 2014. ISSN 1434-6052. doi: 10.1140/epjc/s10052-014-3174-y. URL https://doi.org/10.1140/epjc/s10052-014-3174-y.

[95] CMS Collaboration. Searches for physics beyond the standard model with the M_{T2} variable in hadronic final states with and without disappearing tracks in proton-proton collisions at $\sqrt{s} = 13$ TeV. Technical Report arXiv:1909.03460. CMS-SUS-19-005-003, CERN, Geneva, Sep 2019. URL https://cds.cern.ch/record/2688695.

[96] ATLAS Collaboration. Search for direct pair production of a chargino and a neutralino decaying to the 125 GeV Higgs boson in $\sqrt{s} = 8$ TeV pp collisions with the ATLAS detector. *Eur. Phys. J. C*, 75:208, 2015. doi: 10.1140/epjc/s10052-015-3408-7. URL https://doi.org/10.1140/epjc/s10052-015-3408-7.

[97] CMS Collaboration. Searches for electroweak neutralino and chargino production in channels with Higgs, Z, and W bosons in pp collisions at 8 TeV. *Phys. Rev. D*, 90:092007, 2014. doi: 10.1103/PhysRevD.90.092007. URL https://link.aps.org/doi/10.1103/PhysRevD.90.092007.

[98] CMS Collaboration. Search for supersymmetry with Higgs boson to diphoton decays using the razor variables at $\sqrt{s} = 13$ TeV. *Phys. Lett. B*, 779:166, 2018. doi: 10.1016/j.physletb.2017.12.069. URL https://doi.org/10.1016/j.physletb.2017.12.069.

[99] ATLAS Collaboration. Search for chargino and neutralino production in final states with a Higgs boson and missing transverse momentum at $\sqrt{s} =$ 13 TeV with the ATLAS detector. *Phys. Rev.*, D100(1):012006, 2019. doi:

10.1103/PhysRevD.100.012006. URL https://doi.org/10.1103/PhysRevD.100.012006.

[100] CMS Collaboration. Search for supersymmetry using Higgs boson to diphoton decays at $\sqrt{s} = 13$ TeV. *Journal of High Energy Physics*, 2019(11):109, Dec 2019. ISSN 1029-8479. doi: 10.1007/JHEP11(2019)109. URL https://doi.org/10.1007/JHEP11(2019)109.

[101] C. Rogan. Kinematical variables towards new dynamics at the LHC. *arXiv e-prints*, art. arXiv:1006.2727, Jun 2010.

[102] CMS Collaboration. Inclusive search for supersymmetry using razor variables in pp collisions at $\sqrt{s} = 13$ TeV. *Phys. Rev. D*, 95:012003, 2017. doi: 10.1103/PhysRevD.95.012003. URL https://doi.org/10.1103/PhysRevD.95.012003.

[103] CMS Collaboration. Observation of the diphoton decay of the higgs boson and measurement of its properties. *Eur. Phys. J.*, 74(10):3076, Oct 2014. ISSN 1434-6052. doi: 10.1140/epjc/s10052-014-3076-z. URL https://doi.org/10.1140/epjc/s10052-014-3076-z.

[104] D. de Florian et al. Handbook of LHC Higgs cross sections: 4. deciphering the nature of the Higgs sector. CERN Report CERN-2017-002-M, 2016. URL https://cds.cern.ch/record/2227475.

[105] R. Frederix and S. Frixione. Merging meets matching in MC@NLO. *JHEP*, 12:061, 2012. doi: 10.1007/JHEP12(2012)061. URL https://doi.org/10.1007/JHEP12(2012)061.

[106] T. Sjöstrand et al. An Introduction to PYTHIA 8.2. *Comput. Phys. Commun.*, 191:159, 2015. doi: 10.1016/j.cpc.2015.01.024. URL https://doi.org/10.1016/j.cpc.2015.01.024.

[107] P. Skands, S. Carrazza, and J. Rojo. Tuning PYTHIA 8.1: the Monash 2013 tune. *Eur. Phys. J. C*, 74:3024, 2014. doi: 10.1140/epjc/s10052-014-3024-y. URL https://doi.org/10.1140/epjc/s10052-014-3024-y.

[108] CMS Collaboration. Extraction and validation of a new set of CMS PYTHIA8 tunes from underlying-event measurements. 2020. URL https://doi.org/10.1140/epjc/s10052-019-7499-4.

[109] Richard D. Ball et al. Parton distributions for the LHC Run II. *JHEP*, 04:040, 2015. doi: 10.1007/JHEP04(2015)040. URL http://dx.doi.org/10.1007/JHEP04(2015)040.

[110] Richard D. Ball et al. Parton distributions from high-precision collider data. *Eur. Phys. J. C*, 77:663, 2017. doi: 10.1140/epjc/s10052-017-5199-5. URL https://doi.org/10.1140/epjc/s10052-017-5199-5.

[111] CMS Collaboration. Identification of b-quark jets with the CMS experiment. *JINST*, 8:P04013, 2013. doi: 10.1088/1748-0221/8/04/P04013. URL https://doi.org/10.1088/1748-0221/8/04/P04013.

[112] P.D. Dauncey, M. Kenzie, N. Wardle, and G.J. Davies. Handling uncertainties in background shapes: the discrete profiling method. *Journal of Instrumentation*, 10(04):P04015, 2015. URL http://stacks.iop.org/1748-0221/10/i=04/a=P04015.

[113] CMS luminosity measurement for the 2017 data-taking period at $\sqrt{s} = 13$ TeV. Technical Report CMS-PAS-LUM-17-004, CERN, Geneva, 2018. URL https://cds.cern.ch/record/2621960.

[114] LHC Higgs Cross Section Working Group. Handbook of LHC Higgs Cross Sections: 3. Higgs Properties. *CERN-2013-004*, CERN, Geneva, 2013. doi: 10.5170/CERN-2013-004. URL http://dx.doi.org/10.5170/CERN-2013-004.

[115] Jon Butterworth, Stefano Carrazza, Amanda Cooper-Sarkar, Albert De Roeck, Joël Feltesse, Stefano Forte, Jun Gao, Sasha Glazov, Joey Huston, Zahari Kassabov, Ronan McNulty, Andreas Morsch, Pavel Nadolsky, Voica Radescu, Juan Rojo, and Robert Thorne. PDF4lhc recommendations for LHC run II. *Journal of Physics G: Nuclear and Particle Physics*, 43(2):023001, jan 2016. doi: 10.1088/0954-3899/43/2/023001. URL https://doi.org/10.1088%2F0954-3899%2F43%2F2%2F023001.

[116] A. Kalogeropoulos and J. Alwall. The SysCalc code: A tool to derive theoretical systematic uncertainties, 2018. URL https://arxiv.org/abs/1801.08401.

[117] Alexander L. Read. Presentation of search results: The CL_s technique. *J. Phys. G*, 28:2693, 2002. doi: 10.1088/0954-3899/28/10/313. URL https://doi.org/10.1088%2F0954-3899%2F28%2F10%2F313.

[118] Thomas Junk. Confidence level computation for combining searches with small statistics. *Nuclear Instruments and Methods in Physics Research Section A: Accelerators, Spectrometers, Detectors and Associated Equipment*, 434(2):435 – 443, 1999. ISSN 0168-9002. doi: https://doi.org/10.1016/S0168-9002(99)00498-2. URL http://www.sciencedirect.com/science/article/pii/S0168900299004982.

[119] Glen Cowan, Kyle Cranmer, Eilam Gross, and Ofer Vitells. Asymptotic formulae for likelihood-based tests of new physics. *Eur. Phys. J. C*, 71:1554, 2011. doi: 10.1140/epjc/s10052-011-1554-0. URL https://doi.org/10.1088%2F0954-3899%2F28%2F8%2F313.

[120] ATLAS and CMS Collaborations. Procedure for the LHC Higgs boson search combination in summer 2011. CMS NOTE/ATL-PHYS-PUB ATL-PHYS-PUB-2011-011, CMS-NOTE-2011-005, 2011. URL http://cds.cern.ch/record/1379837.

[121] Search for new physics in the all-hadronic final state with the MT2 variable. Technical Report CMS-PAS-SUS-16-015, CERN, Geneva, 2016. URL https://cds.cern.ch/record/2205162.

E Acknowledgement

I would like to first thank the ETH professors Rainer, Günther and Christoph, you have guided me through various stages in my life as a physicist, from first year lectures to finally this thesis.

Further I would like to thank my former and current colleagues, in particular Francesco, Mario, Bruno and Boris that initiated me into the world of physics analyses. For their help and inputs on this and the other side of the pond I would like to express my gratitude to Frank, Gio, Dominick, Claudio, Avi, FKW, Jason, Mark and Bennett. Working as part of MECCA was at times stressful but it was what pushed me to become a better physicist.

I would also like to thank the Caltech group that I had the pleasure to work alongside. I also thank Pasquale and Vittorio for their help with the flashgg framework.

For the entertainment with their banter I would like to thanks Mario and Bruno again, you probably didn't expect me to stay in the office for this long when I first showed up as a master student. All the colleagues that came and went in my time at ETH, in Zürich and Geneva, who I shared a meal, a beer, a song with, thank you.

Vorrei anche ringraziare Mauro e Maria Giulia per il loro aiuto e in particolare per la lettura e il miglioramento di questa tesi. Ein grosses Dankeschön auch an Vinz für das deutschisieren der Zusammenfassung dieser Dissertation und für unseren Buchklub.

I thank my family and friends for their support and love, I somehow ended up not completely crazy at the end of this PhD thanks to you.

A special thanks goes to my high school physics teacher Daniel Müggler, for sparking my interest in physics. In some parallel universe I probably didn't write this thesis because you didn't take the time to answer my truck load of questions.

마지막으로 샤이니, 빅뱅, 슈퍼주니어, 젝스키스에게 감사드리고 싶습니다. 음악을 잘 들었습니다. 그리고 잘 웃었습니다. 당신이 없었더라면 미칠 뻔 했어요.